Short-bite diphosphine ligands and their transition metal complexes: synthesis, properties and applications

Zur Erlangung des akademischen Grades einer

DOKTORIN DER NATURWISSENSCHAFTEN

(Dr. rer. nat.)

von der KIT-Fakultät für Chemie und Biowissenschaften

des Karlsruher Instituts für Technologie (KIT)

genehmigte

DISSERTATION

von

Franziska Flecken

1. Referentin: T.T.-Prof. Dr. Schirin Hanf
2. Referentin: Prof. Dr. Silke Behrens

Tag der mündlichen Prüfung: 24.10.2024

Für meine Familie

§ 1 Et es wie et es

§ 2 Et kütt wie et kütt

§ 3 Et hätt noch immer jot jejange

Declaration

The presented work in this dissertation was carried out in the Institute for Inorganic Chemistry at the Karlsruhe Institute of Technology under the supervision of TT.-Prof. Schirin Hanf between November 2020 and September 2024. I, Franziska Flecken, declare that I have completed the present thesis independently and without illegitimate assistance from third parties. I have used no other than the specified sources and aids. The thesis has not been submitted to any examination body in this, or similar, form.

_____

City, Date

_____

Signature

Abstract

While conventional short-bite ligands, featuring PCP- and PNP-backbones, have been extensively investigated in the past, the oxygen- (POP) and sulphur-based (PSP) analogues of PPX/PXP-type ligands ($R_2P(=X)-PR_2/R_2P-X-PR_2$; X = O, S; R = alkyl, aryl) have not received much attention. This is surprising, since the unique tautomeric equilibrium of the PPX/PXP-type ligands opens the possibility for a versatile coordination chemistry by allowing the ligand to switch between two tautomers. Consequently, the donor characteristics and coordination modes can be altered and, based on the availability of a hard and a soft donor site, different metal centres can be coordinated. Inspired by this potential, the present work offers new insights into the promising ligand class of oxygen- and sulphur-containing PPX/PXP-type ligands with respect to their coordination chemistry, reactivity as well as their photo-optical and catalytic applications.

In chapter three, a fundamental knowledge of the coordination chemistry of PPO/POP-coordinated transition metal complexes should be established. Coordination studies towards harder metals, such as Fe(II) and Y(III), provide oxygen-coordinated complexes including the PPO tautomer. Contrary, in presence of soft metals, such as Cu(I) and Au(I), a shift to the bridging diphosphine POP tautomer is witnessed, which enables short M–M distances and metallophilic interactions. Through the choice of the solvent, the tautomeric equilibrium in such transition metal complexes can be shifted, as shown by the conversion of $[Cu_2(MeCN)_n(\mu_2\text{-}POP)_2](PF_6)_2$ to $[Cu(MeCN)_n(PPO)]PF_6$.

Chapter four describes how the nuclearity of Cu-based complexes can be directed by the applied synthesis strategy. The formation of trinuclear Cu complexes can be realised through an *in-situ* formation of the PXP ligand in presence of a Cu precursor. Various $[Cu_3(\mu_3\text{-}Hal)_2(\mu_2\text{-}PXP)_3]PF_6$ (Hal = Cl, Br, I; X = O, S) complexes can be synthesised, which reveal a tremendous effect of the ligand backbone on their photo-luminescence properties.

The sulphur containing PPS/PSP ligand system is further explored in nickel halide complexes as part of chapter five. First insights into the catalytic application of this ligand class are gained using the novel chelate complexes $[NiHal_2(PSP)]$ (Hal = Br, I) in Kumada-Tamao-Corriu coupling reactions. The presence of $NiCl_2$ and Ni(0) precursors leads to P–P bond cleavages of PPS and the formation of multinuclear Ni(II) complexes stabilised by Ph_2PSS^-, Ph_2PS^- and Ph_2P^- ligands.

Copper sulphide clusters, stabilised by the PPS-related Ph_2PS^- ligand, are the focus of chapter six. Access to two clusters, $[Cu_{14}(\mu_6\text{-}S)_1(\mu_3\text{-}Ph_2PS)_{12}]$ and $[Cu_{24}(\mu_5\text{-}S)_6(\mu_3\text{-}Ph_2PS)_{12}]$, is given by a facile one-pot reaction, showing a copper-initiated P=S cleavage as a source of S^{2-} anions. $[Cu_{24}(\mu_5\text{-}S)_6(\mu_3\text{-}Ph_2PS)_{12}]$ exhibits remarkable near-infrared photoemission in the solid state and in solution.

Chapter seven covers the formation of a fluorophosphine-stabilised Ni(0) complex $[Ni(PFPh_2)_4]$, which results from an unusual *in-situ* reduction and simultaneous fluorination reaction of PPO with $[Ni(MeCN)_4](BF_4)_2$. The air-stable Ni(0) complex is tested as alternative Ni(0) source in Suzuki-Miyaura coupling reactions, showing an outstanding catalytic

performance, which is clearly superior to [Ni(COD)$_2$] (COD = 1,5-cyclooctadiene). The catalytic performance can even be enhanced by the addition of stabilising ligands, such as dppf (1,1'-bis(diphenylphosphino)ferrocene).

Kurzzusammenfassung

Liganden mit kleinen Bisswinkeln, die auf einem PCP- und PNP-Rückgrat basieren, wurden in den letzten Jahren ausführlich untersucht, während die analogen sauerstoff- (POP) und schwefelhaltigen (PSP) Liganden der PPX/PXP-Ligandenklasse ($R_2P(=X)–PR_2/R_2P–X–PR_2$; X = O, S; R = Alkyl, Aryl) weitaus weniger Beachtung fanden. Dies ist überraschend, da das einzigartige tautomere Gleichgewicht der PPX/PXP-Liganden eine vielseitige Koordinationschemie ermöglicht, basierend auf den zwei tautomeren Formen. Daraus resultieren unterschiedliche Donorfunktionalitäten und Koordinationsweisen, sodass die Koordination verschiedenster Metallzentren realisiert werden kann. Davon inspiriert bietet die vorliegende Arbeit neue Einblicke in die vielversprechende Ligandenklasse der sauerstoff- und schwefelhaltigen PPX/PXP Liganden hinsichtlich ihrer Koordinationschemie, ihrer Reaktivität sowie ihrer photo-optischen und katalytischen Anwendungen.

In Kapitel drei soll ein grundlegendes Verständnis der Koordinationschemie von PPO/POP-koordinierten Übergangsmetallkomplexen erhalten werden. Dabei liefern härtere Metalle, wie Fe(II) und Y(III), eine Koordination über die Sauerstoff-Funktionalität des PPO Tautomers. Mit weicheren Metallen, wie Cu(I) und Au(I), erfolgt eine Verschiebung des Gleichgewichts zu dem bidentaten POP Tautomer, welches kurze M–M Distanzen und somit metallophile Wechselwirkungen ermöglicht. Durch die Wahl des Lösungsmittels kann das tautomere Gleichgewicht der Übergangsmetallkomplexe beeinflusst werden, wie am Umsatz von $[Cu_2(MeCN)_n(\mu_2\text{-}POP)_2](PF_6)_2$ zu $[Cu(MeCN)_n(PPO)]PF_6$ gezeigt werden kann.

Kapitel vier beschreibt, wie durch Anpassung der Synthesestrategie Kupfer-Komplexe mit einer verschiedenen Anzahl an Metallatomen gebildet werden können. Dreikernige Cu-Komplexe, $[Cu_3(\mu_3\text{-}Hal)_2(\mu_2\text{-}PXP)_3]PF_6$ (Hal = Cl, Br, I; X = O, S), können durch eine *in-situ* Bildung des PXP-Liganden in Anwesenheit des Kupfer-Präkursors erhalten werden, anhand derer ein drastischer Einfluss des Ligandenrückgrats auf die photo-optischen Eigenschaften aufgedeckt werden kann.

In Kapitel fünf liegt der Fokus auf weiteren Untersuchungen des schwefelhaltigen PPS/PSP Ligandensystems in Nickelhalogenid Komplexen. Die neuen Chelatkomplexe $[NiHal_2(PSP)]$ (Hal = Br, I) liefern erste Einblicke in die Eignung dieser Ligandenklasse für katalytische Anwendungen in Kumada-Tamao-Corriu Kupplungsreaktionen.

Kapitel sechs behandelt Kupfersulfid Cluster, die von dem PPS-verwandten Ph_2PS^- Liganden stabilisiert werden. Eine *one-pot* Umwandlung, die eine Cu-initiierte P=S Bindungsspaltung als S^{2-} Quelle beinhaltet, bietet den Zugang zu $[Cu_{14}(\mu_6\text{-}S)_1(\mu_3\text{-}Ph_2PS)_{12}]$ und $[Cu_{24}(\mu_5\text{-}S)_6(\mu_3\text{-}Ph_2PS)_{12}]$, der eine beeindruckende, nah-infrarote Photoemission aufweist.

Kapitel sieben behandelt die Bildung eines Fluorophosphan-stabilisierten Ni(0) Komplexes $[Ni(PFPh_2)_4]$, der aus einer ungewöhnlichen *in-situ* Reduktion mit gleichzeitiger Fluorierung des PPO Ligandens mit $[Ni(MeCN)_4](BF_4)_2$ resultiert. Der luftstabile Komplex wird als alternative Ni(0) Quelle in Suzuki-Miyaura Kupplungen eingesetzt, wobei eine ausgezeichnete katalytische Performance erhalten wird, die durch die Zugabe stabilisierender Liganden, wie dppf (1,1′-Bis(diphenylphosphino)ferrocen) weiter erhöht werden kann.

Contents

1 Introduction

The majority of phosphines can be classified as either monodentate ligands with only one incorporated phosphorus donor functionality or as diphosphines, which possess two phosphorus atoms and can therefore coordinate in a bidentate fashion. The importance of bidentate diphosphines is undeniable in the field of transition metal complexes especially with regards to their application in homogeneous catalysis. This is based on the unique modification potential of the electronic and steric properties through tuning of the phosphorus residues and the therewith involved versatile coordination chemistry.[1,2] In bidentate diphosphines special attention should be attributed to the ligand backbone, which bridges the two phosphorus units. The modification of the ligand backbone is a powerful tool to impact the properties of the ligand, which in turn affects the coordination behaviour and ultimately its performance in the catalytic or photo-optical applications.[3-5] Well-established ligand types are hereby bridged *via* carbon-based backbones (PCP), such as CH_2, C_2H_4, or larger carbon skeletons, such as in the widely applied ligands 2,2′-bis(diphenylphosphino)-1,1′-binaphthyl (BINAP) and 4,5-bis(diphenylphosphino)-9,9-dimethylxanthene (Xantphos, Figure 1).[6,7]
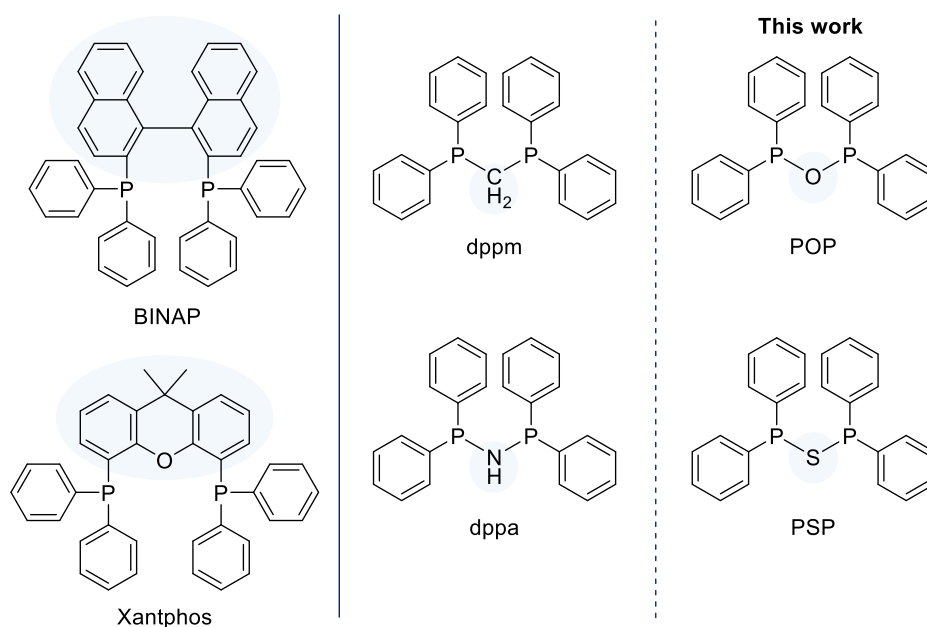
Figure 1. Selected examples of diphosphines with larger bridging units (left) or monoatomic bridges of the two phosphorus units (right).

If only one atom bridges the two phosphorus atoms, as it is the case for $Ph_2PCH_2PPh_2$ (dppm, 1,1-bis(diphenylphosphino)methane, Ph = phenyl), the ligand is referred to as a short-bite ligand. Another important class which can be assigned to this category are PNP-type ligands, in which the two phosphorus atoms are bridged *via* a –N(R)– moiety.[5,8,9] The PNP analogue of the dppm is 1,1-bis(diphenylphosphino)amine (Ph_2P–N(H)–PPh_2, dppa, Ph = phenyl). In PNP-type ligands further tuning of the ligand characteristics can be achieved through the additional residue of the nitrogen atom. On the other hand, the investigation of related short-bite ligands with a heteroatom-containing backbone, namely R_2P–O–PR_2 (POP-type; R = alkyl, aryl) and R_2P–S–PR_2 (PSP-type; R = alkyl, aryl) based ligands, has been neglected

even if these bridging elements are expected to facilitate promising electronic and steric modifications of the diphosphine ligands.[10] Consequently, it is highly likely that investigations of transition metal complexes stabilised by these ligand classes reveal unknown features and new application fields.

1.1 The class of PPX/PXP-type ligands (X = O, S)

1.1.1 Tautomeric equilibrium of PPX/PXP-type compounds

POP- and PSP-type ligands show a unique tautomeric equilibrium, also known as phosphorotropic tautomerism, which describes the potential existence of a PPX ($R_2P(=X)$–PR_2) and a PXP (R_2P–X–PR_2) tautomer.[11-15] This characteristic might also be assumed to complicate the synthesis of the respective metal complexes and is therefore most likely one dominant reason for the very limited amount of scientific reports concerning these ligand classes. Unusual formal oxidation states of +II for the phosphorus atom with the lone pair and +IV for the oxidised phosphorus atom, can be assigned to the PPX form, whereas in the PXP tautomer both P atoms show a +III oxidation state, in analogy to other bidentate diphosphines (Figure 2).
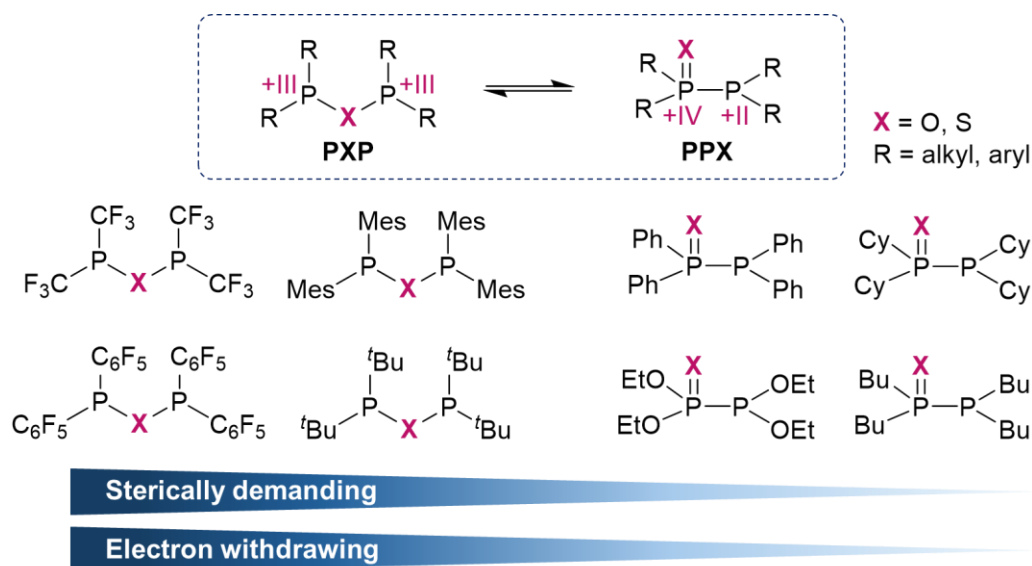
Figure 2. Phosphorotropic tautomerism of the PXP/PPX ligand. The phosphorus atoms can shift in between different oxidation states depending on the tautomer. This figure has been partly adapted from [16].

The position of the equilibrium is influenced by the steric and electronic properties of the phosphorus residues, as well as by the nature of the heteroatom in the ligand backbone. If all residues are identical, two potential forms exist, whereas unidentical substituents of the phosphorus atoms lead to two different PPX forms, additionally to the PXP form.[14,15] Depending on the nature of the phosphorus residues, the equilibrium is either clearly shifted to the PPX or the PXP form or both forms co-exist, whereby the equilibrium can be understood as competitive nucleophilicity of the P atoms and the X atom. If the nucleophilicity of the P centre is decreased to a certain threshold by electron withdrawing groups (EWGs), the X atom acts as nucleophile instead and bridges the two phosphorus atoms. Otherwise P(IV) is more nucleophilic than X and the equilibrium is shifted towards the PPX side.[10,15] While electron

withdrawing groups (EWGs), as well as sterically demanding groups such as CF_3, ^tBu (*tert*-butyl) or Mes (mesityl) were found to stabilise the PXP form, the PPX form is favoured in the case of electron donating and sterically less demanding phosphorus residues (e.g. Ph, OEt or Cy (cyclohexyl)).[10,14,15] The impact of the residues on the tautomeric equilibrium was shown to be more pronounced for O-containing analogues compared to the sulphur counterparts.[14] Further insights can be drawn from DFT (Density functional theory) calculations conducted by Ogawa *et al.,* which have proven that the HOMO (highest occupied molecular orbital) of the PPS ligand is mainly localised within the PPS unit, whereas in the PPO form, there are significant contributions from the phosphorus residues. As a consequence, a higher reactivity and less influence of the P substituents can be expected in the case of the PPS ligand.[17]

It should be mentioned that for PNP-type ligands, examples of iminobiphosphines (R_2P–PR$_2$=N–R', PPN) have been reported, although they have been widely overlooked, as tautomers of the well-explored PNP ligand class. This PPN/PNP equilibrium drastically depends on the nitrogen residue and strong electron withdrawing or sterically demanding groups are required to stabilise the PPN form.[18,19] As shown by Fei *et al.*, the nitrogen residue can in some cases be used to direct the equilibrium through protonation/deprotonation of the nitrogen residue, in which a proton acceptor has to be present.[19] In the case of PNP ligands, it can be assumed that the effect of the P residues on the tautomeric equilibrium is only minor, since the PNP tautomer is always dominating for different P residues, such as CF_3,[20] ^tBu[21] and Ph[22], if no strong EWG or sterically demanding N residues are incorporated. This is contrary to the PPX/PXP tautomerism, which is drastically influenced by the P residues, whereby EWGs and sterically demanding substituents destabilise the PPX tautomer. Furthermore, several iminobiphosphines are pyrophoric, suffer from immediate P–P bond cleavage and rearrange quickly to the PNP form, depending on the substituents.[18] Therefore, the PPN tautomer remained comparably unexplored up-to-now.

1.1.2 Synthetic access to PPX/PXP-type compounds

PPX- and PXP-type compounds can be synthesised *via* various strategies, depending on the nature of the heteroatom X and the residues attached to the phosphorus atoms. Both factors determine if the PPX or the PXP tautomer or a mixture of both is formed.[14] The various reaction approaches, which were reported in the past for the syntheses of PPX/PXP-type compounds with R = (fluorinated) alkyl, aryl, OR or NR$_2$, are presented in Figure 3. Since sulphur-containing compounds are less explored than the oxygen counterparts, a greater number of syntheses was developed for the oxygen-containing compounds. This might also be due to easier-accessible substrates required for the PPO/POP syntheses, such as water for the hydrolytic cleavage (Figure 3, approaches 3 and 7). Consequently, some approaches are valid for both analogues (approaches 1, 9), whereas other ones apply mostly to only one heteroatom. The most common approaches 1-5 involve the conversion of R_2PCl with a sulphur or oxygen source. The S and O sources include R_2P(O)H,[23,24] R_2POR' (R' = H, R, Na, K),[25,26] Na_2S,[15] Li_2S,[27] R_3SiONa,[28] and H_2O.[29,30] Approach 3 describes the reaction of R_2PCl with water, which usually react violently with each other and therefore experimental works with R_2PCl are mostly conducted under inert conditions. However, this reaction was observed as a side-reaction of other attempted syntheses, whereby trace amounts of residual water result

in the formation of PPO/POP as by-product.[24,31-34] Especially PNP-type ligands are susceptible towards such hydrolytic cleavages resulting in the formation of PPO/POP-based compounds. The mechanism of the underlying reaction pathway is not completely understood. However, two options are discussed in literature. Some reports cover the P–N hydrolytic bond cleavage of the PNP tautomer, which provides the PPO ligand through subsequent recombination of two phosphorus units, one of each is oxidised, whereas the other one remains unoxidised.[35] Contrary, Posset *et al.* suggest that prior to P–N bond cleavage, the rearrangement to the PPN tautomer occurs and subsequent P=N bond cleavage yields PPO.[34] Both cases involve the formation of an amine as by-product (approach 7). Another, rather unconventional synthesis of PPX/PXP-type compounds is the rearrangement of $Ph_2P–O–C(=O)R$ (R = Ph[36] or $CH=CH_2$[37]) forming PPO and $(RCO)_2O$ (approach 6). Intensive studies by Ogawas group focused on the radical or UV initiated P–P bond cleavages of $R_2P(=X)PR_2$ and $R_2P(=X)P(=X)R_2$.[38] Thereby, it was found that a UV induced $Ph_2P(=O)\cdot$ radical reacts with R_2PPR_2 to give PPO (approach 8). R_2PPR_2 can also be converted into the respective PPX/PXP-type compound through simple oxidation chemistry, whereby for a highly controlled reaction, the stoichiometric addition of solid sulphur is much easier than the controlled addition of oxygen (approach 9). It should be emphasised that the introduction of different phosphorus residues can only be achieved with methods 1 and 9, since in these strategies two different phosphorus-units (R_2P) are present, whereas in all other methods only one phosphorus unit is involved as precursor material.
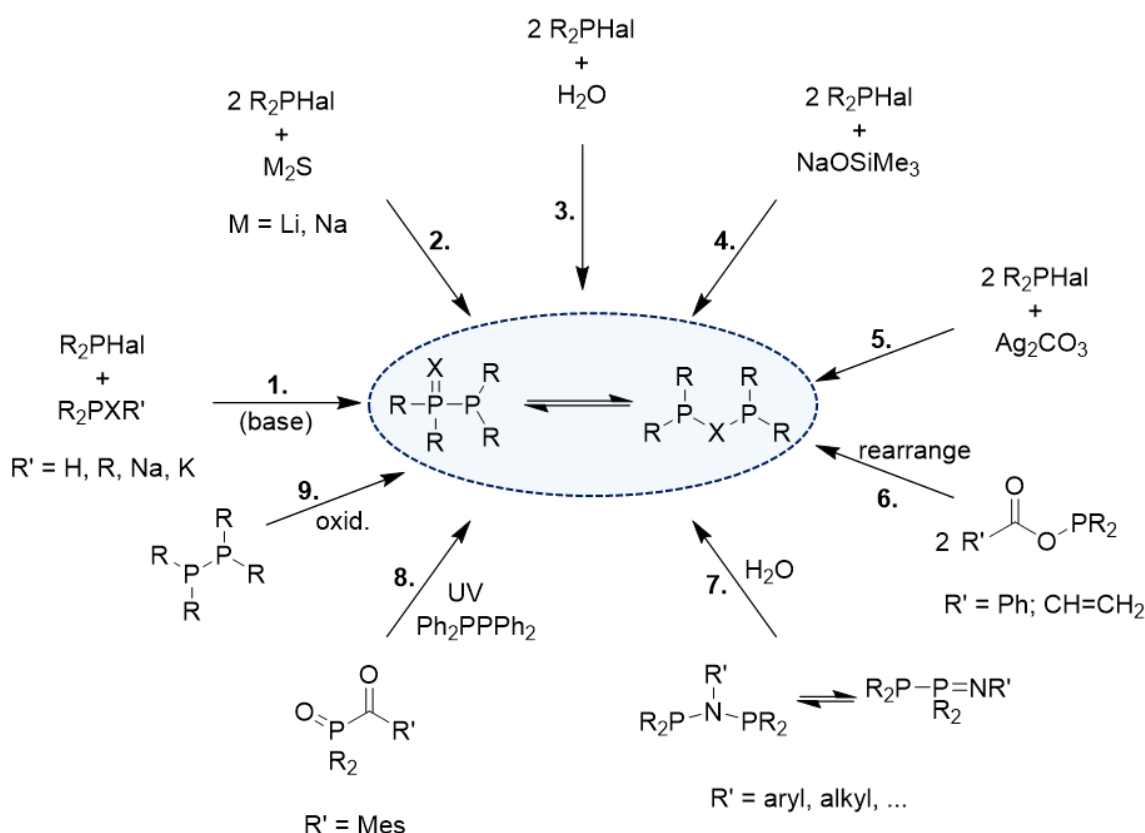

Figure 3. Synthesis methods for PPX- and PXP-type compounds.

1.1.3   Reactivity of PPX/PXP-type compounds

The two PPX and PXP tautomers can show different reactivities since the tautomeric shift causes a change in the electronic nature of the phosphorus and the X atom in the molecules. A majority of the reactivities of the PPX compound stems from P–P bond cleavage. This is the case for the acid-induced hydrolysis of the P–P bond resulting in the formation of R_2POH and R_2PCl[10,39] or for the electrophilic attack of methyl bromide at the P(II) atom, which results in the formation of Ph_2PMe and $Ph_2P(=O)Br$.[40] Furthermore, the group of Ogawa has studied the reactivity of PPX and $R_2P(=X)–P(=X)R_2$ compounds under the influence of UV radiation or in the presence of radical starters.[41] Thereby, they found a unique reactivity of this compound class, since the P–P bond is cleaved homolytically, resulting in the formation of two radicals, $Ph_2P(X)\cdot$ and $Ph_2P\cdot$. These radicals can either recombine and form $R_2P(=X)–P(=X)R_2$, $R_2P–X–P(=X)R_2$, $R_2P(=X)–X–P(=X)R_2$ or $R_2P(=X)–PR_2$ or they can be used for the activation of unsaturated bonds, such as in alkenes and alkynes. The $Ph_2P(X)\cdot$ radical is much more reactive than the $Ph_2P\cdot$ counterpart and in absence of the X atom, as for example in $Ph_2P–PPh_2$, such kind of reactivity cannot be observed. Interestingly, the reactivity is strongly increased in the case of X = S compared to X = O, due to the electron density localisation of the HOMO.[17,38,41-43] Based on similar reaction patters, Takano *et al.* reported the photocatalysed insertion of ethylene into the P–P bond of PPO followed by sulphur oxidation of the P(II) function.[44] Furthermore, PPO has been used in metal-catalysed processes as reported by Yang *et al.* who described a C–F bond activation and simultaneous phosphorylation in presence of $[Ni(COD)_2]$ to convert aryl fluorides with PPO in presence of a base and at elevated temperatures.[45] Also in hydrophosphination reactions of alkynes, PPO can serve as a phosphorus source as it has been applied by Ogawas group for Pd- and Rh-catalysed reactions.[46,47] Thereby, it could be revealed that catalytic amounts of PPO can be used to promote the hydrophosphinations of other phosphine oxides. The application of PPO in these catalytic reactions is again based on a P–P bond cleavage.

One very interesting reactivity pattern has been reported for POP-stabilised Mo-complexes in the presence of water. Hereby, a hydrolytic cleavage of the P–O bond results in a hydrogen-bonded arrangement of two Ph_2PO-ligands $(Ph_2PO–H–OPPh_2)^-$ coordinating to the metal centre.[12] This structure is highly stable and a common coordination mode of the PPO/POP-closely related secondary phosphine oxides.[48] Remarkably, Wong *et al.* demonstrated a strategy to reverse this reaction to the POP ligand through the addition of trifluoro acetic acid in trifluoroacetic anhydride.[12] This offers a possibility to switch between the POP and corresponding POH ($Ph_2P(=O)H$) compounds, which could be used to access new POP-type compounds and it could also be advantageous during the application of such compounds.

1.1.4   PPX/PXP-type coordination compounds

Based on the tautomeric equilibrium described before, the PPX/PXP-type ligand sets offer a very rich coordination chemistry towards various metals in different oxidation states. The coordination can result in so-called coordination-stabilised tautomers meaning a shift of the tautomeric equilibrium to the tautomer which is less stable if the ligand is uncoordinated.
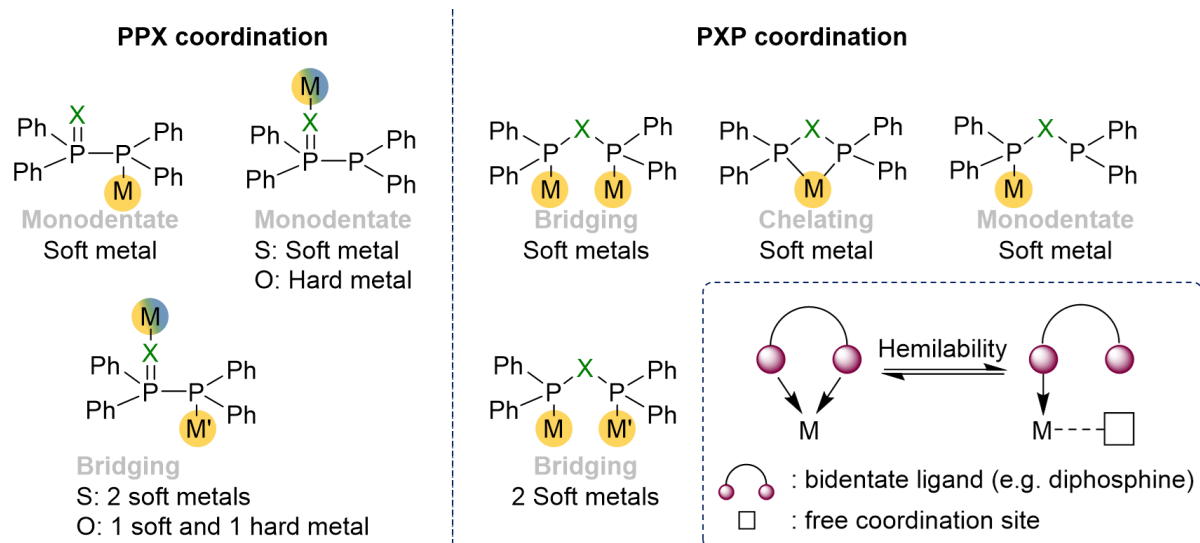
Figure 4. Versatile coordination modes of the PPX/PXP-type ligand, based on its two tautomers. The coordination mode is strongly dependent on the nature of the metal. Softer metals (yellow) are coordinated *via* the P donor function or in case of X = S *via* the sulphur atom, whereas harder metals (blue) can be coordinated by the oxygen atom. Hemilability can occur in the bidentate coordination mode, if one donor functionality dissociates from the metal centre (bottom, right). This figure has been partly adapted from [16].

The PPX tautomer can be considered as a hybrid ligand since coordination can either occur *via* the soft P(II) atom or *via* the X donor site. In the case of X = S, the coordination *via* X provides a second soft donor site, whereas with X = O a hard donor site is introduced into the molecule. These two different donor sites offer the possibility to form heterobimetallic complexes with either two soft metals (X = S) or with one hard and one soft metal (X = O). This could facilitate cooperative effects of the two metal atoms which are known to cause outstanding properties in catalysis, photo-optics and magnetism.[49-52] Screening of the literature indicates that the application of the sulphur-based ligand has received much less attention in the field of coordination chemistry, since there are only two examples of PPS-complexes reported, based on Fe(0)[15] and Cr(0).[53] Whereas in these two complexes coordination takes place *via* the P(II)-functionality, no example is known for a coordination *via* the sulphur atom. Contrary, more examples including the oxygen analogue have been reported, amongst which complexes of P(II) coordination of softer metals (e.g. Cu(I),[35,54] Mo(0),[13] Co(0),[55] Fe(0),[56-59]) as well as O-coordination for harder metals (Ga(III),[60] Zr(IV),[61] Al(III)[62]) were found. Wong *et al.*[13] suggested a potential chelating mode *via* the X and the P(II) atom. However, this mode has never been observed and would require a metal, which is compatible with both donor functions, which excludes the PPO compound due to significantly different functionalities. Since no S-coordination of the PPS has been reported at all, and based on the increased steric hindrance, the rigidity of the P–P=X unit as well as the resulting high ring strain, such a coordination mode is rather unlikely.

As mentioned before, the tautomeric equilibrium can also be shifted to the PXP side, in which the X atom is not actively participating in the coordination chemistry. The PXP forms can be understood as the oxygen- and sulphur-analogues of well-studied short-bite PCP- and PNP-based ligands. For example, the phenyl-based POP ($Ph_2P–O–PPh_2$) and PSP ($Ph_2P–S–PPh_2$) are the counterparts of $Ph_2P–CH_2–PPh_2$ (dppm, PCP) and $Ph_2P–N(H)–PPh_2$ (dppa, PNP),

which are important ligands for applications in photo-optical[63-65] and catalytic applications.[5,66,67] However, PCP- and PNP-based ligands exhibit additional residues at the bridging atoms, which are further influencing the ligands properties and which could also offer the possibility for the deprotonation of the ligand backbone.[5] It should be underlined that the free ligands in their POP and PSP (R = Ph) tautomeric forms cannot be isolated, since the equilibrium is completely shifted towards the PPX tautomer. In the case of the PXP ligand, a bridging or chelating coordination mode has been described.[12,13,15] With the latter one the formation of dinuclear metal complexes can be accomplished. Hereby, it was found that, beside the reaction stoichiometry and the impact of additional ligand molecules, the ligand backbone plays a crucial role, since in cases of a large ring strain and a compression of the PXP angle, the bridging coordination is favoured over the chelating mode.[68] This agrees with PCP analogues, in which the bridging coordination mode is often preferred for ligands which would induce the formation of a four-membered P–C–P–M ring, such as dppm, whereas the extension of the backbone with one additional CH_2 unit, such as in the case of 1,2-bis(diphenylphosphino)ethane (dppe), significantly decreases the ring strain and enables highly stable dppe-chelate complexes.[68]

Examples in which two metal centres are bridged by the PXP ligand include Au,[69] Fe,[70] Cr,[71] Rh[72] or Cu[35,73-75] for POP-type and Ag,[15] W,[76] Mn,[77] and Ni[11] for PSP-type complexes. The chelating coordination mode was reported for Cr,[12] Mo,[78] W,[13] Ru[79,80] and Rh[81,82] as examples for the POP-type ligands, whereas only two reports describe chelating PSP-type ligands in Mo[83] and Ru[27] complexes. In analogy to the PPX counterparts, sulphur-based compounds are, also in the case of the PXP tautomer, far less explored than the oxygen-containing counterparts. The bridging coordination mode of short-bite ligands is particularly important with regard to supported metallophilic interactions. Metallophilic interactions are defined as the unexpected, attractive interaction of two metal centres, which possess a closed-shell electronic configuration, such as Au(I), Ag(I) and Cu(I). Such interactions should usually be repulsive in nature due to Coulomb interactions.[84,85] Supported by the monoatomic bridge of the phosphorus atoms, a small distance of the two metal centres can be facilitated, which results in potential metallophilic interactions whereby the metal–metal (M–M) distance can fall below the sum of the van-der-Waals radii. As a result of these interactions, exceptional features are known to emerge, especially in terms of photo-optical behaviour or in catalysis, since often key intermediate species are based on dinuclear metal species.[86,87] Furthermore, the bridging coordination mode offers the formation of heterobimetallic complexes through the coordination of two different metal atoms. Analogue PCP- and PNP-stabilised complexes have proven that such combinations could be convenient, since they combine cooperative effects of the two metals and the respective functionalities of each metal which can be important in different situations of a catalytic reaction.[49,50]

Another potential coordination mode would be monodentate coordination *via* only one P atom whereas the other P atom remains uncoordinated. Contrary to characterised PNP-[88-91] and PCP-stabilised[92-95] coordination compounds, in which only one P atom is coordinating, such a structure has not been isolated for POP and PSP ligands. This might also be a consequence of the observed tautomerism. However, the monodentate PXP coordination mode could be of

great importance in the context of ligand hemilability, which is defined as the de-coordination of one donor function, whereas the second site remains coordinated (Figure 4).[96] This is especially useful in catalysis since a free coordination site at the metal could be offered for the attachment of substrates. The modification of the P residues in the PXP systems could also be a target point to trigger the hemilabile behaviour. If the two phosphorus atoms comprise different residues, one P–M bond could be more labile than the other one.

Whereas in the case of oxygen- and sulphur-containing short-bite ligands, several coordination-stabilised tautomers have been reported, this possibility has not yet been in much focus for PPN/PNP-type ligands. No example of P-coordination in the PPN tautomer is known, since attempts of synthesising coordination complexes with softer metals, such as Pt(II) or Pd(II), only resulted in an equilibrium shift and consequent PNP coordination.[18] Only two examples have been covering the equilibrium shift from a PNP ligand to the isolation of PPN-type compounds *via* N-coordination. These examples include Zn(II)[97] and Al(III)-based coordination compounds.[62] In the Zn(II) complex, the stabilisation of the PPN-form is supported through the additional coordination of the N residue in the ligand backbone to the metal centre.

1.2 Diphosphines as ligands in photo-optical applications

1.2.1 Photo-optical properties of transition metal complexes

Luminescence is the property of compounds to emit light from an excited state. The development of luminescent materials is fundamental for application in fields like photovoltaic, sensors or light emitting diodes (LEDs).[98-100] The Jablonski diagram can be used for a description of the various processes, which can be responsible for the presence or absence of any emission (Figure 5).[101]
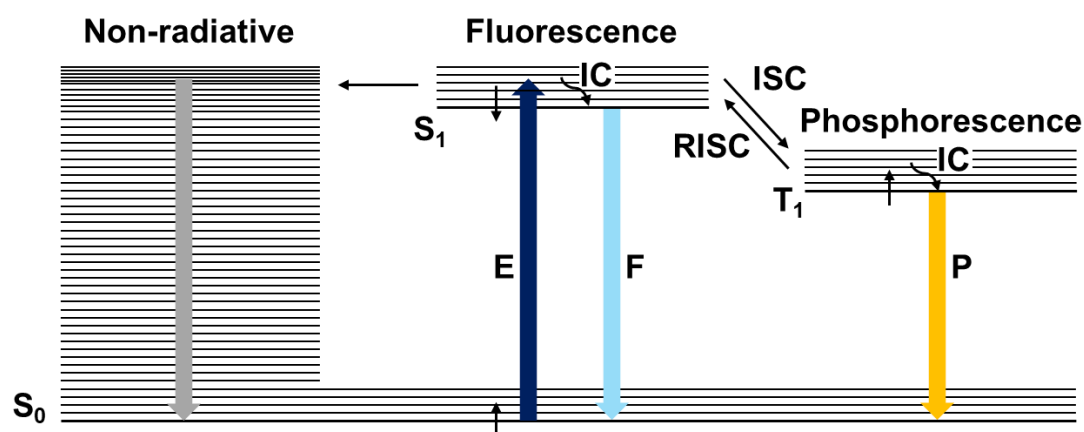
Figure 5. Various transitions initiated through excitation (E) of an electron to its excited singlet state S_1. Either non-radiative decays, (thermally-activated delayed) fluorescence (F) or phosphorescence (P) result in the transition of the electron back to its ground state S_0.

The excitation (E) of an electron involves a transition from the ground state S_0 to its excited state S_1, whereby the electron can occupy various vibrational levels. Within 10^{-12} seconds internal conversion (IC) leads to the relaxation of the electron to the lowest vibrational level of S_1. Subsequently, transitions back to the ground state can either occur *via* non-radiative

decays, showing no emissive behavior, or through an emissive process. Since the excited electron in the singlet state obtains the opposite spin of the electron in the ground state, the $S_1 \rightarrow S_0$ transition is spin allowed and can occur rapidly on a nanosecond time scale.[102] Such decays are called fluorescence (F). Otherwise, the electron can undergo intersystem crossing (ISC) leading to a triplet excited state T_1, which involves the inversion of the spin.[102,103] The transition back to the ground state is consequently spin forbidden and takes place on a longer time scale in the microsecond regime. This process is called phosphorescence (P). In this context, the presence of heavy atoms is known to show a higher degree of spin-orbit coupling, which causes an enhancement of the ISC and consequently an increased phosphorescence.[100] Alternatively to phosphorescent emissions, reverse intersystem crossing (RISC) can re-populate S_1 states, which then undergo $S_1 \rightarrow S_0$ transitions. This process is usually promoted by thermal activations of the RISC and is thus named thermally-activated delayed fluorescence (TADF).[104,105] Luminescent materials often contain d^{10} metal ions, since non-radiative decays based on metal centred transitions, can be prevented. Also, different coordination geometries around the metal centres can be targeted, which can be used to tune the colour of the emission.[106,107]

1.2.2 Diphosphines as ligands in photo-optical applications

The design of luminescent transition metal complexes is strongly connected to the utilised ligands. Therefore, the application of diphosphine ligands is often advantageous due to their strong binding capacity, the electronic impact and their high geometric rigidity especially in contrast to the monodentate ligand counterparts.[107-109] Diphosphine-containing coordination compounds, which show photoemission properties, range from mononuclear species up to large clusters.[107] Mononuclear compounds are mostly coordinated by bulky ligands with sterically demanding backbones, which tend to chelate the metal centre, such as DPEphos (bis[(2-diphenylphosphino)phenyl]ether) or BINAP.[109,110] Polynuclear complexes require ligands, which can adopt a bridging coordination mode. Thereby, with an increasing number of metal atoms, the presence of metallophilic interactions for d^{10} metals becomes more likely, which can in many cases trigger photoemissive behaviour based on cluster centred (CC) transitions in combination with ligand to metal charge transfers.[63,84,99,111] As a foundation for these interactions, ligand frameworks with two short-distanced donor functionalities have shown to be beneficial, since such ligands can bring metal centres in close proximity. To achieve this, short-bite ligands are promising candidates, due to the monoatomic bridging unit of the two donor functionalities.[64,68,112,113] Hereby, semi-supported and fully-supported metallophilic interactions can be distinguished (Figure 6). These interactions are in contrast with un-supported metallophilic interactions, which describe the presence of metallophilic interactions without any ligand stabilisation. The relevance of the ligand on the formation of metallophilic interactions was for example demonstrated by the group of Che, who reported that through the incorporation of the bidentate, bridging dppm ligand, Pt–Pt interactions can evolve, which influence the photoemission in the solid and solution state.[114] It should be noted that the dppm ligand itself is showing photoemission at 500 nm and coordination compounds of this ligand display a red-shift of the maximum photoemission.[115] A study by Leoni *et al.* uncovers the unusual behaviour of the short-bite ligands on the photo-optical properties of

heteroleptic [Cu(NN)(PP)]$^+$ based complexes, by combining a NN-ligand (1,10-phenanthroline (phen) or 4,7-diphenyl-1,10-phenanthroline (Bphen)) with various diphosphines.[116] Therefore, diphosphines, belonging to the family of bis(diphenylphosphino)alkanes (Ph$_2$P–(CH$_2$)$_n$–PPh$_2$), with bridging units with n = 1-4 were applied. Contrary to the diphosphines with larger backbones (n = 2-4), which result in the formation of mononuclear complexes, a dinuclear copper complex is obtained with the short-bite ligand dppm. Furthermore, the authors conclude a higher rigidity of the dppm-bridged compound and consequently, a lower degree of flattening in the excited state. Such flattening distortions are often correlated with a drop in the quantum yield of the compound. As a result, significantly enhanced emission can be realised with the dppm-based compound compared to the monodentate compounds.[116]
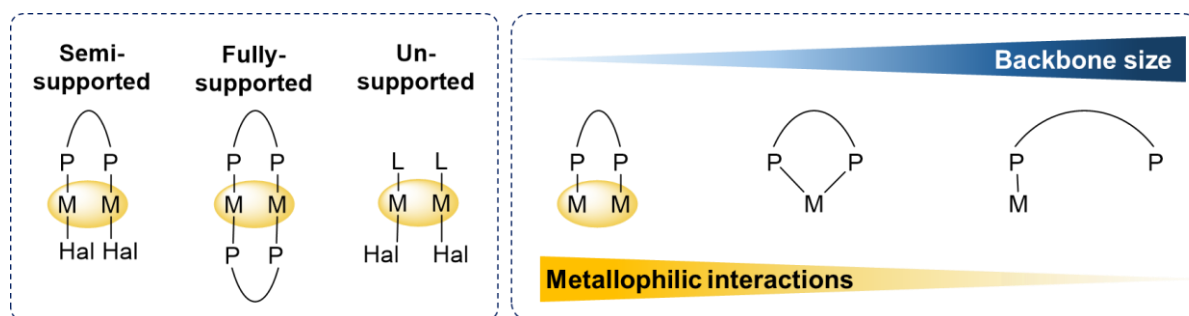
Figure 6. Different types of metallophilic interactions as defined by Schmidbaur[84] (left). Depending on the size of the backbone, different coordination modes are favoured. Short-bite ligands with small backbones of the type PXP can facilitate short M–M distances and consequently metallophilic interactions. Larger backbones cause monodentate chelating modes, which do not support metallophilic interactions (right).

Accordingly, other dppm- and dppa-bridged dinuclear complexes display photo-luminescence. For example, two dppm- or dppa-stabilised dinuclear gold complexes, based on [Au$_2$(μ_2-dppm)$_2$]$^{2+}$ and [Au$_2$(μ_2-dppa)$_2$]$^{2+}$ cations, show bright luminescence in solution at room temperature. Hereby, the dppm complex (λ_{max} = 565 nm)[117] shows a red-shift of the emission maximum compared to the dppa counterpart (λ_{max} = 500 nm).[118] Also, in di- and trinuclear dppm-stabilised copper complexes, photo-luminescence can be observed at room temperature in the solid state with broad emission bands and lifetimes in the microsecond regime.[115,119,120]

1.3 Diphosphines as ligands in catalysis

The application of diphosphine ligands and their transition metal complexes in catalysis is of high importance, not only in academia but also in the chemical industry. Industrially-applied processes which involve the application of phosphine ligands cover hydroformylation reactions, oligomerisations and asymmetric hydrogenations to mention only a few examples.[6,121] The pivotal use of phosphine ligands in catalysis is mainly ascribed to the rich modification potential in order to tailor the properties of the resulting transition metal complexes for defined catalytic applications.[1] Hereby, monodentate phosphines often suffer from a highly dynamic coordination behaviour, which results in stability issues of the metal complexes under reaction conditions. To overcome this challenge, bidentate diphosphines, which contain a bridging unit in between the two phosphorus atoms, have been introduced to confer a higher stability of the metal complexes, even under harsher reaction conditions.[1,2]

The presence of a ligand backbone bridge can be used to modify the electronic and steric properties of the ligand and the respective metal complexes. Thereby, electronic manipulations mainly affect the nature of the active metal centre, including its nucleophilicity and redox capability.[1,2,122] As reported by Tolman, the steric demand of the ligand has a great impact on the coordination behaviour towards metal centres and further influences the interactions of two ligand molecules or of a ligand and a substrate.[1,123] Thereby, it is a widely-accepted fact that the catalyst behaviour often correlates with the bite angle of the diphosphine, which is a compromise of the metal's preferred binding angle and the natural bite angle of the ligand in its free form.[3,4] The significance of the bite angle can be firstly attributed to the accessibility of the active site during the catalytic reaction, due to the steric bulk around the metal centre and secondly to the enforcement of specific coordination geometries based on the scaffold of the ligand.[2,3] This is particularly important if specific geometries promote certain elementary steps. Another crucial factor to consider is the rigidity of the ligand backbone, which can prevent de-coordination and the formation of undesired coordination modes. The backbone can therefore ensure that both phosphorus lone pairs are orientated in the same direction.[1] For example, the dppp ligand often suffers from a high fluctuance of the backbone and consequently a high probability for the formation of bridged bimetallic species instead of chelate complexes.[1,124] One strategy to counteract this fluctuation, is the introduction of ligands with rigid backbones, such as BINAP, DPEphos or Xantphos.[124] During the catalytic cycle, the stabilisation of intermediates of the catalyst can thus be directed through tailored ligand modifications, which allows the control of activity and selectivity.[3,122,124,125]

However, there are still unsolved questions about the effects of the ligand in catalysis, since they are not always straight-forward. Hereby, it could be likely that specific features of the ligand are beneficial for one of the elementary steps whereas for another step different factors would have a greater impact.[124,125] In this context, DFT calculations have indicated that for several oxidative addition reactions, ligands with small bite angles could be useful, since through the oxidative addition, the two P atoms of the diphosphine are forced to come closer due to steric impact through new coordination. Therefore, the forming species could be energetically unfavourable for large bite angle ligands.[124] For further understanding of the ligand effects on the catalytic performance, detailed studies and validation of the effects are required. Tolman suggested two factors which are widely used to understand correlations of the ligands with the catalytic outcome. Thereby, the cone angle[123] defines the sterical demand which is induced by the phosphorus substituents and the Tolman electronic parameter[126] can be used to determine the donor properties of the ligand.

Against the assumption that high catalytic performances are caused by the effects of wide-bite angles, contradicting observations in recent years revealed the likewise advantageous behaviour of short-bite ligands.

The groups of Pringle and Wass,[127,128] investigated the short-bite ligand-based Ni(II) complexes (PCP, PNP) for the oligomerisation and polymerisation of ethylene. Both types of complexes appeared to be highly suitable catalysts, whereby the PNP (NR, R = Me) analogues exhibit an enhanced activity.[127,128] The superior behaviour of the nitrogen-based

counterparts, which has also been observed for other processes,[129] is suggested to derive from the sp^2-like hybridisation of the bridging nitrogen, the resistance towards deprotonation and a higher electronegativity (N > C).[124] Further the activity deviations could be attributed to the higher ring strain in the dppa-analogues.[130] The distinct difference of the two bridging atoms within the PXP ligands underlines the great potential of the modification of ligand backbones, which could be uncovered by further ligand backbone modification through introduction of sulphur or oxygen. Remarkably, when the authors investigated the dependency of the length of the bridging unit in PCP-type ligands, no notable catalytic conversion could be obtained when dppe and dppp chelating nickel complexes were applied. This change in catalytic performance was thought to be based on the easier formation of vacant coordination sites and the highly rigid environment induced by the use of short-bite ligands such as dppm.[127] About 10 years later, Dowson *et al.* studied the catalytic conversion of ethanol for the production of biofuel using PCP-stabilised Ru-complexes (PCP = dppm, dppe, dppp).[92] Again, a similar correlation of catalytic activity and ligand backbone was witnessed. Through the size reduction of the bridging $(CH_2)_n$ unit from n = 3 to 1, the TOF (turn over frequency) could be doubled.[92] A further explanation for this drastic difference came from insights into the molecular structure of the dppm-based catalyst. In different solvents, two various compounds could be isolated, in which the dppm ligand adopts either a chelating or a monodentate coordination mode with one free P atom (Figure 7). Based on these observations, the authors concluded that the flexible coordination chemistry is only easily achievable with the dppm ligand, due to the high ring strain, facilitating the outstanding catalytic behaviour.[92]
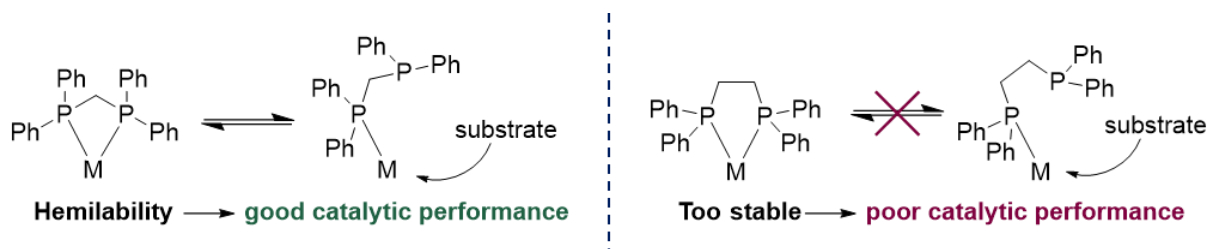
Figure 7. The high ring strain in monoatomic bridges facilitates hemilability (left), whereas complexes with larger ligand backbones (such as dppe) are too stable for an efficient hemilabile behaviour (right). This leads to a significant drop in catalytic activity in the latter case. Other ligands of the metal centre are omitted for clarity.

Further confirmation came from an isolated mononuclear Mn species with a monodentate dppm ligand, which was showing higher conversion of ethanol in the biofuel production than the counterpart containing a chelating dppm ligand. The extension of the backbone chain to n = 2 in dppe again led to no catalytic activity.[131] Comparable findings were also reported for the reductive elimination of ethane using square-planar Pd[132] or Ni[133] complexes. While a fast reaction could be achieved with n = 1, a larger chain length did not provide any efficient conversion. In agreement with the results described by the group of Wass, this was rationalised by a T-shaped intermediate due to the hemilabile ligand behaviour of dppm which is only viable if one CH_2 unit is present in the ligand backbone.

The excellent catalytic behaviour of short-bite ligands can be attributed to an enhanced access to the active sites as it is confirmed by the smaller bite angles and by the presence of

hemilability due to a higher ring strain. This could be further confirmed for other processes, such as the alkyne activation using dppm-stabilised Ru- and Os-complexes, in polyketone synthesis,[134] or in Cr-catalysed ethylene oligomerisations,[62,135] using PNP-based ligands.

1.3.1 Chiral diphosphines as ligands in catalysis

Since enzymes are the pioneering catalysts of asymmetric transformations, great effort is put into the development of chemically synthesised counterparts. Such compounds are crucial to perform catalysis under enantioselective control, which is of great importance for the synthesis of high-value fine chemicals, especially in the fields of pharmaceuticals and agrochemicals.[136] Thereby, phosphine ligands play an essential role, since chiral ligands can be obtained *via* the targeted ligand modification. In the context of chiral diphosphine ligands, the chirality can be introduced in the phosphorus bridgehead itself or it can be implemented in the ligand backbone.[136] The viability of a P-stereogenic centre traces back to the high inversion energy of the P(III) centre and can be achieved through the introduction of three different residues on the phosphorus.[137] On the other hand, the backbone can be engineered to provide axial (e.g. BINAP[7]) or planar (e.g. (*R*)-1-[(*S*P)-2-(diphenylphosphino)-ferrocenyl]-ethyldicyclohexylphosphine: Josiphos[138]) chirality or a stereogenic centre can be incorporated (2,3-*O*-isopropylidene-2,3-dihydroxy-1,4-bis(diphenylphosphino)butane: DIOP[139]). These ligands are often associated with the term "privileged ligands", since such phosphines have shown to be very successful ligands for a range of transition metal complexes, which have found to be applicable in catalysis to numerous substrates but also to a wide range of reactions.[140]

Deriving from the great catalytic potential of small-bite ligands for catalytic applications in the recent years, the demand for chiral analogues of this ligand class was growing. To address this, Yamanoi and Imamoto synthesised the PCP-type P-sterogenic MiniPHOS ligand in 1999, which is bridged by a CH_2 unit (Figure 8).[141] Chelate complexes of this ligand combine a high rigidity based on the four-membered P–C–P–M ring with an asymmetric environment resulting in superior enantioselectivity and catalytic performance.[136] In 2004, Hoge and co-workers presented the C_1 symmetrical Trichickenfootphos (Tcfp), which possesses three adjacent hindered quadrants, according to the quadrant diagram.[142] Both, MiniPHOS and Trichickenfootphos, provide exceptional ligands for metal complexes applied in asymmetric hydrogenations.[141,142] Also, the PNP counterparts of these chiral diphosphines, including MaxPHOS, and their metal complexes were synthesised and have shown again outstanding results as catalysts in hydrogenation reactions.[143-145]
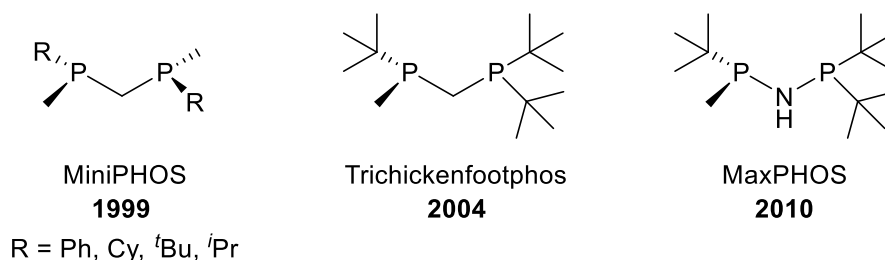

MiniPHOS
1999

Trichickenfootphos
2004

MaxPHOS
2010

R = Ph, Cy, ^{t}Bu, ^{i}Pr

Figure 8. Pioneers of P-stereogenic short-bite ligands of the PCP- (MiniPHOS and Trichickenfootphos) and PNP-type (MaxPHOS).

1.3.2 Tautomeric ligands in catalysis

Only a few examples of tautomeric compounds as ligands for transition metal-based catalysts have been reported so far. One compound class, which is often referred to in this context, is the group of secondary phosphine oxides ($R_2P(=O)H$). Interestingly, PXP-based (X = S, O) compounds can be understood as anhydrides of such secondary phosphine oxides and the respective sulphides. The secondary phosphine oxides (SPO) can shift between a P(III)-phosphine ($R_2P–O–H$) and an often air- and moisture-stable P(V)-phosphine oxide ($R_2P(=O)H$) tautomer.[48,146,147] In analogy to the PXP-system, soft metals are coordinated *via* the phosphorus functionality whereas harder metals are coordinated *via* the oxygen. In addition to the neutral ligand, an anionic form can be obtained through deprotonation, resulting in a large versatility of different coordination modes. Thereby, coordination modes are likely which involve one neutral ligand and one anionic ligand or bridged structures.[146] The rich coordination behaviour and high stability makes the corresponding transition metal complexes prominent candidates as (pre-)catalysts in catalysis, such as in Ru-catalysed C–H arylations,[148] Pt-catalysed hydroformylation[149] or Ir-catalysed hydrogenation[150] reactions. During these catalytic reactions, the oxygen and phosphorus functionalities are often used to perform different tasks. If the phosphorus atom is responsible for the coordination of the metal atom, the oxygen was shown to act as nucleophile for directing the substrates instead of coordinating to the metal.[48,146,151-153]

In other classes, such as PNP-type ligands, the potential tautomeric equilibrium of the ligand systems is often not taken into consideration. However, a critical impact of the tautomeric equilibrium on the catalytic performance has recently been uncovered by Lifschitz *et al.*[62] During the Cr-catalysed ethylene oligomerisation, using PNP-type chromium complexes together with Al-based activators, a tremendous ligand effect could be observed. The Al-based additive was hereby shown to interact with the ligand resulting in a shift of the tautomeric equilibrium to the PPN site and consequently a dramatic decrease in selectivity. These findings underline once again, that with PXP-type ligands, the tautomeric behaviour can be utilised to direct the course of the catalytic processes, for example through blocking or offering of catalytic active sites.

2 Project aims

Since POP- and PSP-type transition metal complexes are widely overlooked compared to their PCP and PNP analogues, systematic studies of the versatile coordination chemistry of these ligand classes are required. Therefore, the primary goal of this thesis is to broaden the knowledge of the unique coordination behaviour of oxygen- and sulphur-containing PPX/PXP-type ligands towards a range of transition metals. It should be specified that the PPX/PXP (X = O, S) term in this work corresponds always to the phenyl derivates of these compounds ($Ph_2P(=O)$–PPh_2/Ph_2P–O–PPh_2 and $Ph_2P(=S)$–PPh_2/Ph_2P–S–PPh_2).
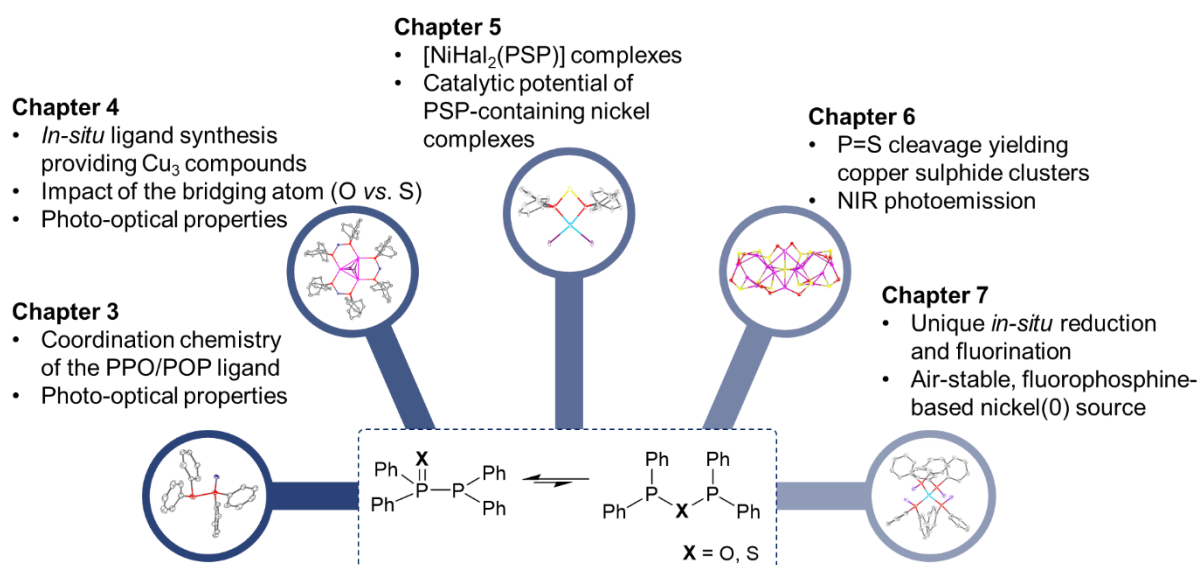
Figure 9. Overview of the research aims of this thesis based on the PPX/PXP ligands. NIR: Near-infrared.

Chapter 3: Coordination chemistry and photo-optical application

To gain an in-depth understanding of the PPO/POP ligand system, the coordination chemistry of this ligand towards hard metals, such as Fe(II) and Y(III), as well as soft metals, such as Cu(I) and Au(I), should be investigated. As part of this study, a focus will be laid on the impact of the tautomeric equilibrium of the ligand during the metal coordination and the effect on photo-optical properties of the PPX/PXP-based coordination compounds.

Chapter 4: Coordination chemistry and photo-optical application

The impact of the bridging atom of the ligand backbone, namely oxygen or sulphur, on the molecular structure and photo-optical properties should be studied. Therefore, trinuclear copper complexes based on either the PSP or the POP ligand are utilised exemplarily.

Chapter 5: Coordination chemistry and catalytic application

PPS/PSP-based nickel halide complexes are in the focus of this chapter to establish this ligand class as alternative for short-bite PCP analogues. The impact of the sulphur-backbone on the compounds properties and application should be evaluated. Therefore, the catalytic potential

of the PSP-based compounds in Kumada-Tamao-Corriu coupling reactions will be investigated.

Chapter 6: Reactivity and photo-optical application

As part of this chapter, cluster compounds and their photo-optical properties will be discussed, which are based on diphenylphosphine sulphide ligands.

Chapter 7: Reactivity and catalytic application

The product of an unusual reactivity of the PPO ligand with $[Ni(MeCN)_4](BF_4)_2$ will be in the focus of this chapter. The fluorophosphine-stabilised nickel(0) source will be investigated to acquire new knowledge about this ligand class and to explore the compound's catalytic potential.

3   Transition metal complexes of the PPO/POP-based ligand

The results discussed in this chapter were partially published in:

F. Flecken, T. Grell and S. Hanf, *Dalton Trans.*, **2022**, *51*, 8975–8985 under the license CC BY 3.0.

Figure 11, 13, 14, 18, 19 and Table 1 and 2 are (partly) adapted from this publication.

Theoretical calculations were conducted by Schirin Hanf. Crystallographic data were processed by Toni Grell.

Additional data in open file formats can be accessed on Zenodo, DOI: 10.5281/zenodo.13732343

One unique feature of the PPO/POP ligand system is the versatile coordination chemistry, which can be facilitated by the different donor sites available in the two tautomers, that can be adopted.[12,13,15] The different nature of the available donor functionalities in the PPO- and POP-tautomers opens a wide spectrum of metals in various oxidation states as potential coordination partner for PPO/POP-based complexes. Hence, further exploration of the coordination behaviour is required to deepen the knowledge of this ligand class and to expand the understanding of factors, which influence the tautomeric equilibrium and the formation of coordination-stabilised tautomers.

3.1   Synthesis of PPO/POP-based transition metal complexes

DFT calculations confirmed that under ambient conditions, the PPO form dominates over the POP form ($\Delta E = 41$ kJ mol^{-1}; B3LYP, def2-TZVP, gas phase). The same behaviour can be witnessed in solution, as seen from the ^{31}P{^{1}H} NMR spectrum of the ligand in various solvent, which displays solely signals of the PPO form ($\delta = 35.8$ ppm, d, $^{1}J_{PP} = 227.7$ Hz, P(IV); -22.5 ppm, d, $^{1}J_{PP} = 227.7$ Hz, P(II) in CD$_2$Cl$_2$). No shift of the equilibrium can be observed in different solvents, such as CD$_2$Cl$_2$ or C$_6$D$_6$. The predominant PPO form obtains one hard (oxygen) and one soft (P(II), phosphorus of the Ph$_2$P-unit) donor site according to the HSAB (hard and soft acids and bases) principle. This chapter describes a systematic study on transition metal complexes of the PPO/POP ligand, focussing on the formation of different coordination modes and the effect of metal coordination on the tautomeric equilibrium through the formation of coordination-stabilised tautomers. Therefore, Fe(II) and Y(III) as harder metals as well as the soft coinage metals, Cu(I) and Au(I), were chosen as coordination partners (Figure 10).
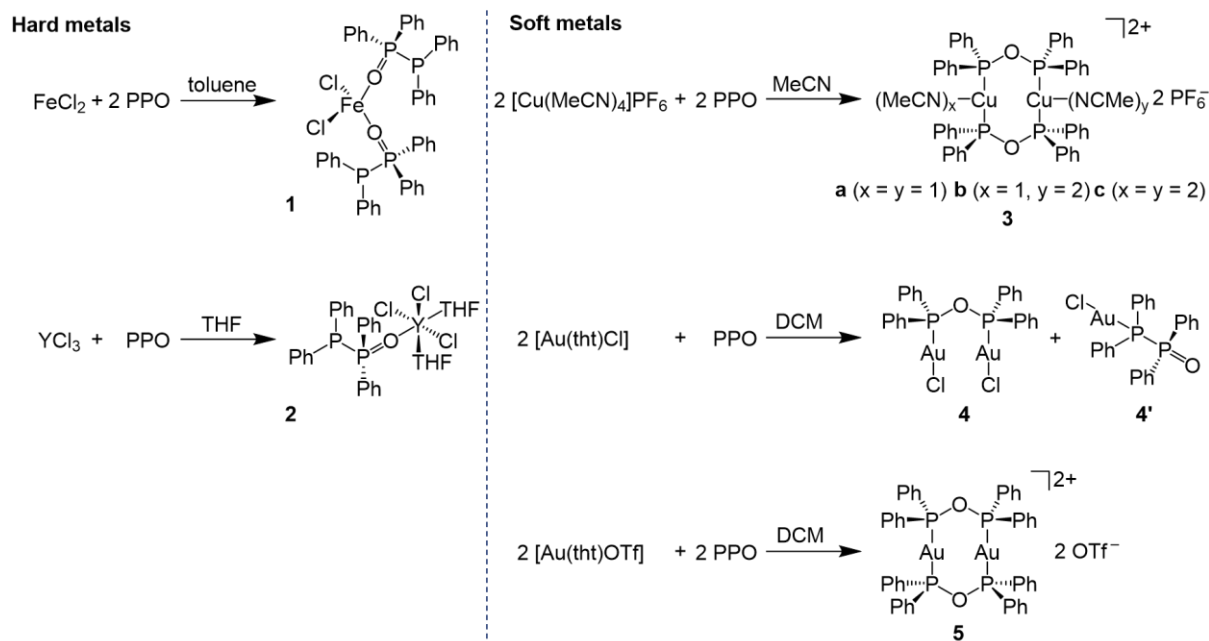
Figure 10. Coordination chemistry of the PPO/POP ligand system in presence of harder (Fe(II) and Y(III)) or soft transition metals (Cu(I) and Au(I)).

As expected, both representatives of harder transition metals, namely Fe(II) and Y(III), are coordinated through the oxygen atom of the PPO tautomer, while the softer phosphorus donor site remains uncoordinated. The reaction of the PPO ligand with $FeCl_2$ (1:2) at room temperature resulted in the formation of pale-yellow crystals of $[FeCl_2(PPO)_2]$ (**1**), which were suitable for single-crystal X-ray diffraction (SC-XRD) after layering the saturated toluene solution with *n*-pentane in 37% crystalline yield. Single-crystal XRD revealed a tetrahedral coordination environment of the Fe(II) centre, which is coordinated by two chloro and two PPO ligands. The yellow colour of the complex indicated a paramagnetic high spin configuration of the Fe(II) centre, which can be confirmed *via* NMR spectroscopy since no distinct signals can be detected.

With YCl_3, as a second example of a hard metal centre, again the coordination *via* the oxygen atom could be achieved as confirmed by single-crystal XRD analysis of colourless crystals of $[YCl_3(THF)_2(PPO)]$ (**2**), which were grown from a saturated THF solution layered with *n*-pentane (Figure 11). Whereas, the Fe-based structure involves two coordinating PPO ligands, with YCl_3 only one PPO ligand is being present. The octahedral coordination sphere of the Y centre is additionally filled with two THF molecules and three chloro ligands. $^{31}P\{^1H\}$ NMR studies of **2** confirm the coordination *via* the oxygen atom of the PPO ligand in solution, since a downfield shift of the P(IV) signal (δ = 51.8–44.1 ppm, m) can be observed compared to the free ligand, while the signal of the P(II) (δ = −19.9 ppm, d, $^1J_{PP}$ = 271.7 Hz) is comparable to the chemical shift of this P centre within the free PPO ligand. The coupling pattern of the P(IV) signal stems from the coupling with the Y nucleus, according to an ABX spin system (I = 1/2, natural abundance = 100%).
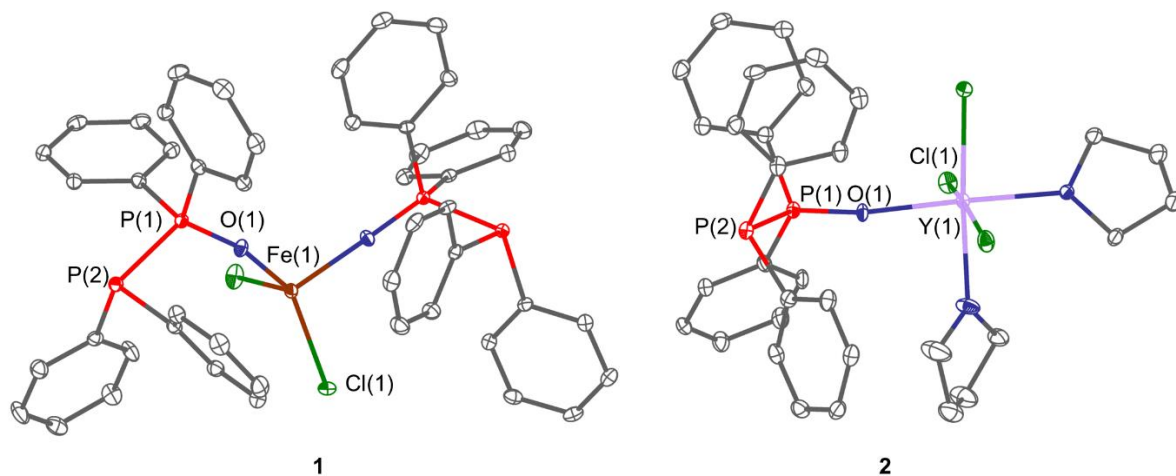
Figure 11. Molecular structures of compounds **1** and **2**. Hydrogen atoms and solvent molecules are omitted for clarity. Selected bond lengths [Å] and angles [°] for **1**: Fe(1)–(O1) 2.017(2), Fe(1)–(O2) 2.006(3), P(1)–(O1)1.506(3), P(1)–P(2) 2.202(1), P(3)–(O2) 1.493(3), P(3)–P(4) 2.188(1), O(1)–Fe(1)–O(2) 97.9(1), Cl(1)–Fe(1)–Cl(2) 114.90(4), O(1)–P(1)–P(2) 117.3(1), O(2)–P(3)–P(4) 117.8(1) P(1)–O(1)–Fe(1) 151.90(11), P(3)–O(2)–Fe(1) 178.44(13) and for **2**: Y(1)–O(1) 2.204(4), P(1)–O(1) 1.502(4), P(1)–P(2) 2.188(2), O(1)–P(1)–P(2) 116.3(2). This figure has been adapted from [154] (license CC BY 3.0).

Upon coordination to the metal centres, a reduction of the P–P bond (**1**: 2.202(1) Å; **2**: 2.188(2) Å) and simultaneously an extension of the P=O bond (**1**: 1.506(3) Å; **2**: 1.502(4) Å) occurs compared to the free ligand (P–P: 2.2128(6) Å; P=O: 1.389(1) Å).[34] The P–P bond reduction is slightly more pronounced for the Y complex **2**, whereas the P=O bonds are almost equal for both complexes. Only a very small impact of the coordination on the P–P–O angles can be identified (**1**: 117.3(1)°–117.8(1)°; **2**: 116.3(2)°; free PPO: 117.9(1)°). Similar conclusions can be drawn from the literature-known Al, Ga and Zr complexes which are, to the best of our knowledge the only three reported complexes including coordination of the PPO ligand *via* the oxygen functionality. Hereby, a Zr(IV)-based complex, [ZrCl$_4$(PPO)$_2$],[61] is the only example of a transition metal complex, whereas other complexes are aluminium [AlCl$_3$(PPO)][62] and gallium [GaClMe$_2$(PPO)][60] based. Whereas the P–P bonds of the Y and the Al complexes are in the same range, the P=O bonds are slightly more elongated for the Zr and Al examples compared to the herein reported complexes **1** and **2**. Besides **1**, the reported Zr complex is another example obtaining two coordinating PPO ligands. In contrast to **1**, an octahedral coordination geometry is present in the Zr based complex whereby an ideal linear arrangement of the two ligands (O–Zr–O: 180.0°) can be observed. In **1** a distorted tetrahedral geometry is present around the Fe(II)-centre (O–Fe–O: 97.9(1)°). Furthermore, the P–O–M angles of the two coordinating PPO ligands in **1** indicate a certain degree of flexibility, since one PPO ligand obtains an angle which is about 25° larger than the one in the other ligand (151.90(11)° and 178.44(13)°). Contrary, in the Zr complex both PPO ligands exhibit the same P–O–M angle of 155.6°.

It should be underlined that the free phosphorus coordination site within the PPO hybrid ligand is particularly interesting with regards to the preparation of heterobimetallic complexes. Through coordination of a second metal centre heterobimetallic complexes could be obtained, in which cooperative effects could potentially play a key role.[50,52,155,156]

The majority of literature known examples concerning the coordination chemistry of PPO, describes the P(II) coordination of softer metals, such as Cu(I),[35,54] Mo,[13] Co[55] and Fe[56-59] in zero-oxidation state. Therefore, the coordination chemistry of the PPO/POP ligand was extended towards Au(I) and Cu(I) as part of this work. [Cu(MeCN)$_4$]PF$_6$ as well as the two Au-precursors [Au(tht)Cl] and [Au(tht)OTf] have been selected. The use of CuCl as alternative Cu source provided crystals of [(Cu$_4$(μ_3-Cl)$_2$(μ_2-Cl)$_2$(μ_2-POP)$_2$], a structure, which has already been reported as a side-product in an attempted synthesis of an aminodiphosphine-stabilised copper complex.[35] In this work, ^{31}P{^{1}H} NMR studies imply a different reaction outcome instead of a P(II) coordination of PPO. In presence of the metal precursors, the two doublets of the PPO ligand diminish and new singlets appear with a strong downfield shift to 106.1 ppm (**3**, [Cu$_2$(MeCN)$_n$(μ_2-POP)$_2$](PF$_6$)$_2$, CD$_2$Cl$_2$), 116.1 ppm (**4**, [Au$_2$Cl$_2$(μ_2-POP)], CD$_2$Cl$_2$) and 132.0 ppm (**5**, [Au$_2$(μ_2-POP)$_2$](OTf)$_2$, CD$_2$Cl$_2$). For **4**, additional signals were obtained at 32.2 ppm (P(IV)-PPO, d, $^1J_{PP}$ = 33.0 Hz) and 16.7 ppm (P(II)-PPO, d, $^1J_{PP}$ = 33.0 Hz). The appearance of the singlet signals points towards the formation of coordination-stabilised tautomers, in which the coordination occurs *via* the two phosphorus atoms of the diphosphine-type POP tautomer. Signals appearing additionally in the spectrum of **4**, reveal that, besides the formation of the dinuclear POP-bridged complex, a P(II)-coordinated, mononuclear [AuCl(PPO)]) complex (**4'**) can simultaneously be formed (Figure 12). The coordination *via* P(II) becomes obvious from a downfield shift in the ^{31}P{^{1}H} NMR spectrum compared to the P(II) signal in the free ligand, whereas the P(IV) signal remains at a similar chemical shift.
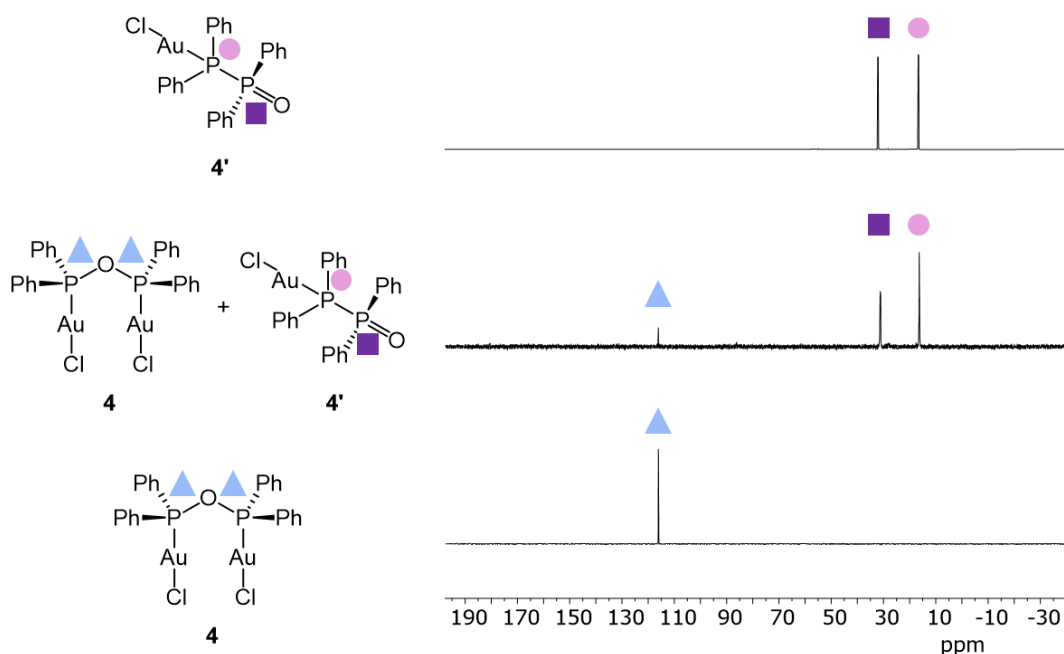
Figure 12. The reaction of [Au(tht)Cl] and PPO can result either in the formation of **4** or of **4'** as revealed by ^{31}P{^{1}H} NMR spectroscopic studies of three different reaction approaches which either yielded pure **4'** (top), a mixture of **4** and **4'** (middle) or majorly **4** (bottom).

Single-crystal XRD analysis of the compounds confirmed the POP tautomer of the ligand in presence of the softer metal ions. This agrees with earlier literature-reported studies, in which the POP form can be stabilised *via* metal coordination.[15,157] Hereby the bridging coordination

mode is often favoured over chelate complexes, due to a higher ring strain in latter ones, which destabilises the formation of such compounds.[68] The bridging coordination mode of the ligand facilitates the close proximity and thus metallophilic interactions of two metal atoms, due to the small ligand backbone bridge of the two phosphorus units. This opens the opportunity for fascinating features in terms of photo-optics and catalysis, especially in processes, which require two active metal centres.[84,87,111]

In **3**, two Cu atoms are bridged from both sides *via* the POP ligand. Interestingly, the proximity of the two metal centres strongly depends on the number of coordinating MeCN molecules, since a decreasing number of MeCN molecules correlates with smaller Cu–Cu distances (Figure 13). With four coordinating MeCN molecules, such as in **3a** $[Cu_2(MeCN)_4(\mu_2\text{-POP})_2](PF_6)_2$, a Cu–Cu distance of 3.371(3) Å is found in the solid state structure. With three MeCN molecules, such as in **3c** $[Cu_2(MeCN)_3(\mu_2\text{-POP})_2](PF_6)_2$, the Cu–Cu distance of 2.8965 Å approaches the sum of the van-der-Waals radii and can even underscore this threshold when only two coordinating MeCN molecules are present. In the case of **3b** $[Cu_2(MeCN)_2(\mu_2\text{-POP})_2](PF_6)_2$, a Cu–Cu distance of 2.4408(23) Å was found. As a result, weak cuprophilic interactions can be formed, which are capable of initiating cooperative effects and consequently photo-optical or catalytic features. Since the Cu atoms are coordinated by two POP ligands from both sides, the cuprophilic interactions are classified as fully-supported (Figure 6).[84] It should be noted, that neither the P–O–P angle (119.85(12)°) nor the P–O bond lengths (1.6173(27)–1.6408(24) Å) are affected by the copper movement, since equal bond lengths and angles are determined for **3a**, **3b** and **3c**.

3a
Cu(2)···Cu(2)
3.371(3) Å

3b
Cu(1)···Cu(1)
2.4408(23) Å

3c
Cu(2)···Cu(1)
2.8965(24) Å
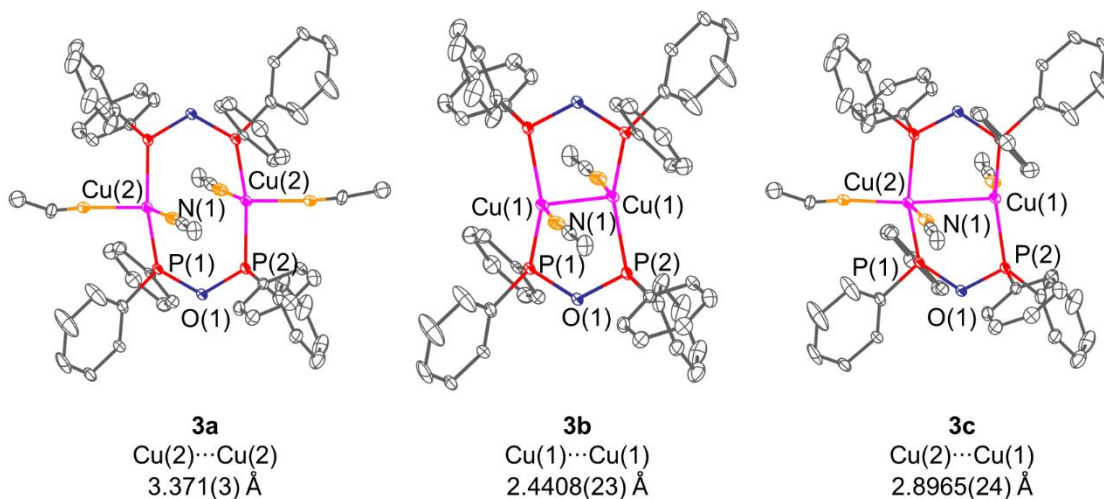
Figure 13. Molecular structures of compound **3a**, **3b** and **3c**, in which different numbers of acetonitrile molecules at the Cu centres are present. The number of coordinated acetonitrile molecules influences the Cu–Cu distance. Selected bond lengths (Å) and angles (°) for **3a**: Cu(2)–P(1) 2.2449(21), Cu(1)–P(2) 2.1987(21), Cu(2)–Cu(2) 3.371(3), P(1)–O(1) 1.6408(24), P(2)–O(1) 1.6173(27), P(1)–O(1)–P(2) 119.85(12), P(1)–Cu(2)–P(2) 139.97(8). Selected bond lengths (Å) and angles (°) for **3b**: Cu(1)–P(1) 2.2272(21), Cu(1)–P(2) 2.2671(21), Cu(1)–Cu(1)2.4408(23), P(1)–O(1) 1.6408(24), P(2)–O(1) 1.6173(27), P(1)–O(1)–P(2) 119.85(12), P(1)–Cu(1)–P(2) 136.55(7). Selected bond lengths (Å) and angles (°) for **3c**: Cu(1)–P(1) 2.2271(21), Cu(1)–P(2) 2.2672(21), Cu(2)–P(1) 2.2449(21), Cu(1)–P(2) 2.1987(21), P(1)–O(1) 1.6408(24), P(2)–O(1) 1.6173(27), P(1)–Cu(1)–P(2) 136.55(7), P(1)–Cu(2)–P(2) 139.97(8). This figure has been adapted from [154] (license CC BY 3.0).

The dependency of the Cu–Cu distance on the number of coordinating MeCN molecules, has also been observed with analogue PCP (C = CH_2, dppm) and PNP (N = NH, dppa) compounds. While four MeCN molecules provide Cu–Cu distances of 3.755–3.7679(7) Å (PCP, dppm)[158,159] and 3.341(2) Å (PNP, dppa),[22] three coordinating molecules result in Cu–Cu distances of 3.3885(7) Å (PCP)[159] and 2.869(4) Å (PNP)[22]. Hereby, a significant larger Cu–Cu distance with PCP ligands compared to POP- and PNP-based compounds underlines the structural differences, resulting from the different ligand backbones. This effect might be a result of the smaller size of the oxygen and nitrogen backbones compared to the one of carbon (covalent radii [pm]: C = 77 > N = 70 > O = 66).[160] It can be concluded that POP- and PNP-type ligands facilitate similar coordination environments, while the PCP ligands enlarge the metal–metal distance. Consequently, there is a higher probability of metallophilic interactions in PNP- and POP-based complexes.

Insights into the electronic impact of the ligand backbone can be gained from the comparison of the $^{31}P\{^{1}H\}$ NMR spectrum of the POP-based complex **3** with the ones of the dppa and dppm analogues. Hereby a tremendous upfield shift can be observed for the dppa analogue (around 50 ppm)[22] and an even higher impact is ascribed to the dppm compound (–8 ppm)[158] compared to the POP compound (106.1 ppm). It becomes obvious that, correlating with the electronegativity of the bridging element [C (2.55) < N (3.04) < O (3.44)], a drastic increase in deshielding of the P atoms can be observed. This once more underlines, not only the spatial but also the electronic impact of the ligand backbone on the properties of the P donor atoms in short-bite diphosphines and confirms the urge for detailed studies of compounds of these types.

Moving from copper to its heavier analogue gold, the two complexes **4** and **5** were isolated from the reaction of the PPO/POP ligand with [Au(tht)Cl] and [Au(tht)OTf] respectively (Figure 14). In both complexes the metal atoms are coordinated in a linear manner. In **4**, one POP ligand bridges the two metal atoms, which on the other side are coordinated by Cl ligands. Although no species of the mononuclear [AuCl(PPO)] complex (**4'**) could be isolated and characterised by means of single-crystal XRD, it can be assumed that this species also contributes to the isolated crystalline material of **4**. Elemental analysis of one sample of **4/4'** strongly indicates a mixture of 80% of **4** and 20% of **4'** in this specific case. It is noteworthy that the air-stability of **4'** is increased, since the P(II) atom is protected from oxidation through the gold coordination. If a mixture of **4** and **4'** is stored in air for 14 days the majority of the complex **4'** is maintained as confirmed by NMR spectroscopic studies. Storage of **4** and of the free PPO ligand in air under the same conditions leads to degradation of these compounds.
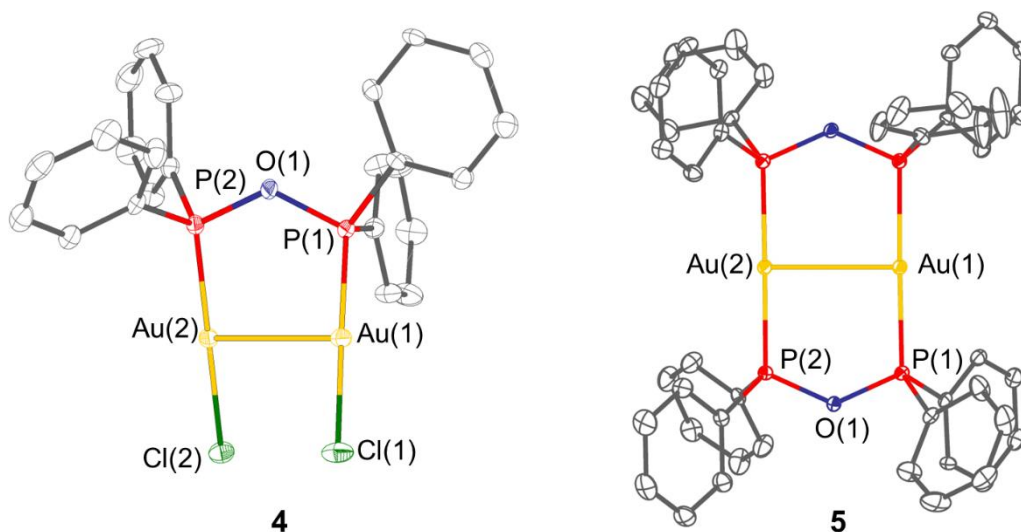
Figure 14. Molecular structures of the two POP-coordinated Au-complexes **4** and **5**. Selected bond lengths (Å) and angles (°) for **4**: Au(1)–P(1) 2.204(1), Au(2)–P(2) 2.208(1), Au(1)–Cl(1) 2.275(1), Au(2)–Cl(2) 2.287(1), Au(1)–Au(2) 3.2055(5), P(1)–O(1) 1.615(3), P(2)–O(1) 1.616(3), P(1)–O(1)–P(2) 125.3(2). Selected bond lengths (Å) and angles (°) for **5**: Au(1)–P(1) 2.312(1), Au(1)–P(2) 2.313(2), Au(2)–P(3) 2.309(1), Au(2)–P(4) 2.304(2), Au(1)–Au(2) 2.9302(7), P(1)–O(1) 1.626(4), P(2)–O(2) 1.627(4), P(3)–O(1) 1.626(4), P(4)–O(2) 1.629(4), P(1)–O(1)–P(3) 131.2(2), P(2)–O(2)–P(4) 131.7(2), P(1)–Au(1)–P(2) 179.00(6), P(3)–Au(3)–P(4) 177.52(6). This figure has been adapted from [154] (license CC BY 3.0).

An analogue [Au$_2$Cl$_2$(µ$_2$-Et$_2$POPEt$_2$)] complex of **4** has been isolated in reactions of nanoparticles stabilised by a diethylphosphine oxide ligand. The structural parameters can be found in a similar range whereby a slight decrease in the P–O–P angle as well as in Au–P distances and P–O bonds can be observed in **4**. The Au–Au distances in **4** are slightly larger than in the reported complex of van Leeuwen and coworkers.[69]

A second Au-complex was isolated in the form of compound **5**, in which the two Au atoms are bridged *via* one POP ligand from each side. The Au–P bonds and P–O bonds in **5** (Au–P: 2.304(2)–2.313(2) Å, P–O: 1.626(4)–1.629(4) Å) are slightly longer than in **4** (Au–P: 2.204(1)–2.208(1) Å, P–O: 1.615(3)–1.616(3) Å). The P–O–P angle is significantly more linear in **5** (131.2(2)–131.7(2)°) than in **4** (125.3(2)°). Whereas in **4** the two Au atoms are only semi-supported for aurophilic interactions, **5** serves as an example of fully-supported aurophilic interactions. This results in a decreased rigidity in **4** compared to **5**, since the chloro ligands tend to be more flexible and could be oriented in different directions whereas the movement of the phosphorus units in **5** is restricted by the framework of the bidentate POP ligand. The higher flexibility of the chloro ligands in **4** can be confirmed by the respective PNP and PCP counterparts. For example, the dppa-analogue of **4** shows a variation in Au–Au distance of 3.121 Å[161]–5.617 Å.[162] This dynamic has a significant impact on the Au–Au distances and consequently on the aurophilic interactions. In **5**, Au–Au distances of 2.9302(7) Å can be found, which in contrast to the Cu-complex, are similar as the one found in the PCP analogue (2.9258(9)[163]–3.120 Å[164], dppm). These Au–Au distances already fall below the sum of the van-der-Waals radii (3.80 Å[84]) and point towards the presence of aurophilic interactions. No solid state structure of the analogue PNP (dppa) complex was isolated up-to-now and only compounds with modified residues at the nitrogen atom can be taken for comparison (R = 2,6-

iPr$_2$C$_6$H$_3$, R = Et). Hereby, even smaller Au–Au distances of 2.7944(19)[165] and 2.838(2) Å[118] are reported.

The comparison of the P–X–P angles in **3-5** (X = O) with other PCP- and PNP-type reveals an interesting difference of the PXP ligands, since in the O-containing complexes a much higher variation of the bond angle can be observed in the gold and copper complexes (Table 15). The POP angles show a difference of almost 12° whereby a significant more linear POP can be found in **5** compared to **3**. PNP and PCP do not show such a flexibility with differences in PXP angles of 6° in PNP-based complexes and only 3° in PCP-based complexes.

In accordance with **3**, similar electronic effects of the bridging atom in the Au complexes **4** and **5** can be seen from the chemical ^{31}P{^{1}H} NMR shift. Hereby, chemical shifts of PCP (dppm) analogues are again around 100 ppm upfield shifted compared to POP-type complexes ([Au$_2$Cl$_2$(μ$_2$-dppm)]: 23.5 ppm[166] and [Au$_2$(μ$_2$-dppm)$_2$): 35.3 ppm)[167] whereas the signals of the PNP analogue can be found in between POP and PCP ([Au$_2$(μ$_2$-dppa)$_2$]: 100 ppm; N(Et)[118]).

The PPO- and POP-containing complexes can be further identified by infrared (IR) spectroscopy (Figure 15). The P=O stretch of the PPO tautomer can be detected at wavenumbers of 1175 cm^{-1} and the P–O–P stretch can be found in the region of 700–900 cm^{-1}.[12,28,168] Upon coordination of the PPO ligand to metal centres, as seen in **1** and **2**, a red-shift of the P=O stretch can be observed, due to the weakening of the P=O bond. If the PPO ligand tautomerises to the POP form, the P=O stretch disappears, and a band can be displayed in the region of POP stretches. As described above, the reaction of PPO with [Au(tht)Cl] results in a mixture of **4** and **4'**. Therefore, samples which can be assigned with ^{31}P{^{1}H} NMR spectroscopy majorly to **4** or **4'** have been compared by IR spectroscopy to confirm the presence of the two tautomers. In the sample which contains mainly compound **4**, minor contributions of a P=O stretch are detected and a significant POP band is visible. On the other hand, in the IR spectrum of the sample which consists majorly of **4'** no POP contribution is identified whereas a blue-shifted P=O stretch is found. This again underlines the different PPO-based coordination modes in **4'**(P(II) coordination) and **1** and **2** in which the metal centre is coordinated *via* the oxygen atom.
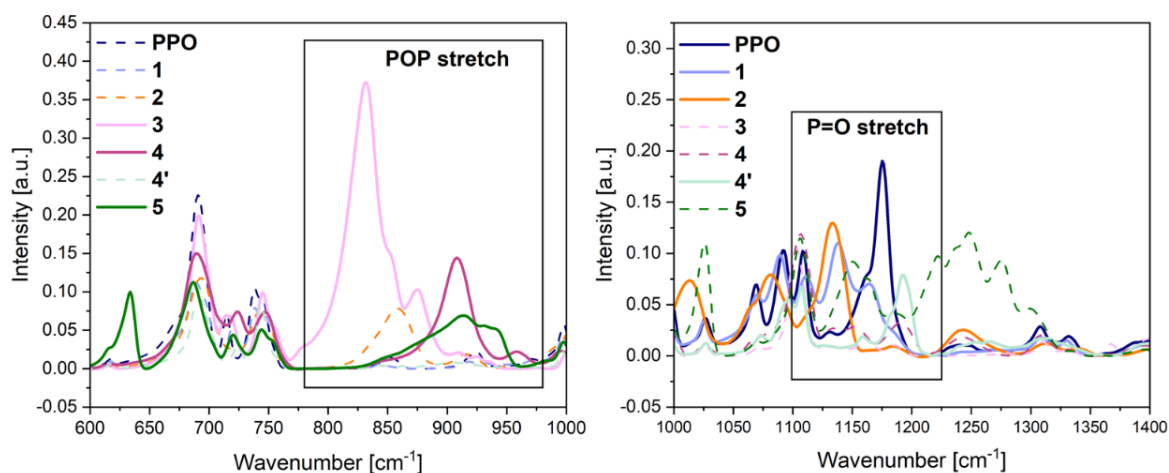

Figure 15. IR spectra of compounds **1-5** displaying the regions of the POP (left) and P=O (right) vibration for identification of the two tautomers.

3.2   Solvent-induced tautomeric equilibrium shift of transition metal complexes

The tautomeric equilibrium might not only play a role in the free PPX/PXP ligand and upon coordination which can induce an equilibrium shift *via* the formation of coordination-stabilised tautomers. Also, in the transition metal complexes both tautomers can be present, as seen for the POP-stabilised compound **4** which appears to form in parallel with the PPO-based complex **4'**. Therefore, investigations have been concentrated on the potential shift of the equilibrium of the ligand within transition metal complexes initiated by external stimuli, such as non-coordinating or coordinating solvents. However, with **4** the equilibrium appears to be difficult to direct and often mixtures of both tautomers are present within the complex. More precisely, by changing the nature of the solvent no predictable effect on the state of the equilibrium can be determined. Furthermore, in **4** and **4'** different ratios of ligand:gold atoms are obtained. Hence, the transition of **4** to **4'** is accompanied by the loss of AuCl and can cause the formation of bulk gold, which would hinder the equilibrium shift back to **4**. For the related gold complex **5**, no impact of the solvents on the tautomeric equilibrium can be identified since in all solvents solely the POP tautomer is present in the corresponding complex. The higher dynamics surrounding the Au atoms in **4** have already been described in the context of the Au–Au distances and might be a major reason why the equilibrium shift in **4** is more likely than in **5**. Whereas in the Au complexes, the linear coordination limits the coordination number to two, in the Cu complex **3**, higher coordination numbers occur, which were shown to vary, depending on the number of coordinated MeCN molecules. Given its higher dynamic behaviour, the equilibrium in **3** could likely be more responsive to external stimuli. Indeed, for the dinuclear Cu complex **3**, $^{31}P\{^1H\}$ NMR and ESI-MS (Electrospray Ionization Mass Spectrometry) spectra confirm a reversible, tautomeric equilibrium shift from **3** to **3'** ($[Cu(MeCN)_n(PPO)]PF_6$) using solvents of coordinating or non-coordinating nature. Despite several attempts to isolate the PPO-based complex **3'**, no crystals suitable for single-crystal XRD could be obtained. In non-coordinating solvents (e.g. DCM, $CHCl_3$) the equilibrium is strongly shifted to the dinuclear POP site, while with coordinating solvents, such as MeCN or THF a mononuclear complex, including the PPO tautomer, can be obtained (Figure 16). The singlet in the $^{31}P\{^1H\}$ NMR spectrum, corresponding to the POP tautomer, diminishes completely and two doublets at 32.6 ppm and –21.4 ppm appear in the area of PPO, whereby latter one is broadened. The coupling constant is strongly decreased to 151 Hz (*versus* free PPO: 227.7 Hz). The comparison with **4'** and literature examples of PPO-based transition metal complexes reveals that the impact of metal coordination on the P(II) signal in $^{31}P\{^1H\}$ NMR is strongly dependent on the metal involved.[13,35] A similar equilibrium shift was reported by Wong *et al.* when heating up a $[Mo(CO)_5(PPO)]$ complex.[12] Through the heating process, one CO ligand dissociated from the Mo centre and provided a free coordination site. This coordination site was occupied by the ligand, which converted into the POP tautomer to chelate the metal centre. With complex **3**, this transition appears to be much easier to access under mild conditions. For all three samples **3**-**5**, no effects of ultraviolet (UV) radiation (254 and 365 nm) or heating on the equilibria could be identified.
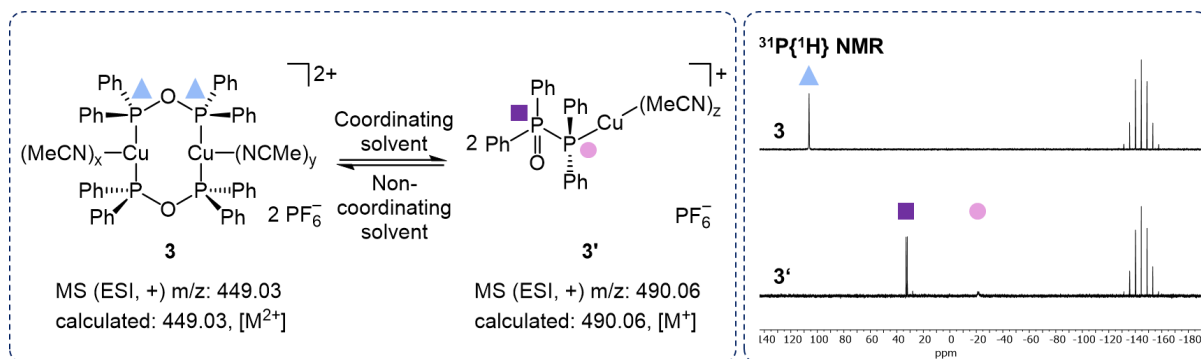
Figure 16. The solvent-induced tautomeric equilibrium shift of the PPO/POP-based Cu-complex **3** which shifts to **3'** in the presence of coordinating solvents and can be displayed by ^{31}P{^{1}H} NMR spectroscopy.

In analogy to the solvent-induced equilibrium shift, it can be assumed that substrates in catalysis can also be capable to cause such a shift. Hereby, it is remarkable that both forms of the tautomeric ligand can form complexes with the same transition metal depending on the influence of other ligands on the metal. This unique feature could be useful in both directions, meaning the TM$_2$PXP$_2$ and the TM–PPX side (X = O, S), since in the first case the two metal atoms can come in close proximity to each other, which is especially useful in catalysed reactions that involve two metal centres. If the bidentate PXP coordination mode shifts towards the monodentate PPX coordination, an easier access and a free coordination site at the active site emerges (Figure 17). Additionally, the non-coordinating X atom offers the possibility of substrate direction and stabilisation *via* the free X donor site during catalysis.[152] This would be in accordance with the related secondary phosphine oxides, in which the uncoordinated oxygen centre acts as a nucleophile as for example reported for the hydrogenation of nitriles.[48,153] Consequently, vacant active sites could be either offered through conventional hemilability, meaning the de-coordination of one P atom of the PXP ligand, due to a high ring strain. This type of hemilability was identified to significantly enhance catalytic processes, such as polymerisation reactions[127-129] or biofuel production,[92,131] which involve PCP- and PNP-based transition metal catalysts.[92,127,129,131] Additionally with the PXP/PPX ligand system the tautomerism shift can be understood as a novel type of hemilability.
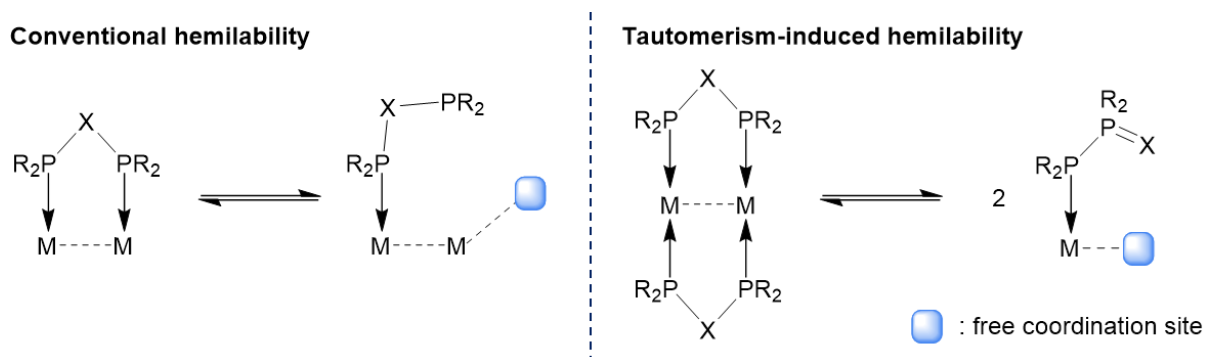
Figure 17. Conventional hemilability can be described by dissociation of one donor site from the metal centre (left). Tautomerism-induced hemilability: through the presence of other substances, the equilibrium can be shifted from the PXP to the PPX side (X = O, S). Thereby, a free coordination site is available at the catalytically active site (right).

3.3 Photo-optical properties of PPO/POP-based transition metal complexes

As seen from the solid state structures of **3-5**, the small backbones of short-bite ligands can facilitate short M–M distances in the bridging coordination mode of the ligands, which result in the formation of metallophilic interactions. Based on this feature, an exceptional photo-optical behaviour of the complexes can be witnessed. Reported examples include PNP- and PCP-based transition metal complexes, such as $Ph_2PNRPPh_2$ (R = Et,[118] C_6H_5,[169] 2,6-$Me_2C_6H_3$,[169] $C_6H_3N_2S$[97]) or $Ph_2PCH_2PPh_2$[120,170] whereas POP- and PSP-coordinated analogues have not received much attention. With the compounds **1-5** in hand, their photo-optical behaviour was investigated as part of this work, with the aim to acquire knowledge about the underexplored PPO/POP ligand class in the field of photo-optics.

Under UV radiation (365 nm) all samples, except **1,** display photoemission at 77 K, whereby only the free PPO ligand and **2** show emission at room temperature (Figure 18). This is in contrast to dppa- and dppm-based counterparts of compound **3** and **5,** which display bright photoemission already at room temperature in solution.[117,118,120] One reason for these different photoemissions might be a higher degree of non-radiative decays which could stem from increased flexibility in the oxygen-backbone. Additionally, compound **3** exhibits thermochromic behaviour, since at 77 K a blueish photoemission can be observed which changes to orange upon warming of the sample.
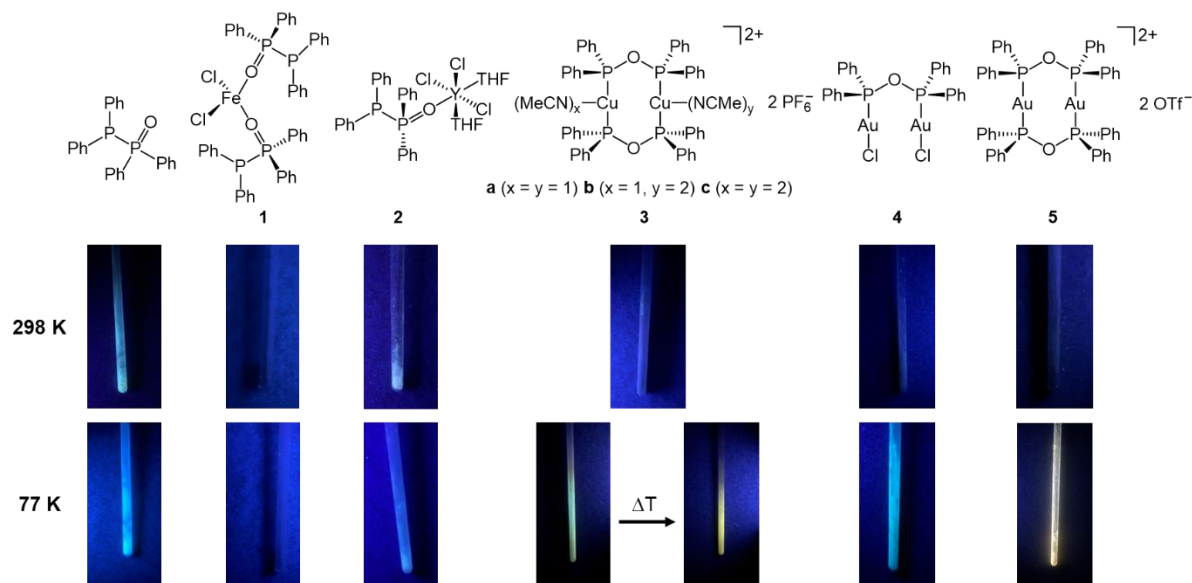
Figure 18. Samples **1-5** and the free PPO ligand under UV radiation (365 nm) at 298 K and 77 K. Compound **3** shows a thermochromic behaviour. This figure has been adapted from [154] (license CC BY 3.0).

For further details on the photoemission characteristics, photo-luminescence excitation (PLE) and emission spectra (PL) have been recorded (Table 1). These photo-optical investigations have been conducted at room temperature and at 77 K, since at this temperature, non-radiative decays can be minimised, while the intrinsic photoemission behaviour of the compounds can be maximised, especially if phosphorescence-type transitions take place. Therefore, the main discussion is focussed on the low-temperature measurements. However,

quantum yield determinations could only be conducted at room temperature due to technical limitations of the setup used.

Table 1. Photo-luminescence data for the PPO ligand and the complexes **2–5** in the solid state at 77 K and 298 K. This table has been adapted from [154] (license CC BY 3.0).

	T [K]	λ_{ex} [nm]	λ_{em} [nm]	Lifetime$_{eff.}$ [µs] [a]	M–M [Å]
PPO	77	367	456	6	
	298	367	456	6	
2	77	352	414	6	
	298	352	414	6	
3	77	373	483	99	2.4408(23)–3.371(3)
	298	400	440	5	
4	77	361	499	7	3.2055(5)
	298	387	470	6	
5	77	350	445	7	2.9302(7)
	298	364	452	6	

[a] For biexponential decays (DCM, 77 K), the effective lifetimes were calculated. More information concerning these calculations can be found in the experimental part of this thesis.

Initially, solid samples were investigated to circumvent the impact of solvent effects. It becomes obvious that none of the compounds displays PLE and PL spectra, which are in accordance with the mirror rule (Figure 19). This experimental observation points towards the fact that the photoemission is not only based on simple $S_1 \rightarrow S_0$ transitions, but rather on transitions involving various energy levels. The large Stokes shifts point towards the occurrence of non-radiative processes, such as ISC, and finally transitions of lower lying energy levels, which cause the photoemission behaviour. In agreement with the observation that **1** shows no photoemission, only very low intensity spectra can be recorded for this compound. PPO shows broad PLE and PL spectra with a maximum emission at 456 nm. This emission maximum is blue-shifted to 414 nm, if PPO is coordinating to Y(III) in **2,** pointing towards a transition to the ground state from a higher energy level. For compounds **3** and **4**, broad and symmetrical emission spectra are detected, which are characteristic for d^{10} coordination compounds. With 499 nm, the emission maximum for **4** is slightly red-shifted compared to the one of **3** with 483 nm. The large Stokes shifts can be an indication for phosphorescence instead of fluorescence. However, with transition metal complexes, a distinct assignment to one of the two emission types is in most cases challenging.[102] In the PLE and PL spectrum of **5**, two maxima arise which is untypical for d^{10} metal-based complexes and implies that different processes are responsible for the photoemission behaviour. The courses of the PL spectra in the solid state and in frozen DCM solution (77 K, Figure 53, appendix) show distinct variations, which points towards a solid state effect due to crystal packing or aggregation-induced emission which contributes to this emission.

Furthermore, emission lifetimes have been recorded for the photo-luminescent samples. As already indicated by the larger Stokes shifts, the nature of the photoemission can be mainly attributed to a transition from triplet excited states since the recorded lifetimes are found in the microsecond range. Compound **3**, which already showed unique thermochromic behaviour, displays long lifetimes of a biexponential decay of 215 and 67 µs ($\tau_{eff.}$ = 99 µs, equation 2, chapter 9.3) which exceeds other reported lifetimes for dinuclear Cu(I) complexes, such as bis(dicyclo-hexylphosphino)methane-,[171] diphenylphosphino-pyridine[172,173] or pyridylphospholane-bridged[174] copper complexes. This might again be a result of the dynamic behaviour around the Cu centres, which enables the close proximity of the metal centres and hence strong cuprophilic interactions through the POP ligand.
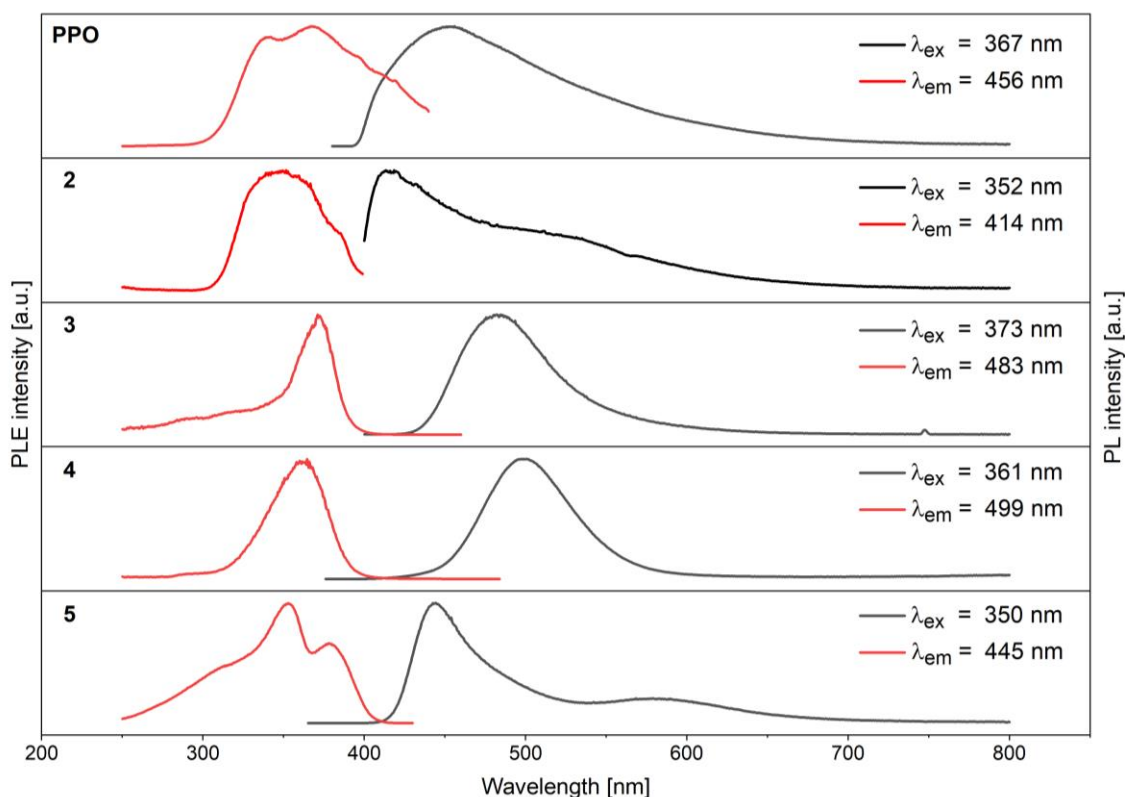
Figure 19. Photo-luminescence emission (PL) and excitation (PLE) spectra of the PPO ligand and complexes **2**–**5** at 77 K in the solid state. This figure has been adapted from [154] (license CC BY 3.0).

It should be mentioned that the discussed tautomerism of the Cu complex **3** could be used as switch for turning the photo-optical properties on or off. This would derive from the cuprophilic interactions, which are present in the POP-bridged Cu$_2$ species **3**, whereas a shift to the PPO side **3'** would provide a species with only one Cu atom and therefore no cuprophilic interactions within the molecule. Since the cuprophilic interactions are presumed to be the origin for the photo-optical properties, with PPO-based species the emission could be deactivated.

3.4 Catalytic application of [Cu(MeCN)$_n$(PPO)]PF$_6$ for Ullmann-type coupling reactions

Inspired by the adjustable tautomeric equilibrium of **3/3'**, the influence of the tautomerism on the catalytic activity of **3/3'** was investigated. Therefore, Ullmann-type cross coupling reactions of phenol with iodobenzene in presence of either **3** in DCM or **3'** in MeCN were conducted, since Cu(I) compounds are known to be efficient catalysts for this type of coupling reactions (Scheme 1). Before 2000, harsh reaction conditions were required for Ullmann-type couplings, including temperatures up to 210°C, large amounts of copper and long reaction times.[175,176] In recent years, advances in the field of ligand design facilitated the application of milder reaction conditions, such as lower temperatures of around 100°C and smaller quantities of copper.[175]
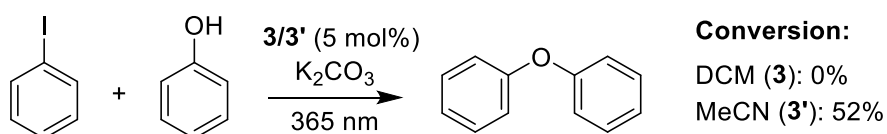
Scheme 1. Ullmann-type coupling reaction using **3** or **3'** as catalyst (5 mol%), at room temperature under UV radiation (365 nm) for 24 h in presence of K$_2$CO$_3$ (2 eq.) in either DCM or in MeCN.

The aim of this study was to apply relatively mild conditions for the C–O coupling, while investigating the potential of **3** and **3'** as homogeneous (pre-)catalysts. When the catalytic reaction was carried out at room temperature, no product formation could be witnessed. Therefore, the reaction mixture was irradiated with UV light (365 nm) at room temperature and indeed the production of diphenyl ether could be achieved. Surprisingly, the product formation could only be achieved if the reaction was conducted in MeCN and not in DCM. It should be underlined that previous studies (chapter 3.2) have shown that **3'** is the dominant species in MeCN, whereas in DCM **3** is majorly observed. The catalytic inactivity in DCM was confirmed by using a solvent mixture (1:1, DCM : MeCN), which led to a drop in the conversion compared to pure MeCN. Furthermore, no conversion could be achieved in the absence of UV radiation.

To understand the impact of the solvent and the corresponding tautomeric forms **3** or **3'**, ^{31}P{^{1}H} NMR spectroscopic studies of the reaction mixtures after the catalytic reactions in DCM and MeCN were recorded (Figure 54, appendix). In both solvents, the ^{31}P{^{1}H} NMR spectra point towards a change of the initial species **3** in DCM and **3'** in MeCN. For the reaction mixture in DCM, a major signal at 31.5 ppm in the ^{31}P{^{1}H} NMR spectrum of the final reaction mixture was observed. Surprisingly, no PF$_6^-$ signal remains after the reaction. Despite no successful isolation of this species, the chemical shift points towards a similar compound as found by Naktode, namely a POP-stabilised tetranuclear Cu$_4$Cl$_4$ species.[35] This would involve an anion-directed nuclearity change, which has been reported for similar dppm-based copper complexes by Bera *et al.*[120] Since in DCM no catalytic conversion can be detected, the formed compound can be regarded as catalyst sink, which does not provide any vacant active sites for substrate binding and might be a result of strongly binding iodo ligands stemming from iodobenzene, since no PF$_6^-$ anions can be detected any more. Furthermore, after 24 h of radiating (365 nm) compound **3** in DCM, no compound-specific signal can be displayed at all in the ^{31}P{^{1}H} NMR spectrum, which points towards ligand degradation processes. Contrary, in the reaction mixture of **3'** in MeCN after the catalytic reaction, the presence of PF$_6^-$ can be

confirmed by ^{31}P{^{1}H} NMR spectroscopy. This is advantageous in terms of catalysis, since with this loosely bound anion the active centre might be easier accessible in comparison to strongly binding anions, such as halides. In addition to the PF_6^- signal, a main peak at 29.9 ppm (s) became obvious, which is assumed to be the catalytically active species of the coupling reaction.

To gain further insights into the catalytically active species, NMR spectroscopic studies were conducted, focussing on the impact of the UV radiation on **3'** in MeCN in the presence of the different substrates. Therefore, samples of a) the pure copper-species **3'**, b) the species in presence of K_2CO_3 and phenol (ratio 1:1:1) and c) the species in presence of K_2CO_3 and iodobenzene were investigated (1:1:1). With a) no change of the nature of **3'** could be observed, which confirms that **3'** is stable under UV light. Also, in presence of phenol and K_2CO_3 (b) **3'** is the major species, whereby minor formation of a phosphine oxide species can be witnessed. Sample c) proves, that for the formation of the catalytically active species (δ = 29.9 ppm), the presence of iodobenzene is required. However, structural insights of this species could not be gained, since several attempts to isolate this compound did not succeed.

These findings give a first insight into how the tautomerism can influence the catalytic activities of PPO/POP-based coordination compounds. Interestingly, the POP-stabilised complex **3** seems to be no efficient (pre-)catalyst for C–O coupling reactions, whereas with the PPO-based copper complex **3'** an efficient conversion of the substrates can be achieved. It is suggested that this contrary behaviour stems from different stabilities of the two tautomers and a more accessible Cu centre in the PPO-based complex **3'** in MeCN. It has to be mentioned, that several important factors still remain unknown, such as the real catalytically active species and the underlying reaction mechanism, which is, however, a general obstacle in Ullmann-type coupling reactions.[176]

3.5 Concluding remarks

The PPO/POP ligand set is capable of coordinating various hard and soft metals, due to its different available donor sites based on the presence of two tautomers. Harder metals are coordinated *via* the hard oxygen donor functionality in the potential hybrid ligand PPO. Through the formation of coordination-stabilised tautomers of the POP form in presence of the soft coinage metals Cu(I) and Au(I), complexes with the oxygen-analogue ligand to the well-known dppm and dppa ligands can be isolated. The short-bite ligands promote short M–M distances, which induce metallophilic interactions of the d^{10} metals. Hereby it was shown that the ligand backbone has a strong impact on the characteristics of the different metal complexes, as it can be seen from investigations of the molecular structures in the solid state, of the NMR spectroscopic properties and of the photo-optical properties. Thereby POP-stabilised complexes do not show any photoemission at room temperature in contrast to equivalent dppm- and dppa-based complexes.[117,118,120] However, at 77 K, all dinuclear d^{10}-based complexes exhibit bright photo-luminescence. A particularly long emission lifetime of 99 µs was determined for the Cu complex **3,** which additionally features a thermochromic behaviour. This might be connected to its highly dynamic Cu–Cu distances, which also vary with changing number of attached MeCN molecules. Furthermore, the tautomeric equilibrium

of the PPO/POP ligand is highly relevant in **3**, since a shift from the dinuclear, POP-bridged Cu-species to a mononuclear, PPO-coordinated complex can be triggered in presence of coordinating solvents. This observation is of great significance for catalytic applications, since it introduces a potential new type of tautomerism-induced hemilability. If such a behaviour can be induced by substrates in a catalytic cycle, a facile access to a vacant site of the active centre for substrate binding can be given. Initial studies therefore focussed on Ullmann-type coupling reactions and confirmed the catalytic activity of the PPO-coordinated copper complex **3'** in MeCN, whereas **3** in DCM appeared to be catalytically inactive.

4 Trinuclear copper complexes and photo-optical properties

The results discussed in this chapter were partially published in:

F. Flecken, A. Knapp, T. Grell, C. Dreßler and S. Hanf, *Inorg. Chem.*, 2023, **62**, 13038-13049.

Figure 21, 23 and 26 as well as Table 4 and Scheme 3 are (partly) adapted from this publication. Copyright **2023** American Chemical Society.

A part of the results is also discussed in the article: F. Flecken and S. Hanf, *Dalton Trans.*, 2024, **53**, 17123-17131 including Table 3 (license CC BY 3.0).

Theoretical calculations were conducted by Schirin Hanf and Christian Dreßler. Crystallographic data were processed by Toni Grell.

Additional data in open file formats can be accessed on Zenodo, DOI: 10.5281/zenodo.13732424

Various trinuclear transition metal complexes have been synthesised based on PCP- and PNP-ligands, including cores consisting of Ni(II), Pd(II), Cu(I), Ag(I) and Au(I).[66,177-183] In such complexes, the metal core is capped from both sides by a halide ligand forming the central TM_3Hal_2 motif (TM = transition metal). These transition metal complexes possess fascinating redox[184,185] and photo-optical properties[177,179,186] and could show interesting magnetic potential for applications in quantum computing, if suitable metals, such as Cu(II), are being incorporated.[187,188] Whereas trinuclear compounds based on PCP- and PNP-ligands are widely studied, examples including a sulphur- or oxygen-containing ligand backbone have mainly been overlooked. To gain knowledge about the impact of the oxygen or sulphur backbone, this work presents a systematic study of POP- and PSP-based trinuclear copper complexes with different capping halides (Cl, Br, I).

4.1 Synthesis of POP-based trinuclear copper complexes

The reaction of the PPO ligand with the two Cu precursors, $[Cu(MeCN)_4]PF_6$ and CuCl, already demonstrated the effect of the choice of metal precursor on the product formation, providing Cu complexes with different nuclearities. Whereas the use of $[Cu(MeCN)_4]PF_6$ as precursor provided the dinuclear compound $[Cu_2(MeCN)_n(\mu_2\text{-POP})_2](PF_6)_2)$ (**3**), with CuCl a tetranuclear complex $[(Cu_4(\mu_3\text{-Cl})_2(\mu_2\text{-Cl})_2(\mu_2\text{-POP})_2$ can be obtained (Scheme 2).
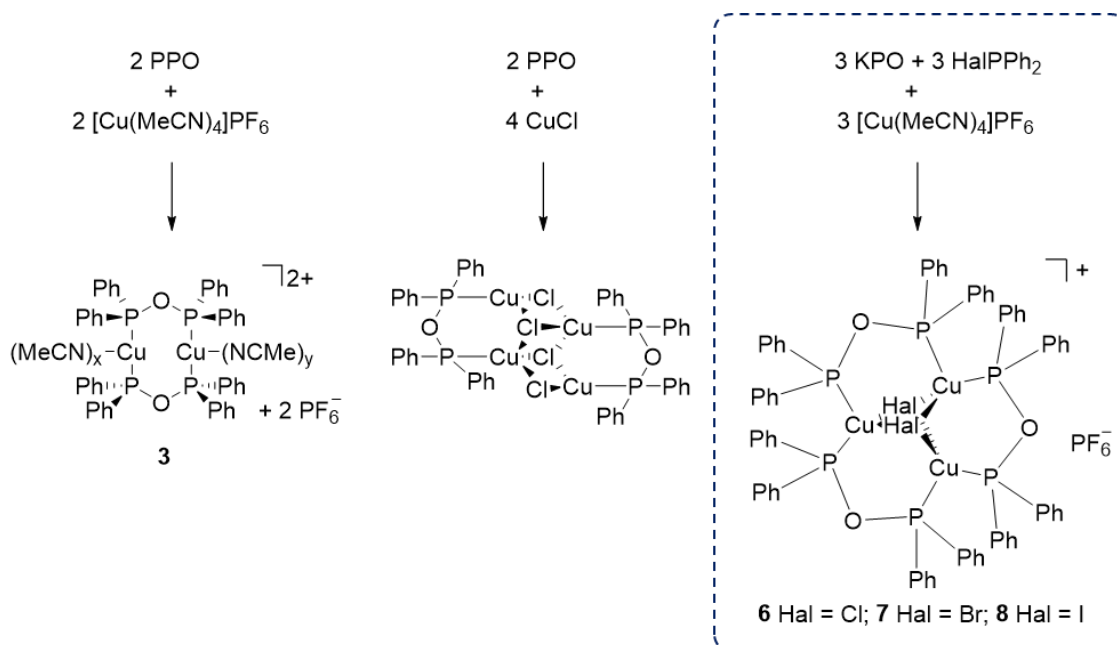
Scheme 2. Synthesis of POP-stabilised copper compounds with different nuclearities.

A very interesting result could be achieved through the *in-situ* formation of the POP ligand, from the potassium salt of diphenylphosphine oxide ($Ph_2P(=O)K$, KPO) and chlorodiphenylphosphine ($ClPPh_2$), in the presence of $[Cu(MeCN)_4]PF_6$. Whereas in the absence of a metal source, this reaction gives access to the pure PPO ligand, in presence of $[Cu(MeCN)_4]PF_6$, the $ClPPh_2$ serves as precursor for the coordinating ligand and additional as halide source, resulting in the formation of a trinuclear copper complex, $[Cu_3(\mu_3\text{-}Cl)_2(\mu_2\text{-}POP)_3]PF_6$ (**6**), which is stabilised by the POP ligand and the Cu_3 core is further capped by one halide ion on each side of the triangular core.

By using this approach the addition of an external halide source can be circumvented which is often mandatory for the formation of similar structures.[120,186] Attempts to extend this protocol to other halides could be achieved through switching from $ClPPh_2$ to $BrPPh_2$ and $IPPh_2$, providing $[Cu_3(\mu_3\text{-}Br)_2(\mu_2\text{-}POP)_3]PF_6$ (**7**) and $[Cu_3(\mu_3\text{-}I)_2(\mu_2\text{-}POP)_3]PF_6$ (**8**). The formation of the compounds can be confirmed by single-crystal XRD and NMR spectroscopy (Figure 20). In the IR spectrums, the presence of the POP tautomer is again confirmed by the presence of P–O–P stretches at 889 (**6**), 893 (**7**) and 881 (**8**) cm^{-1}, respectively.
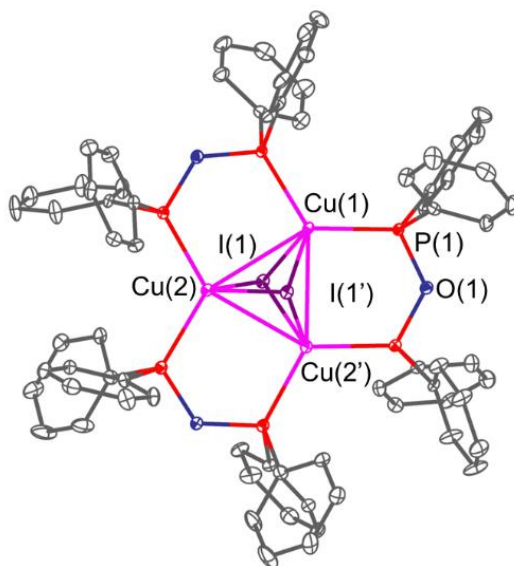
Figure 20. Molecular structure of the cation of $[Cu_3(\mu_3\text{-}I)_2(\mu_2\text{-}POP)_3]PF_6$ (**8**) as an example for POP-stabilised compounds **6-8**. The counter anion is omitted for clarity. Selected bond lengths and angles of these compounds are given in Table 2.

The formation of the trinuclear copper complexes requires a precise control of the reaction stoichiometry. If an excess of iododiphenylphosphine is used, instead of the trinuclear complex, $[Cu_4(\mu_3\text{-}I)_4(Ph_2PI)_4]$ (**9**) can be isolated (Figure 21). A Cu_4I_4 unit forms the core of the structure, whereby each Cu(I) centre is additionally coordinated by one iododiphenylphosphine ligand, resulting in a tetrahedral coordination geometry. Such cubane-like Cu_4I_4-based compounds exhibit distinctive photo-optical properties, which is often a result of short Cu–Cu distances enabling cuprophilic interactions.[189,190] This also becomes obvious from the Cu–Cu distances of 2.8566(7) and 2.7781(8) Å in compound **9**, whereby latter one is below the sum of the van-der-Waals radii. Other coordination compounds, in which iododiphenylphosphines as ligand for transition metals are present, are rare (TM = Fe, Au, Nd, Re),[191-194] and include no Cu-based compound.
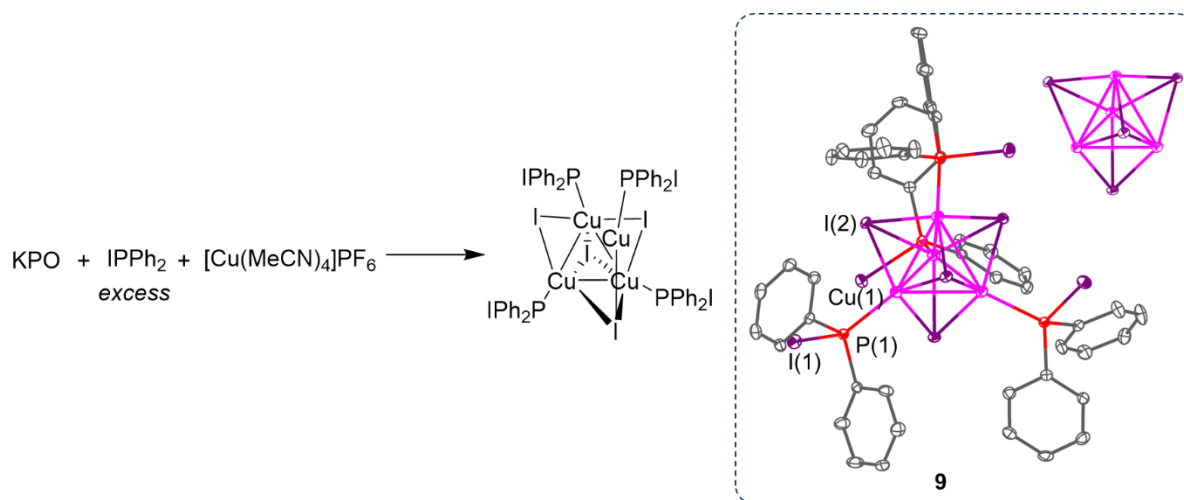
Figure 21. Formation of an iododiphenylphosphine stabilised Cu_4I_4 (**9**) cluster in excess of iododiphenylphosphine. Right side adapted with permission from [195]. Copyright 2023 American Chemical Society.

4.2   Synthesis of PSP-based trinuclear copper complexes

Both ligand systems, PPO/POP and PPS/PSP, share the same tautomeric behaviour whereby in analogy to the PPO compound, the uncoordinated PPS form is about 28 kJ mol^{-1} more stable than the PSP form at ambient conditions according to DFT calculations (B3LYP, def2-TZVP, gas phase). This is also confirmed in solution by ^{31}P{^{1}H} NMR spectroscopic studies, since solely signals corresponding to the PPS form are visible. In analogy to the PPO/POP counterpart, it was assumed that the PSP tautomer could be formed and isolated as ligand through coordination-stabilised tautomers in the presence of transition metal ions. Such an equilibrium shift can indeed be accomplished in the case of the *in-situ* formation method transferred to the PSP-based analogue by substituting the oxygen salt with the respective sulphur salt, potassium diphenylphosphine sulphide (Ph$_2$P(=S)K, KPS, Scheme 3).

$$3\ KPS + 3\ HalPPh_2 + [3\ Cu(MeCN)_4]PF_6 \xrightarrow[\substack{-\ KHal \\ -\ 2\ KPF_6 \\ -\ 12\ MeCN}]{DCM}$$

10 Hal = Cl; **11** Hal = Br; **12** Hal = I

Scheme 3. Synthesis of PSP-based trinuclear copper complexes **10**-**12** with capping halides through *in-situ* formation of the ligand in presence of the copper precursor. Adapted with permission from [195]. Copyright 2023 American Chemical Society.

This synthetic strategy opens the possibility for analogue trinuclear POP and PSP complexes to investigate the effect of the monoatomic ligand backbone. Using this approach, [Cu$_3$(μ_3-Br)$_2$(μ_2-PSP)$_3$]PF$_6$ (**10**), [Cu$_3$(μ_3-Br)$_2$(μ_2-PSP)$_3$]PF$_6$ (**11**) and [Cu$_3$(μ_3-I)$_2$(μ_2-PSP)$_3$]PF$_6$ (**12**) can be synthesised (Figure 22). Unfortunately, the PSP-coordinated compounds suffer from a slight drop in yield, which could be traced back *via* ^{31}P{^{1}H} NMR spectroscopic studies which reveal a high tendency of the Ph$_2$PS$^-$ ligand to coordinate to the Cu-centre initiating the formation of other by-products. Also in the synthesis of the PSP-stabilised Cu$_3$ complexes, the application of the exact stoichiometry of 1:1:1 is important since otherwise one PSP ligand is replaced by one bridging iodo ligand forming [Cu$_3$(μ_3-I)$_2$(μ_2-I)(μ_2-PSP)$_2$] (**13,** Figure 23). In this complex one of the PSP ligands is replaced by an iodo ligand, which bridges two copper centres.
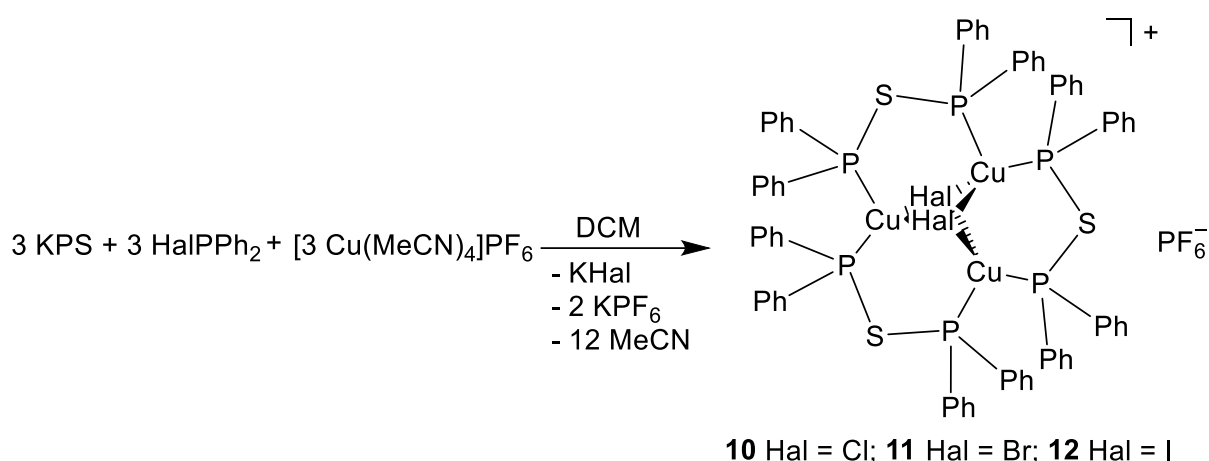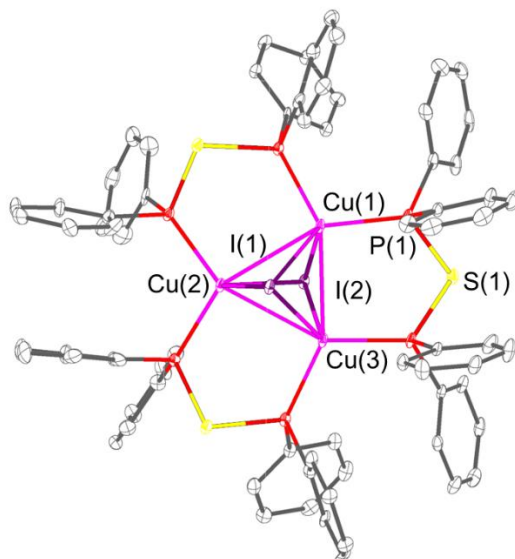
Figure 22. Molecular structure of the cation of [Cu$_3$(µ$_3$-I)$_2$(µ$_2$-PSP)$_3$]PF$_6$ (**12**) as an example for PSP-stabilised compounds **10**-**12**. The counter anion is omitted for clarity. Selected bond lengths and angles are given in Table 2.

When the PPS/PSP ligand is directly reacted with [Cu(MeCN)$_4$]PF$_6$, no PSP-coordinated dinuclear complexes, in analogy to the POP-based copper complex **3**, can be isolated. Instead a tetraphenyl diphosphine-ligated Cu complex ([Cu$_2$(MeCN)$_4$(µ$_2$-P$_2$Ph$_4$)$_2$](PF$_6$)$_2$) (**14**) was isolated and determined with single-crystal XRD (Figure 23). The formation of the sulphur-free tetraphenyldiphosphine ligand can most likely be attributed to rearrangements of the PPS ligand, through a homolytic bond cleavage of the P–P bond and subsequent recombination. Similar observations have been described by the group of Ogawa for such phosphine sulphide-based compounds through initiation by radical starters or UV light.[17,41] The fact that this reactivity is only observed in the case of PPS, can be attributed to conducted DFT calculations by Ogawa and co-workers, who predict a higher reactivity for PPS than for PPO.[17] This is rationalised by the HOMO in PPS, which is mainly localised at the PPS fragment itself, whereas in PPO it is distributed over the whole molecule including the phosphorus substituents.
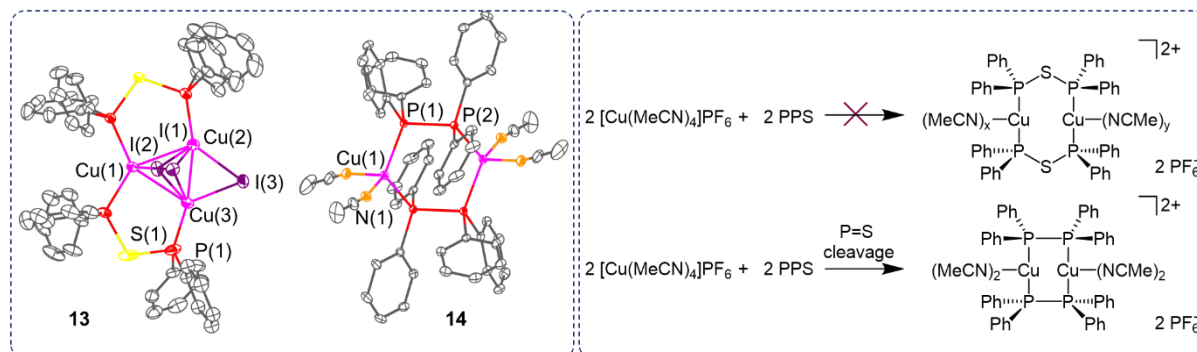
Figure 23. Molecular structures of **13** and **14**. The counter anion is omitted for clarity. Compound **13** is obtained in the presence of an excess of IPPh$_2$. The reaction of [Cu(MeCN)$_4$](PF$_6$)$_2$ with PPS does not result in the formation of a PSP-stabilised Cu$_2$ complex as reported for **3** with the POP-analogue. Instead, P=S bond cleavage provides a tetraphenyl diphosphine-based Cu$_2$ (**14**) complex. Adapted with permission from [195]. Copyright 2023 American Chemical Society.

4.3 Impact of the backbone on the structural parameters

The molecular structures of the POP- and PSP-stabilised trinuclear copper complexes were analysed by single-crystal XRD. The obtained crystal structures can be utilised to uncover structural effects induced by the heteroatom in the backbone. Hereby it was shown that the Cu_3 triangle forms the core of the structures and is capped by one halide ion on both sides. Three bridging PXP ligands surround this central unit forming a D_{3h}-like symmetry, under the assumption of freely rotating phenyl groups. The Cu–Hal bond increases with increasing halide size (Cl < Br < I), ranging from 2.2433(2)–2.483(2) Å to 2.7144(9)–2.7477(6) Å for POP and from 2.421(2)–2.456(2) Å to 2.680(1)–2.721(1) Å for PSP ligands. The larger sizes and longer Cu–Hal distances correlate with more acute Cu–Hal–Cu bond angles (Table 2). In the presence of chloro capping ligands, Cu–Hal–Cu bond angles of 71.15(5)–76.26(5)° (POP) and 74.78(7)–77.10(7)° (PSP) can be obtained which drop to values of 63.12(2)–65.72(0)° (POP) and 65.40(3)–68.7(3)° (PSP) in compounds **8** and **12** with iodo capping ligands. The Cu–Cu distances for all compounds exceed the sum of the van-der-Waals radii, indicating that no cuprophilic interactions are present. This can be traced back to the capping halides, which act as spacers of the Cu ions. A slight decrease can be observed for the Cu–Cu distances in iodo-containing samples **8** and **12** compared to the other compounds. This might again be due to the size of the iodo ligand, which leads to an increased distance of the large halide ligand from the central Cu_3 core, whereas the bromo and chloro ligands can arrange closer to the Cu_3 plane. No significant effect of the ligand backbones on the structural parameters within the Cu_3Hal_2 unit can be specified.

Table 2. Selected bond length and angles for complexes **6-8** and **10-12**. Adapted with permission from [195]. Copyright 2023 American Chemical Society.

	P–Cu [Å]	P–X [Å]	Cu–Hal [Å]	Cu–Cu [Å]	P–X–P [°]	Cu–Hal–Cu [°]
6 Hal=Cl	2.222(2)– 2.241(2)	1.642(4)– 1.653(4)	2.2433(2)– 2.483(2)	2.950(1)– 3.033(1)	120.9(3)– 124.8(2)	71.15(5)– 76.26(5)
7 Hal=Br	2.213(0)– 2.223(2)	1.637(7)– 1.645(0)	2.540(1)– 2.574(1)	3.014(1)– 3.057(2)	124.0(4)– 124.9(0)	72.03(0)– 73.42(4)
8 Hal=I	2.235(2)– 2.254(0)	1.635(5)– 1.647(0)	2.7144(9)– 2.7477(6)	2.859(1)- 2.940(0)	124.7(0)- 125.5(3)	63.12(2)– 65.72(0)
10 Hal=Cl	2.246(2)– 2.257(2)	2.111(3)– 2.118(3)	2.421(2)– 2.465(2)	2.992(2)– 3.046(1)	99.6(1)– 101.6(1)	74.78(7)– 77.10(7)
11 Hal=Br	2.2536(0)– 2.2587(8)	2.1120(9)– 2.1167(9)	2.5440(0)– 2.5783(0)	2.9899(6)– 3.0536(0)	98.30(0)– 101.38(4)	70.88(0)– 73.26(0)
12 Hal=I	2.261(2)– 2.276(2)	2.108(3)– 2.120(3)	2.680(1)– 2.721(1)	2.939(1)– 3.036(1)	97.6(1)– 103.1(1)	65.40(3)– 68.7(3)°

This is contrary to the ligand sphere, which reveals a clear difference in structural parameters, that can be ascribed to the exchange of oxygen by sulphur within the ligand backbone. Majorly, the P–X bonds and the P–X–P bond angles display drastic changes (Table 2). P–O bond

lengths can be found in the range of 1.635(5)–1.653(4) Å, whereas extended P–S bonds with lengths of 2.108(3)–2.120(3) Å can be measured as a consequence of the larger covalent radius of sulphur (104 pm) compared to oxygen (66 pm). A further outcome of the sulphur size can be found in the P–S–P bond angles, which show a reduction of 20° in contrast to the P–O–P angles (POP: 120.9(3)–125.5(3)° *vs*. PSP: 97.6(1)–103.1(1)°). This supports the exceptional acuteness of the ligand backbone. Furthermore, with sulphur slightly elongated P–Cu bonds can be identified (P–Cu: 2.246(2)–2.276(2) Å) compared to the POP-analogues (2.213(0)–2.223(2) Å). Since dppm and dppa analogues of the chloro-containing cations have been reported, the investigation of the ligand backbone on the structural parameters can be extended to the CH_2 and NH ligand backbone (Table 3). Hereby, it must be mentioned that the covalent radii of the bridging atoms decrease in the order of S (104 pm) > C (77 pm) > N (70 pm) > O (66 pm).[160] The trends identified for the molecular structures based on POP and PSP can be confirmed by looking at the PCP and PNP analogues.[196,197] The P–X bond decreases in the order of S > C > N ~ O and P–X–P angles increase in the order of S < C < N ~ O. This is in agreement with literature reports, describing the more linear angles in PNP- compared to PCP-type complexes.[198] It becomes obvious that the PNP (dppa) and POP ligands show similar structural parameters, which can be attributed to the similar sizes and additional contribution of the residue of nitrogen. Furthermore, it should be underlined that the corresponding dppm and dppa ligands are also not capable of bringing the Cu atoms in the trinuclear, halide-capped complexes in closer proximity. Thus, also in these complexes no cuprophilic interactions can be observed.

Table 3. Comparison of the structural parameters of complexes **6** and **10** with literature-reported dppa and dppm analogues. This table has been adapted from [16] (license CC BY 3.0).

	Cu–P [Å]	P–X [Å]	Cu–Cu [Å]	P–X–P [°]	δ [ppm]
POP	2.222(2)–2.241(2)	1.642(4)–1.653(4)	2.950(1)–3.033(1)	120.9(3)–124.8(2)	101.7
PSP	2.246(2)–2.257(2)	2.111(3)–2.118(3)	2.992(2)–3.046(1)	99.6(1)–101.6(1)	23.9
dppa[196]	2.236(4)–2.274(3)	1.627–1.705	2.937(2)–3.040(2)	124.66–124.95	37.2
dppm[197]	2.248(3)–2.273(5)	1.823–1.841	3.063(3)–3.328(2)	112.1(5)–116.0(7)	−14.4

4.4 NMR-spectroscopic analysis of trinuclear copper complexes

The POP-type copper complexes **6-8** and PSP-based counterparts **10-12** were characterised by $^{31}P\{^1H\}$ NMR spectroscopic studies to gain insights into the electronic changes caused by the different ligand backbones. Hereby it could be shown that the highly symmetric structure of the complexes can be maintained in solution, since for all samples, singlets can be detected in addition to a septet (δ = −144.2 ppm), which can be assigned to the PF_6^- anion. The comparison of POP- (δ ~ 100 ppm) and PSP-based (δ ~ 20 ppm) complexes uncovers a drastic upfield shift of the phosphorus signals of around 80 ppm. This can be attributed to the increased electronegativity of oxygen (3.44) compared to sulphur (2.58), which causes a

significant stronger deshielding of the phosphorus nuclei in POP. The impact of the halide atoms is much smaller and leads to a higher deshielding with more electronegative halides and thus larger chemical shifts in the order of Cl > Br > I. Analogue literature-reported [Cu_3(μ_3-Cl)$_2$(μ_2-PXP)$_3$]PF$_6$ cations, based on the far more explored dppm[197] and dppa[196] ligands, confirm the tremendous impact of the ligand backbone. Whereas, the chemical shift of the dppa-based compound (δ = 37.2 ppm)[196] can be found in between the ones of POP and PSP, with dppm[197] a further upfield shift to –14.4 ppm is observed. Again, the degree of deshielding can be correlated with the electronegativities in the order of O > N > S > C. Similar trends have already been observed with the dinuclear POP-stabilised Cu and Au complexes **3**-**5**.

4.5 Photo-optical properties of the trinuclear copper complexes

Inspired by the bright photoemission of the POP-stabilised dinuclear Cu complex **3** and related dppm-based trinuclear copper complexes [Cu_3(μ_3-Cl)$_2$(μ_2-dppm)$_3$]ClO$_4$,[120] the photo-optical properties of the PXP-stabilised complexes **6**-**8** and **10**-**12** were investigated. Thereby, further insights into the ligand backbone on the compounds' properties should be gained with a particular focus on the impact of the ligand backbone.

Irradiating liquid nitrogen cooled samples with UV light (365 nm) revealed a bright luminescence for POP-based compounds **6**-**8,** amongst which **6** and **7** show blue and **8** an intense yellow emission. A substantial different behaviour can be observed for the PSP-based complexes, which do not display any photoemission at all under the same conditions, pointing towards a tremendous impact of the ligand backbone.
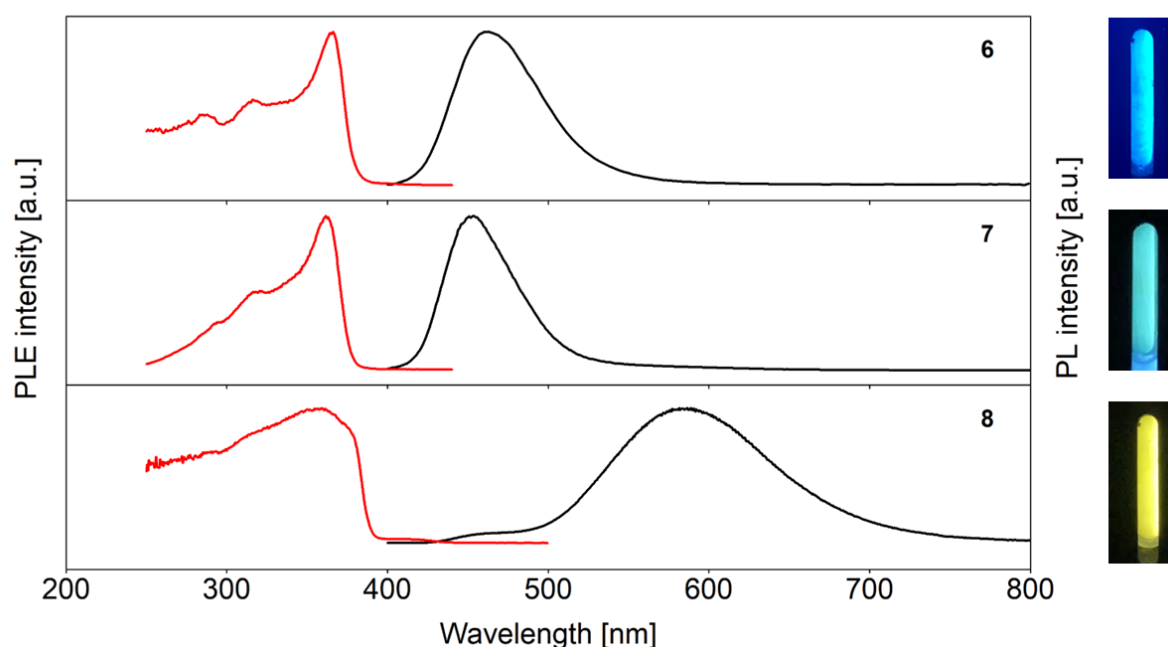

Figure 24. Normalised photo-luminescence excitation (PLE, red) and emission (PL, black) spectra of complexes **6**–**8** at 77 K in the solid state. Respective emission and excitation maxima are given in Table 4. Photographs of the samples under UV radiation (365 nm) are given on the right.

To gain further insights into these initial findings, PLE and PL spectra have been recorded. Initially, measurements were conducted using freshly crystallised solid samples to neglect any solvent influence. Solid state samples of **6-8** do all obtain one broad maximum in the emission spectra (Figure 24). The iodide-containing sample **8** (590 nm) features a red-shift of the emission maximum of above 130 nm compared to the chloride- (**6**, 463 nm) and bromide-containing (**7**, 456 nm) complexes (Table 4). Therefore, transitions from lower energy states back into the ground state cause the yellow photoemission of **8**. For **6** and **7**, transitions take place from higher energy levels. In addition to the broad maximum, **8** shows a shoulder which can be attributed to a transition from a higher energy level at around 468 nm. This finding points towards two parallel processes, which are involved in the photoemission processes. The broadened signals can be attributed to a higher number of transitions between various vibrational energy levels.

Table 4. Photo-luminescence data for the trinuclear copper complexes **6-8** and **10-12** at 77 K in the solid state. Adapted with permission from [195]. Copyright 2023 American Chemical Society.

	T [K]	λ_{ex} [nm]	λ_{em} [nm]	Lifetime$_{eff.}$ [µs] [a]	M–M [Å]
6	77	367	463	24	2.950(1)–3.033(1)
7	77	361	456	35	3.014(1)–3.057(2)
8	77	361	590	161	2.859(1)–2.940(0)
10	77	373	431	6	2.992(2)–3.046(1)
			524	6	
11	77	367	418	6	2.9899(6)–3.0536(0)
			440	6	
			524	6	
12	77	362	418	5	2.939(1)–3.036(1)
			438	5	
			521	6	

[a] For biexponential decays the effective lifetimes were calculated. More information concerning these calculations can be found in the experimental part of this thesis.

Similar emission characteristics were reported by Samuelson and co-workers for solid state samples of the dppm-analogues of the cations. For $[Cu_3(\mu_3\text{-}Cl)_2(\mu_2\text{-}dppm)_3]ClO_4$ one broad maximum could be observed, whereas the iodide-containing analogue $[Cu_3(\mu_3\text{-}I)_2(\mu_2\text{-}dppm)_3]I \cdot CH_2Cl_2 \cdot CH_3OH$ showed shoulder-like signals at 466 nm and 520 nm and the maximum emission at 574 nm.[120]

In a next step, lifetime measurements of the maximal emissions were carried out to investigate the nature of the emission mechanisms and assign the phenomena to phosphorescence- or fluorescence-based processes. The classification can be done based on the time scales of the lifetimes, since lifetimes in the nanosecond regime are classified as fluorescence whereas

phosphorescence can be identified for materials showing microsecond lifetimes.[199] To detect photoemission lifetimes on the two time scales, either a DeltaDiode, for the nanosecond regime, or a PTI XenonFlash lamp, for processes in the microsecond time frame, were used. Further information can be found in the experimental part of this thesis. However, it should be mentioned that for transition metal compounds, a distinct assignment of the underlying processes is often challenging.[102]

A first measurable indication for the occurrence of phosphorescence is the presence of large Stokes shifts, which often stems from intersystem crossing from exited singlet to triplet states. The largest Stokes shift can be detected for **8** with 229 nm, which is more than double the value of the ones for **6** (96 nm) and **7** (95 nm). The assignment of the emissions of **8** to phosphorescence can be manifested by looking at the lifetime of the transition with a duration of 161 µs. For **6** and **7**, the effective lifetimes τ_{eff} have to be calculated with equation 2 (chapter 9.3), since these emissions are based on biexponential decays. Thereby, it was found that the replacement of capping iodo by chloro and bromo ligands is accompanied by a distinct reduction of the emission lifetimes to 35 µs for **7** and 24 µs for **6,** revealing a decreasing lifetime in the order of I > Br > Cl. Despite the significantly lower lifetimes, the photoemissions of **6** and **7** can also be classified as phosphorescence due to the microsecond time range. This finding can be attributed to the so-called heavy atom effect, which describes the increase in spin-orbit coupling due to the heavy atom and thus a higher degree of transitions from singlet excited states into the triplet excited states resulting in phosphorescence.[100]

In DCM solutions comparable PL spectra could be recorded for **6**-**8,** revealing similar emission colours as in the solid state. **6** and **7** again show similar maxima in the emission spectra, whereas **8** is red-shifted to higher wavelength and exhibits a longer emission lifetime.

In contrast to the POP-based compounds, with PSP-analogue samples completely different PLE and PL spectra were recorded (Figure 25). The absence of visible photoemission under UV radiation might be a consequence of relatively weak PLE spectra. The emission spectra display several bands with maxima at 524 nm for **10** and **11** and 438 nm for **12**. However, all PL spectra show a rather flat course of the emission, confirming the absence of a highly emissive transition. The same observations can be made for a DCM solution of the PSP-containing complex **10,** which is characterised by a very flat emission spectrum and no evidence for photoemission neither at 77 K nor at room temperature. The major difference of POP- and PSP-containing compounds is the monoatomic bridge of the two phosphorus units in the ligand. The comparison of the crystal structures did not point towards a change of the structural parameters within the Cu_3Hal_2 core. Contrary, the ligand shell is crucially dependent on the bridging atom, since the much larger sulphur atom causes a significant P–X bond elongation and a very acute P–S–P bond angle. It is assumed that the extended P–X bonds and the acuter P–X–P angles entail an increased flexibility of the ligand backbone. This would justify the absence of strong photoemissions in PSP-compounds, since molecular vibrations are responsible for non-radiative decays, which counteract the emissive transitions.[200]
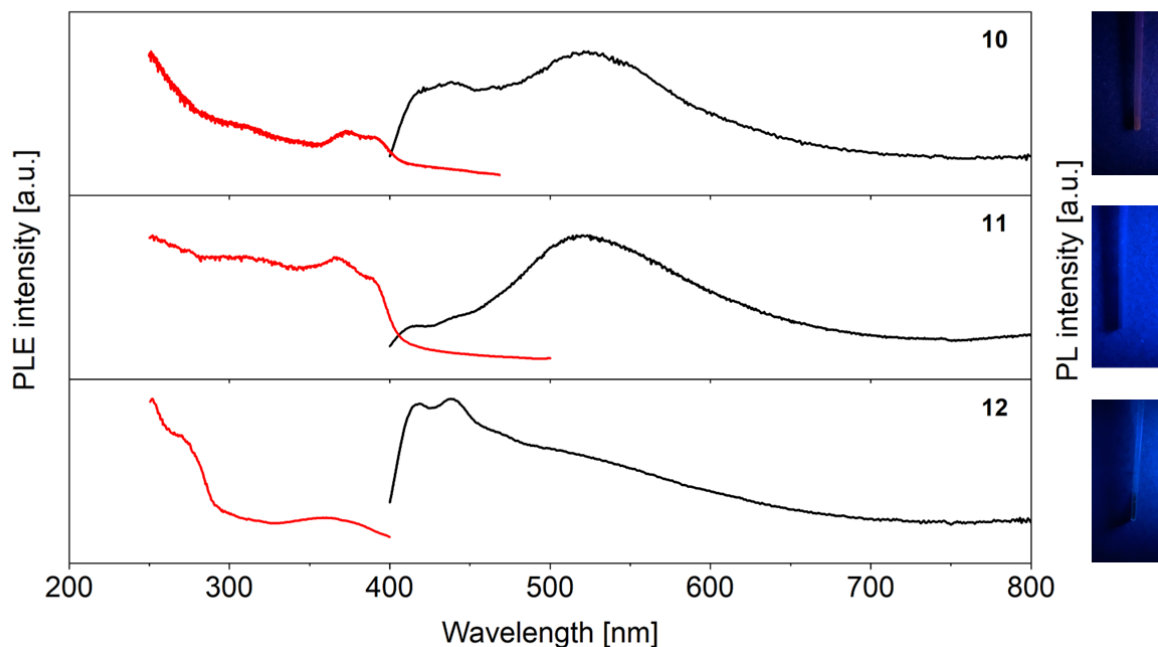
Figure 25. Normalised photo-luminescence excitation (PLE, red) and emission (PL, black) spectra of complexes **10**–**12** at 77 K in the solid state. Respective emission and excitation maxima are given in Table 4. Photographs of the samples under UV radiation (365 nm) are given on the right.

4.6   Theoretical investigations

The impact of the ligand backbone on the photo-optical properties is tremendous, and up-to-now could only be explained by means of structural changes due to the larger sulphur size in contrast to oxygen. To get further insights into the nature of the underlying electronic transitions in POP- and PSP-based copper complexes, DFT calculations were performed for **6-8** and **10** and **11**. DFT calculations should provide further explanations why photoemission is present in POP-containing complexes and absent in PSP-containing complexes. Therefore, UV/Vis absorption spectra were calculated by time dependent DFT (TD-DFT) under the assumption of the Tamm–Dancoff approximation at the B3LYP/[201-203]def2-TZVP[204,205] level of theory. The B3LYP functional was chosen since it was matching the best with the recorded PLE spectrum.

By means of Loewdin population analysis, the impact of the ligand backbone on the electronic distribution could be investigated (Figure 26). All compounds have in common, that the HOMO is distributed over the PXP ligand sphere, the Cu_3 core and slightly over the halide ions. Hereby, the electron density at the capping halides increases in the order of Cl < Br < I. The comparison of POP with PSP compounds points towards a higher contribution of the bridging sulphur atom to the HOMO. By looking at the various LUMOs, a much more intensive deviation becomes obvious for oxygen- and sulphur-containing samples. In general, the LUMO is less localised at the Cu_3Hal_2 unit and can mainly be found at the ligand. Whereas in the PSP-analogues only trace electron density can be detected at the Cu_3Hal_2, the amount in POP-containing samples is higher. Furthermore, and in analogy to observations of the HOMO, a much more intense influence of the bridging sulphur can be displayed than for the oxygen.

These results highlight the impact of the different backbones on the electronical properties of the trinuclear copper complexes.
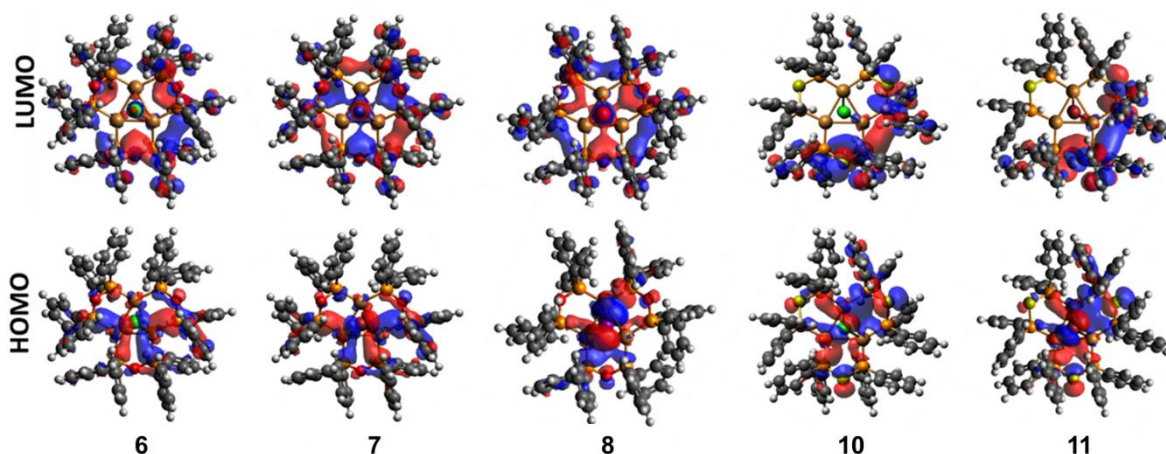
Figure 26. TD-DFT-derived HOMO−N ($N = 0$) and LUMO+N ($N = 0$) frontier orbital plots of compounds **6**–**8**, **10**, and **11**. Adapted with permission from [195]. Copyright 2023 American Chemical Society.

The calculated UV/Vis absorption spectra of **6-8** all show similar courses with two characteristic bands, which can be divided into a lower energy (LE) band (350-360 nm) and in a higher energy (HE) band (250-300 nm) (Figure 27). The LE band is thereby slightly blue-shifted compared to the experimental data, which is a known phenomenon in TD-DFT calculations.[206] The DFT calculations indicate that the transitions which are responsible for the HE bands are impacted by multiple orbitals, whereas orbitals influencing the transitions of the LE band can be specified more precisely. For example, the transition of **6** at around 349 nm can be majorly assigned to HOMO → LUMO+2 (86%).

Figure 27. Calculated UV/Vis absorption spectra of compounds **6-8**, **10** and **11**.

The comparison of the calculated absorption spectra and the experimentally determined PLE spectra for POP-containing compounds, reveals that a large contribution of the photoemission

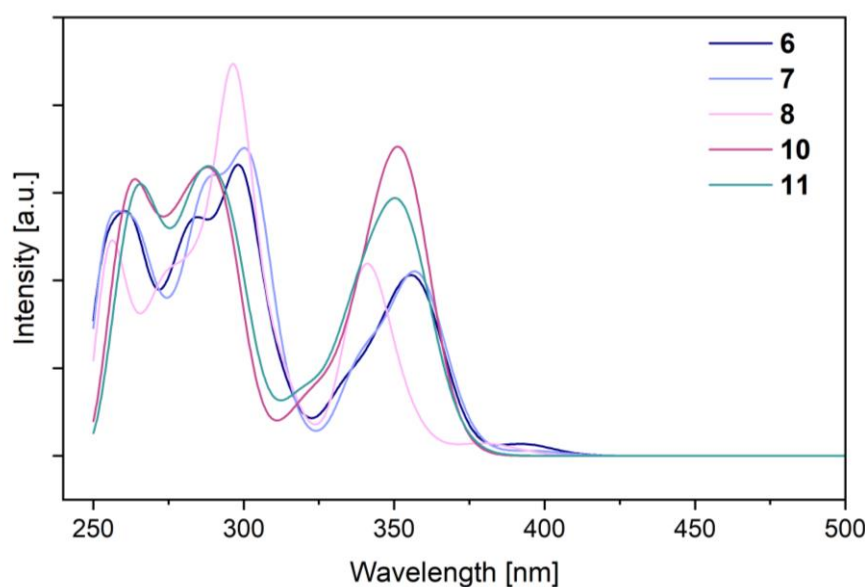can be attributed to the LE bands at around 360 nm, which are in the region of the excitation wavelengths of **6-8**. The nature of these transitions can be identified as a combination of metal-to-ligand charge transfer (MLCT) and halogen-to-ligand charge transfer (XLCT) processes. This is in accordance with examples from the literature, such as a study reported by the group of Bräse which described a Cu_2Hal_2 system stabilised by diphenylphosphinopyridine-type P^N ligands.[173] In contrast, calculated UV/Vis absorption spectra and recorded PLE spectra of PSP-based compounds (**10-12**) do not show a high similarity, indicating that the observed transitions in the absorption spectra majorly result in non-radiative decays. This is in accordance with the absence of any photoemission in these compounds.

The photoemissions of **6-8** have been majorly classified as phosphorescence due to large Stokes shifts and since all lifetimes are found on the µs time scale. Phosphorescence stems from intersystem crossing into triplet excited states which is strongly influenced by the spin-orbit coupling. For a deeper understanding of these processes, TD-DFT calculations were conducted for the singlet and triplet excited states and to determine spin-orbit coupling (SOC) matrices between these two states. Even though phosphorescence transitions are fundamentally forbidden in the absence of relativistic treatment, spin-orbit coupling interactions can herein generate non-zero transition intensities. Again, a significant impact of the ligand backbone can be verified since with POP-based compounds spin-orbit coupling appears to be much more intensive than with the PSP-counterparts. Hereby, the degree of singlet-triplet mixing increases in the order of Cl < Br < I. This can be attributed to the heavy atom effect, which promotes spin-orbit coupling, and additionally to the shortest Cu–Cu bonds as it has been rationalised by Yersin *et al.*[103] The impact of this spin-orbit coupling can be visualised by the strong photoemission properties of compound **8**.

4.7 Trinuclear copper complexes as precursors for POP-stabilised nanoparticles

Beyond the photo-optical application of POP-based copper complexes, such complexes can find application for the synthesis of ligand-decorated nanoparticles. Hereby, it was found recently that the presence of ligands in nanoparticles does not only stabilise the particles during the synthesis, but also can influence their shape, size and uniformity.[207] Furthermore, ligand-decorated nanoparticles attract a great deal of attention as catalysts, since they combine features of heterogeneous catalysts, such as the facile catalyst separation from the reaction mixture and subsequent catalysts recycling, with the precise definition of the active centres in accordance with homogeneous catalysts, which can provide highly selective product formations.[208] On the downside of this stabilising ligand layer, a too high stability can result in blocking of the catalytically active metal centres. Therefore, ligands are required, which show a dynamic behaviour, especially in presence of substrates to offer vacant sites at the catalytically active metal centre. As shown before, such a behaviour can be observed for metal complexes of the PPO/POP ligand system, such as in **3**, due to the tautomeric equilibrium.

The trinuclear copper complexes are highly suitable for the synthesis of ligand-decorated nanoparticles since the ligand is already present in the precursor and the capping halide atoms

can facilitate a reduction of the trinuclear copper complexes with NaBH$_4$. Therefore, a THF solution of **6** was treated with NaBH$_4$. During this reaction a colour change from colourless to dark-yellow and finally to brownish upon addition of the reducing agent became obvious. Consequently, the particles were precipitated through addition of *n*-heptane and were stored in the fridge. The precipitated nanoparticles could be analysed by IR spectroscopy, which revealed the presence of the P–O–P stretch (833 cm^{-1}) and consequently confirmed the successful formation of ligand-stabilised nanoparticles (Figure 28).
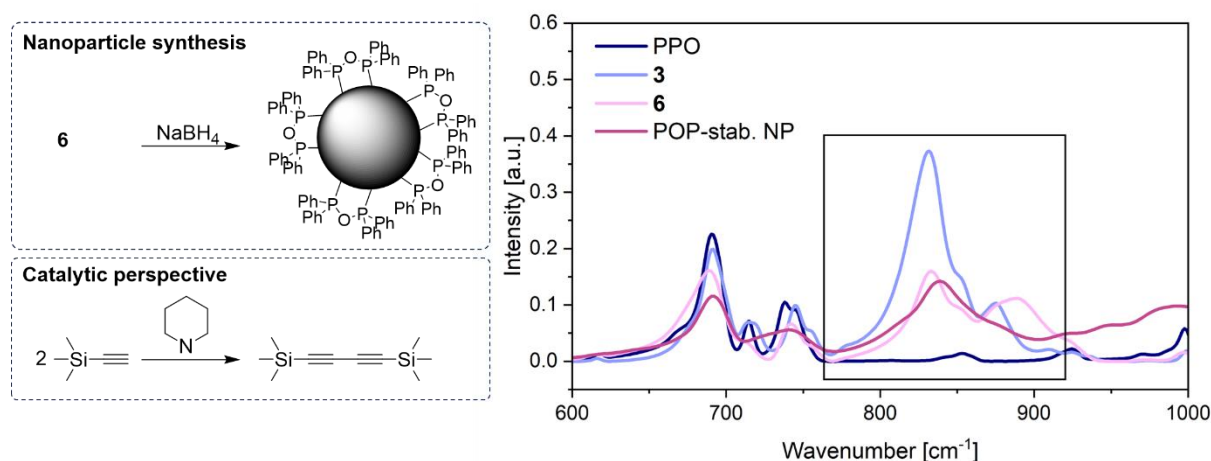

Figure 28. Perspective application of trinuclear copper complexes (**6**) for the synthesis of ligand-decorated nanoparticles. The P–O–P stretch in the IR spectrum confirms the presence of the ligands on the nanoparticle surface.

Further the catalytic potential of these ligand-decorated nanoparticles was investigated in coupling reactions, whereby the coupling of trimethylsilyl acetylene was attempted (Figure 28). However, the yield is still very low and modifications of the reaction parameters need to be conducted to optimise the catalytic reactions. Nevertheless, the preliminary investigations reveal the great potential of this compound class for the synthesis of nano-based catalysts, whereby the direction of the tautomeric equilibrium of the POP ligand could be a key for fine tuning of the catalytic performance.

4.8 Concluding remarks

Through a rational adjustment of the synthetic procedure, the nuclearity of PXP-stabilised copper complexes can be directed. In this context, an *in-situ* ligand synthesis in presence of the metal-precursor provides trinuclear copper complexes. Notably, the formation of PSP-coordinated copper compounds can only be realised *via* the herein applied *in-situ* route since the direct conversion of the PPS ligand with copper precursors cannot be accomplished due to a predominant P=S bond cleavage. The formed complexes of the general formula [Cu$_3$(μ_3-Hal)$_2$(μ_2-PXP)$_3$]PF$_6$ with X = O, S and Hal = Cl, Br, I feature Cu$_3$Hal$_2$ cores, which are either surrounded by three PSP or POP ligands. These complexes provide systematic insights into how the oxygen or sulphur ligand backbone can affect the compounds structural features and photo-optical properties. Since molecular structures of the dppm[197] and dppa[196] copper complexes have also been reported, the comparison can be extended to the PNP- and PCP-type counterparts. Only a minor impact of the ligand sphere on the Cu$_3$Hal$_2$ core can be

determined, whereas large differences can be observed in the ligands sphere. The P–X bond as well as the P–X–P angle strongly depend on the size of X (O < N < C < S) whereby drastic differences of the oxygen and sulphur analogues are uncovered (Δ(P–X) = 0.5 Å, Δ(P–X–P) = 20°). The PSP ligand entails long P–X bonds as well as a highly acute backbone which is causing an increased degree of flexibility in these compounds. Furthermore, a strong correlation of the electronic effect of the ligand backbone with the electronegativity of the respective elements can be revealed since with higher electronegativity (O > N > S > C), an increased degree of deshielding of the phosphorus atoms is observed *via* NMR spectroscopic studies.

The effect of the backbone (POP *vs*. PSP) can be visualised by looking at the photo-optical properties of these compounds using photo-luminescence spectroscopy. The analysis of POP-containing compounds displays bright luminescence at 77 K, whereas no emission can be witnessed with the PSP-analogues, which can be traced back to the higher flexibility in the PSP-backbone and consequently more non-radiative decays. Interestingly, the colour of the emission of POP-complexes could be directed through the capping halides. The bromide- and chloride-based complexes show blueish colours and emission lifetimes of around 30 μs. For the iodide-containing sample a bright, yellow luminescence can be seen with a lifetime of 161 μs. The strong luminescence is accompanied by a large Stokes shift pointing towards a higher degree of spin-orbit coupling due to the heavy atom effect.

By means of DFT calculations, firstly the transitions responsible for the underlying emissions could be assigned to metal-to-ligand and halogen-to-ligand charge transfers. Furthermore, Loewdin population analyses confirmed the drastic impact of the nature of the PXP ligand backbone. The comparison of calculated absorption spectra and recorded PLE spectra of the PSP-based samples displays only minimal alignment. This agrees with the absence of any photoemission since a quenching of the photoemission occurs *via* non-radiative channels.

5   Short-bite PSP-type ligands for nickel halide complexes

The results discussed in this chapter can be partially accessed on chemrxiv *via*: PSP-coordinated nickel(II) complexes as Kumada coupling catalysts, F. Flecken, T. Grell, S. Hanf, **2024**, DOI: 10.26434/chemrxiv-2024-fdgcn under the license CC BY NC ND 4.0.

Figure 29, 30, 32, 33, 34 and Table 5-8 are (partly) adapted from this publication.

Crystallographic data were processed by Toni Grell.

Additional data in open file formats can be accessed on Zenodo, DOI: 10.5281/zenodo.13234536

Chelate complexes of PCP-type ligands have attracted much interest since the discovery of nickel phosphine catalysed C–C coupling reactions of Grignard reagents with aryl halides in 1972.[209] Already the first publication of Kumada stated a tremendous impact of the ligands in the metal complexes on the catalytic performance, whereby firstly, diphosphines display a superior activity compared to monophosphines and secondly, the ligand backbone played a significant role. More precisely, the length of the bridge between the two phosphorus atoms was shown to be decisive, since the catalytic performance decreased in the order of dppp > dppe > dppb (dppp: 1,3-bis(diphenylphosphino)propane, dppb: 1,4-bis(diphenylphosphino)butane).[209,210] However, chelate complexes of the short-bite ligand dppm were not considered in this study, which might be due to the high ring strain in the four membered M-P-C-P ring which leads to a preferred bridging coordination mode of the ligand in many cases.[68] However, recent studies by the Wass group have revealed that ligands with a monoatomic bridge can often enhance the catalytic activity compared to analogues with longer backbone chains, due to an increased hemilability, as shown for example in biofuel production or polymerisation reactions.[92,127,131] Based on these observations, it becomes obvious that short-bite ligands offer a substantial potential for catalytic applications and that further modifications of the ligand backbone through the incorporation of a heteroatom, such as in the case of PNP, POP and PSP ligands, could result in even more drastic changes in the catalyst performance. In this context, PSP-based complexes are by far the least investigated ligand class whereby only two studies reported the isolation of PSP-containing chelate complexes involving Mo[83] and Ru[27] complexes. For the consideration of PSP-based metal complexes as counterparts for the well-known PCP-based complexes, studies have to be concentrated on the exploration of this alternative ligand class to gain insights into the effect of the sulphur backbone. For a reasonable comparison, PSP-coordinated nickel halide complexes are presented in this work in analogy to the well-studied [NiHal$_2$(PCP)] complexes.

5.1 Synthesis of PSP-based nickel halide complexes

Since previous studies have shown that the direct conversion of a metal precursor with the PPS ligand for the production of PSP-stabilised complexes, suffered from P=S bond cleavage (chapter 4.2), initial attempts to synthesise PSP-based nickel halide complexes focused on the *in-situ* formation of the ligand from Ph_2PCl and $Ph_2P(=S)K$ (KPS) in the presence of the nickel halides. As shown for trinuclear copper complexes, this strategy could be applied to circumvent the undesired P=S bond cleavage. By pursuing this method, mononuclear nickel halide complexes could be isolated in the case of $NiBr_2$ and NiI_2. In contrast to the Cu precursors, also the direct conversion of $NiBr_2$ and NiI_2 with PPS, under reflux conditions in acetonitrile, has proven to be successful.
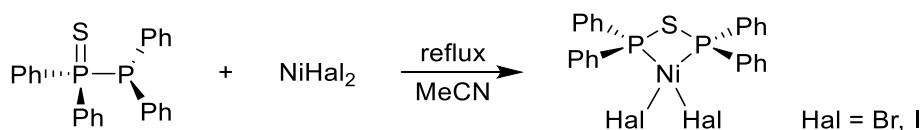
Scheme 4. Synthesis of $[NiHal_2(PSP)]$ through refluxing the PPS ligand with the nickel halide in acetonitrile.

Single-crystal XRD revealed the solid state molecular structures of $[NiBr_2(PSP)]$ (**15**) and $[NiI_2(PSP)]$ (**16**) (Figure 29). Thereby, the phosphorotropic equilibrium is completely shifted from the PPS to the PSP tautomer through the coordination to the nickel centre. The central element of the chelating complex is a four-membered Ni–P–S–P ring. Hereby, very acute backbones of the PSP ligand are observed (P–S–P in **15:** 80.81(3)° and P–S–P in **16**: 81.51(15)°) in contrast to the PCP-type analogue $[NiBr_2(dppm)]$ with 91.94°.[211] The acuteness of P–S–P angles has already been observed in trinuclear copper complexes (Chapter 4.3) and is the major structural difference compared to other PXP-type (X = O, C, N) ligands. The origin of this feature can be found in the larger size of sulphur compared to C, O and N, which facilitates longer and more flexible P–X bonds. This can be confirmed in the cases of **15** and **16** (**15**: 2.1146(7)–2.1183(7) Å and **16**: 2.117(3) Å *vs.* 1.833 Å for $[NiBr_2(dppm)]$).[211] Another consequence of the larger size of sulphur are the wider bite angles of around 80° for **15** and **16** compared to the PCP analogue $[NiBr_2(dppm)]$ with 75.95(8)°.[211] The bite angles in **15** and **16** lie in between the bite angle for the $[NiBr_2(dppm)]$ and $[NiBr_2(dppe)]$ (86.85(5)°)[212] counterparts, whereby latter one is approaching the natural metal bond angle of 90° and is assumed to be an ideal candidate for chelating complexes.[68]
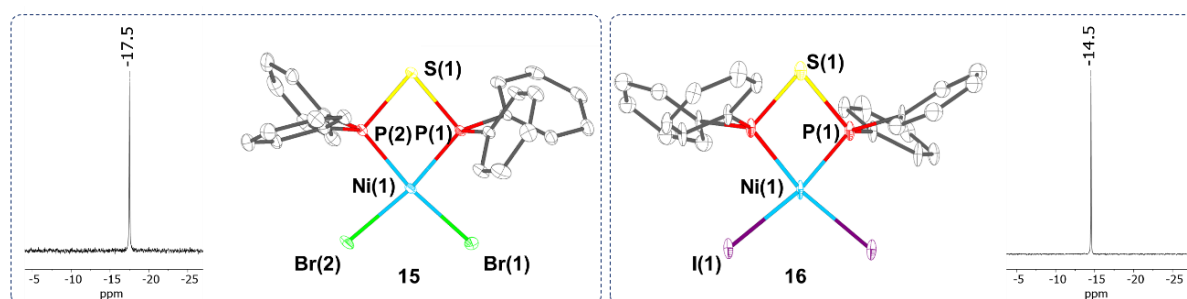

Figure 29. $^{31}P\{^1H\}$ NMR signals and molecular structures of **15** and **16**. Selected bond lengths and angles are given in Table 5. This figure has been partly adapted from [213] (license CC BY NC ND 4.0).

Since PSP ligands have been widely overlooked in literature, only two examples of PSP-based chelate complexes are known based on Mo[83] and Ru.[27] In these complexes the P–S–P angles approach even more the natural bond angle (86.9° for Mo[83] and 82.1°–82.46° for the Ru complexes[27]), which once more underlines the flexibility of the ligand backbone. Furthermore, the P–S bond lengths in the Mo and Ru complexes are slightly longer compared to the P–S bond length in **15** (2.1146(7)–2.1183(7) Å) and **16** (2.117(3) Å), which are similar to the P–S bond lengths in the discussed trinuclear copper compounds (chapter 4.3).

To classify the geometry around the Ni centres, deviations from the best plane and the structural index parameter τ'_4 were determined. The best plane is defined by the two coordinating P atoms and the two coordinating halides. Okuniewski *et al.* suggested equation **1** for the determination of the structural index parameter, which can be used to reveal deviations from an ideal square-planar coordination.[214] If $\tau'_4 = 0$, an ideal square-planar coordination can be confirmed, whereas a value of 1 corresponds to a tetrahedral geometry.

$$\tau'_4 = \frac{\beta-\alpha}{360°-\theta} + \frac{180°-\beta}{180°-\theta}$$

(1)

β, α: largest valence angles $\beta > \alpha$

θ: tetrahedral angle $\cos^{-1}(-1/3) \sim 109.47°$

Table 5. Selected bond lengths [Å], angles [°] and structural parameters of **15** and **16** in the solid state. This table has been adapted from [213] (license CC BY NC ND 4.0).

	[NiBr$_2$(PSP)] (**15**)	[NiI$_2$(PSP)] (**16**)
P–S	2.1146(7)–2.1183(7)	2.117(3)
P–Ni	2.1347(6)–2.1425(6)	2.137(3)
Ni–X	2.3271(4)–2.3370(4)	2.5251(7)
P–C	1.799(2)–1.812(2)	1.814(6)–1.816(7)
X–Ni–X	97.234(13)	100.57(8)
X–Ni–P	91.613(19)–171.07(2)	89.93(7)–167.36(6)
Ni–P–S	99.43(3)–99.80(3)	98.93(10)
P–S–P	80.81(3)	81.51(15)
P–Ni–P	79.80(2)	80.62(13)
Distance Ni–best plane	0.008	0.000
τ'_4	0.13	0.18

For both complexes **15** and **16**, a nearly ideally square-planar coordination becomes obvious. For **15**, a slight deviation of Ni from the best plane (0.008 Å) can be found, whereas in **16**, the Ni centre is located perfectly within the best plane. This square-planar coordination environment gives rise to the diamagnetic nature of the complexes, which can be confirmed

by sharp signals in the NMR spectra (Figure 29). Surprisingly, the $^{31}P\{^1H\}$ NMR spectra indicate an upfield shift of **15** (–17.5 ppm) compared to **16** (–14.5 ppm), which is against the expectations based on the corresponding halide ligands. Due to the higher electronegativity of the bromide, a stronger deshielding of the P nuclei would be expected for **15** compared to **16,** resulting in a downfield shift. However, similar discrepancies have been reported by Fergusson and Heveldt in the context of square-planar noble-metal complexes of the form [MHal$_2$(PR$_3$)$_2$] (M = Pd, Pt; Hal = Cl, Br, I). The authors suggested that either a polarisation effect or M → Hal π-backbonding in the order of Cl < Br < I is responsible for these observations.[215]

Another characteristic of the two complexes, are their intense colours, whereby **15** appears in red-violet and **16** in dark-violet. UV/Vis absorption spectra have been recorded revealing broad maxima in the visible region, which cause these colourations (Figure 30). The maximum of **16** (564 nm, ε = 2297 dm^3 mol^{-1} cm^{-1}) is red-shifted to the one in **15** (510 nm, ε = 2391 dm^3 mol^{-1} cm^{-1}), which stems from the greater ligand field splitting initiated by the bromide resulting in a higher energy demand for the underlying transition. Based on the intense colour and emission coefficients, both transitions can be classified as M–L charge transfer transitions.
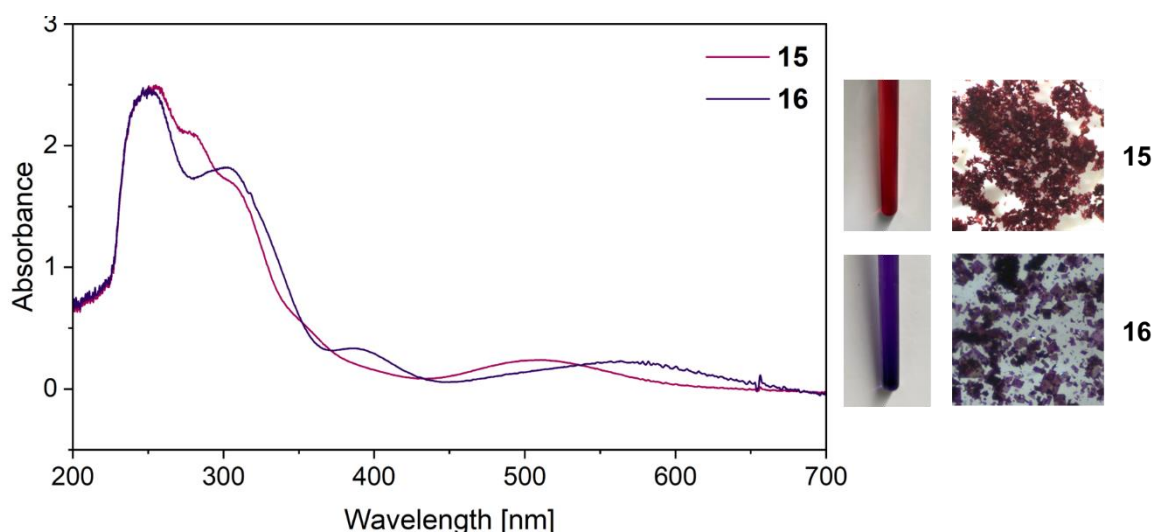
Figure 30. UV/Vis absorption spectra of the complexes **15** and **16** in DCM solutions (c = 1·10^{-4} mol L^{-1}). Broad maxima in the visible range at 510 nm (**15**) and 564 nm (**16**) are causing the intense red-violet (**15**) and dark-violet (**16**) colours of the compounds. Right: colour of the samples in solution and under the microscope in the solid state. This figure has been partly adapted from [213] (license CC BY NC ND 4.0).

Similar syntheses of POP-analogue nickel complexes have been attempted but did not provide any isolatable [NiHal$_2$(POP)] product. Synthesis methods included ligand exchange reactions, the *in-situ* formation of the ligand in presence of the nickel precursor or the direct conversion of the nickel halides with the PPO ligand. Interestingly, if [Ni(MeCN)$_4$](BF$_4$)$_2$ was reacted with the PPO ligand or with the KPO (Ph$_2$P(=O)K) and ClPPh$_2$ precursors of the ligands for the *in-situ* formation, a fluorophosphine stabilised Ni(0) complex was obtained, which will be the focus of chapter 7. The unsuccessful formations of [NiHal$_2$(POP)] (Hal = Cl, Br, I) complexes might be due to the requirement of sufficiently acute P–X–P bond angles. The P–O–P angle in other transition metal complexes, such as in the case of the trinuclear

copper complexes, was comparably more linear than the angles found in P–S–P complexes and therefore might hinder the formation of [NiHal$_2$(POP)] complexes, due to the enhanced P–O–P–M ring strain. It is assumed that a significant lower amount of energy is required for the compression of the PSP angle than for other PXP angles, due to the higher flexibility, which can be achieved with the larger sulphur atom. Consequently, the chelating coordination mode, might be more likely for the PSP ligand than for other PXP compounds.

Whereas bromide- and iodide-analogues could be synthesised very straight forward, the formation of the chloride-containing analogue could neither be detected *via* NMR spectroscopic analysis nor isolated in crystalline form. Various attempts have been made, including the direct conversion of NiCl$_2$ with PPS, the *in-situ* formation in presence of the Ni precursors or ligand exchange reactions (Figure 31). In all reaction mixtures instead of a singlet signal in the ^{31}P{^{1}H} NMR spectrum, which would be expected for a [NiCl$_2$(PSP)] complex, different multiplets could be found at higher chemical shifts. Dark brown crystals were obtained from the reaction of NiCl$_2$ with PPS, which were determined to be [Ni$_2$(μ$_2$-Ph$_2$P)(μ$_2$-Ph$_2$PS)(Ph$_2$PSS)$_2$] (**17**) by single-crystal XRD analysis. It becomes obvious that a rearrangement of the PPS ligand takes place resulting in the new ligands Ph$_2$PSS$^-$, Ph$_2$PS$^-$ and Ph$_2$P$^-$. Interestingly, similar products are formed in attempts to generate a PSP-stabilised Ni(0) species through the conversion of [Ni(COD)$_2$] (COD = 1,5-cyclooctadiene) with the PPS ligand, yielding [Ni$_3$(μ$_2$-Ph$_2$P)$_2$(μ$_2$-Ph$_2$PS)$_2$(Ph$_2$PS)$_2$] (**18**). A similar multinuclear complex can be obtained from the reaction of KPS (Ph$_2$P(=S)K) and ClPPh$_2$ with [Ni(COD)$_2$] giving [Ni$_2$(μ$_2$-Ph$_2$P)(μ$_2$-Ph$_2$PS)(Ph$_2$PS)(Ph$_2$PSS)] (**19**). In all multinuclear complexes, the Ni(0) is oxidised to Ni(II) during the reactions while reduction takes place within the ligand species (Figure 31). Similar ligand rearrangement processes have been reported by Ogawa and co-workers, who have investigated UV- or radical-initiated rearrangements of the PPS ligand *via* P–P bond cleavages.[17,42,43,47] It was shown that the homolytic bond cleavage yields two radicals, namely Ph$_2$PS· and Ph$_2$P·, which can recombine or activate unsaturated bonds. The reason of this reactivity, was traced back to the HOMO, which is mainly localised at the PPS unit rather than at the P substituents.[17] The obtained compounds **17-19** point towards a similar activation of the PPS in the presence of Ni precursors. It should be underlined that the choice of nickel precursor tremendously influences this reactivity, since with NiBr$_2$ and NiI$_2$, either no or only minimal amounts of such multinuclear complexes can be detected during the synthesis. In contrast to the PPS activation reported by Ogawa, external factors, such as temperature or UV radiation, do not play a role in presence of nickel, neither during the synthesis nor if **15** and **16** are exposed to these conditions.
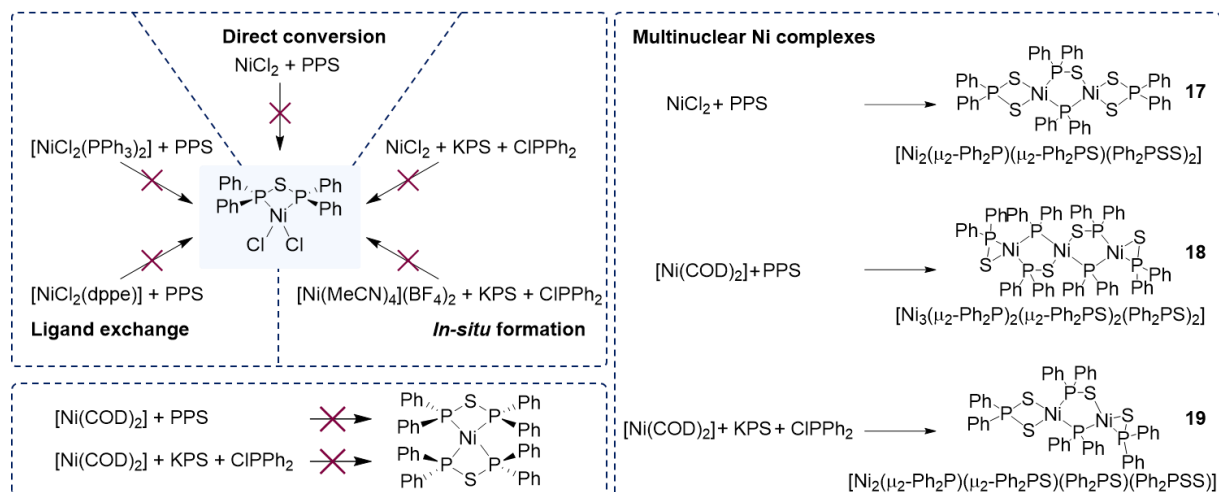
Figure 31. Despite several attempts to synthesise the chloride-containing complex [NiCl$_2$(PSP)], none of these conversions provided the targeted product. Also conversions of [Ni(COD)$_2$] did not yield the desired PSP-stabilised Ni(0) complex (left). Instead multinuclear Ni(II) complexes **17**-**19** were obtained (right).

All molecular structures of **17**-**19** (Figure 32) have in common, that in the inner core two Ni centres are bridged by one Ph$_2$PS$^-$ and one diametrically opposite Ph$_2$P$^-$ ligand, through which five-membered metallacycles are formed. The two terminal Ni atoms are either chelated by two Ph$_2$PSS$^-$ ligands (**17**), two Ph$_2$PS$^-$ ligands (**18**) or by one Ph$_2$PSS$^-$ and one Ph$_2$PS$^-$ ligand (**19**). When the Ph$_2$PS$^-$ ligand coordinates in the bridging mode, a slight extension of the P–S bond occurs, while the S–Ni bond is decreasing. The structural parameters of the three ligands in compounds **17**-**19** are all matching with reported angles and bond lengths of these ligands in nickel complexes such as [Ni(Ph$_2$PSS)$_2$], [Ni$_2$Cp$_2$(μ_2-Ph$_2$PS)$_2$] or [Ni$_2$Cp$_2$(μ_2-Ph$_2$P)$_2$].[27,83,216-220]

17	**18**	**19**
[Ni$_2$(μ_2-Ph$_2$P)(μ_2-Ph$_2$PS)(Ph$_2$PSS)$_2$]	[Ni$_3$(μ_2-Ph$_2$P)$_2$(μ_2-Ph$_2$PS)$_2$(Ph$_2$PS)$_2$]	[Ni$_2$(μ_2-Ph$_2$P)(μ_2-Ph$_2$PS)(Ph$_2$PS)(Ph$_2$PSS)]

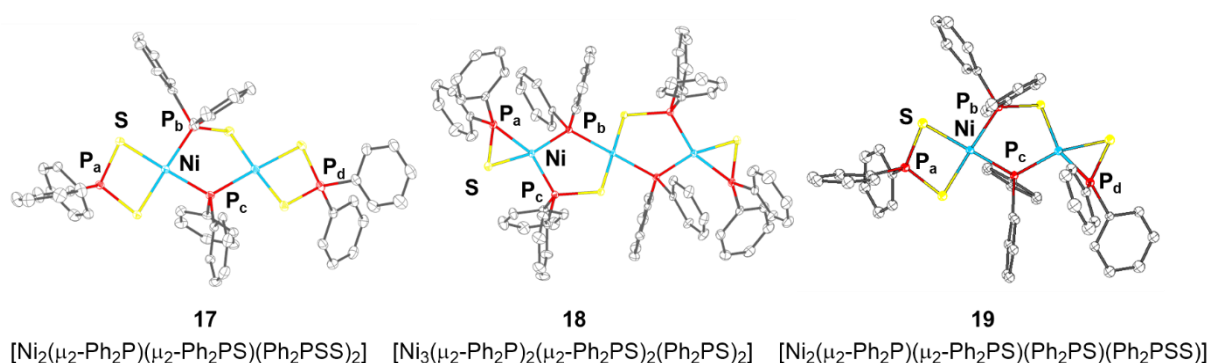**Figure 32.** Molecular structures of the multinuclear Ni(II) complexes **17**, **18** and **19,** which result from PPS ligand rearrangement processes. Selected bond lengths and angles are given in Table 6. This figure has been partly adapted from [213] (license CC BY NC ND 4.0).

Table 6. Selected bond lengths [Å] in the different ligands (Ph_2PS^-, Ph_2PSS^- and Ph_2P^-) of the multinuclear Ni complexes **17, 18, 19.** This table has been adapted from [213] (license CC BY NC ND 4.0).

| Compound	Ligand	P–S	P–Ni	S–Ni
17	$Ph_2PS_2^-$	1.9949(11)–2.0176(10)	*2.8200(8)–2.8385(8)*[a]	2.2311(9)–2.2826(8)
19	$Ph_2PS_2^-$	2.0084(10)–2.0086(10)	*2.8208(7)*[a]	2.2428(7)–2.2664(8)
17	Ph_2PS^- (intern.)	2.0357(10)–2.0394(10)	2.1448(9)–2.1467(8)	2.1784(9)–2.1900(9)
18	Ph_2PS^- (term.)	2.0246(7)	2.1477(5)	2.2102(5)
18	Ph_2PS^- (intern.)	2.0616(6)	2.1353(5)	2.1739(4)
19	Ph_2PS^- (term.)	2.0064(10)	2.0962(7)	2.2498(7)
19	Ph_2PS^- (intern.)	2.0421(9)	2.1642(7)	2.2078(7)
17	Ph_2P^-	-	2.1999(8)–2.2045(8)	-
18	Ph_2P^-	-	2.1844(5); 2.2711(4)	-
19	Ph_2P^-	-	2.1665(7); 2.1915(7)	-

[a] no real bond, only P–Ni distance

Further insights into the coordination geometry around the Ni(II) centres were gained by the calculation of τ'_4 (equation 1, Table 7) and the determination of the Ni distance from the best plane, defined by the four coordinating atoms of the Ni centre. Regarding the distance from the best plane, in **17** a significant difference can be recognised with either the S or the P atom of the Ph_2PS^- ligand coordinating. If the coordination takes place *via* the S atom, the Ni centre is further away from the best plane than in the case of P coordination. Also, the geometry around the Ni centres in **17** is slightly less ideally square-planar according to an increased value of τ'_4. In **18**, two specific coordination cases have to be distinguished, since the terminal Ph_2PS^- ligand leads to a distortion of the square-planar geometry, whereas on the other hand, the central Ni(II) centre obtains ideal square-planar coordination geometry, which might be due to the highly symmetric surrounding. P–Ni–P and S–Ni–S angles of 180° are found, which enable the perfect arrangement of the nickel centre in the PSPS plane. Consequently, a τ'_4 value of 0 can be calculated. This is not the case for the outer Ni atoms in **18**, which were found to deviate 0.099 Å from the best plane. This feature appears to drastically influence the NMR spectra of **18**, which exhibit broad signals especially in the $^{31}P\{^1H\}$ NMR spectrum. In **19**, the distortion induced by terminal Ph_2PS^- ligands can also be observed for the Ni(II) centre coordinated to P_d (Figure 32). In contrast to **18**, the Ni atom is however closer to the best plane.

Table 7. Distance of the Ni(II) atoms to the best plane [Å] which is defined by the four coordinating molecules of the Ni(II) centre and the respective structural index parameters τ'_4 [-] for **17**, **18** and **19**. This table has been adapted from [213] (license CC BY NC ND 4.0).

	17	**18**	**19**
Distance Ni–best plane	0.003–0.079	0.000–0.099	0.001–0.056
τ'_4	0.03–0.10	0.000–0.24	0.13–0.27

Whereas the NMR spectrum of **18** is greatly influenced by paramagnetic contributions, for **17** and **19** sharp signals can be observed, which agree with the molecular structures. $^2J_{PP} > 30$ Hz and $^3J_{PP} < 10$ Hz couplings can be detected in the ^{31}P{^{1}H} NMR spectra, which can be used for the assignment of the signals to the ligands (Figure 33). The naming scheme for the different phosphorus atoms is given in Figure 32. Signals at around 30 ppm can be attributed to the terminal Ph$_2$PS$^-$ ligand due to an absence of this signal in the ^{31}P{^{1}H} NMR spectrum of **17** (**19**: 31.1 ppm, P$_d$). The internal Ph$_2$PS$^-$ ligand exhibits a drastic downfield shift to chemical shifts around 90 ppm (**17**: 92.0 ppm, P$_b$; **19**: 90.1 ppm, P$_b$). The signal of the terminal Ph$_2$PSS$^-$ ligand can be found in the region of 73 ppm (**17**: 72.7 ppm, P$_d$; **19**: 73.0 ppm, P$_a$). The bridging Ph$_2$P$^-$ ligand can be observed at 60.4 (P$_c$) ppm for **17** and 56.3 (P$_c$) ppm for **19**.
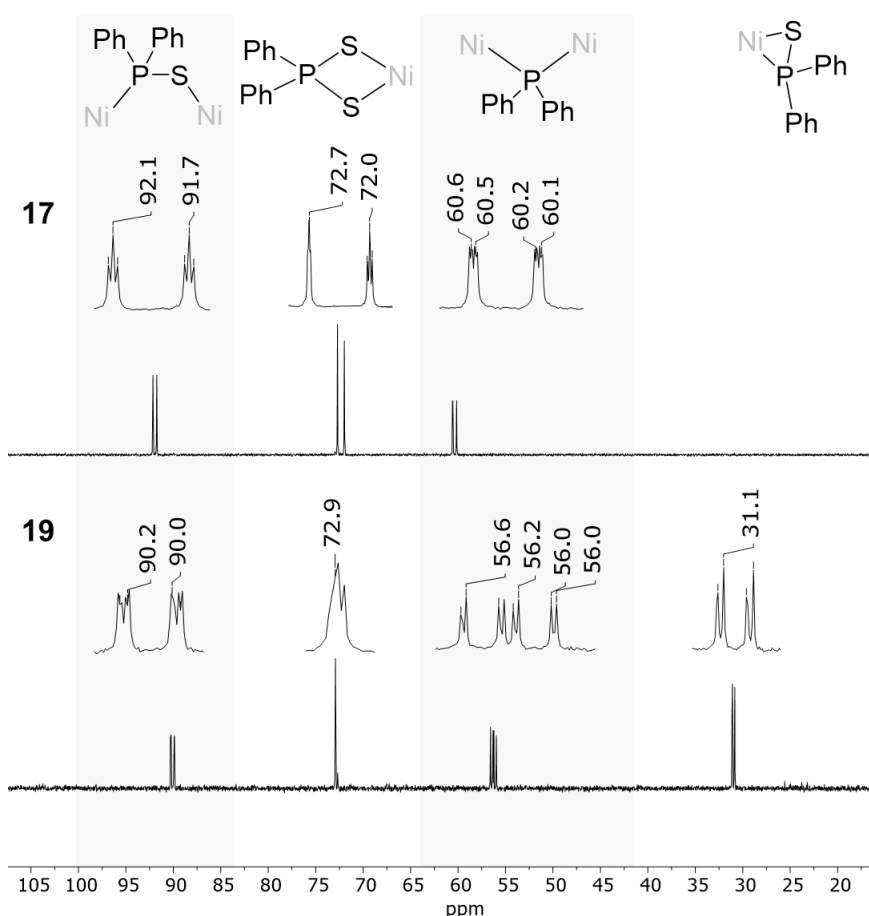
Figure 33. ^{31}P{^{1}H} NMR (298 K, CD$_2$Cl$_2$, 162 MHz) spectra of **17** and **19** and assignment of the signals to the different ligands. This figure has been adapted from [213] (license CC BY NC ND 4.0).

5.2 [NiHal$_2$(PSP)] complexes for catalytic application in Kumada couplings

Due to the significance of diphosphine-based chelate Ni complexes in Kumada coupling reactions, compounds **15** and **16** are potential catalyst candidates, which give the possibility to study the impact of the heteroatom-containing ligand backbone. Since the bite angle in **15** can be found in between the bite angles of related dppm and dppe complexes, the well-established [NiBr$_2$(dppe)] analogue has been used as reference catalyst for a reliable classification and benchmarking of the catalytic potential of the PSP-based nickel complexes. The application of sulphur-based ligands is particularly interesting, since sulphur-containing compounds are in several cases poisoning the catalyst *via* strong metal-sulphur interactions. Thus, such compounds are often not taken into consideration as potential catalysts, leading to a disregard of the positive effects, which could be accomplished through the incorporation of sulphur.[147,221] In this context, a study by Li and co-workers investigated the use of monodentate diphenylphosphine sulphide ((^{t}Bu)$_2$PSH)-stabilised nickel complexes in Kumada-Tamao-Corriu coupling reactions of aryl Grignard reagents with aryl chlorides. This study indicated the positive impact of sulphur-based ligands in catalysis.[147] With **15** and **16**, a sulphur coordination to the nickel centre could result from an equilibrium shift of the PSP ligand to the PPS tautomer.

5.2.1 Solvent behaviour of [NiHal$_2$(PSP)]

As described for the copper complex **3**, [Cu$_2$(MeCN)$_n$(μ_2-POP)$_2$](PF$_6$)$_2$ (chapter 3.2), the solvent can initiate an equilibrium shift of the bridging PXP ligand to the monodentate PPX tautomer. To investigate if such a behaviour can also be observed for the PSP ligand in **15** and **16** in solution, ^{31}P{^{1}H} NMR spectroscopic studies have been conducted in different solvents (Figure 34). A shift of the equilibrium of the chelating PSP ligand in the corresponding nickel complex, could have a tremendous impact on the catalytic performance since coordination *via* the sulphur atom of the PPS tautomer could inhibit the catalytically active site. As mentioned before the behaviour of [NiBr$_2$(dppe)] was taken as reference point.
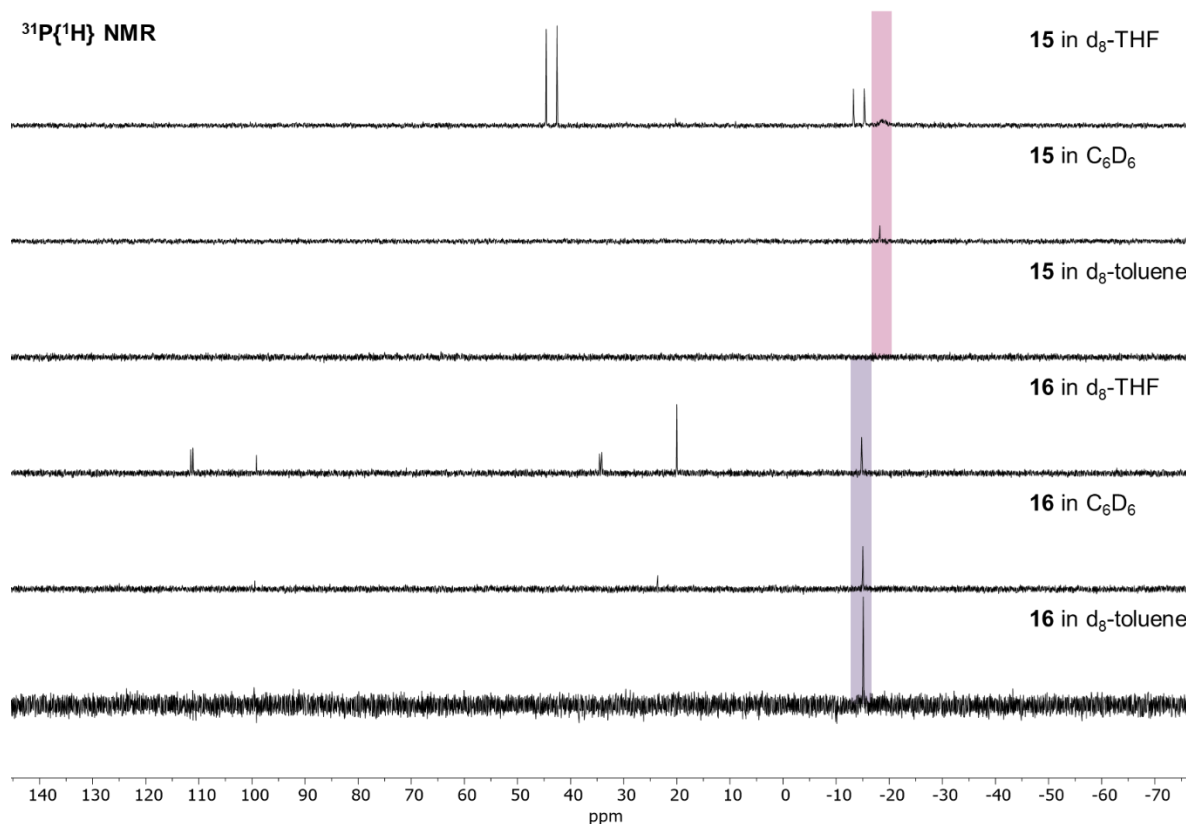
Figure 34. Solvent behaviour of **15** and **16** in solution in d_8-THF, C_6D_6 and d_8-toluene. Compounds **15** and **16** are highlighted. This figure has been partly adapted from [213] (license CC BY NC ND 4.0).
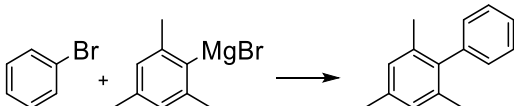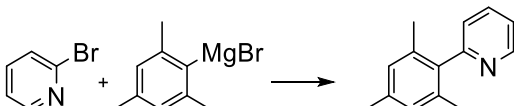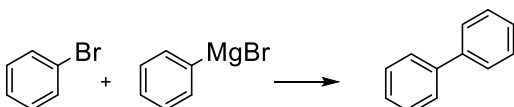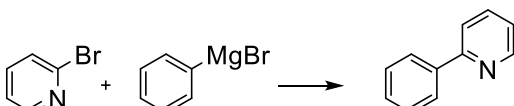
In DCM and CDCl$_3$ solely the ^{31}P{^{1}H} NMR signals, which can be assigned to compounds **15** and **16,** can be detected. Further, the behaviours of **15** and **16** in THF, benzene and toluene were investigated, since these solvents were used in the catalytic tests. A highly solvent-dependent behaviour is brought to light: Firstly, the solubility of the bromide-containing complex **15** was very low in toluene and no signal can be detected in the ^{31}P{^{1}H} NMR spectrum. In THF this pictures changes, since THF, as coordinating solvent, is capable of replacing phosphine ligands from the nickel centres. This competitive solvent coordination is strongly influenced by the nature of the halide in the [NiHal$_2$(PSP)] complex. Whereas in **15** a high quantity of free PPS ligand (δ = 43.9 ppm, d, $^1J_{PP}$ = 247.3 Hz, P(IV); –14.0 ppm, d, $^1J_{PP}$ = 247.3 Hz, P(II)) can be detected, which points towards THF coordination, this has not been observed in the case for **16**. Through the dissociation of the PPS/PSP ligand, free-coordination sites are created, which can be occupied by solvent molecules and during the catalytic reaction, by substrates. However, on the other hand this could result in a drop of the selectivity due to a lower influence of the ligand. In **16**, two new doublets at δ = 111.3 ppm and 34.6 ppm, both with a coupling constant of 51.3 Hz, can be detected in the ^{31}P{^{1}H} NMR spectrum, which point towards the formation of new complexes. It is highly likely that these signals stem from a PPS-coordinated nickel complex or from a monodentate PSP-stabilised Ni species, as similarly shown in Figure 17. However, further proof for this hypothesis is missing, since despite several attempts, these species could not be isolated. It should be mentioned, that no hints towards the formation of bulk Ni(0) has been observed. The ^{31}P{^{1}H} NMR spectra of the reference catalyst [NiBr$_2$(dppe)] revealed a high solubility in d_8-THF with solely one signal of

the reference catalyst (δ = 65.2 ppm, s) whereas solubility in C_6D_6 and toluene dropped under the detection limit.

5.2.2 Catalytic application

15 and **16**, were investigated as (pre-)catalysts for Kumada-Tamao-Corriu coupling reactions. To the best of our knowledge, this is the first example of a sulphur-based diphosphine PSP complex in catalysis. For this study, simple phenyl substrates, heterocycles (2-bromopyridine) as well as sterically more demanding (MesMgBr) substrates have been chosen for C(sp^2)-C(sp^2) couplings. In contrast to the widely accepted role of sulphur as catalyst poison, in this work the application of PSP-ligands did not point towards any poisoning effect and efficient conversions of the substrates could be achieved. Interestingly, the catalytic activity and selectivity is drastically influenced by the nature of the solvents and substrates.

Table 8. Results of the Kumada-Tamao-Corriu coupling reactions using **15**, **16** or [NiBr2(dppe)] (ref) as catalysts (5 mol%) in the coupling of aryl halides and Grignard reagents. Reaction conditions: aryl halide (1 eq.) and Grignard reagent (1 eq.) are reacted in the respective solvents for 20 h at room temperature. The conversions of aryl halides were determined by GC-MS using *n*-decane as internal standard. This figure has been adapted from [213] (license CC BY NC ND 4.0).

		Conversion [%]			Selectivity [%]		
		THF	C_6D_6	Tol.	THF	C_6D_6	Tol.
PhBr + MesMgBr → product	**15**	45	26	63	100	100	100
	16	48	14	52	100	100	100
	ref	74	0	14	100	-	100
2-bromopyridine + MesMgBr → product	**15**	39	69	75	50	90	91
	16	28	75	82	63	95	86
	ref	20	29	53	61	100	100
PhBr + PhMgBr → product	**15**	58	40	50	100	100	94
	16	45	46	49	100	100	85
	ref	72	73	62	100	100	100
2-bromopyridine + PhMgBr → product	**15**	84	46	79	55	78	72
	16	76	20	77	63	84	79
	ref	84	42	86	95	94	92

Both PSP-based complexes, **15** and **16,** display similar catalytic performances (Table 8). In most cases the PSP-based complexes suffer from a lower selectivity than the dppe-based counterpart, which might result from the highly dynamic behaviour of the PSP ligand as already indicated by $^{31}P\{^1H\}$ NMR spectroscopic studies. The origin of the dynamic ligand behaviour stems from the high ring strain in the four-membered P–S–P–Ni ring and the larger size of sulphur, which induces a higher degree of ligand dissociation and a more flexible ligand backbone. Especially in the case of THF as solvent, a severe drop in selectivity is observed. The drop in selectivity can be attributed to off-pathway reactions, which describe the undesired

reaction routes towards side-products often due to a challenging control of the catalytically active species.[2] Herein, off-pathway reactions yield in the formation of homocoupling products which is particularly high in the reaction of 2-bromopyridine with MesMgBr. In this case also the reference catalyst shows unsatisfactory performance with a low conversion of 20% and a selectivity of only 61%. In other solvents higher selectivities and conversions were observed, whereby the application of PSP-based compounds appears to be especially suitable for sterically more demanding substrates. Hereby, the conversions with the PSP-based complexes as catalysts significantly exceed the values for the reference catalyst, as seen in toluene for the reaction of bromobenzene and MesMgBr or 2-bromopyridine and MesMgBr. The conversion of MesMgBr with 2-bromopyridine yields conversions of 75% (**15**) and 82% (**16**) whereas the reference catalyst results in a drop of above 20% (conversion: 53%). An even higher effect of the PSP-based complexes can be seen if MesMgBr is coupled with bromobenzene leading to a decrease from 63% (**15**) and 52% (**16**) to only minor conversions in the case of the dppe-stabilised reference catalyst. This experimental finding can be explained again by the higher dynamic surrounding of the Ni(II) centre in complexes **15** and **16** in solution based on the smaller bite angles. The higher flexibility of these compounds facilitates vacant sites at the metal centre and less steric hindrance, which ultimately results in an enhanced conversion of sterically demanding substrates. Contrary, the coordination of the dppe ligand to Ni(II) results in a highly stable complex, due to a lower ring strain and exerts a larger steric hindrance. Catalytic tests were expanded towards $C(sp^3)$–$C(sp^3)$ and $C(sp^2)$–$C(sp^3)$ coupling reactions, which have attracted a great deal of attention in the pharmaceutical industry.[222,223] Such reactions often suffer from side-reactions due to β-hydride elimination or homocouplings.[224,225] For the $C(sp^3)$–$C(sp^3)$ coupling, bromocyclohexane was coupled with CyMgBr (cyclohexyl magnesium bromide) yielding only trace amounts of product with all three catalysts, **15**, **16** and [NiBr$_2$(dppe)]. The $C(sp^2)$–$C(sp^3)$ coupling was attempted for bromobenzene and CyMgBr. Hereby, a slight increase in activity for dppe was witnessed compared to the PSP-based complexes (conversion ref: 86% *vs.* PSP **15** and **16**: ~ 70%). From these initial studies of PSP-coordinated Ni-complexes as catalysts, no poisoning through the ligand and a promising performance can be concluded, especially for the coupling of sterically demanding substrates. This can be traced back to a higher dynamic ligand behaviour which can be induced by the sulphur backbone. However, future studies are required to optimise reaction conditions for this ligand class and gain mechanistic details for a targeted engineering of the ligand. A particular emphasis should be laid on the tautomeric behaviour of the ligand during the course of the catalytic process to facilitate controlled offering of vacant active sites for the substrates.

5.3 Concluding Remarks

As part of this chapter, the PPS/PSP ligand is applied for the synthesis of PSP-coordinated nickel halide ([NiHal$_2$(PSP)] Hal = Br (**15**), I (**16**)) complexes. PSP-based chelate complexes are very rare in literature and therefore widely unexplored. In contrast to reactions of PPS with Cu precursors, which resulted in a P=S bond cleavage of the ligand, with NiHal$_2$ (Hal = Br, I) the direct conversion with the PPS ligand can be accomplished. However, the presence of NiCl$_2$, [Ni(MeCN)$_4$](BF$_4$)$_2$ and [Ni(COD)$_2$] initiates degradation of the PPS ligand, which

involves a P–P bond cleavage and the formation of Ph_2PSS^-, Ph_2PS^- and Ph_2P^- ligands. These ligands are found in di- and trinuclear Ni(II) complexes whereby Ni(0) is oxidised to Ni(II).

The [NiHal$_2$(PSP)] complexes are strongly related to the PCP-based Kumada-Tamao-Corriu coupling catalysts, whereby the bite angles in the PSP-stabilised complexes are found in between the one of the dppm and the dppe analogue. This can mainly be ascribed to the larger size of sulphur compared to carbon in the ligand backbone. The comparison enables valuable insights into the impact of the sulphur backbone. In this context, investigations of the solvent behaviour of [NiBr$_2$(PSP)], [NiI$_2$(PSP)] and [NiBr$_2$(dppe)] have revealed a highly dynamic ligand behaviour in the PSP-complexes. First insights into the catalytic potential of the PSP-containing complexes were gained from the application in Kumada-Tamao-Corriu coupling reactions which were selected since [NiBr$_2$(dppe)] is a well-established catalyst for this process. Against general conclusions that sulphur-containing compounds are catalysts poisons, the PSP-based nickel complexes were successfully applied in the coupling reactions of aryl halides with Grignard reagents. During the catalytic tests, drastic solvent effects have been revealed which also played a crucial role in the case of the reference catalyst [NiBr$_2$(dppe)]. The dynamic behaviour of the PSP ligand facilitates a facile access for the substrate to the catalytic active centre *via* (partly) ligand de-coordination which on the other hand provokes a drop in selectivity due to off-pathway reactions. However, the dynamic ligand de-coordination behaviour can be employed to activate sterically demanding substrates, which is more challenging to achieve with the reference catalyst.

6   Diphenylphosphine sulphide-stabilised coinage metal clusters

The results discussed in this chapter have not been published yet.

Crystallographic data were processed by Toni Grell.

Nanoscale coinage metal clusters describe a class of compounds, which bridges molecular complexes with bulk materials, not only in terms of the compounds' dimensions but also in terms of their physical and electronical properties. In contrast to nanoparticles, the exact number of atoms in coinage metal clusters is clearly defined, and the molecular structures can be revealed by single-crystal XRD analyses. As a result, targeted modifications can be conducted to tune the clusters properties.[108,226] The structure of nanoclusters consists of a metal core, with at least three metal atoms with two bonds to each other, and of an outer, stabilising ligand sphere. Suitable ligands are in most cases based on phosphorus and sulphur donor functionalities.[227] Such compounds have been reported, whereby the incorporated chalcogenides show a drastic effect on the compounds characteristics, such as the photo-optical properties.[228]
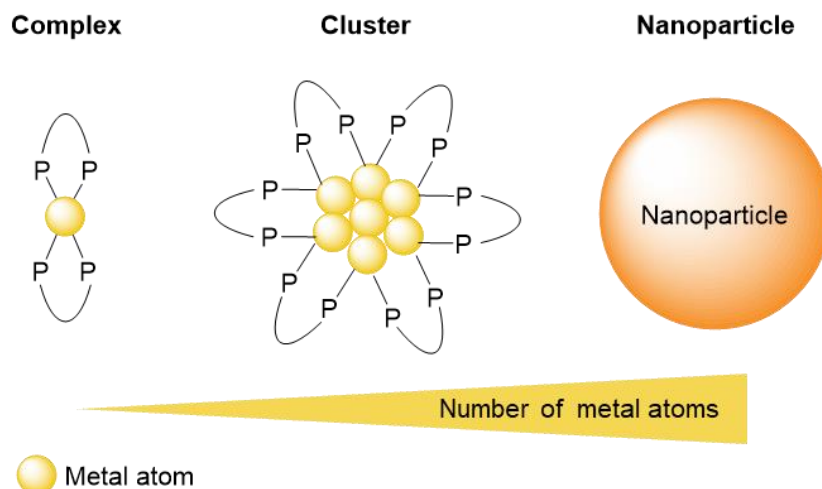

Figure 35. Clusters can be classified in between ligand-stabilised transition metal complexes with one or two metal atoms and bulk nanoparticles. Thereby clusters possess a precise number of atoms and are in most cases stabilised by ligands.

The most-widely applied synthetic route to access copper sulphide clusters comprises a two-step process, which involves an initial coordination of the metal precursor by a ligand, followed by the cluster formation step. This step is initiated by the addition of an external sulphur source, such as $S(SiMe_3)_2$ or $RSSiMe_3$ (R = organic rest).[227,229] The nature of the product depends majorly on the applied ligand and the counterion of the metal precursor as well as on reaction parameters such as the solvent, reaction stoichiometry or temperature. The driving force of this type of reaction is the formation of Me_3SiY compounds (Y = counterion, halogen or pseudohalogen). An alternative procedure is the direct conversion of metal thiolates (MSR) with bidentate phosphines, whereby the cluster formation mainly depends on the substituent R in the metal thiolate (M: metal, R = Mes, Nph (naphtyl), Cy).[230]

61

It should be underlined that sufficient stabilisation of the cluster core has to be ensured since insufficient stabilisation results in the cluster decomposition towards Cu_2S, due to the thermodynamic instability. A classification for copper sulphide clusters was proposed which correlates with the similarity to the parent Cu_2S material and is based on their small and large scale arrangements. The similarity to the bulk Cu_2S phase, meaning a sulphur atom arrangement similar to the one found in the fcc-lattice, was shown to increase with increasing cluster size.[227] Whereas the structure in the solid state can clearly be determined, the behaviour of the clusters in solution is not completely uncovered and might be influenced by the presence of various species.[227] Furthermore, clusters have been reported which possess two structural isomers.[229]

Application fields of coinage metal clusters can be found in the areas of bioimaging,[226] optoelectronic devices[231] or catalysis.[232] One field, which attracted much interest in cluster-based catalysis, is the electro- and photo-catalysed CO_2 reduction.[233-235] Through the utilisation of nanoclusters, monodisperse systems with high metal efficiency and highly defined catalytically active centres can be provided. In addition to the application in catalysis, cluster compounds and copper-based metal clusters in particular, are often showing intense photo-optical properties with large Stokes shifts and emission lifetimes in the microsecond regime.[236-238] The photo-optical properties are directed by the contributions of the d-orbitals, size confinement effects, surface defects and the isomerisation of the structures.[231] The close proximity of the metal atoms is beneficial for the development of metallophilic interactions, which can have a tremendous impact on the photo-optical properties. As a result, the d → s separation can be decreased, which promotes metal centred transitions (MC).[239,240] Therefore, many clusters show emissions, which are mainly based on the cluster core in a triplet excited state ^3CC ("cluster centred") and less influenced by the ligand shell.[239,240] The existence of photoemissive properties of copper-based clusters is supported by the highly rigid environment within the cluster core, which leads to the suppression of non-radiative decays. The presence of heteroatoms, such as sulphur in the cluster core was shown to have tremendous impact.[239,241] Fackler and Avdeed conducted a molecular orbital study of a copper sulphide cluster containing a $Cu_8S_{12}^{4-}$ core.[242] In this study the authors revealed that the HOMO can mainly be assigned to the sulphur atoms, whereas the LUMO is majorly localised at the copper atoms, which results in an intense sulphur to metal charge transfer. The presence of heteroatoms in the cluster core can thus significantly promote SMCT (sulphur to metal charge transfer), which can be used to tune the photoemission properties.[228]

The interest in atomically precise coinage metal clusters does not only stem from their remarkable structures and properties. The clusters can also serve as model systems for quantum dots and bulk CuS_2 materials. This opens the possibility to gain further knowledge on the processes at the atomic scale, which can be transferred to the bulk analogues. This knowledge is fundamental for a future material development. As part of this work, copper sulphide clusters are presented which can be obtained from an uncommon reactivity of the PPS-related Ph_2PSH ligand in presence of mesityl copper.

6.1   Synthesis of a diphenylphosphine sulphide gold cluster

Based on the established synthetic route for Au-POP complexes (**4**, **5**), the behaviour of the Au metal in presence of the PPS/PSP ligand was investigated. However, the reaction of PPS with [Au(tht)Cl] did not yield an expected PPS/PSP-based complex in analogy to the POP-compound **4**. Instead, a P–P bond cleavage provided colourless crystals of an Au_6 cluster (**20**), stabilised by six anionic Ph_2PS^- ligands (Figure 36). To optimise the atom efficiency of the formation of this compound, the direct reactions of the Ph_2PSH analogue with the gold precursor was attempted. It should be underlined that the PPS ligand can be considered as the anhydride form of Ph_2PSH (PS), which features a similar tautomeric equilibrium between the $Ph_2P(=S)H$ and the $Ph_2P–S–H$ tautomers. This tautomeric equilibrium can also be influenced by coordination to transition metals, whereby various coordination modes have been reported.[48] However, the direct conversion of Ph_2PSH with [Au(tht)Cl] did not lead to the targeted compound. Therefore, the respective potassium salt $Ph_2PS^-K^+$ (KPS) was reacted with [Au(tht)Cl], yielding the $[Au_6(\mu_2\text{-}Ph_2PS)_6]$ cluster. The reactivity of PPS in presence of the gold precursor is similar to the one reported for PPS in presence of Ni(II) and Ni(0) compounds. In contrast to the nickel compounds, with gold there is no indication from single-crystal XRD or NMR analyses for the formation of gold-based compounds containing other types of ligands, such as Ph_2P^- and Ph_2PSS^-, which have been identified in **17-19**.
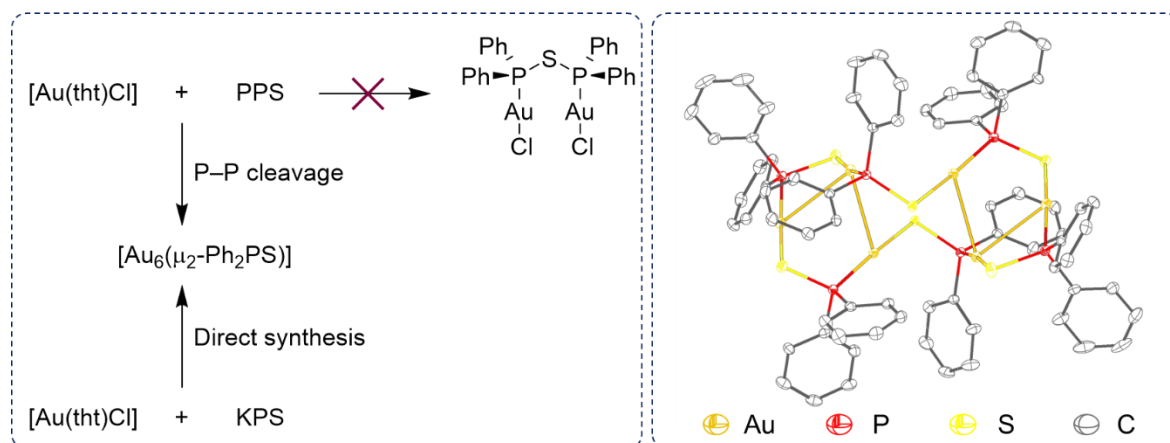
Figure 36. P–P bond cleavage of the PPS ligand results in the formation of $[Au_6(\mu_2\text{-}Ph_2PS)]$ (**20**). Selected bond lengths (Å) and angles (°): S(1)–P(1) 2.056(2), S(3)–P(3) 2.060(2), P(1)–Au(1) 2.2635(9), P(2)–Au(2) 2.263(1), P(3)–Au(3) 2.258(1), Au(1)–Au(3) 3.1896(4), Au(1)–S(3) 2.346(1), Au(2)–S(1) 2.325(1), Au(3)–S(2) 2.318(1), P(3)–Au(3)–S(2) 173.94(4), S(3)–Au(1)–P(1) 172.48(4), S(1)–Au(2)–P(2) 172.47(4), Au(3)–P(3)–S(3) 109.14(6), Au(1)–P(1)–S(1) 116.55(5), P(3)–S(3)–Au(1) 93.14(5), P(1)–S(1)–Au(2) 96.58(5).

The Ph_2PS^- ligands in **20** are present in the bridging coordinating mode and each phosphorus and each sulphur atom coordinate to one gold centre. Due to the nature of the ligand, a slightly distorted linear coordination of the gold atoms can be observed. The P–S bond lengths are comparable with the bridging Ph_2PS^- ligands in **17**, **18**, **19**. Furthermore, the Au–Au (3.1896(4) Å) distances are found to be well below the sum of the van-der-Waals radii (3.80 Å), indicating the presence of aurophilic interactions in **20**.

6.2 Synthesis of diphenylphosphine sulphide copper clusters

Inspired by the interesting structure of the hexanuclear Au_6 complex **20**, the PS ligand was further applied for the coordination of the coinage metal copper. It should be mentioned, that the direct conversion of the PPS ligand with the $[Cu(MeCN)_4]PF_6$ salt does not result in the formation of a PSP-based Cu complex. As mentioned in chapter 4.2, P=S bond cleavage initiates the formation of $[Cu_2(MeCN)_4(\mu_2\text{-}P_2Ph_4)_2](PF_6)_2$ instead. Consequently, PPS/PSP complexes cannot be accessed *via* this route and the focus of the following study was laid on the application of Ph_2PSH as ligand.

Mesityl copper (CuMes) was therefore chosen as metal precursor, since it can be used to simultaneously act as the Cu source and as the deprotonation agent, forming mesitylene as by-product which can easily be separated from the reaction mixture. Another appealing feature of CuMes is the occurrence of different oligomers in solution, which can be directed by the nature of the solvents.[243] While the majority of CuMes is present as a tetramer, a pentameric species contributes to a minor extent. The influence of the solvent is also reflected in the isolated solid state structures, since toluene provides the pentameric form, while with THF the tetrameric structure can be obtained.[243]

Interestingly the conversion of CuMes and Ph_2PSH did not only lead to the simple deprotonation of the ligand followed by complex formation. In addition to that, also the P=S bond cleavage of the ligand is taking place, as already seen in the direct conversion of PPS with $[Cu(MeCN)_4]PF_6$. Through a precise adjustment of the reaction conditions, two different copper sulphide clusters could be isolated from different reaction conditions, namely $[Cu_{14}(\mu_6\text{-}S)_1(\mu_3\text{-}Ph_2PS)_{12}]$ (**21**) and $[Cu_{24}(\mu_5\text{-}S)_6(\mu_3\text{-}Ph_2PS)_{12}]$ (**22**) (Scheme 5). Hereby, factors that favour the smaller cluster **21** were identified to be a low concentration of the reagents, the use of a coordinating solvent, such as THF, a fast ligand addition at room temperature and a slow stirring speed. In order to obtain **22**, a high temperature was applied, whereby a hot injection of the ligand is fundamental for the successful synthesis of the cluster, high concentrations of the reagents, a high stirring speed and a short reaction time were utilised. Importantly, the variation of the reaction conditions did solely result in the formation of either **21** or **22,** indicating a high tendency for the formation of these clusters.
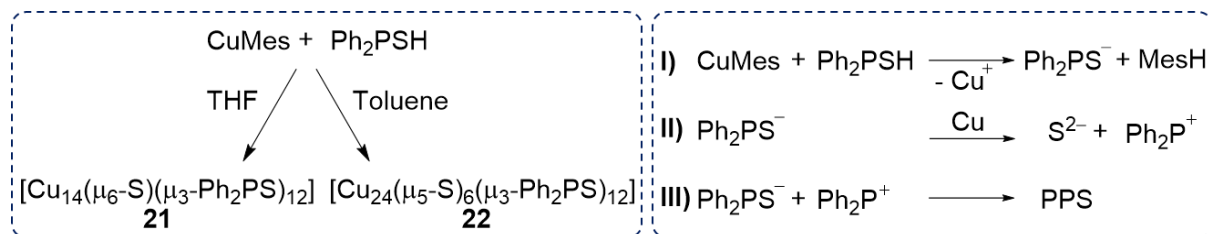
Scheme 5. Synthesis of copper clusters in THF (**21**) or toluene (**22**) (left). Key steps involve the deprotonation with the mesityl copper source (I), the Cu-catalysed P=S bond cleavage (II) and the formation of the by-product PPS (III) which is a consequence of I and II (right).

A reason for this predominance can be found in the formation pathways and corresponding by-products (Scheme 5). $^{31}P\{^1H\}$ NMR spectroscopic studies revealed the formation of PPS as a by-product, which most likely stems from the recombination of the phosphorus species

after P=S cleavage with another Ph_2PS^- ligand. Thus, the reaction stoichiometry limits the formation of other cluster cores, since per incorporated S^{2-}, one free Ph_2PSH ligand is consumed to react with the cationic Ph_2P^+ species yielding PPS. The stoichiometric ratio is limited to 1:1 (CuMes:PSH), due to the nature of CuMes which delivers one Cu^+ for incorporation into the cluster, while it is simultaneously acting as deprotonation agent for one Ph_2PSH ligand. As a result, the sum of Ph_2PS^- (PS) and S^{2-} ligands in the cluster and Ph_2P^+ catcher has to be equal to the number of ligands used. Under the assumption that the ligand shell exists out of 12 Ph_2PS^- ligands, the stoichiometry is balanced only for the compounds **21** and **22** explaining the high probability for the formation of these compounds. However, it should be noted that according to $^{31}P\{^1H\}$ NMR spectroscopic studies the P=S bond of the by-product PPS is also cleaved in the presence of CuMes forming tetraphenyldiphosphine, which could also have an impact on the formation of the cluster.

The nature of **21** and **22** was further confirmed by elemental analysis and by ESI-MS measurements in which the molecular ion peaks of the two clusters and a clear fragmentation, involving the stepwise loss of sulphur and Ph_2P-units, can be observed. The solid state structures of the yellow **21** and the orange **22** were determined by means of single-crystal XRD (Figure 37 and Figure 38).

In **21**, twelve bridging Ph_2PS^- ligands surround the $Cu_{14}S_1$ metal core, whereby the sulphur atom coordinates to two Cu atoms and the phosphorus atom to one. In the centre of this structure, a μ_6-S anion is localised stemming from the P–S cleavage, which is surrounded by a distorted Cu_6 octahedron. The Cu atoms at the bottom and top vertices are each coordinated by two phosphorus atoms of two PS ligands. The four Cu atoms in the central plane are each coordinated by two sulphur atoms, amongst which one belongs to the Ph_2PS^- molecule, which also coordinates the Cu atoms alternatively at the top or bottom. All copper atoms are in the +I oxidation state and are coordinated in a distorted trigonal planar fashion. This is in accordance with the copper environment in the bulk chalcocite Cu_2S.[244] Furthermore, the copper sulphide core possesses C_2 symmetry. The Cu–S bonds are found in the range of 2.2191(14)–2.3393(19) Å, whereby the bonds to the central sulphur ligand (2.3183(8)–2.3393(19) Å) are extended compared to the other Cu–S (all μ_3-S) bonds in the molecule indicating a dependency of the bond lengths on the sulphur coordination mode. Similar observations have also been reported for other copper sulphide clusters, such as $[Cu_{52}S_{12}(SCH_2C_6H_4{}^tBu)_{28}(PPh_3)_8]$ for two-, three- and six-fold sulphur coordination.[245] Compared to the before-reported Ph_2PS^--based nickel complexes (**17**, **18**, **19**) and the Au_6 cluster (**20**), the P–S bonds are slightly elongated (Table 9).
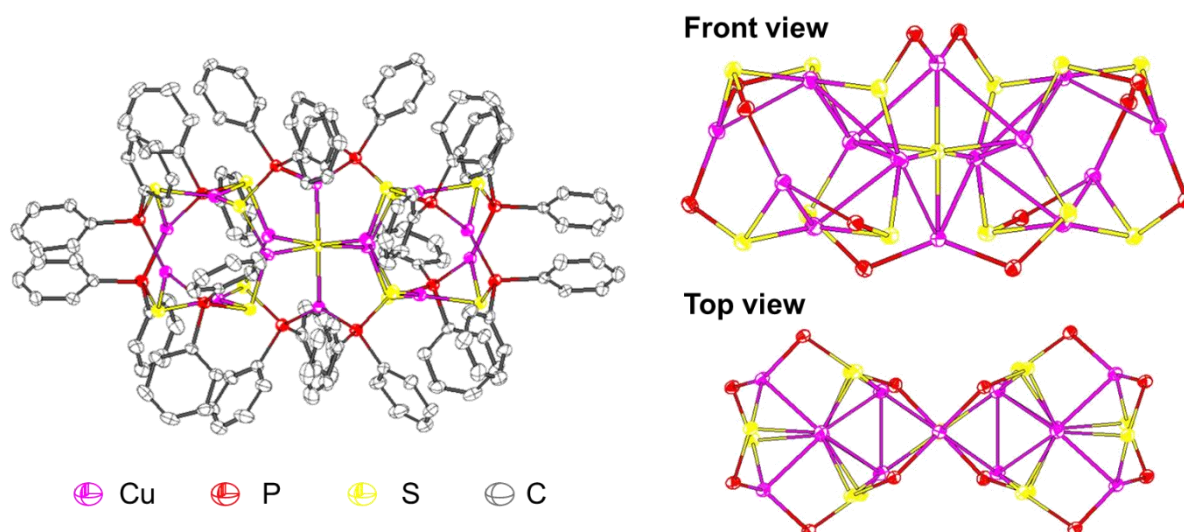
Figure 37. Molecular structure of the cluster **21** (left) and the cluster core without phenyl groups for clarity (right). Selected bond lengths are given in Table 9.

22 is based on a more extended $Cu_{24}S_6$ core, which is again surrounded by twelve Ph_2PS^- ligands. Again, the oxidation states of all copper atoms are +I and P-based donor sites of the ligand coordinate one Cu centre whereas the S-based donor sites of the PS ligand coordinate two copper atoms. According to single-crystal XRD analysis, four copper atoms can be found in the centre of the structure, which each spilt over two positions forming a cube of eight partially occupied (50%) atoms. On each side of this cube, one S^{2-} ligand can be found, which stems again from P–S bond cleavage, constructing a S_6 octahedron. This leads to a distorted trigonal coordination of the four central Cu atoms. The S^{2-} anions act in a μ_5 coordination mode which involves the coordination of four half-occupied Cu atoms. On the other side, the S^{2-} anions are connected to the outer ligand sphere either *via* a Cu atom, which is additionally coordinated by two Ph_2PS^- ligands, or in the case of six Cu atoms (Cu(2), Cu(3), Cu(4)) *via* a Cu centre which is only coordinated by one other PS ligand resulting in a distorted linear coordination geometry. The linear coordination mode is also common for similar copper sulphide clusters.[229]
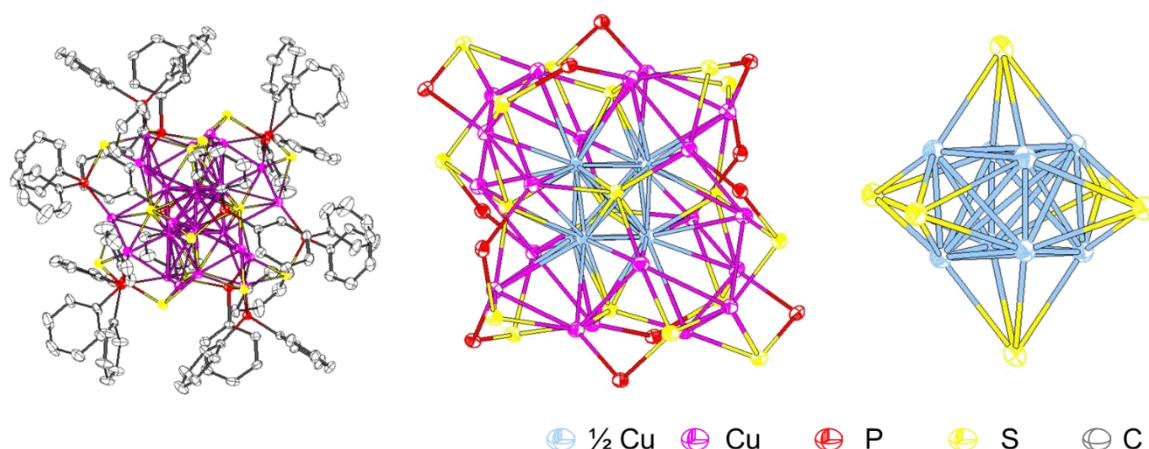
½ Cu   Cu   P   S   C

Figure 38. Molecular structure of **22**. Left: complete structure including phenyl groups, middle: phenyl groups are omitted for clarity and partially occupied Cu atoms in the centre of the molecule are marked in light blue. Right: the central unit of the cluster is formed by a cube of partially occupied Cu atoms which is surrounded by a S_6 octahedron. Selected bond lengths are given in Table 9.

Comparable Cu–P and Cu–S bonds can be found for **21** and **22,** whereas the P–S bonds of **22** are slightly more distributed over a wider range, indicating a lower degree of symmetry than in **21**. This is further confirmed by the space groups for **21** (*C2/c*) and **22** (*P2₁/n*).

Table 9. Selected bond lengths of the two Cu-clusters **21** and **22**.

	Cu–Cu [Å]	Cu–P [Å]	Cu–S [Å]	P–S [Å]
21	2.7097(10)– 2.8850(10)	2.2092(14)– 2.2572(14)	2.2191(14)– 2.3079(14)	2.0834(16)– 2.0956(16)
22	2.5958(17)– 2.9511(17)	2.2080(16)– 2.2417(16)	2.1407(16)– 2.3278(16)	2.077(2)– 2.108(2)

6.3 Photo-optical properties of the copper sulphide clusters

Several Cu–Cu distances of **21** (2.7097(10)–2.8850(10) Å) and **22** (2.5958(17)–2.9511(17) Å) are below the sum of the van-der-Waals radii of two Cu atoms (2.80 Å), which is an indication for the presence of cuprophilic interactions in these clusters. Therefore, the photo-optical properties of the clusters **21** and **22** in solution and in solid state have been investigated.

The UV/Vis spectroscopic analyses of both samples recorded in DCM show similar spectra with a maximum absorption at 230 nm, which can be mainly assigned to ligand-centred transitions (Figure 39). However, the absorption band of **22** is slightly broadened towards higher wavelength resulting in the orange colour of **22** whereas **21** is yellow.
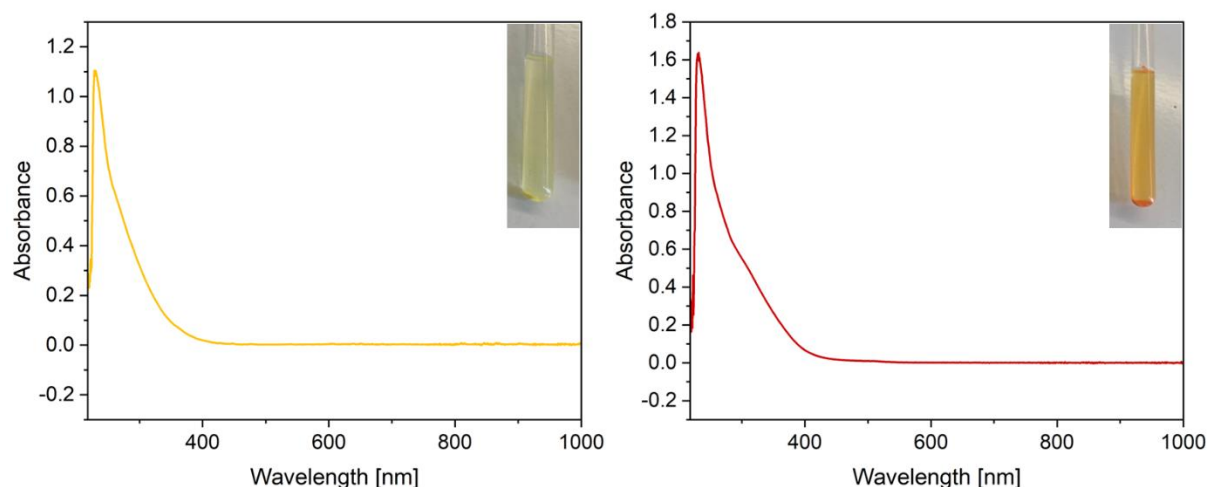
Figure 39. UV/Vis absorption spectra in DCM of **21** (left, $1 \cdot 10^{-6}$ M) and **22** (right, $1 \cdot 10^{-5}$ M).

An intense orange emission can be observed for **22** under UV light (365 nm), whereas **21** does not show a strong photo-luminescence. PLE and PL spectra were recorded and emission lifetimes were measured for **22** in DCM solution ($3 \cdot 10^{-5}$ M; 77 K and r.t.) and in solid state (r.t., Table 10). All emission and excitation spectra show broad and intensive bands, which are common for photoemission spectra of d^{10} metals (Figure 40 and Figure 55, appendix). In solution and in the solid state **22** displays a near-infrared photoemission whereby a bathochromic shift can be observed for the solution sample. At 77 K, in DCM solution, two excitation maxima could be identified at 367 nm and at 450 nm, whereas at 298 K only one main excitation maximum is visible in solution, which is blue-shifted to 320 nm. The solid state sample shows a very broad excitation spectrum in the area from 250 nm until 550 nm. Again, the PL spectrum of the solid state sample is broadened showing maximal values in the area between 700 and 800 nm. The comparison of solution samples at 77 K and 298 K shows, as expected, a red-shift at higher temperatures.[228,246,247] Emission lifetimes in the microsecond range can be recorded whereby larger values can be measured at lower temperatures due to a decreased degree of non-radiative decays stemming from molecule vibrations. Based on the large Stokes shifts with emission maxima > 700 nm and the long emission lifetimes, it can be suggested that the responsible transition can be attributed to a triplet cluster centred excited state (^{3}CC). Further it is suggested that the excited ^{3}CC state consists of contributions of the sulphur to metal charge transfer (SMCT) as well as metal centred (MC) $3d \rightarrow 4s$, $4p$ transitions, due to presence of cuprophilic interactions, which are considered to decrease the $d \rightarrow s$ separation.[239,240]

Table 10. Excitation, emission wavelengths and lifetimes for **22** in DCM solution (77 K, 298 K) and in the solid state (298 K).

State	T [K]	λ_{ex} [nm]	λ_{em} [nm]	Lifetime$_{eff.}$ [µs] [a]
Solid	298	420	736	10
Solution	298	320	900	9
Solution	77	367; 450	800	69

[a] For biexponential decays, the effective lifetimes were calculated, more information can be found in the experimental part of this thesis
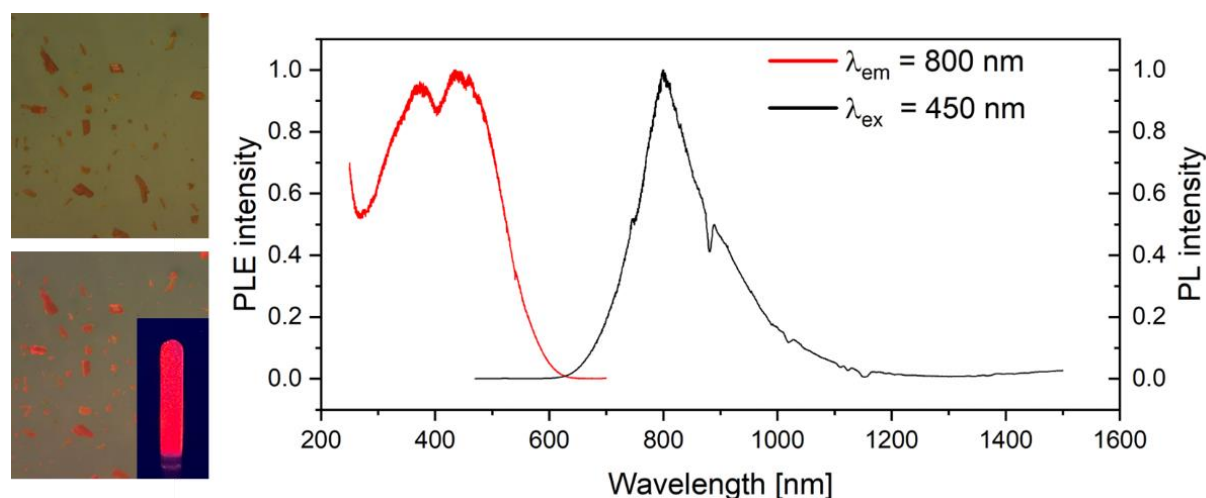
Figure 40. Photoemission of compound **22**. Microscope images without (left, top) and with UV radiation (365 nm, left, bottom) and photoemission of crystals in the solid state at room temperature (left, bottom). PLE and PL spectra of **22** in DCM at 77 K.

Further investigations are required to uncover the origin for the absence of any photoemission in **21**. However, if the cluster centred excited state is a combination of sulphur to metal charge transfers and copper-centred transitions, both factors are superior in the Cu$_{24}$ cluster **22** than in the Cu$_{14}$ cluster **21**. This can be explained by a higher number of incorporated S^{2-} ions, which can enhance the SMCT and smaller Cu–Cu distances in **22** which support better metal-centred transitions.

If compound **22** is dissolved in DCM and stirred for 1.5 hours, the photo-optical properties of the solution sample diminish, which is an indication for the degradation of the cluster in solution. ^{31}P{^{1}H} NMR spectroscopic studies confirm this observation and reveal the formation of PPS in solution, which would involve a P–S cleavage and a recombination of the Ph$_2$P$^+$ unit with the Ph$_2$PS$^-$ ligand. Attempts to reverse this process to form **22** again by UV radiation (254 nm, 365 nm) or higher temperatures were not successful. It is noteworthy that if a second bidentate ligand, BINAP, was added to a solution of the Cu$_{24}$ cluster **22** in DCM, the photoemission properties could be retained. In the ^{31}P{^{1}H} NMR spectrum no indication towards the coordination of the BINAP ligand can be witnessed since only signals belonging

to the free BINAP ligand can be witnessed. No crystals could be isolated from this reaction mixture, to get further information from the molecular structure.

Therefore, focus was laid on synthesising clusters with the Ph_2PSH ligand and an additional diphosphine using BINAP, DPEphos and dppe (Cu precursor:Ph_2PSH/Ph_2PSK:diphosphine = 1:0.5:0.25) *via* either a one-pot reaction or the conversion of the copper precursor with the diphosphine, followed by addition of Ph_2PSH/K after 1 hour. Also the potassium salt of the ligand was used in combination with other copper precursors, such as $[Cu(MeCN)_4]PF_6$. However, the introduction of the diphosphine could not be accomplished, since only **22** could be isolated from these approaches. It might be likely that the bulky, rigid backbones of BINAP and DPEphos counteract the bridging coordinating mode and that sterical hindrance counteracts sufficient stabilisation of the cluster core resulting in no successful isolation of clusters containing these ligands. To overcome this challenge, dppe, a less sterically demanding and more flexible backbone has been used as additional diphosphine ligand and indeed, by applying an excess amount of Ph_2PSK with $[Cu(MeCN)_4]PF_6$ and dppe (KPS: Cu-precursor:dppe = 1:0.85:0.25) in DCM, bright yellow crystals could be grown, which contain both, dppe and Ph_2PS^- ligands (Figure 41). Also, in **23**, all Cu atoms are in +I oxidation state. In the centre of the molecule four Ph_2PS^- ligands can be found with alternating direction. Thereby, the four phosphorus atoms create a central rectangle, which is localised in between two other rectangles constructed by two copper and two sulphur atoms each. The P–S (2.0705 Å) and Cu–P bonds (2.2467–2.2934 Å) are in the region of the ones in the copper clusters **21** and **22** whereas the Cu–S bonds (2.4009–2.4016 Å) exceed the one in the clusters. This also correlates with larger Cu–Cu distances (2.9302 Å) which exceed the sum of the van-der-Waals radii. Consequently, **23** does not display photoemission under UV-light.
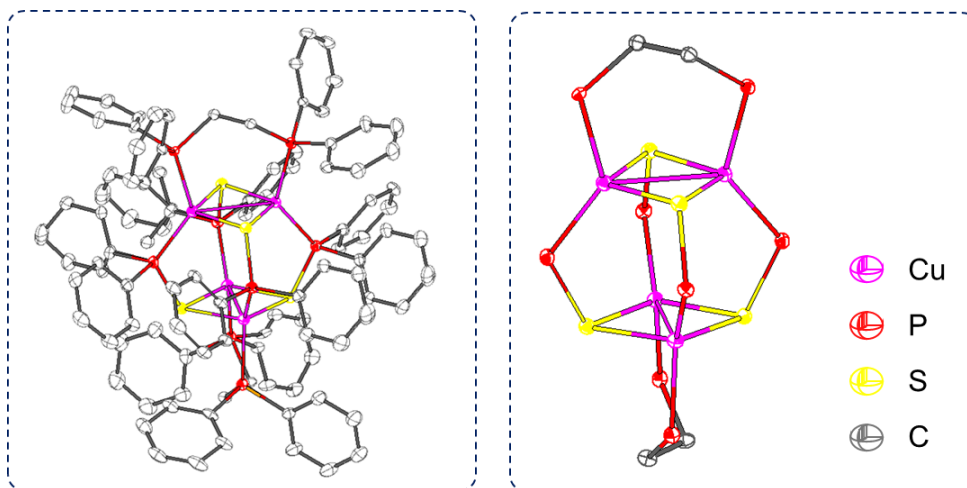
Figure 41. The tetranuclear Cu-complex **23** is stabilised by two dppe and four Ph_2PS^- ligands. Selected bond lengths (Å) and angles (°): Cu–Cu: 2.9302, Cu–S 2.4009–2.4016, Cu–P 2.2467–2.2934, S–P 2.0705 S–Cu–S 104.78 S–P–Cu 114.87 Cu–S–Cu 75.20.

6.4 Concluding remarks

As seen before, the PPS/PSP ligand is highly susceptible for ligand rearrangement processes *via* P–P bond cleavage in the presence of transition metals. This behaviour has also been observed in the presence of [Au(tht)Cl], where the reaction of [Au(tht)Cl] with PPS provides

access to a new hexanuclear gold compound, $[Au_6(\mu_2\text{-}Ph_2PS)_6]$ stabilised by Ph_2PS^- ligands. This compound can also be obtained directly from the synthesis of the Ph_2PSK ligand with $[Au(tht)Cl]$ to circumvent the PSP ligand decomposition. This synthesis strategy was extended towards the 3d analogue copper. Through the facile one-pot synthesis of Ph_2PSH with the deprotonating copper source CuMes, atomically precise copper sulphide nanoclusters can be obtained, which are highly desirable materials since they bridge the gap between transition metal complexes and larger nanoparticles. *Via* this synthetic route two new copper sulphide clusters, namely $[Cu_{14}(\mu_6\text{-}S)_1(\mu_3\text{-}Ph_2PS)_{12}]$ (**21**) and $[Cu_{24}(\mu_5\text{-}S)_6(\mu_3\text{-}Ph_2PS)_{12}]$ (**22**), can be obtained, deriving from a P=S bond cleavage. The major structural differences between the two clusters are their size, the number of incorporated S^{2-} anions and the coordination modes of the copper centres, since in the Cu_{14} cluster **21** all Cu(I) atoms are coordinated in a trigonal fashion, whereas in the Cu_{24} compound **22** additionally linear coordination modes are observed. Whereas $[Cu_{14}(\mu_6\text{-}S)_1(\mu_3\text{-}Ph_2PS)_{12}]$ displays no visible photo-luminescence, an intensive orange, near-infrared photoemission can be observed for $[Cu_{24}(\mu_5\text{-}S)_6(\mu_3\text{-}Ph_2PS)_{12}]$ in solution and in the solid state. However, the clusters suffer from degradation processes in solution accompanied by an extinction of the photo-luminescence. Therefore, strategies are required to stabilise the clusters through the modification of the ligand shell.

7 A bench-stable fluorophosphine nickel(0) complex and its catalytic application

The results discussed in this chapter can be partially accessed on chemrxiv *via*: A bench-stable fluorophosphine nickel(0) complex and its catalytic application, F. Flecken, A. Neyyathala, T. Grell, S. Hanf, **2024**, DOI: 10.26434/chemrxiv-2024-vtmqd under the license BY NC ND 4.0.

Figure 43-49 and 56-59 (appendix), Table 12-14 and Scheme 6 and 9 are (partly) adapted from this publication.

Theoretical calculations were conducted by Schirin Hanf. Crystallographic data and line-shape analysis were processed by Toni Grell.

Additional data in open file formats can be accessed on Zenodo, DOI: 10.5281/zenodo.13691979

In the field of phosphine ligands, fluorophosphines (R_2PF, R = alkyl, aryl, F, CF_3, NR) are, up-to-date, widely overlooked, despite their interesting high π-acceptor and σ-donating capabilities, which can facilitate the stabilisation of metals in different oxidation states.[248-251] This could also be very beneficial in catalytic applications. The most common synthesis method for fluorophosphines is the direct reaction of the respective chloride- or bromide-based analogue of the phosphine with metal fluorides, such as CsF,[249,252] NaF[249,253-255] or AgF.[256] However, fluorophosphines suffer from a high susceptibility towards disproportionation, whereby P–P coupled products (R_2P–PR_2) and difluorophosphoranes R_2PF_3 are formed (Figure 42). This hinders their complete characterisation and application in many cases.[257] Approaches to counteract this degradation process involve the introduction of electron-withdrawing groups on the phosphorus centre, such as CF_3 groups, or of sterically demanding residues, such as *tert*-butyl (*t*Bu) groups.[249,258]
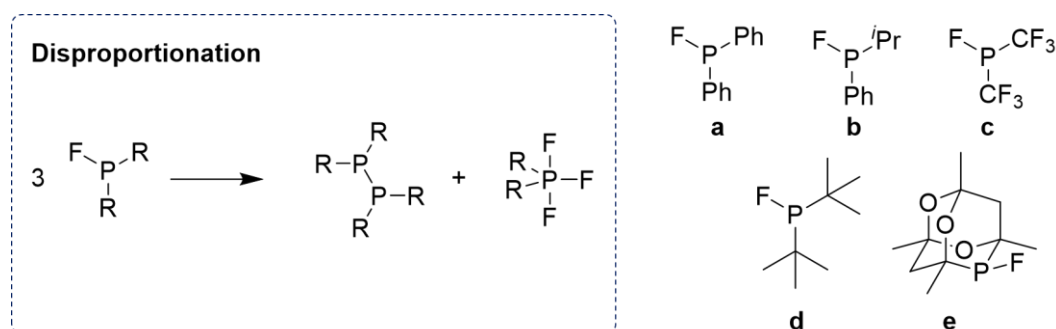
Figure 42. Fluorophosphines tend to disproportionate in solution into Ph_2P–PPh_2 and R_2PF_3 (left). Selected examples of fluorophosphines are given on the right.[249,253-255,259] Strategies to increase the stability are to incorporate sterically demanding or electron withdrawing groups, such as in the case of c, d and e.

Coordination compounds, involving fluorophosphine ligands, are consequently rare. Only in the case of sterically and electronically stabilised fluorophosphines, such compounds can be

synthesised from the direct reaction of the free fluorophosphine with suitable metal precursors.[249,252,260] However, this procedure cannot be transferred to less-stable fluorophosphines, such as the simple phenyl-based derivative, Ph_2PF, since for such ligands the disproportionation dominates over the metal coordination. One strategy to circumvent this, is the formation of an unfluorinated phosphine complex, which is subsequently fluorinated under P–N,[261] P–C[262-264] or acid-induced P–O[265] bond cleavage, while the coordination to the metal centre is maintained. For such reactions, the fluoride source itself is either already coordinated to the metal centre[263,264] or external fluorination agents are required including $BF_3 \cdot OEt_2$,[261] HBF_4[262,265] or HF ($Et_3N \cdot 3$ HF).[264]

Recently, Fey *et al.* have reported the first examples of fluorophosphine ligands in Rh- and Ni-based catalysis for hydrocyanation and hydroformylation reactions, which showed superior performance over industrially applied catalysts, stabilised by PPh_3 or $P(O$-*o*-Tol$)_3$ ligands.[249] The exploration of new ligand classes is particularly important in the context of novel nickel-based catalysts, since through a tailored design of the ligands, nickel complexes can be developed, which are capable of substituting the noble metal palladium.[266-271] Especially, in the field of C–C coupling reactions, the use of Ni is favoured, since such reactions are majorly catalysed by Pd-based catalysts up-to-date.[271] Compared to the common oxidation states of palladium of 0 and +II during the catalytic cycle, with nickel a versatility of oxidation states becomes accessible including 0, +I, +II and +III. This correlates also with an increased tendency of nickel for homolytic bond cleavages, which often result in radical pathways.[271] Furthermore, a higher reactivity in oxidative additions and reductive eliminations can be ascribed to nickel compared to its group 10 partners, platinum and palladium according to the respective activation energies for oxidative additions and reductive eliminations including C–C bond activation.[269] Based on these characteristics of nickel, new reaction pathways and activations of unreactive substrates, such as aryl chlorides and fluorides as well as alkyl halides, can be accessed.[266-271] On the downside of this high reactivity, the catalytic reactions are often challenging to control in a selective manner and mechanistical insights often remain unexplored.[269] To address this, the targeted ligand design is an essential instrument to gain precise control of the catalysts and prevent the formation of side-products through off-pathway reactions.[268,269,272,273]

Since Ni(0) species are often the starting point in nickel catalysis, suitable and easy methods have to be established to access these species. One approach is the *in-situ* reduction of more stable Ni(II) compounds. However, for the activation of Ni(II) precursors strong reducing agents, such as Zn[274], KC_8[275] or $NaBH_4$[276], are needed, which can lead to catalyst degradation and off-pathway reactions, which result in the formation of side-products.[2,277,278] Alternatively commercially available Ni(0) sources can be used as pre-catalysts, which are ready-to-use without any further manipulation.[279-282] However, such Ni(0) precursors often suffer from an increased susceptibility towards oxidation and therefore oxygen- and moisture-free handling under inert gas is required. This is also the case for [Ni(COD)$_2$], which is still the most-used Ni(0) source in catalysis, despite its high air-, water-, light and temperature-sensitivity.[2,282] Additionally, the application of the commercially available [Ni(COD)$_2$] is often connected with high costs, which can even range up to the costs of Pd-based compounds.[2] Consequently,

73

there is an urge to develop new Ni(0) sources, which stand out due to lower costs, easy handling and no requirement of additional reducing agents. Further criteria concern the reactivity, since firstly ligand dissociation from the initial Ni(0) complex has to occur under reaction conditions to offer an empty site for substrate binding and to consequently initiate the catalysis. Secondly, the dissociated ligand should not block active sites during the course of the reaction, as it has been reported for [Ni(COD)$_2$].[2,279,280,283,284] Pioneering work in the development of novel Ni(0) sources has been accomplished by Engle and co-workers[279,280] who substituted one COD ligand of [Ni(COD)$_2$] by a duroquinone, quinone, cyclopentadienone, thiophene-S-oxide and fulvene to afford [Ni(COD)(L)] complexes. Similar efforts towards this direction were made very recently by the group of Cornella,[281,282] which developed 16-electron stilbene-based complexes [Ni(stb)$_3$], [Ni($^{4-CF3}$stb)$_3$] (stb = tris(stilbene)), and [Ni($^{4-tBu}$stb)$_3$], which can be handled under ambient conditions.

This work unveils a new Ni(0) source, which can be accessed through an uncommon *in-situ* formation of a fluorophosphine ligand starting from PPO in the presence of a nickel(II) precursor. The application of this exceptional ligand class in nickel complexes unlocks their great potential as catalysts in Suzuki-Miyaura couplings.

7.1   Synthesis of [Ni(PFPh$_2$)$_4$]

Surprisingly, the one-pot reaction of PPO with [Ni(MeCN)$_4$](BF$_4$)$_2$ did not yield an expected PPO/POP-coordinated Ni(II) complex. Instead, a nickel(0) complex of the form [Ni(PFPh$_2$)$_4$] (**24**) was obtained *via* the *in-situ* reduction of the Ni(II) precursor and a simultaneous fluorination of the PPO/POP ligand initiated by the BF$_4^-$ anion. Although several examples of BF$_4^-$ as fluorination agent have been reported in the literature, the fluorination and the subsequent formation of fluorophosphines is only described in very few cases.[262,265] Metal reductions initiated by BF$_4^-$ have been described for Pd(II) and Ni(II) to the zero-oxidation state eliminating the need for reducing agents.[285-290] However, during these reductions, the fluorine itself is not incorporated into the final product and the ligand remains unchanged. To the best of our knowledge, the present example is therefore the first case of a simultaneously occurring fluorination and reduction reaction. This once more underlines the unique reactivity of the POP ligand in presence of transition metal precursors, which leads to the isolation of **24** in 25% crystalline yield through layering of a saturated DCM solution with acetonitrile. The molecular structure was determined by single-crystal XRD and is shown in Figure 43. The tetrahedrally coordinated Ni(0) centre is surrounded by four PFPh$_2$ ligands with P–Ni–P bond angles of 108.732(12)–110.96(2)°, ensuring a 18-electron configuration. The Ni–P bonds show a length of 2.1296(4) Å, which is below the Ni–P bond length in the literature-reported [NiBr$_2$(PF^{t}Bu$_2$)$_2$] (2.232(3) Å).[291] Further comparison of these two structures reveals an extended P–F bond in **24** (1.6465(12) Å) compared to the ^{t}butyl-stabilised fluorophosphine complex. **24** was further characterised by IR spectroscopy and the matching calculated and experimental IR spectra prove the presence of **24** (Figure 56, appendix). The P–F stretch can be identified at a wavenumber of 730 cm^{-1}. Also, ^{31}P{^{1}H} and ^{19}F{^{1}H} NMR spectra confirm the structural integrity of **24** in solution and reveal an AA'A''A'''XX'X''X''' spin system (T_d symmetrisation) which can be identified using automated line-shape analysis. In the ^{31}P{^{1}H} NMR spectrum a multiplet at 173.1 ppm ($^2J_{PP}$ = –23.26 Hz, $^1J_{PF}$ = –850.25 Hz, $^3J_{PF}$ = +45.50 Hz) is detected,

whereas in the $^{19}F\{^1H\}$ NMR spectrum a multiplet appears at a chemical shift of −134.6 ppm ($^1J_{PF}$ = −850.25 Hz, $^3J_{PF}$ = +45.50 Hz, $^4J_{FF}$ = −1.4 Hz). Again, the experimental spectra are in complete agreement with the simulated spectra (Figure 43). The sharp signals point towards the diamagnetic nature of the complex, due to the reduction of Ni(II) to Ni(0), which can further be verified by the absence of a signal in the EPR spectrum. Further confirmation of the purity of **24** comes from elemental analysis, mass spectrometry with electrospray ionisation (ESI-MS, *m/z* calculated for [**24** + H]$^+$ 875.14 [*M*]; found: 875.14) and powder X-ray diffraction measurements, also in comparison with the calculated powder pattern (Figure 57, appendix).
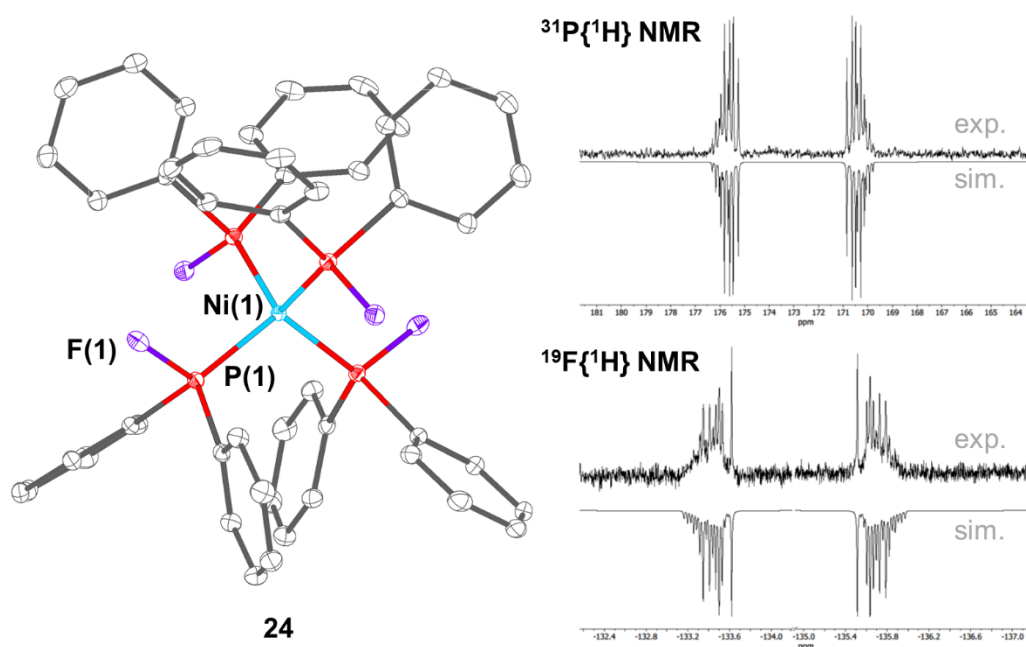

Figure 43. Molecular structure of **24** and recorded and calculated $^{31}P\{^1H\}$ and $^{19}F\{^1H\}$ NMR spectra recorded in C_6D_6. Selected bond lengths (Å) and angles (°): Ni(1)–P(1) 2.1296(4), F(1)–P(1) 1.6465(12), P(1)–C(2) 1.8211(19), P(1)–C(3) 1.8232(19), P(1)–Ni(1)–P(1) 108.732(12)–110.96(2), F(1)–P(1)–Ni(1) 114.97(5), F(1)–P(1)–C(2) 97.42(7), F(1)–P(1)–C(3) 97.17(7), C(2)–P(1)–Ni(1) 117.08(6), C(3)–P(1)–Ni(1) 124.53(6). This figure has been adapted from [292] (license BY NC ND 4.0).

Since alternative Ni(0) sources are required, which are easier to handle than conventionally used [Ni(COD)$_2$], stability studies of **24** were conducted. It becomes obvious, that **24** is highly hydrophobic and consequently insoluble in various solvents, such as water, alcohols, acetone, alkanes, NMP (*N*-methyl-2-pyrrolidone) or DMSO (dimethyl sulfoxide). **24** is partially soluble in ethers, acetonitrile, DCM and benzene. When **24** is stored in these solvents under air over a prolonged amount of time, the oxidation of **24** occurs, leading to the formation of Ph$_2$P(=O)F. However, **24** can be stored in its solid form, in air over months without any detectable degradation. This is an incredible finding since nickel(0) complexes usually suffer from oxidation under air. Furthermore, insights into the heat sensitivity were gained from heating the sample in toluene up to temperatures of 130°C, whereby no structural changes were observed according to NMR spectroscopy. During attempts to determine the melting point, a decomposition temperature of the solid at 161°C could be detected. These findings support the high stability of **24**, which facilitates an easy handling and manipulation especially in comparison with the bench-mark [Ni(COD)$_2$]. The enhanced stability might be a consequence

of the effective space filling of the ligands around the metal centre, as indicated by the space filling diagram (Figure 58, appendix).

7.1.1 Mechanistic discussion for the formation of [Ni(PFPh$_2$)$_4$]

The unique reactivity of PPO/POP in the presence of a nickel(II) precursor, leading to the *in-situ* reduction and fluorination, is most likely a consequence of the uncommon oxidation states present in the PPO ligand. Instead of the common oxidation states +III and + V which can usually be ascribed to phosphines (R$_3$P) and phosphine oxides [R$_3$P(=O)], in PPO formal oxidation states of +IV an +II can be assumed. In the product, however, the phosphorus oxidation state in the fluorophosphine ligands is determined to be +III. To confirm that the combination of a Ni(II) precursor, the BF$_4^-$ anion and the PPO ligand is mandatory for the product formation, PPO was reacted with other BF$_4^-$ salts, namely KBF$_4$, NEt$_4$BF$_4$ and NH$_4$BF$_4$. In none of these reactions the formation of a fluorophosphine species could be observed. This was also not the case, if the analogue Cu salt, [Cu(MeCN)$_4$]BF$_4$, was reacted with the PPO ligand.

To gain further insights into the mechanism, which facilitates this redox-chemistry, and to identify intermediates or by-products, detailed ^{31}P{^{1}H} and ^{19}F{^{1}H} NMR spectroscopic studies were conducted. However, it must be mentioned that the presence of paramagnetic Ni(II) species could not be identified *via* NMR studies, which could be important by-products and intermediates. For the NMR spectroscopic investigation, the stoichiometric ratio of [Ni(MeCN)$_4$](BF$_4$)$_2$:PPO was varied from 1:1, 1:2, 1:4, 1:5 and 1:10 (Figure 44).
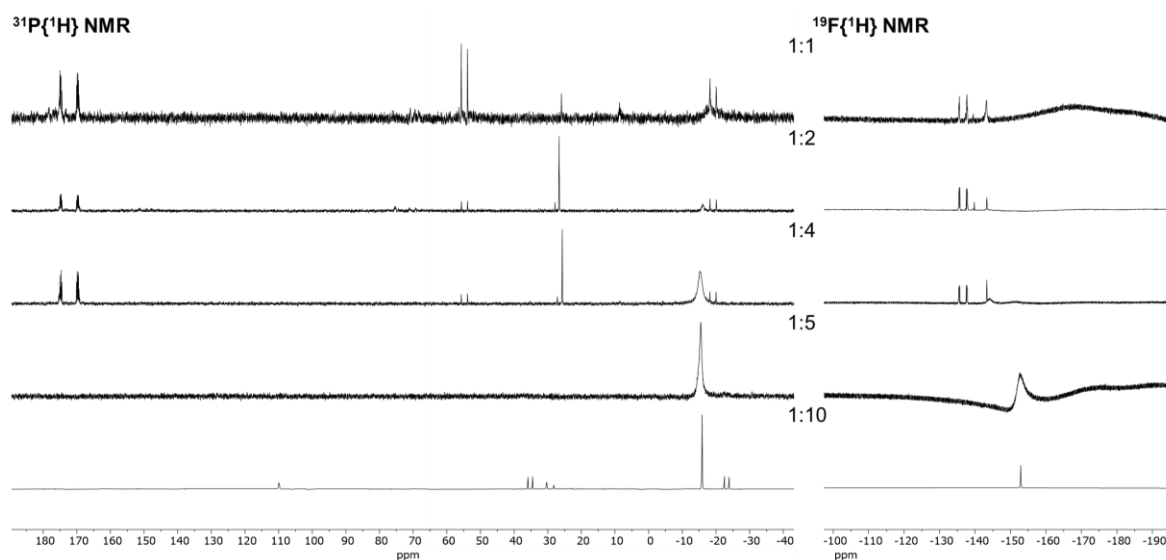
Figure 44. ^{31}P{^{1}H} and ^{19}F{^{1}H} NMR spectra of various stoichiometries of the starting materials [Ni(MeCN)$_4$](BF$_4$)$_2$:PPO in DCM. This figure has been partly adapted from [292] (license BY NC ND 4.0).

For the ratios of 1:5 and 1:10 no fluorination can be detected according to the ^{19}F{^{1}H} NMR spectrum, which shows a sole signal for the BF$_4^-$ anion and no indication towards a fluorophosphine compound. In the ^{31}P{^{1}H} NMR spectrum of the 1:10 mixture, signals are present, which can be attributed to the formation of Ph$_2$P(=O)–O–PPh$_2$ (δ = 108.1, 28.5 ppm) and Ph$_2$P(=O)–P(=O)Ph$_2$ (δ = 26.4 ppm) as well as unreacted PPO. The ^{31}P{^{1}H} NMR

spectrum of the 1:5 mixture reveals that all PPO ligand is converted. However, in this case only one signal can be monitored after 30 minutes which witnesses the formation of Ph_2PPPh_2. (−14.7 ppm, s). If the Ni:PPO ratio is decreased further below 1:5, a different behaviour can be observed, which involves the formation of fluorinated phosphorus compounds, as can be concluded from the occurring coupling patterns in $^{31}P\{^1H\}$ and $^{19}F\{^1H\}$ NMR spectra. In all three approaches, at 1:1, 1:2 and 1:4 ratios, the NMR spectroscopic studies point towards a similar reaction pathway. A broadening of the signals in the approach of 1:1, is highly likely caused by remaining paramagnetic Ni(II) species. However, the formation of the targeted compound **24** can be confirmed by $^{31}P\{^1H\}$ and $^{19}F\{^1H\}$ NMR spectra. Other signals can be assigned again to Ph_2PPPh_2 (−14.7 ppm, s), to tetraphenyl diphosphine dioxide ($Ph_2P(=O)P(=O)Ph_2$, 26.4 ppm, s) and to a PPO-coordinated nickel species (55.5 ppm, d, $^1J_{PP}$ = 301.7 Hz; −18.4 ppm, d, $^1J_{PP}$ = 301.7 Hz), which coordinates to the Ni centre *via* the oxygen of the PPO tautomer. The oxidation state of the Ni centre must be in +II oxidation state, since in presence of the softer Ni(0), an equilibrium shift of the PPO towards the POP tautomer and subsequent coordination *via* the P(III) would be highly likely, as discussed in chapter 3. There is no evidence for the formation of such compound. The $^{19}F\{^1H\}$ NMR spectrum shows other B_xF_y-containing compounds, beside the one of **24**, which cannot clearly be assigned. The NMR studies also suggest that a higher quantity of PPO correlates with an increasing formation of Ph_2PPPh_2 and $Ph_2P(=O)P(=O)Ph_2$. These findings lead to the following conclusions:

1. Two different reactivities result from the conversion of PPO with $[Ni(MeCN)_4](BF_4)_2$, which compete. Either rearrangement reactions at the Ni(II) centre take place or the fluorination of the PPO yielding the $PFPh_2$ ligand occurs.
2. The stoichiometric ratio of the starting materials determines which reaction pathway is favoured, since larger PPO quantities promote exclusively rearrangement reactions. When lower amounts of PPO are used, or more precisely at higher quantities of the fluorination agent BF_4^-, the fluorination and the subsequent formation of the fluorophosphine ligand takes place.
3. Rearrangement reactions at the Ni(II) centre lead to the formation of Ph_2PPPh_2, $Ph_2P(=O)–O–PPh_2$ and $Ph_2P(=O)–P(=O)Ph_2$.

In addition to point three it should be mentioned, that no oxygen-containing sample can be detected in the approach 1:5 with $^{31}P\{^1H\}$ NMR spectroscopy, whereas in the sample of 1:10 signals of $Ph_2P(=O)–O–PPh_2$ and $Ph_2P(=O)–P(=O)Ph_2$ can be identified. It is assumed that in the 1:5 approach the oxygen-containing phosphorus compounds are coordinating to the Ni(II) centre *via* the oxygen resulting in paramagnetic coordination compounds, which are not detectable in the NMR spectra. The oxygen-free Ph_2PPPh_2 does not coordinate to the Ni(II), since the P functionality is too soft to coordinate to Ni(II), which is considered to be rather hard. Therefore, Ph_2PPPh_2 can be identified in the NMR spectra. In the 1:10 sample there are too less Ni(II) coordination sites for all oxygen-containing phosphorus samples, which are present in a large excess. Consequently, $Ph_2P(=O)–O–PPh_2$ and $Ph_2P(=O)–P(=O)Ph_2$ are released into solution and can be monitored by NMR spectroscopy.

After one day of reaction time, new signals appear in the $^{31}P\{^1H\}$ and $^{19}F\{^1H\}$ NMR spectra for the stoichiometric ratios 1:1, 1:2 and 1:4, which can be assigned to a F- and P-containing by-

product (^{31}P{^{1}H} NMR: 32.7 ppm, q, $^3J_{PF}$ = 10.3 Hz and ^{19}F{^{1}H} NMR: 139.7 ppm, t, $^3J_{PF}$ = 10.3 Hz). These signals are becoming more intense with longer reaction times. It should be underlined that this species does not form in the 1:5 and 1:10 reactions, which again strongly indicates, that two competing reactivities can be initiated from the reagents and that compound **24** does not result from the rearrangement pathway. Attempts to isolate this before mentioned compound were successful by layering the DCM reaction mixture with *n*-pentane. Single-crystal XRD analysis of colourless crystals revealed the formation of Ph$_2$PO$_2$(BF$_2$)$_2$O$_2$PPh$_2$ (**25**). Besides, a second colourless by-product could be crystallised from this reaction mixture, which was identified as [Ni(OPOPh$_2$)$_6$(BF)$_2$] (**26**) (Figure 45). Since both by-products are highly soluble in acetonitrile, whereas **24** is nearly insoluble, the by-products could be easily separated by washing **24** with acetonitrile.
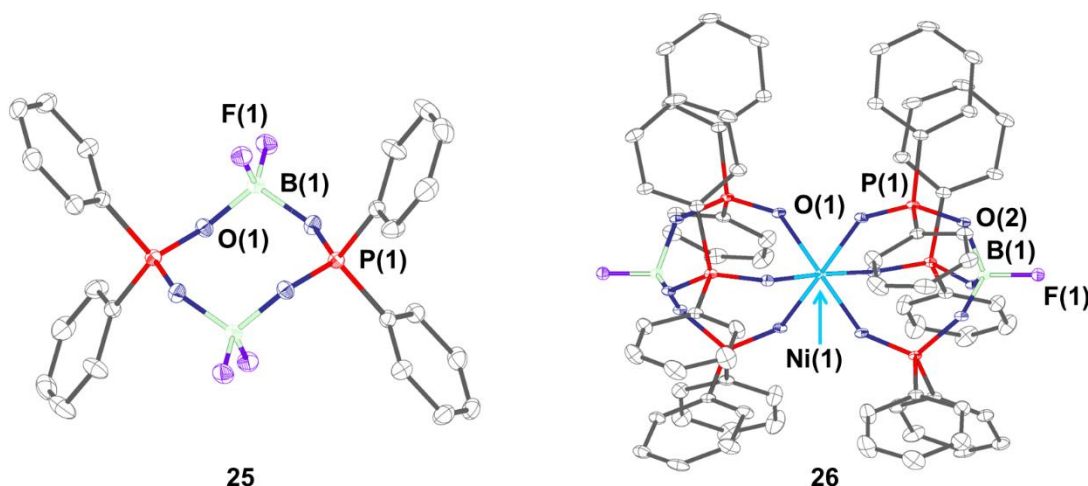
Figure 45. Molecular structures of compounds **25** and **26,** which can be isolated as by-products from the synthesis of **24.** Selected bond lengths (Å) and angles (°): **25**: C(1)–P(1) 1.7816(11) C(7)–P(1) 1.7787(12) B(1)–F(1) 1.3800(15) B(1)–F(2) 1.3586(14) B(1)–O(1) 1.4910(14) B(1)–O(2) 1.4960(15) O(1)–P(1) 1.5314(8) O(2)–P(1) 1.5360(8) F(1)–B(1)–O(1) 110.01(10) F(1)–B(1)–O(2) 109.70(9) F(2)–B(1)–O(1) 108.68(10) F(2)–B(1)–O(2) 108.25(9) B(1)–O(1)–P(1) 129.40(7)–129.81(7) C(7)–P(1)–C(1) 110.32(5) O(1)–P(1)–O(2) 115.16(5) **26**: Ni(1)–O(1) 2.0501(13)–2.0502(13) B(1)–F(1) 1.369(4) C(1)–P(1) 1.797(2) C(7)–P(1) 1.793(2) P(1)–O(1) 1.4867(13) P(1)–O(2) 1.5566(14) O(2)–B(1) 1.4776(18) F(1)–B(1)–O(2) 108.59(15)–108.59(15) B(1)–O(2)–P1 132.46(15) O(2)–P(1)–O(1) P(1)–O(1)–Ni(1) 144.24(9). This figure has been adapted from [292] (license BY NC ND 4.0).

In both by-products **25** and **26**, the anionic ligand Ph$_2$POO$^-$ is incorporated. In the metal-free species **25** two Ph$_2$POO$^-$ ligands are bridged *via* a BF$_2$ unit on each side. In **26**, the central Ni(II) atom is octahedrally coordinated by six Ph$_2$POO$^-$ ligands, whereby on each side three ligands are terminated by one BF^{2+} unit. Another common feature of **25** and **26** is the tetrahedral coordination of the boron, which offers high stability of these compounds through the coordination of the p-orbital. Compound **26** has been isolated before from a reaction of [Ph$_3$CP(H)Ph$_2$][BF$_4$] and NiCl$_2$ in DCM whereby oxygen has to stem from air-contamination.[293] However, the authors identified this compound as [Ni(OP(H)Ph$_2$)$_6$(BF$_4$)$_2$] whereby the outer oxygen atoms in **26,** in between the B and P atoms, were falsely determined to be F atoms as part of BF$_4^-$ units. Therefore, the ligands are required to be protonated to be neutral for a reasonable balance of the compound's overall charge as reported by the authors. This

strongly contradicts the nearly ideal tetrahedral coordination geometry of the P atoms. Hence, there is not enough space for hydrogen atoms and with a negative ligand Ph_2PO^-, the overall charge would be –6, if nickel was in the +2 oxidation state. In **26** the negatively charged ligands are balanced by the two BF^{2+} units and the central Ni(II) atom. The real identity of these atoms to be oxygen can additionally be confirmed by the Hirshfeld analysis with which a large difference of the anisotropic displacement parameters is determined if the atoms were fluorine atoms. This indicates that the assignment of the atoms has to be wrong in the earlier report of this compound.[293] Reasonable values can be obtained if the F atoms are replaced by O atoms confirming the nature of **26**. Both by-products show similar solubilities in different solvents and a separation of the two compounds appears to be not feasible especially since both are crystallising under the same conditions. Consequently, NMR spectroscopic studies had to be conducted for the compound mixture. Whereas, signals of **25** can be clearly identified in the $^{31}P\{^1H\}$ NMR (33.6 ppm, m, $^3J_{PF}$ = 10.9 Hz) and $^{19}F\{^1H\}$ NMR spectrum (139.9 ppm, m, $^3J_{PF}$ = 10.9 Hz), no signal of **26** can be detected in the $^{31}P\{^1H\}$ spectrum, due to the paramagnetic nature of Ni(II). However, in the $^{19}F\{^1H\}$ spectrum compound **26** shows a signal at 147.2 ppm ($^1J_{BF}$ = 11.0 Hz). It is noteworthy that the two by-products do react further in the solvent resulting in the formation of $Ph_2P(=O)F$ ($^{31}P\{^1H\}$ NMR: 40 ppm, d, $^1J_{PF}$ = 1020 Hz; $^{19}F\{^1H\}$ NMR: –75.2 ppm, d, $^1J_{PF}$ = 1020 Hz). Similar observations have been made by Miller *et al.*[294] who described the deoxyfluorination of the protonated ligand, Ph_2POOH, yielding $Ph_2P(=O)F$ in presence of a base and a fluorination agent. Since both by-products contain a $BF_{x,\ (x\ =\ 1,\ 2)}$ fragment and no evidence for similar compounds can be found in the reaction approaches of the 1:5 and 1:10 mixtures, the formation of the compounds **25** and **26** can unambiguously be assigned to the fluorination pathway. Consequently, Ph_2POO^- can be considered as the oxygen-containing counterpart of the oxygen-free fluorophosphine. The presence of the BF_2^+- and the BF^{2+}-unit reveals a stepwise fluorination caused by the BF_4^- anion within the nickel precursor.

Based on the identified by-products and correlations of the compounds, the mechanism presented in Scheme 6 can be proposed for the exceptional reactivity of $[Ni(MeCN)_4](BF_4)_2$ and PPO, which finally results in the formation of the fluorophosphine Ni(0) complex **24**. In this context it must be mentioned that several attempts to decrease the degree of competing rearrangement reactions through the variation of the reaction temperature or speed of addition of the reagents were pursued. However, no modification of these parameters appeared to efficiently influence the reaction outcome.
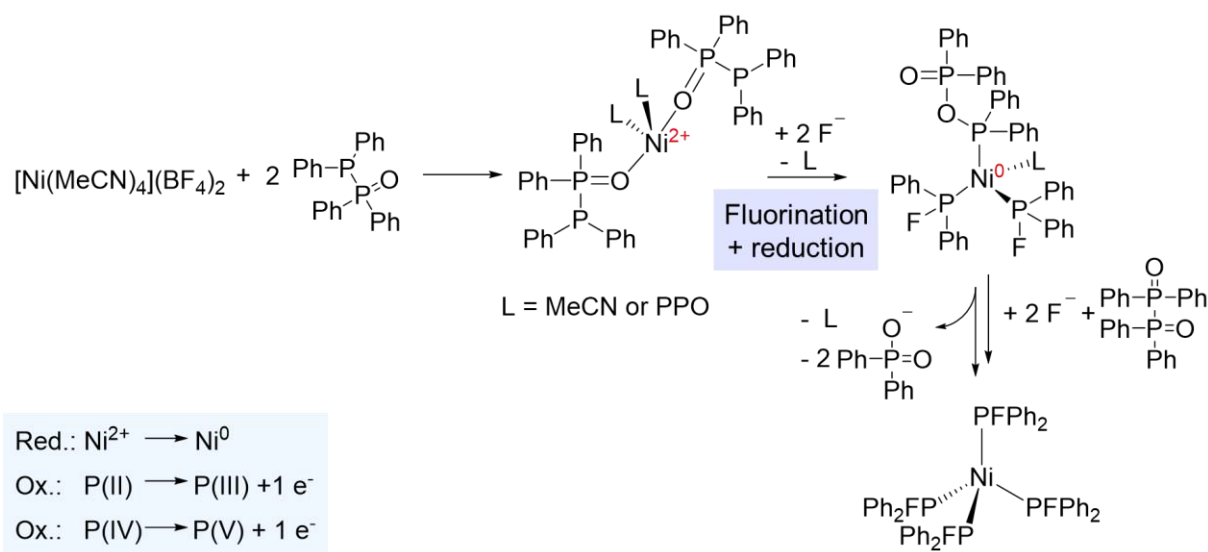
Scheme 6. Proposed mechanism for the formation of **24** starting from PPO and [Ni(MeCN)$_4$](BF$_4$)$_2$. This scheme has been partly adapted from [292] (license BY NC ND 4.0).

As part of the formation of **24**, the PPO ligand coordinates to the Ni(II) centre *via* the harder oxygen functionality in the first step. Starting from this species, the decisive step of the simultaneous fluorination and reduction of Ni(II) to Ni(0) is initiated. Two PPO ligands are required for this step, which includes the P–P bond cleavage within the ligand since two electrons have to be transferred to the central Ni(II) ion. The fragment containing the P(II) atom is fluorinated and the P atom is oxidised to P(III). The two Ph$_2$P(=O) fragments combine forming Ph$_2$P(=O)P(=O)Ph$_2$, which is also known to show a characteristic tautomerism with the Ph$_2$P(=O)–O–PPh$_2$ tautomer. It should be underlined that the two oxygen-containing phosphorus fragments are not affected by the redox-chemistry up to this step since they keep in average the formal oxidation state of +IV. However, this compound shifts to its tautomeric Ph$_2$P(=O)–O–PPh$_2$ form with the oxidation states of the two phosphorus atoms of +V and +III. It is most likely that this compound coordinates to the Ni(0) *via* its soft P(III) functionality. In a next step, the P(III) can be fluorinated, under cleavage of the P–O bond liberating Ph$_2$POO$^-$, which was identified *via* NMR spectroscopic studies as well as by the isolated crystals of compounds **25** and **26**. The last step has to be repeated for the production of the final product **24**. Thus, the uncommon oxidation states of the phosphorus atoms in PPO are a key factor for this unique reactivity whereby the fluorine atom is incorporated into the final product. This is in contrast to other reported BF$_4^-$ reductions with phosphine ligands which do not involve a simultaneous fluorination.

7.2 Theoretical investigations

To gain further insights into the donor or acceptor properties of this fluorophosphine ligand, DFT calculations were carried out to determine the Tolman electronic parameter (TEP).[126] The theoretical determination of the TEP is highly beneficial to circumvent the usage of highly toxic [Ni(CO)$_4$] and since experimental procedures are often time-consuming and challenging since the targeted species [Ni(CO)$_3$L] has to be produced selectively, isolated and spectroscopically characterised. Instead DFT calculations provide the required parameter, namely the symmetric A1 carbonyl vibration, much more easily. Therefore, TEP's for literature known

phosphines as well as for the diphenylfluorophosphine ligand have been calculated (Figure 46).
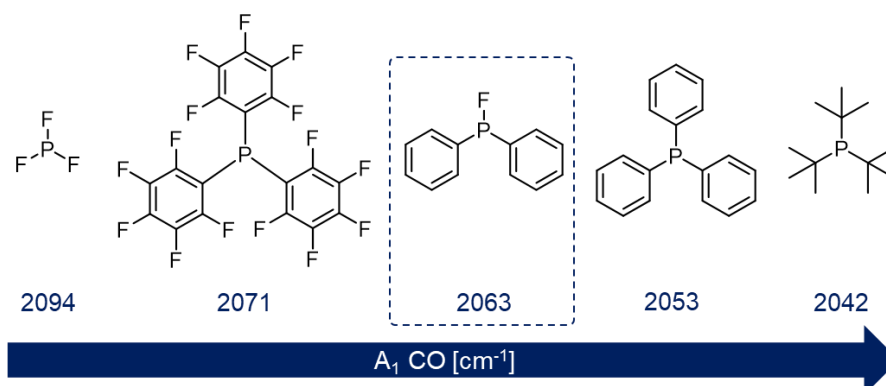
Figure 46. Tolman's electronic parameter of the fluorophosphine ligand present in **24** in comparison to other known phosphines. This figure has been adapted from [292] (license BY NC ND 4.0).

To achieve a proper classification of the $PFPh_2$ donor strength, extremes for other phosphines have been selected, which show either strong π-backbonding properties, such as PF_3 or strong σ-donating properties, such as $P(^tBu)_3$. In addition, widely applied phosphines, $P(C_6F_5)_3$ and PPh_3, were chosen for a comparison. With a TEP of 2063 cm^{-1}, $PFPh_2$ is positioned in the centre of these phosphines and can therefore be mainly considered as π-acceptor. Thus, the ligand opens the possibility for new reactivities and applications of the respective coordination compounds, which can be especially advantageous if the coordination compound is applied in catalysis.

Furthermore, computational investigations concentrated on the comparison of compound **24** with other literature known Ni(0) sources, based on population analysis and calculations of the degree of backbonding from d-orbitals of the Ni-centre to the ligands (Figure 47). Therefore, [Ni(COD)$_2$], as the most frequently used Ni(0) source as well as advanced compounds from the last years, namely [Ni(COD)L] (L = 2,3,4,5-tetraphenylthiophene-1-oxide) and [Ni(^{F}stb)$_3$] (^{F}stb = *trans*-1,2-bis(4-(trifluoromethyl)phenyl)ethene) were selected.[279,282,295]
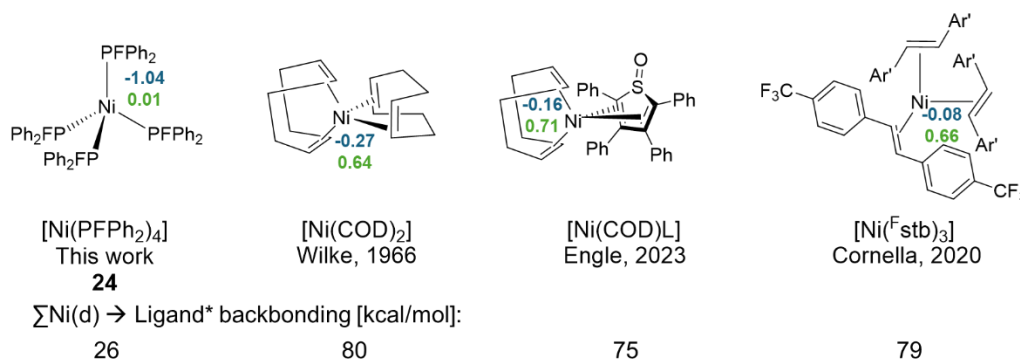
Figure 47. Computational investigation of **24** along with other Ni(0) complexes. Loewdin charges from Loewdin population analysis are marked in blue and natural charges from natural population analysis are highlighted in green. The sum of the Ni(d) to ligand* backbonding, obtained from second order perturbation analyses, is shown (B3LYP/def2-TZVP).[202-205] This figure has been adapted from [292] (license BY NC ND 4.0).

All reference Ni(0) sources show high similarities regarding Loewdin and natural charges as well as the degree of backbonding from metal d-orbitals to the ligand. It becomes obvious that the fluorophosphine ligand leads to a tremendously different electron distribution in the fluorophosphine-stabilised Ni(0) complex. A significantly more negative charge can be determined for the Ni(0) centre, which correlates with a strong decrease in π-backbonding of about 50 kcal mol^{-1} compared to the olefin-stabilised Ni(0) complexes. Based on the high electron density, which is mainly localised at the Ni(0) centre, alternative reactivities compared to the other state of the art Ni compounds can be expected, which can be particularly favourable for catalytic applications.

7.3 Ligand exchange studies

To explore the catalytic potential of **24** as alternative Ni(0) source, initially the behaviour of this compound in solution under different conditions was investigated. Other [Ni(0)L$_4$] complexes are known to dissociate one ligand in solution yielding three-coordinate [NiL$_3$], which could be one option to offer a vacant site for substrate binding in catalysis.[126,296,297] Such a behaviour can neither be observed for **24** at room temperature nor at higher temperatures. In a next step the solution-behaviour of **24** under UV light was studied, whereby the formation of dark nickel(0) particles could be observed. NMR spectroscopic studies reveal the formation of PF$_3$Ph$_2$ and Ph$_2$P–PF$_2$Ph$_2$, which are known disproportionation products of the free ligand (Figure 48). The UV-initiated degradation can be monitored by UV/Vis absorption spectroscopy, which matches with TD-DFT calculated spectra of the Ni complex and of the final degradation products (Figure 59). Therefore, the UV radiation can be considered as potential strategy for creating vacant coordination sites at the Ni centre through ligand degradation. However, it has to be ensured that the homogeneous nature of the nickel complex remains intact and no agglomeration to nickel particles occurs due to an insufficient stability.
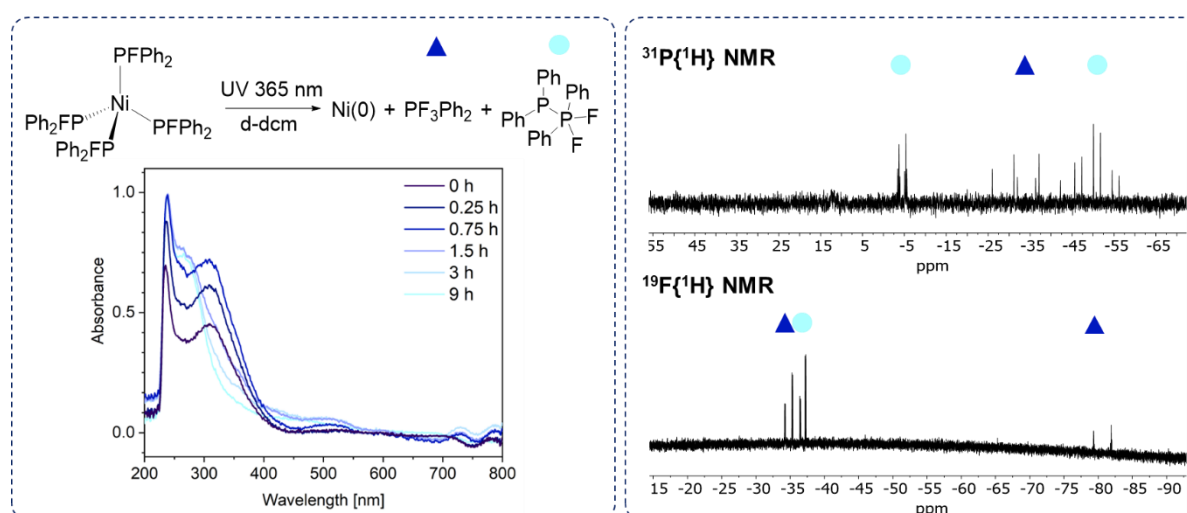

Figure 48. UV/Vis-induced degradation of the fluorophosphine-stabilised Ni(0) complex **24**. The degradation can be monitored by UV/Vis absorption spectroscopy and by NMR spectroscopic studies. This figure has been adapted from [292] (license BY NC ND 4.0).

To increase the stability of the, from UV radiation, resulting Ni(0) species, ligand substitution reactions of **24** were attempted in C_6D_6 with 4 equivalents of monodentate and 2 equivalents of bidentate ligands. Firstly, the potential ligand exchange at room temperature was investigated, followed by elevated temperatures of 100°C and ultimately the impact of UV radiation (365 nm) was studied. The need for an activation step, such as the elevated temperature or UV radiation, is often reported for Ni(0) compounds, since strong Ni–P bonds are formed with Ni(0) centres. In contrast, for Ni(II) compounds ligand dissociations often require less energy due to weaker Ni–P bonds.[269] All studies were monitored by NMR spectroscopy. 1,5-cyclooctadiene (COD), triphenyl phosphine (PPh₃), 1,2-bis(diphenylphosphino)ethane (dppe), 1,1'-bis(diphenylphosphino)ferrocene (dppf) and 2,2'-bis(diphenylphosphino)-1,1'-binaphthyl (BINAP) were the candidates for ligand exchange reactions, since all of them are known to exhibit great properties in catalysis (Figure 49).[2]

If PPh₃ is added to **24**, no change can be observed at room or elevated temperature. Thus, UV radiation (365 nm) was applied and indeed, this causes the ligand dissociation from **24** as well as subsequent ligand substitution, as it can be concluded from the NMR spectra. Firstly, signals of the disproportionation products, PF₃Ph₂ (^{31}P{^{1}H} NMR: –34.8 ppm, 2t, $^1J_{PF, eq}$ = 973.1 Hz, $^1J_{PF, ax}$ = 832.4 Hz; ^{19}F{^{1}H} NMR: –34.1 ppm, dd, $^1J_{PF, ax}$ = 832.4 Hz, $^2J_{FF}$ = 39.5 Hz, –79.8 ppm, dt, $^1J_{PF, eq}$ = 973.1 Hz, $^2J_{FF}$ = 39.5 Hz) and Ph₂P–PPh₂ (^{31}P{^{1}H} NMR: –14.9 ppm, s), can be observed, which confirm the successful PFPh₂ dissociation. The proof, that the Ni(0) centre can be stabilised through coordination of PPh₃ is given by the signal at 25 ppm, which can be assigned to the coordinated PPh₃ ligand. The monodentate nature of PPh₃ leads to a dynamic solution behaviour and fast dissociation and association of the PPh₃, which can be seen from the broadened signal of free PPh₃ (–5 ppm) as well as by the occurrence of various signals in the area of **24** (around 170 ppm), due to different numbers of ligands attached to Ni(0) in $[Ni(PFPh_2)_x(PPh_3)_y]$.
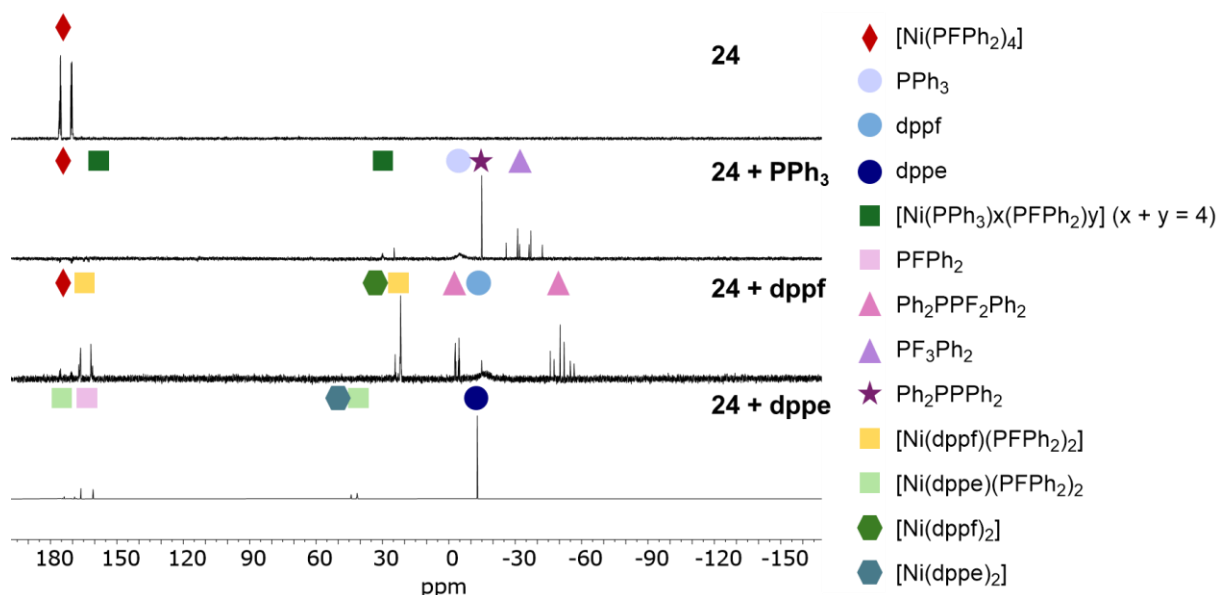

Figure 49. Investigation of ligand exchange of **24** with PPh₃, dppf and dppe by ^{31}P{^{1}H} NMR spectroscopy. Products of the studies are marked. For PPh₃ and dppf, ligand exchange can be achieved through UV radiation (365 nm), while heat (100°C) is sufficient in the case of dppe. This figure has been partly adapted from [292] (license BY NC ND 4.0).

Also with dppf, UV light is required to initiate ligand exchange reactions (Scheme 7). Hereby, the disproportionation of PFPh$_2$ results in the formation of Ph$_2$P–PF$_2$Ph$_2$ (^{31}P{^{1}H} NMR: –4.1 ppm, dt, $^1J_{PaPb}$ = 269.1 Hz, $^2J_{PaF}$ = 43.3 Hz; –51.4 ppm, 2t, $^1J_{PaPb}$ = 269.1 Hz, $^1J_{PbF}$ = 724.3 Hz; ^{19}F{^{1}H} NMR: –35.1 ppm, dd, $^2J_{PaF}$ = 43.3 Hz, $^1J_{PbF}$ = 724.3 Hz). Interestingly, no PF$_3$Ph$_2$ formation can be observed as in the case of PPh$_3$. The different degradation products can be attributed to larger number of PFPh$_2$ molecules involved in the disproportionation in the presence of PPh$_3$ than in the case of dppf, due to the higher dynamic nature of the monodentate PPh$_3$ ligand. As reported by Haenel and Riesel,[257] the disproportionation reaction of two PFPh$_2$ molecules yields Ph$_2$P–PF$_2$Ph$_2$, whereas involvement of a third molecule results in the production of Ph$_2$P–PPh$_2$ and Ph$_2$PF$_3$. At the cost of two PFPh$_2$ ligands, one dppf coordinates to the metal centre providing [Ni(PFPh$_2$)$_2$(dppf)] (^{31}P{^{1}H} NMR: 164.0 ppm, m; 21.7 ppm, m; ^{19}F{^{1}H} NMR: –130.4 ppm, m). Minor amounts of [Ni(dppf)$_2$] (^{31}P{^{1}H} NMR: 24.2 ppm, s) are detected, deriving from complete ligand substitution. It should be mentioned that such species were reported to be catalyst sinks, decreasing the overall catalyst performance.[2] Therefore it is noteworthy that, despite the stoichiometry (1:2 Ni:ligand), only trace amounts of these potential catalyst sinks are formed.
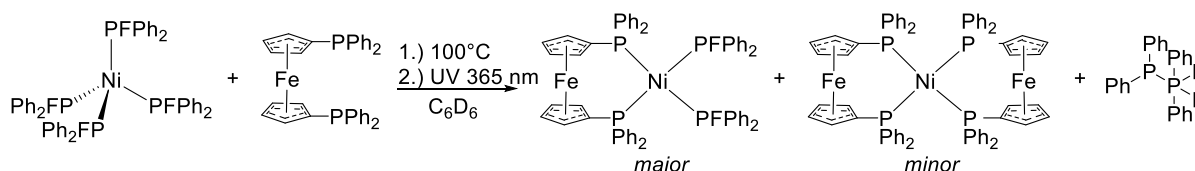
Scheme 7. Ligand exchange of **24** with dppf. Through UV radiation (365 nm), ligand exchange can be initiated forming majorly [Ni(PFPh$_2$)$_2$(dppf)] and minor quantities of [Ni(dppf)$_2$]. The dissociating ligand is disproportionated in solution forming Ph$_2$P–PF$_2$Ph$_2$.

Remarkably, for dppe ligand substitution can already be accomplished at a temperature of 100°C resulting in [Ni(PFPh$_2$)$_2$(dppe)] (^{31}P{^{1}H} NMR: 171.2 ppm, m; 41.4 ppm, m; ^{19}F{^{1}H} NMR: –128.6 ppm, m). In this case also, trace amounts of [Ni(dppe)$_2$] (^{31}P{^{1}H} NMR: 44.1 ppm, s), due to complete ligand substitution, can be observed. Since no UV radiation is required for the promotion of the ligand exchange, the intact PFPh$_2$ ligand can be detected (^{31}P{^{1}H} NMR: 163.5 ppm, d, $^1J_{PF}$ = 884.3 Hz and ^{19}F{^{1}H} NMR: –195.4 ppm, d, $^1J_{PF}$ = 884.3 Hz).
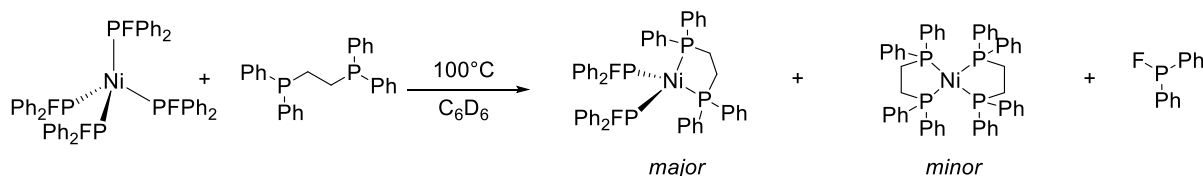
Scheme 8. Ligand exchange of **24** with dppe. A temperature of 100°C is sufficient for ligand exchange forming majorly [Ni(PFPh$_2$)$_2$(dppe)] and minor quantities of [Ni(dppe)$_2$]. The dissociating PFPh$_2$ ligand remains intact.

With COD, neither in the ^{31}P{^{1}H} nor in the ^{1}H NMR spectrum, changes in the nature of **24** or formation of [Ni(COD)$_2$] could be observed, despite heating and UV radiation. Only in the highly sensitive ^{19}F{^{1}H} NMR spectrum, minor amounts of new signals in the area of **24** can be observed, which could stem from very small percentages of ligand exchange products. The

addition of the BINAP ligand to **24** showed similar results, since only minimal quantities of signals, which could be assigned to a complex with different ligands and degradation products PF_3Ph_2 and $Ph_2P–PF_2Ph_2$ of $PFPh_2$, can be detected.

7.4   Catalytic application of [Ni(PFPh₂)₄] in Suzuki-Miyaura coupling reactions

The tendency of fluorophosphine ligands to disproportionate leads to the fact that their application in catalysis has been widely overlooked. There is, to the best of our knowledge only one example of a fluorophosphine in catalysis. Fey *et al.* tested sterically constrained fluorophosphine ligands CgPF (Cg = phosphatrioxa-adamantane cage) and PhobPF (Phob = phobane) in Ni- and Rh-complexes along with the $^tBu_2PF$ ligand as catalysts in hydroformylation and hydrocyanation reactions.[249] Through the application of fluorophosphine ligands either comparable or even better performance than the industrially relevant catalysts could be achieved. The use of fluorophosphines for C–C coupling reactions has never been described but will be as part of this work. In the field of C–C coupling reactions, increasing importance is ascribed to the development of new catalysts based on nickel instead of the more expensive and less abundant element palladium, due to alternative reaction pathways and activation of new substrates, which can be achieved with nickel.[268,273,298] [Ni(PFPh₂)₄] (**24**) is expected to show promising catalytic behaviour due to the zero-oxidation state of nickel, which opens a direct access into the catalytic cycle and facilitates the exploration of a new ligand class in C–C coupling reactions. In this work, the catalytic potential of **24** as (pre-)catalyst was tested in the example of Suzuki-Miyaura coupling reactions of aryl halides with boronic acids in presence of the base K_2CO_3 (Scheme 9).

The reaction of phenyl boronic acid with iodobenzene was first investigated for **24** (2.5 mol%), without the addition of any stabilising ligand, at room temperature without and with initial 15 minutes of UV radiation at 365 nm (Table 11, entry 1 and 2). At room temperature no conversion could be observed. Therefore, the reaction was repeated at elevated temperatures (100°C), again with and without UV radiation. Indeed, conversions of 60% (without UV) and 72% (with UV radiation) could be achieved (Table 11, entry 3 and 4). However, as it had already been observed in the stability studies of **24** under UV light, the formation of Ni(0) black can be witnessed which might lead to either the formation of a heterogenous catalyst or to catalyst deactivation.
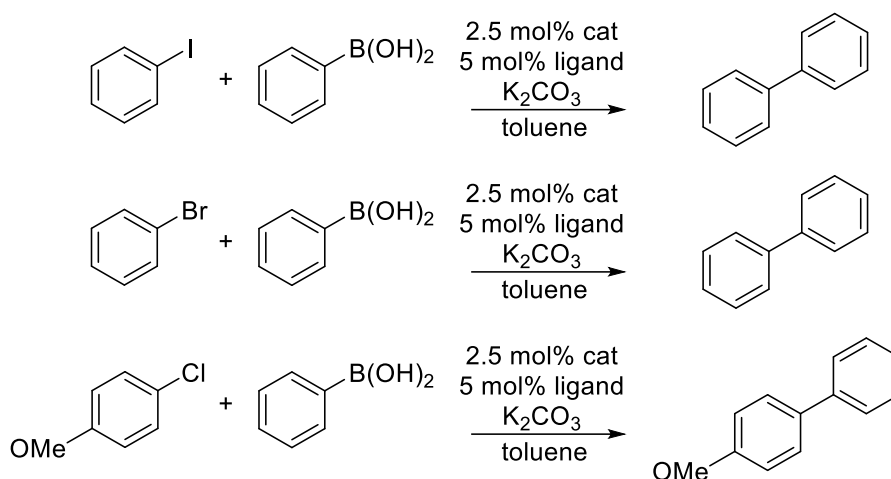
Scheme 9. Application of **24** as (pre-)catalysts in Suzuki-Miyaura couplings of aryl halides with phenylboronic acids (1.5 eq.). Reaction conditions: 2.5 mol% catalyst, 5 mol% ligand, 3 equivalents K_2CO_3, toluene as solvent and *n*-decane as internal standard. Samples were exposed to UV light (365 nm, 15 min) and heated to 100°C for 14 h. Conversions of arylhalides were determined by GC-MS.

To counteract the catalyst degradation, additional ligands, such as PPh_3, dppf and dppe (5 mol%, ligand:Ni(0) = 2:1) were added to the reaction mixture, since these phosphines were shown to confer stability towards the Ni(0) centre in ligand exchange studies. As described above, the initiation of the ligand exchanges requires either elevated temperatures for dppe or UV radiation for PPh_3 and dppf. Samples with dppe can also be activated by UV radiation (Table 11, entry 6 and 7). To ensure sufficient UV activation, the samples were irradiated with UV light (365 nm) for 15 minutes prior to heating up to 100°C (Table 11, entry 5, 7, 10). However, it becomes obvious, that with dppe and PPh_3, the addition of external ligands results in a drop of conversion of aryl halide. Especially with dppe conversions of only 22% are obtained (**24**, without ligand addition: 72% conversion), which might be attributed to a high stability of the dppe complex since the ligand seems to have a high tendency to coordinate to the Ni(0) centre. Nonetheless, with PPh_3 and dppe the stability of the nickel species can be increased compared to the ligand-less approaches. The addition of dppf provides a different outcome since a significant increase in catalytic activity can be achieved along with enhanced catalyst stability, resulting in full conversion of the starting material (Table 11, entry 10). Through the application of the initial UV radiation protocol, an improvement of 20% in conversion can be achieved (Table 11, entry 8) and higher temperatures are required to achieve reasonable conversion since with UV activation and a reaction at room temperature a conversion of only 13% can be witnessed (Table 11, entry 9). Control experiments were conducted to exclude any catalytic influence of the pure dppf ligand showing no conversion in absence of the Ni(0) source (Table 11, entry 12-15). Furthermore, the addition of the base is required since otherwise insufficient catalyst regeneration occurs and no conversion can be detected (Table 11, entry 11). These results already point towards an efficient catalytic performance of **24** as pre-catalyst in Suzuki-Miyaura coupling reactions.

Table 11. Nickel-catalysed Suzuki-Miyaura coupling reactions. Reaction conditions: 2.5 mol% catalyst, 5 mol% ligand, 3 equivalents K_2CO_3, toluene as solvent and *n*-decane as internal standard. Activation conditions are mentioned in the table whereby UV is defined as 15 minutes of UV radiation (365 nm) prior to heating up. The reactions were conducted for 14 h. Conversions of arylhalides were determined by GC-MS.

Entry	Ni(0) source	Ligand	Conditions	Conv. [%]	Entry	Ni(0) source	Ligand	Conditions	Conv. [%]
1	**24**	-	r.t.	0	9	**24**	dppf	UV	13
2	**24**	-	UV, r.t.	0	10	**24**	dppf	UV, 100°C	100
3	**24**	-	100°C	60	11	**24** [a]	dppf	UV, 100°C	0
4	**24**	-	UV, 100°C	72	12	-	dppf	r.t.	0
5	**24**	PPh$_3$	UV, 100°C	47	13	-	dppf	UV, r.t.	0
6	**24**	dppe	100°C	22	14	-	dppf	100°C	0
7	**24**	dppe	UV, 100°C	18	15	-	dppf	UV, 100°C	0
8	**24**	dppf	100°C	80	16	**24** [b]	dppf	UV, 100°C	81

[a] in absence of K_2CO_3 [b] with addition of COD (COD:**24** = 2:1)

In a next step, the substrate scope of aryl halides was extended towards bromide- and chloride-containing compounds, since the activation of stronger C–Br and C–Cl bonds is in general more challenging (bond dissociation energies *D* [kcal mol^{-1}]: C–I = 65; C–Br = 81; C–Cl = 96; C–F = 126).[299,300] On the basis of the initial catalyst tests, for these reactions the activation procedure based on UV light radiation and heat was applied. Besides iodobenzene, bromobenzene and 4-chloroanisole were chosen as substrates (Table 12). The catalytic performance regarding bromobenzene is very similar to the one observed for iodobenzene, showing a decrease in conversion for approaches with PPh$_3$ and dppe, whereas the addition of dppf gives a conversion of 100%. The activation of aryl chlorides is often challenging due to a low reactivity of these substrates. Therefore, there is an urge to find alternative catalysts, which are capable of activating C–Cl bonds. Complex **24** appears to be suitable for this reaction, however, in comparison with the bromide and iodide counterparts, a slight decrease in conversion can be observed. The addition of dppf again provides superior results showing a conversion of 72%. Due to the substituent of 4-chloroanisole, the selectivity of this reaction can be evaluated. Hereby it was shown that the addition of other phosphine ligands is mandatory to achieve a selective product formation. Without the addition of an additional phosphine, the selectivity drops to only 63%. In presence of stabilising ligands, the selective conversion of phenylboronic acid and 4-chloroanisole to afford 4-methoxy biphenyl can be accomplished, whereby the use of **24** in combination with dppf outperforms the other catalytic systems showing a selectivity of 95%.

For a better interpretation of the catalytic tests data concerning **24**, comparison experiments were conducted under the same conditions with the well-established [Ni(COD)$_2$] (Table 12, entry 5-8). Pure [Ni(COD)$_2$], in absence of any additional ligand added, revealed a poor

catalytic activity, whereby only C–I bonds could be activated. This already underlines the different activities of **24** and [Ni(COD)$_2$]. In analogy to experiments conducted with **24**, also in the case of [Ni(COD)$_2$] phosphine ligands were added, resulting in an enhanced catalytic performance in the case of PPh$_3$ and dppf, whereas with dppe comparable behaviour as reported for the pure Ni(0) source was detected. In analogy to **24**, dppf was shown to strongly outperform the other ligands whereby double the conversions can be achieved for dppf compared to PPh$_3$ for all three aryl halides. Whereas in the case of [Ni(COD)$_2$] the ligands denticity had an impact on the selectivity, similar findings were not made in the case of **24**, as with PPh$_3$ and dppf similar selectivities could be achieved. The comparison of the systems based on **24** or [Ni(COD)$_2$], shown in Table 11 and Table 12, highlights the remarkable potential which can be achieved with the widely-overlooked class of fluorophosphines in catalysis and might be a result of the unique electronic properties initiated by this uncommon ligand class. Another impact factor which should not be neglected is the effect of the liberated ligands on the catalysis. It is well-known that the liberated COD can inhibit the catalytic performance and act as catalyst poison.[2,301,302] As UV/Vis absorption and NMR spectroscopic studies have revealed, liberated ligands of **24** are further degraded. Therefore, a blocking of the active sites by fluorophosphines ligands can be circumvented. To investigate the impact of COD, this compound was added to the reaction mixture of an approach using **24** and dppf. Interestingly, the conversion decreases to a value of 81%, confirming the blocking of active sites through COD (Table 11, entry 16).

Table 12. Suzuki-Miyaura couplings of phenylboronic acid (1.5 eq.) and iodobenzene, bromobenzene or 4-chloroanisole without and with additional ligands (PPh$_3$, dppe, dppf) addition. Reaction conditions: 2.5 mol% catalyst, 5 mol% ligand, 3 eq. K$_2$CO$_3$, solvent: toluene and *n*-decane as internal standard. For the activation, samples were exposed to UV light (365 nm) for 15 mins and subsequently heated to 100°C for 14 h. Conversions of aryl halides were determined *via* GC-MS and the selectivity towards 4-methoxy biphenyl is calculated. For the reactions of phenylboronic acid with iodo- and bromobenzene biphenyl is obtained in 100% selectivity. This table has been adapted from [292] (license BY NC ND 4.0).

Entry	Ni(0) source	Ligand	Conv. [%] I-benz.	Conv. [%] Br-benz.	Conv. [%] Cl-anisole	Select. [%] product
1	**24**	-	72	82	21	63
2	**24**	PPh$_3$	47	42	35	92
3	**24**	dppe	18	0	0	0
4	**24**	dppf	100	100	72	95
5	[Ni(COD)$_2$]	-	15	0	0	0
6	[Ni(COD)$_2$]	PPh$_3$	31	27	24	62
7	[Ni(COD)$_2$]	dppe	20	0	0	0
8	[Ni(COD)$_2$]	dppf	82	52	56	99
9	-	-	0	0	0	0

To widen the substrate scope and test functional group tolerance of **24**-based systems, Suzuki-Miyaura couplings of various bromo halides and phenyl boronic acids were investigated (Scheme 10). Therefore, the best-performing system based on **24** and dppf was applied as catalyst for reaction times of 14 h at 100°C in the presence of K_2CO_3. For phenylboronic acids, the effect of an introduced methyl group and of a Cl-substituent were evaluated. Hereby, no impact of the methyl group could be observed since complete conversion yields the product in high selectivity (99%). The introduction of a chloro substituent, however, results in a distinct drop in conversion and poor selectivity. On the other hand, changes of the aryl halide were investigated. Despite the presence of an electron withdrawing group, such as in 4-bromo acetophenone, high conversions of 82% can be accomplished using **24**/dppf with 99% selectivity. However, the conversion of 1-chloro-2-nitrobenzene with phenylboronic acid did not succeed, which might be due to the higher stability of the C–Cl bond and deactivating contributions of the electron-withdrawing nitro group. It was also found that steric hindrance slows down the reaction, as indicated by the conversion of 2-bromo-*m*-xylene with phenylboronic acid. Earlier reports on Ni/dppf-catalysed Suzuki-Miyaura coupling reactions of α-halo-N-heterocycles with phenyl boronic acid describe the formation of a dimeric nickel compound, acting as catalyst sinks.[272] In contrast to these studies, with **24** and dppf, no evidence of a catalyst sink can be observed since conversions of 72% can be obtained.
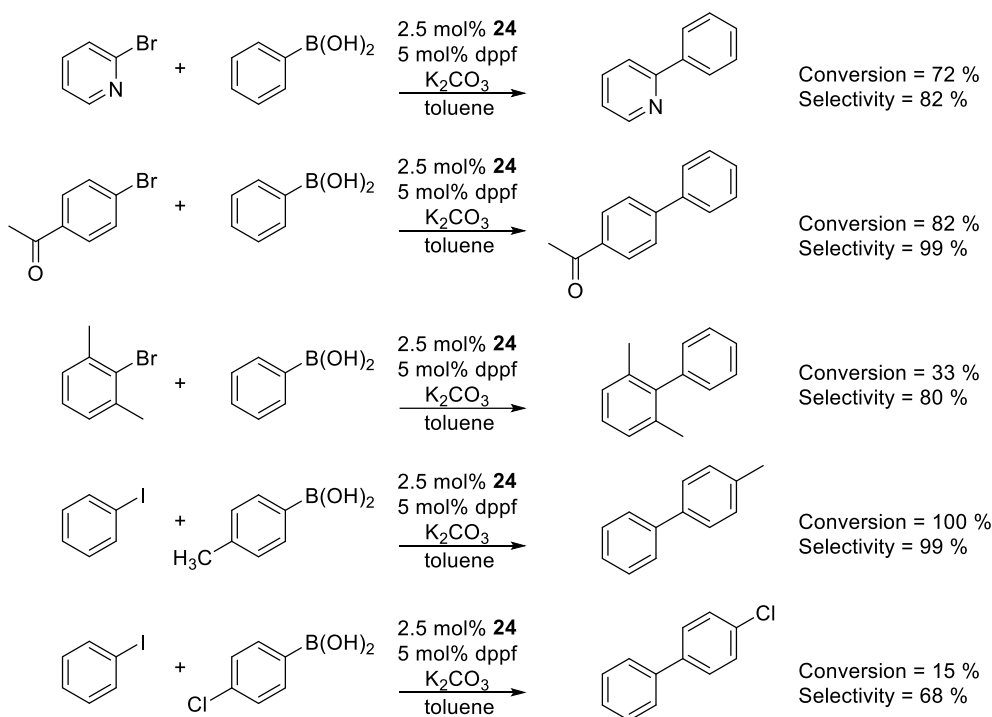
Scheme 10. Extension of the substrate scope using **24** and dppf as catalyst in Suzuki-Miyaura couplings after a UV activation procedure. This scheme has been adapted from [292] (license BY NC ND 4.0).

7.4.1 Catalyst poisoning studies

Whereas in samples of pure **24** after UV radiation the formation of Ni(0) particles points towards a degradation of the coordination compound, the stabilisation of the catalytically

active species could be achieved through the addition of phosphine ligands, dppe, PPh$_3$ and dppf. The impact of the various ligands on the catalyst performance of **24**, as well as the reduced conversion upon COD addition to **24**, already point towards the homogenous nature of the **24**-based catalyst. Additional proof for successful stabilisation of the Ni(0) centre and consequently a homogeneous nature of the catalytically active species should be gained from poisoning experiments and filtration tests (further information can be found in the experimental section). Despite an extensive search for a universal method to distinguish in between the homogeneous and heterogeneous nature of the catalytically active species, most strategies are still limited to specific groups of catalysts. Major research on poisoning studies has concentrated on 4d and 5d metals, whereas developed concepts cannot be directly transferred to 3d metals in most cases. Therefore, a combination of different methods is required in the case of 3d transition metal-based catalysts in order to allow a distinct classification between a homogeneous and a heterogeneous catalyst.[303]

As part of this work, dct (dibenzo[a,e]cyclooctatetraene) and CS$_2$ were chosen as catalyst poisons. Dct is a highly rigid and stable olefin, which is known to selectively bind to the metal centres in homogeneous catalysts, especially in 4d and 5d metals.[304] However, 3d-based complexes can form significantly weaker complexes with dct than the heavier analogues which can result in limited informative value about the catalyst's nature.[303] In contrast to homogeneous catalysts, the interactions between dct and heterogeneous catalysts should in most cases be very weak, due to the rigid tub conformation of this compound.[304] Consequently, for homogeneous catalysts efficient poisoning could be expected with dct, whereas only a minimal poisoning effect should be observed for heterogeneous catalysts. For example, the conversion of a heterogeneous nickel catalysed olefin hydrogenation was only slightly reduced (5%) in presence of 2 equivalents of dct per [Ni].[305] As part of this study poisoning tests were conducted for several poison:catalyst ratios (1:2, 1:1, 2:1, 4:1, Table 13) revealing an increasing catalyst deactivation with higher amounts of poison. However, no complete poisoning could be achieved since also at a stoichiometric ratio of 4:1 (poison:catalyst) a conversion of 35% could be obtained. A similar outcome of the dct-poisoning test was reported by the group of Hey-Hawkins, who investigated copper catalysed Suzuki-Miyaura couplings.[306] In alignment with the herein reported results, the dct catalyst poison was also not completely efficient, due to insufficient interactions of dct with the metal complex. It should be mentioned that in the **24**/dppf system, the timing of poison addition is decisive, as shown by the addition of poison to catalyst 1 hour before the introduction of substrates. In this case the poisoning is more efficient than if all substrates and the poison are added together and thus compete for coordination at the metal centre. Since no clear conclusion can be drawn on the basis of the dct poisoning experiments, CS$_2$ was introduced into the reaction mixture since it is highly suitable for the quantitative poisoning of heterogeneous catalysts. A complete catalyst inhibition can therefore already be expected at sub-stoichiometric amounts of CS$_2$ due to the presence of inactive metal atoms within the heterogeneous particles, while for homogeneous systems the addition of one or more equivalents of CS$_2$ would be required since all active sites should be accessible. In the **24**/dppf system the addition of 0.25 eq. of CS$_2$ caused a drop in conversion from 100% to 31% but did not completely inhibit the catalytic activity, as it would be the case for heterogeneous systems.

Additionally, also in presence of 2 equivalents catalyst poison, a conversion of 15% can be observed, which leads again to the conclusion that the catalyst can be considered as homogeneous species.

Table 13. Poisoning experiments of Suzuki-Miyaura coupling reactions of iodobenzene (1 eq.) and phenylboronic acid (1.5 eq.) using different amounts of dct or CS_2 which were added to the reaction mixture with the reagents, if not noted otherwise. Reaction conditions: 2.5 mol% catalyst, 5 mol% ligand, 3 equivalents K_2CO_3, toluene as solvent and *n*-decane as internal standard. The catalytic tests were conducted at 100°C after 15 min of exposure to UV light (365 nm). Total reaction times were 14 h. The conversions of arylhalides were determined using GC-MS. All product formations occur with 100% selectivity. This table has been adapted from [292] (license BY NC ND 4.0).

Entry	Poison	Reaction time [h]	Eq. poison related to **24**	Conversion [%]
1	-	2.5	-	29
2	-	14	-	100
3	dct	14	0.5	100
4	dct	14	1.0	75
5	dct	14	2.0	59
6	dct	14	4.0	35
7	dct	14[a]	2.0	56
8	dct	14[b]	2.0	43
9	CS_2	14	0.25	29
10	CS_2	14	2.0	15

[a] addition of dct after 2.5 h of reaction time [b] addition of dct to **24**, 1 h prior to start of the reaction.

Besides poisoning tests, which are based on the chemical interactions of catalysts and poisons, the Maitlis filtration test was carried out. This tests relies on the physical state of the catalyst and should give further insights into the real nature of the catalyst.[307] The aim is hereby to separate the solid material, which contains potentially the heterogeneous catalyst, from the reaction mixture, after the reaction has already proceeded for a certain time. Therefore, **24** and dppf were allowed to react for 2.5 hours and the reaction mixture was subsequently filtered over celite in a column. The column was washed with toluene and the filtrate was allowed to react further, whereby additional base (0.5 of initial amount) was added to the solution, since due to a certain insolubility, some base remained in the filter column. In parallel, the filter aid was collected, and new substrates, base and solvent were added (further information can be found in the experimental part). Both mixtures were allowed to react for a total reaction time of eight hours and the conversion of the substrate was analysed by GC-MS. Additionally, one control experiment was conducted for the same reaction time without any filtration. For the filtrate and the control experiments, similar conversions of 61% and 64% can be determined, whereas the reaction approach of the filter aid does only provide a low conversion of 28% (Table 14). The small conversion can most likely be attributed to the remaining catalyst material in the filter aid, which precipitated during the filtration and is re-dissolved at the elevated temperature under reaction conditions. Based on these results of the Maitlis filtration test, a homogeneous nature of the catalytically active species can again be underlined.

Table 14. Filtration tests of **24**/dppf as catalyst combination to determine the nature of the real active species. This table has been adapted from [292] (license BY NC ND 4.0).

Entry	Description	Conversion [%]
1	No filtration	64
2	Filtrate[a]	61
3	Filter aid[b]	28

7.5 Catalytic application of [Ni(OPOPh$_2$)$_6$(BF)$_2$] in the isomerisation of 1-octene

Interestingly, a trace amount of the Ni(II) complex **26** was found to be an efficient catalysts for the isomerisation of 1-octene.
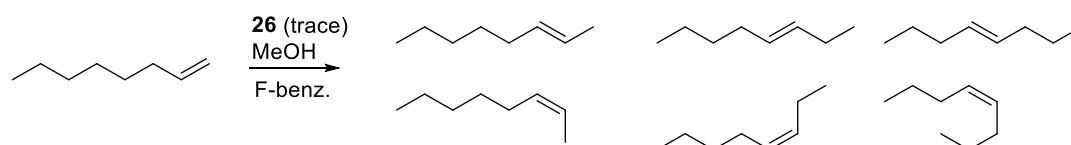
Scheme 11. Catalysed isomerisation of 1-octene in the presence of **26** and potential product spectrum. Methanol is applied as proton source.

A reaction mixture of 1-octene, the proton-source MeOH, *n*-decane as the internal standard and the solvent were allowed to react and products were analysed by GC-MS. A significant impact of the solvent can be observed since THF was completely inhibiting the reaction. A similar finding was witnessed, if water or NH$_3$ were present. The most promising results were obtained in fluorobenzene. In absence of a proton source, conversion of 1-octene could be achieved but to a lower extent. Another optimisation of the reaction conditions could be achieved by conducting the reaction in a microwave reactor. After only 10 minutes of reaction time at 66°C, 55% of 1-octene were isomerised selectively to 2-octene. Further investigations are required to explore this catalyst class and to optimise the reaction conditions.

7.6 Concluding Remarks

A unique reactivity of the PPO ligand with the Ni(II) precursor [Ni(MeCN)$_4$](BF$_4$)$_2$ was discovered, which allowed access to the rare ligand class of fluorophosphines. Based on a simultaneous fluorination and an *in-situ* reduction, [Ni(PFPh$_2$)$_4$] (**24**) can be obtained. Regarding the urge of alternative Ni(0) precursors to replace the most commonly used moisture-, air-, heat- and light sensitive [Ni(COD)$_2$], **24** does not only stand out due to its great stability towards air and therewith involved straight forward handling, but also due to its bright catalytic potential. The application of [Ni(PFPh$_2$)$_4$] in Suzuki-Miyaura couplings of aryl halides with phenyl boronic acids has been investigated in presence and absence of additional ligands. UV radiation of the compound results in bulk Ni(0) formation and disproportionation of the ligand. However, this characteristic is used to activate a ligand exchange in presence of PPh$_3$, dppe and dppf. A successful stabilisation of the Ni(0) centre can be achieved and the formed species show advantageous behaviour in catalysis, particularly in the combination of **24** with dppf. The comparison of [Ni(COD)$_2$] with [Ni(PFPh$_2$)$_4$] underlines the great catalytic performance for latter one. Theoretical investigations have been conducted to gain further insights. Thereby, a significantly more negative Ni(0) centre is found if fluorophosphine ligands

replace alkene-type ligands, such as COD, due to a lower degree of backbonding. Another advantage of the fluorophosphine-based system compared to conventional alkene-based Ni(0) pre-catalysts, is that through degradation of the $PFPh_2$ ligand under UV light, a blocking of the active sites during the catalytic reaction can be prevented. In contrast, in the case of $[Ni(COD)_2]$ remaining COD in the reaction mixture was shown to decrease the catalyst activity.

8 Conclusion and future work

The tautomeric equilibrium of the PPX/PXP (X = O, S) based ligand system offers different donor functionalities in the two tautomers, whereby coordination-stabilised tautomers can be formed through an equilibrium shift in presence of metal centres. The unique coordination chemistry of this ligand system reveals a versatile application potential of these compounds in photo-optics and catalysis. Based on the HSAB principle, hard and soft metal centres can be coordinated by the different coordination sites of these ligands. Harder metals are typically coordinated by the oxygen functionality of the PPO tautomer, yielding $[FeCl_2(PPO)_2]$ (**1**) and $[YCl_3(THF)_2(PPO)]$ (**2**), in which the P(II) donor atom remains uncoordinated. In the presence of softer metal ions, a shift of the tautomeric equilibrium is taking place, which leads to the formation of coordination-stabilised tautomers in $[Cu_2(MeCN)_n(\mu_2\text{-}POP)_2](PF_6)_2$ (**3**), $[Au_2Cl_2(\mu_2\text{-}POP)]$ (**4**), and $[Au_2(\mu_2\text{-}POP)_2](OTf)_2$ (**5**). In these complexes the POP acts as bridging ligand, similar to transition metal complexes of the well-explored short-bite ligands dppm and dppa. Thereby, close M–M distances are facilitated and subsequently bright photoemissions with microsecond lifetimes at 77 K can emerge. Interestingly, during the synthesis of **4**, the formation of a second species is observed, which was identified to be a mononuclear PPO-based gold complex, $[AuCl(PPO)]$ (**4'**), in which Au coordination occurs through the P(II) atom. However, the identification of directing factors for the selective synthesis of only one compound, **4** or **4'**, could not be accomplished. A similar shift of the tautomeric equilibrium to the PPO form can be observed for **3,** which was found to be responsive to the nature of the solvent. In presence of coordinating solvents, such as acetonitrile, the equilibrium is shifted from **3** to the P(II)-coordinated **3'** $[Cu(MeCN)_n(PPO)]PF_6$. This observation led to the introduction of a tautomerism-induced hemilability, which can have a tremendous impact in catalysis. If the equilibrium is shifted under reaction conditions, a vacant coordination site at the active centre can emerge easily with little steric hindrance.

The synthesis of trinuclear copper complexes of the type $[Cu_3(\mu_3\text{-}Hal)_2(\mu_2\text{-}PXP)_3]PF_6$ (X = O: Hal = Cl (**6**), Br (**7**), I (**8**); X = S: Cl (**10**), Br (**11**), I (**12**)) allowed a systematic study of the ligand backbone on the structural and photo-optical properties. Literature reported analogues of the PCP (dppm) and PNP (dppa) ligand sets enabled a further extension of this investigation to the carbon- and nitrogen-based counterparts. Despite the similar coordination behaviour of the four types of short-bite ligands, such as the often-preferred bridging over chelating coordination mode, drastic effects of the backbone can be revealed and a strong correlation with the size and electronegativity of the bridging atom can be detected. Chemical shifts in the $^{31}P\{^1H\}$ NMR spectra underline the intense electronic differences caused by the bridging atom (δ [ppm]: POP > PNP > PSP > PCP), whereby chemical shifts of the POP and PCP analogues are separated by more than 100 ppm. Besides the electronic effects, drastic variations of the structural parameters of the compounds can be seen. Whereas POP- and PNP-type trinuclear copper complexes display similar bond lengths and angles, PCP-based analogues show a slight deviation and in the PSP-type analogue a strong increase in the P–X bond length along with very acute P–X–P angles is revealed. This distinct difference can be attributed to the larger size of the sulphur atom in the ligand backbone. The larger size also causes an

increased level of flexibility in the backbone. The investigation of the photo-optical properties displays a further consequence of the flexibility, which is connected to a higher degree of non-radiative transitions from the excited state to the ground state. Thus, no photoemission can be detected for the PSP-containing compounds **10-12**. On the other hand, for the POP-stabilised Cu_3 complexes, a bright photo-luminescence at 77 K can be witnessed. Interestingly, the colour of the emission can be directed through the nature of the capping halide atoms with particularly strong yellow photoemission in the case of $[Cu_3(\mu_3\text{-}I)_2(\mu_2\text{-POP})_3]PF_6$ (**8**) and long emission lifetimes of 161 µs. Theoretical calculations support the drastic impact of the ligand backbone and confirm the predominant non-radiative nature of transitions from the excited state to the ground state in the case of the PSP-containing complexes **10-12**.

In order to investigate the impact of the ligand backbone on the catalytic potential of PXP-chelated Ni(II) complexes, $[NiHal_2(PSP)]$ (Hal = Br (**15**), I (**16**)) are synthesised *via* a facile one-pot reaction of the free ligand with $NiBr_2$ and NiI_2. An unusual reactivity of the PPS/PSP ligand in presence of $NiCl_2$, $[Ni(COD)_2]$ or $[Ni(MeCN)_4](BF_4)_2$ is revealed, whereby P–P bond cleavage and the subsequent formation of Ph_2PSS^-, Ph_2PS^- and Ph_2P^- ligands takes place, which can be isolated in di- and trinuclear Ni(II) complexes. The strong similarity between the $[NiHal_2(PSP)]$ complexes and their $[NiHal_2(dppe)]$ counterparts encouraged first explorations of PSP-based compounds in Kumada-Tamao-Corriu coupling reactions, in which dppe-based analogues are commonly employed as catalysts. The PSP-containing complexes did not show any evidence for a poisoning of the catalyst by the sulphur-containing ligand and provided promising results for the application of the PPX/PXP-ligand classes in catalysis. The presence of the PSP ligand offers a highly dynamic environment of the catalytically active centre. Thereby, an easy access for the substrates to the active centre can be enabled, resulting in a high activity and particularly suitable conditions for sterically demanding substrates.

Furthermore, the synthesis of PPS/PSP-coordinated Au complexes was attempted, whereby the direct reaction of PPS with [Au(tht)Cl] did not provide the expected PSP-stabilised dinuclear complexes in analogy to the PPO/POP. Instead, P–P bond cleavage is initiated, which leads to the formation of a hexanuclear $[Au_6(\mu_2\text{-}Ph_2PS)_6]$ (**20**) compound. The same compound could be obtained by substituting the PPS ligand by its diphenylphosphine sulphide analogue in presence of a base. Inspired by this compound formation, a related synthesis was attempted with copper precursors, using Ph_2PSH and mesityl copper as deprotonating copper source. Again, a different reactivity can be detected since the Ph_2PSH source does not only function as the ligand precursor, but also as a S^{2-} source, resulting in the isolation of two copper sulphide clusters, $[Cu_{14}(\mu_6\text{-}S)_1(\mu_3\text{-}Ph_2PS)_{12}]$ (**21**) and $[Cu_{24}(\mu_5\text{-}S)_6(\mu_3\text{-}Ph_2PS)_{12}]$ (**22**). The formation of S^{2-} can be attributed to a copper induced P=S bond cleavage, as it has already been observed before during the direct reaction of the PPS ligand with $[Cu(MeCN)_4]PF_6$. Whereas **21,** based on the $Cu_{14}S_1$ core, does not show photoemissive behaviour, strong near-infrared emission can be witnessed in the case of the $Cu_{24}S_6$ containing compound **22** in solution and in solid state. It should be underlined that different reactivity patterns of the PPS compound can be observed in presence of different metals.

Whereas in the presence of Cu(I) the cleavage of P=S is preferred, Ni(II) and Ni(0) initiate P–P bond cleavage.

In terms of PPX/PXP reactivities, another very unexpected reactivity emerged from the conversion of the oxygen-analogue PPO ligand with the nickel precursor $[Ni(MeCN)_4](BF_4)_2$. A P–P bond cleavage, accompanied by fluorination of the Ph_2P-fragment and simultaneous *in-situ* reduction to Ni(0) provided the fluorophosphine-stabilised complex $[Ni(PFPh_2)_4]$ (**24**). This unique reactivity can be attributed to the unusual oxidation states in the PPO ligand and the tautomeric equilibrium, which is a main driving force for the access of the Ph_2P-fragments. In **24** not only a fluorophosphine ligand is stabilised, which in its free form would readily disproportionate, but also a nickel(0) centre is present. Due to the high air stability of **24**, it could account as alternative for the commonly-used nickel(0) source, $[Ni(COD)_2]$. Theoretical calculations describe a unique environment of the Ni(0) centre compared to Ni(0) sources stabilised by alkene ligands, such as $[Ni(COD)_2]$. This can be attributed to the fluorophosphine ligand, which does not tend to enable a high degree of backbonding. Consequently, the Ni(0) centre is comparably more negatively charged. Since fluorophosphine ligands are widely unexplored especially in the field of catalysis, Suzuki-Miyaura coupling reactions are attempted using **24** as catalyst. To circumvent catalyst degradation under reaction conditions, additional phosphine ligands (PPh_3, dppe, dppf) are introduced to counteract any catalyst loss. The ligand substitution can be activated by UV radiation, which simultaneously initiates the disproportionation of the liberated fluorophosphine ligand. By pursuing this approach, highly active, homogeneous catalysts can be obtained, which are even capable of outperforming analogue $[Ni(COD)_2]$-based systems. A remarkable catalytic performance results from the combination of **24** with dppf. The drop in catalytic activity of $[Ni(COD)_2]$ can be ascribed to the remaining COD in the reaction mixture, which tends to block active sites. Since fluorophosphines are known to degrade in solution under UV light, such a behaviour can be prevented if **24** is applied.

In conclusion, this thesis reveals the underexplored potential of the strongly backbone-dependent PPX/PXP ligand systems based on X = oxygen or sulphur. The exceptional versatility in their coordination chemistry along with the exploitation of their tautomeric equilibrium pave the way for future applications of these ligand classes. The following strategies outline the essential steps, which are required to further deepen the knowledge of these ligands and their applications.

Formation of heterobimetallic complexes

The PPX tautomer offers the possibility for the formation of heterobimetallic complexes. The different donor functionalities provide the foundation to achieve this, since harder metals can coordinate *via* the oxygen atom, whereas the P(II) coordination could be utilised for softer metals. Such complexes often show interesting photo-optical, magnetic or catalytic behaviour due to cooperative effects of the two metals.[50,52,156]
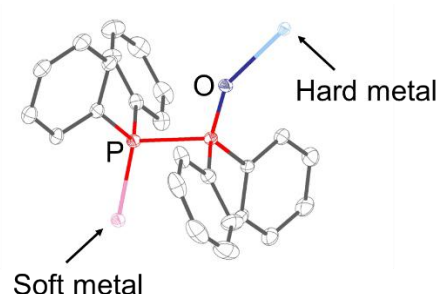
Figure 50. Perspective: synthesis of heterobimetallic complexes using PPO and a hard and soft metal through coordination of the different donor functionalities.

As shown for related PCP- and PNP-analogues, heterobimetallic complexes can also be considered for the PXP tautomer.[49,50] In this context, the PCP- and PNP-counterparts have evidenced a promising catalytic behaviour stemming from the cooperative effects of the two metals.

Modification of the phosphorus residues

In this work, PPX/PXP ligands were applied, which possess phenyl substituents at the phosphorus atoms. The targeted modification of the phosphorus residues can be pursued in the future to fine tune the performances of the compounds in photo-optical and catalytic applications. Firstly, the residues could be replaced by alkyl groups, or the aryl ring could be modified through the introduction of additional functional groups. The introduction of new phosphorus residues again effects the state of the tautomeric equilibrium, which is particularly interesting in the context of the coordination behaviour and the respective applications for photo-optical and catalytic purposes. A systematic exploration of the tautomeric equilibrium in analogue PNP/PPN-compounds could be of high importance, which has up-to-date mainly been overlooked.

In the catalysis context, Pringle, Dosset and Wass described the modification of the ortho position of related PCP- and PNP-based nickel(II) complexes as a tool to increase the selectivity in ethylene-polymerisation and -copolymerisation with CO.[128,129] This could also be an effective strategy to minimise the loss in selectivity, resulting from application of PSP-ligands in nickel catalysed Kumada-Tamao-Corriu couplings reactions.

Through the targeted modification of the phosphorus residues, a new class of chiral POP- and PSP-based ligand systems could also be developed, which would be highly beneficial in the field of enantioselective homogenous catalysis. The chirality can be achieved through engineering of the phosphorus residues to give P-stereogenic centres or through the introduction of chiral substituents. Pioneering work in the field of chiral PCP- and PNP-type ligands has led to the development of the MaxPHOS, MiniPHOS and Trichickenfootphos. Complexes based on these chiral ligands show outstanding catalytic performance in enantioselective hydrogenation reactions.[141,142,144] Deriving from these compounds, the related POP- and PSP-based analogues could extend the family of chiral short-bite ligands.

R = Ph, Cy, ^{t}Bu, ^{i}Pr

X = O, S
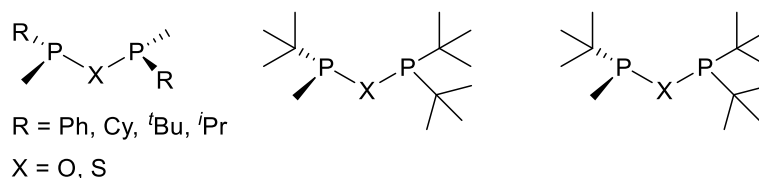
Scheme 12. Perspective: proposed oxygen- and sulphur-based chiral ligands, similar to MiniPHOS, Trichickenfootphos and MaxPHOS.

Catalytic studies

This work has uncovered the fundamental principles of the coordination chemistry of PPX/PXP-type ligands and their resulting transition metal complexes as foundation for potential applications in catalysis. Thereby, the use of [Cu(MeCN)$_n$(PPO)]PF$_6$ in Ullmann-type couplings and of [NiHal$_2$(PSP)] complexes in Kumada-Tamao-Corriu couplings has revealed an easily-accessible catalytically active site. In a catalytic cycle, chelate complexes of the PPX/PXP ligand classes are assumed to show hemilabile behaviour due to the high ring strain in the four-membered M–P–X–P ring, which has also been reported for dppm and dppa counterparts.[127,128,132,133] Additionally, the tautomeric equilibrium of PPX/PXP-type ligands can facilitate access to the active centre by switching from a bidentate to a monodentate coordination mode.

$\boxed{}$: free coordination site
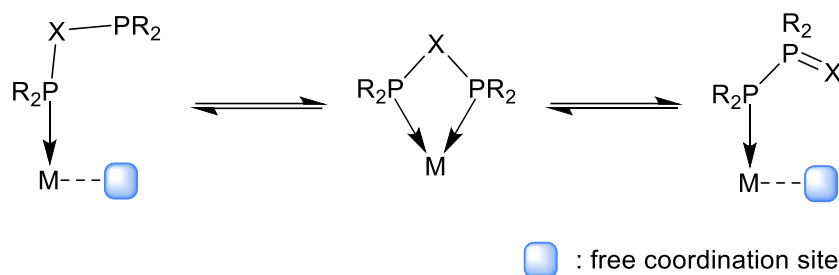
Figure 51. Perspective: different forms of hemilability, which can be highly beneficial if PPX/PXP (X = O, S) ligands and their transition metal complexes are applied in catalysis.

To further explore the potential of PPX/PXP-type ligands and their corresponding transition metal complexes in catalysis, it is essential to identify processes, in which the application of the short-bite POP- and PSP-based ligands can be advantageous. Hereby, previous studies, which apply similar PCP- and PNP-type ligands, for example in oligomerisation and polymerisation reactions, can be used as an orientation.[127,128] These studies identified the hemilability of the short-bite ligands as origin of the impressive catalytic activity. The comparison of dppm and dppa analogues revealed a tremendous impact of the ligand backbone with a significantly enhanced performance in the case of the nitrogen bridge. One explanation therefore was the increased electronegativity of nitrogen, which again highlights the enormous potential of backbone replacement by oxygen or sulphur.[124,129] With suitable catalytic processes in hand, in-depth studies of the ligand behaviour during the catalytic cycle must be conducted focussing on the hemilability induced by phosphorus dissociation or by a tautomeric equilibrium shift. A key achievement in catalytic studies will also be the application of above-described chiral short-bite ligands based on an oxygen- or sulphur-backbone to facilitate enantioselective catalysis.

Catalyst immobilisation

Posset *et al.* reported a method to immobilise the PPO ligand on a silica surface *via* an oxygen linkage.[34] This method opens access to potential single-site heterogeneous catalysts since the soft phosphorus moiety of the PPO ligand offers a free coordination site for transition metals, as the present work has shown.[308] The resulting systems would fuse benefits of homogeneous catalysts, including the well-defined active centres, with advantages of heterogeneous catalysts, such as the facile catalysts recovery and recycling ability. This combination sets the foundation for highly selective, active and reusable catalysts.
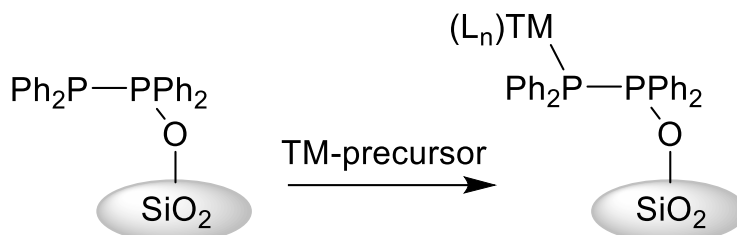

Figure 52. Perspective: synthesis of single-site heterogeneous catalysts using an anchored PPO ligand on SiO_2 with a free P(II) coordination site. L_n: other ligands of transition metal TM.

9 Experimental details

9.1 General considerations and analytic methods

All experiments were carried out on a Schlenk-line under Ar atmosphere or in an Ar filled glove box (MBraun) to ensure a moisture- and air-free atmosphere. Reactions involving light-sensitive substances, such as gold(I) precursors or $[Ni(COD)_2]$, were carried out in the absence of light if not noted otherwise. Solvents were dried and degassed before use and afterwards stored over activated molecular sieves (4 Å all solvents except MeCN which was stored over 3 Å). Toluene, tetrahydrofuran (THF), *n*-pentane and *n*-heptane were dried using a MBraun solvent purification system (SPS-800) and degassed before use. THF was additionally dried over potassium/benzophenone. Acetonitrile (MeCN), dichloromethane (DCM), fluorobenzene and triethyl amine (Et_3N) were distilled over calcium hydride. In the case of deuterated solvents, no heat was applied for drying to circumvent any deuterium-exchange. $CDCl_3$ and CD_2Cl_2 were dried over P_2O_5 while C_6D_6, d_8-toluene and CD_3CN were dried over CaH_2. Before application, deuterated solvents were degassed by freeze-pump-thaw cycles. Chlorodiphenylphosphine was purified by distillation. All other chemicals were used without further purification.

NMR spectra were recorded on a Bruker AVANCE III 300 MHz, AVANCE (III) 400 MHz or on a Ascend-500 MHz spectrometer at 298 K. Chemical shifts are given in ppm and are referred to residual solvent signals of the deuterated solvents. Unambiguous assignments were determined on the basis of chemical shifts, coupling patterns and 2D NMR experiments (^{1}H–^{1}H COSY, ^{1}H–^{13}C HMQC, and ^{1}H–^{13}C HMBC). The multiplicity of the NMR signals is denoted as s = singlet, d = doublet, dd = doublet of doublets, ddd = doublet of doublets of doublets, dt = doublet of triplets, t = triplet, q = quartet, sep = septet, m = multiplet, and br = broad. The NMR data was processed using MestreNova.[309]

IR spectra were recorded in the region of 4000–400 cm^{-1} on a Bruker Tensor 37 FTIR spectrometer equipped with a room temperature DLaTGS detector, a diamond ATR (attenuated total reflection) unit and a nitrogen-flushed measurement chamber. IR signals were classified according to their intensities (vs = very strong, s = strong, m = medium, w = weak, vw = very weak). Data was processed with the program Origin.[310]

UV/Vis spectra were recorded using an Ocean FX UV/Vis spectrometer from Ocean Optics and on a Agilent Cary 60 UV/Vis spectrometer (compound **21** and **22**). Therefore, diluted solutions with concentrations in the region of $1 \cdot 10^{-4}$-10^{-5} mol L^{-1} were prepared. Exact concentrations are sample dependent and are given alongside with the recorded spectra. The obtained data was processed with the program Origin.[310]

The elemental analyses of the samples were conducted using a vario EL cube, a vario MICRO cube (Elementar Analysensysteme GmbH), a Perkin Elmer Model 2400 Series II analyser, or an Elementar UNICUBE analyser.

For EPR spectroscopic measurements, a Bruker EMXplus spectrometer was used, whereby the field was calibrated against 2,2-diphenyl-1-picrylhydrazine (DDPH) with a *g* value of 2.0036.

ESI-MS measurements were performed on a Fisher Scientific LTQ Orbitrap XLQ Exactive. Samples of low concentrations (10^{-4} mol L^{-1}) were prepared. All signals are referred to the mass-to-charge ratio (m/z).

PXRD measurements were conducted in a glass capillary on a Stoe STADI-MP diffractometer operating with a Ge-mono-chromatised Cu-Kα (λ = 1.54178 Å) radiation in transmission mode. Calculated PXRD patterns were obtained with the program Mercury.[311]

9.2 Single-crystal XRD

Single-crystal X-ray diffraction data were collected with three different setups:

- STOE IPDS II diffractometer (2-circle) equipped with a STOE Imaging Plate (34 cm diameter) at a temperature of 150 K using a sealed X-Ray tube (Mo-Kα, λ=0.71073 Å) with a graphite monochromator as radiation source
- STOE STADIVARI diffractometer equipped with an open Eulerian cradle (4-circle) and a DECTRIS PILATUS pixel detector at a temperature of 100 K using a microfocus molybdenum source (Mo-Kα, λ=0.71073 Å) with a graphite monochromator as radiation source
- STOE METAL JET D2 diffractometer (2-circle) equipped with an EIGER4M detector at a temperature of 150 K using a sealed X-Ray tube (Ga-Kα, λ=1.34143 Å) with a Graded multilayer mirror monochromator using a liquid-gallium-jet anode as radiation source

For all measurements the data reduction was carried out with the X-Area version 1.73.1.0 (STOE, 2018)[312] using the semi-empirical absorption correction by X-RED[312] with scaling of the reflection intensities by LANA incorporated in X-Area. Structures were solved by means of dual space methods with SHELXT-2015[313] and the subsequent refinement was performed with SHELXL-2018[314] using the WinGX[315] program suite. Full-matrix least-square routines against F^2 were carried out. Hydrogen atoms were calculated on idealised positions. Pictures of the crystal structures were generated with the program DIAMOND.[316] In all graphical representations thermal ellipsoids are presented with 30% probability and hydrogen atoms, additional solvent molecules, present in the crystal structure, and anions are omitted for clarity.

Following CCDC numbers were assigned to the samples:

Chapter 3: CCDC 2163970 (**1**), 2163971 (**2**·0.5THF), 2163973 (**3**), 2163972 (**4**), 2163974 (**5**·2.3DCM).

Chapter 4: CCDC 2176829 (**6**·F-C_6H_5), CCDC 2176828 (**7**·DCM), CCDC 2176834 (**8**·DCM), CCDC 2176831 (**9**·2DCM), CCDC 2176830 (**10**), CCDC 2176833 (**11**), CCDC 2256153 (**12**), CCDC 2176832 (**13**·1.47DCM), CCDC 2176827 (**14**).

Chapter 5: CCDC 2375582 (**15**), CCDC 2375583 (**16**), CCDC 2375585 (**17**), CCDC 2375584 (**18**·DCM**)**, and CCDC 2375581 (**19**·toluene·*n*-pentane).

Chapter 6: No CCDC numbers yet

Chapter 7: CCDC 2379067 (**24**), CCDC 2379068 (**25**), 2379069 (**26**).

These data and additional information can be obtained free of charge *via* https://summary.ccdc.cam.ac.uk/structure-summary-form (or from the Cambridge Crystallographic Data Centre, 12 Union Road, Cambridge CB2 1EZ, UK; fax: (+44)1223-336-033; or deposit@ccdc.cam.uk). https://www.ccdc.cam.ac.uk/structures/

9.3 Investigation of the photo-optical properties

For the investigation of the photo-optical properties, samples were first irradiated with UV light (365 nm and 254 nm) at room temperature and 77 K (cooling with liquid nitrogen) to determine whether the samples display any photo-luminescence. Photo-luminescence measurements were conducted on a PTI QuantaMaster™ 8075-22 spectrometer, equipped with double monochromators (HORIBA Jobin Yvon GmbH) for emission and excitation spectra. Emission spectra were detected using a R928 photomultiplier (HORIBA Jobin Yvon GmbH) and a DSS-IGA020L/CUS detector for the IR area which must be cooled with liquid nitrogen. Lifetime measurements of the luminescence were carried out with either a DeltaDiode (HORIBA Jobin Yvon GmbH, Model DD-370, λ_{Exc} = 371 nm, pulse <2 ns, 2 µW) or a PTI XenonFlash™ (frequency max. 300 MHz). With the DeltaDiode emission decays in the nanosecond range can be measured and with the PTI XenonFlash™ decays in the microsecond range. The PL quantum yields at ambient temperature were determined using an integrating sphere out of optical PTFE, which was installed into the sample chamber of the spectrometer, according to the method of Friend *et al.*[317] The uncertainty of these measurements was estimated to be ca. 10%. No suitable setup was available for quantum yield measurements at 77 K.

For the measurements solid and dissolved samples were placed into EPR Suprasil® tubes (for solutions: low concentrations around 10^{-5} mol L^{-1}) and were measured at 77 K by cooling with liquid nitrogen and at 298 K. In an iterative process of switching between PLE and PL measurements, the maximum emission and excitation wavelengths were identified. Samples were firstly measured at 77 K and afterwards at 298 K since at lower temperatures non-radiative decays can be suppressed, which often enables better insights into the properties of the sample.

Lifetimes were determined for the maximum emission and excitation wavelengths. With the DeltaDiode a fixed excitation wavelength of 371 nm is pre-set. Fitting of the recorded decays with exponential functions provided the lifetimes. If the decay is defined by a biexponential decay, the effective lifetime τ_{eff} of the two processes can be calculated with equation 2.[318]

$$\tau_{eff} = \frac{A_1 \cdot \tau_1 + A_2 \cdot \tau_2}{A_1 + A_2}$$
(2)

A_1: Pre-exponential factors of respective decay

τ_1: Lifetime of respective decay

9.4 Theoretical calculations

Transition metal complexes of the PPO/POP-based ligand

Theoretical calculations were carried out with the ORCA package (version 4.0.0.1) in the gas phase.[319,320] Therefore, atom-pairwise dispersion corrections with the Becke-Johnson damping scheme (D3BJ)[321,322] and the RIJCOSX[323] approximation were applied. For a confirmation of the absence of imaginary frequencies, geometry optimisations and frequency analyses, were calculated using the B3LYP[202,203] functional in conjunction with the def2-TZVP[204,205] basis set. Single point calculations on a higher level of theory were utilised. To determine the PPO/POP equilibrium the B3LYP[202,203] functional and the def2-QZVP[204,205] basis set were applied.

Trinuclear copper complexes and photo-optical properties

The program package ORCA was used for all quantum chemical calculations.[320] The calculations did only consider the Cu_3-based cations and not the PF_6^- anions. Geometry optimisations of the compounds **6**, **7**, **8**, **10** and **11** were performed in the gas phase. Therefore DFT at the BLYP/def2-TZVP level was used.[201,204,205,324] The dispersion interactions were described using the D4 correction of Grimme.[325] Relaxed structures were confirmed as true local energy minimum structures by frequency calculations. Time-dependent DFT (TD-DFT) assuming the Tamm−Dancoff approximation (TDA-DFT) was used to calculate the UV/Vis absorption spectra. In this context, different functionals (B3LYP[201-203] CAM[326], PBE0[327], M06L[328], SCAN[329] and ωB97- X[D4][330]) were utilised and coupled with the same basis as used for the geometry optimizations. By comparison of the calculated spectra of compound **10** with the experimental data, the B3LYP[201-203] functional was selected for the calculation of the absorption spectra of the remaining compounds. Spin-orbit coupling was considered in the TD-DFT[331] calculations at the B3LYP[201-203]/def2-TZVP[204,205] level of theory. Since in the program package Orca effective core potentials (ECPs) are not yet available for TD-DFT calculations that take spin-orbit coupling into account, we have used a non-relativistic all-electron variant of the def-TZVP[332] basis for the calculation of the spin-orbit coupling matrix of compound **8**. To determine the PPS/PSP equilibrium the B3LYP[202,203] functional and the def2-QZVP[204,205] basis set were applied.

A bench-stable fluorophosphine nickel(0) complex and its catalytic application

Except the natural bond orbital (NBO) analyses, all calculations were carried out using the ORCA package in the gas phase.[319,320] Therefore, atom-pairwise dispersion corrections with the Becke-Johnson damping scheme (D3BJ) were utilised.[321,322] Density fitting techniques (also called resolution-of-identity approximation (RI)), were used for Generalized Gradient Approximation (GGA) calculations. The RIJCOSX[323] approximation was used for hybrid calculations. Geometry optimisations and frequency analyses, were carried out at the B3LYP[202,203]/def2-TZVP[204,205] level of theory for the confirmation that no imaginary frequencies are present. This functional was chosen since it resembles the experimental IR spectrum of **24** the most, especially with respect to the P–F stretching frequency. The TPSS[333,334] functional was used as a reference. Charge distributions of various Ni(0) complexes were

examined of successful geometry optimised and frequency calculation. Therefore CHELPG charges were chosen which describe the charges from electrostatic potentials using a grid-based method[335] using the ORCA package at the B3LYP[202,203]/def2-TZVP[204,205] level of theory. Furthermore, NBO/NPA analyses[336,337] were conducted using the NBO 6.0 package to get more insights into the charge distribution.[338] The Tolman electronic parameter was calculated, for which geometry optimisation and subsequent frequency analyses (to identify the symmetric A_1 CO stretch) of various [Ni(CO)$_3$L] complexes using B3LYP[202,203]/def2-TZVP[204,205] were conducted. Time-dependent density functional theory[339] calculations at the B3LYP[202,203]/def2-TZVP[204,205] level of theory were used to analyse the degradation reaction of **24** in presence of UV radiation. Therefore, solvent effects were investigated by using a conductor-like polarizable continuum model (CPCM) with a refractive index of 1.424 and the dielectric constant of 9.08 (DCM). For plotting the spectra, the orca_mapspc programme was used with a 10 cm^{-1} broadening for the IR spectra using a 2500 cm^{-1} broadening for the UV/Vis spectra.

9.5 Catalytic tests

Catalytic tests were qualitatively and quantitatively evaluated by GC-MS using an Agilent 8860 GC and a 5977B MSD, whereby *n*-decane was used as internal standard.

Transition metal complexes of the PPO/POP-based ligand

Ullmann-type coupling reactions were conducted in MeCN, DCM or a mixture (1:1) of the two solvents. The substrates iodobenzene (33 µL, 60 mg, 0.3 mmol) and phenol (41 mg, 0.45 mmol, 1.5 eq.) were given into a reaction tube with 0.6 mL solvent. The catalyst (5 mol%), *n*-decane (30 µL) as the internal standard and the base K$_2$CO$_3$ (2 eq.) were added and the reaction was conducted at room temperature for 24 hours in presence or absence of UV radiation (365 nm). GC-MS samples were prepared by filtering and diluting 100 µL of the reaction mixture in 1 mL ethanol.

Trinuclear copper complexes and photo-optical properties

Initial catalytic tests in homocoupling were conducted for ligand-decorated copper nanoparticles. Therefore, trimethylsilylacetylene (100 µL, 72 mg, 0.7 mmol), in the presence of piperidine (4 eq.) was heated up to 50°C for 5 h in THF. Filtered samples (100 µL) were diluted in 1 mL acetone and analysed by GC-MS.

Short-bite PSP-type ligands for nickel halide complexes

All catalytic tests have been conducted in Young-NMR tubes under Argon atmosphere at room temperature for 20 h, if not noted otherwise. The catalytic studies were conducted with **15**, **16** and in parallel with the reference catalyst [NiBr$_2$(dppe)]. The aryl halide (0.1 mmol) and Grignard reagent (1.0 eq., 0.1 mmol), catalyst (5.0 mol%), and the internal standard *n*-decane (20 µL) have been dissolved in 0.5 mL of solvent (either THF, benzene or toluene). For C(sp^2)-C(sp^3) couplings, the quantity of the catalysts was increased to 10 mol%. The reactions were started at a temperature of 0–5°C and the mixtures were then allowed to slowly warm to room temperature overnight. After completion of the reaction time, the reaction mixture was filtered and analysed by GC-MS (100 µL sample in 1 mL EtOH).

A bench-stable fluorophosphine nickel(0) complex and its catalytic application

Suzuki-Miyaura coupling reactions

All catalytic tests have been carried out in Young-NMR tubes or in Schlenk-flasks equipped with a stirring bar under Argon atmosphere. The substrates (aryl halide (0.1 mmol) and phenyl boronic acid (1.5 eq., 0.15 mmol)), base (3 eq., 0.3 mmol), catalyst (2.5 mol%), ligand (5 mol%) and the internal standard (*n*-decane, 10 µL) were dissolved in toluene (0.6 mL). The catalyst was activated with different activation modes (heat; UV at 365 nm) and the reaction mixture was heated to 100°C, if not noted otherwise. After completion of the reaction time, the reaction mixture was allowed to cool down to room temperature and filtered off. The products (100 µL) were analysed by GC-MS diluted in 1 mL MeCN or EtOH. MeCN was used since the catalyst is not soluble in this solvent.

Isomerisation reactions

Isomerisation reactions of 1-octene were conducted with **26** as catalyst. Therefore, 1-octene (35 µL), the proton source MeOH (1 µL), *n*-decane as internal standard (10 µL) were dissolved in benzene (0.6 mL). Different reaction times and temperatures were applied which are noted in the discussion part. Product samples were filtered and diluted in ethanol for GC-MS measurements.

9.5.1   Confirmation tests for homogeneous catalyst nature

It is highly recommended to clarify the real nature, homogeneous or heterogeneous, of the catalyst, since homogeneous species have often been found to form heterogeneous particles under reaction conditions. This is for example the case, if nanoparticle formation of Ni(0) cannot be excluded and the nanoparticle could act as real catalyst instead of a homogeneous coordination compound. There are several known procedures, which can be applied for this purpose, such as a targeted poisoning of heterogeneous or homogeneous species or a filtration tests to separate solid and dissolved compounds. However, the reported examples cannot always be transferred to all catalysts and 3d metals are widely underexplored in this context.[303] Consequently, some tests might give false positive results. Therefore, it is advisable to use a combination of different techniques.

Catalyst poisoning studies

In this work such a procedure was utilised to clarify the nature of the catalyst species in chapter 7, deriving from [Ni(PFPh$_2$)$_4$] and dppf. Therefore, approaches with the homogeneous catalyst poison (dibenzo[a,e]cyclooctatetraene, dct) or with a heterogeneous catalyst poison (CS$_2$) have been carried out using standard procedures for the catalytic tests (aryl halide (0.1 mmol), phenyl boronic acid (1.5 eq., 0.15 mmol), base (3 eq., 0.3 mmol), catalyst (2.5 mol%), ligands (5 mol%), internal standard (*n*-decane, 10 µL) in toluene (0.6 mL), activation with UV radiation (365 nm), T = 100°C, 14 h).

For dct a stock solution of dct was prepared (22.0 mg dct in 440 µL toluene). Aliquots corresponding to 0.25, 0.5, 1, 2 and 4 equivalents (dct:**24**) were added to the standard reaction solutions of iodobenzene and phenylboronic acid before the start of the reaction (as described

in the section Suzuki-Miyaura coupling reactions) and the catalytic test was conducted as usual. One test was conducted in which the addition of dct (2 eq.) was done 2.5 hours after the start of the reaction to investigate how the poison impacts the conversion during the course of the reaction. In another test, the poison (2 eq.) was added to the reaction mixture which did not contain the iodobenzene and the mixture was irradiated with UV (365 nm, 15 min) and heated to 100°C for 1 hour before addition of iodobenzene. The reaction was conducted for 14 hours. The point of addition showed a tremendous impact. Thus, an addition of the poison 1-2 h before addition of the reagents can be recommended to achieve sufficient catalyst poisoning.

For CS_2, as heterogeneous catalyst poison, a stock solution (6 µL CS_2 and 630 µL toluene) was prepared to facilitate the addition of 0.25, 0.5, 1 and 2 equivalents (CS_2:**24**). For efficient heterogeneous catalyst poisons, a sub-stoichiometric amount can be assumed to completely stop the catalytic conversion, since metal atoms in the inner particle can neither be accessed from the substrate nor from the poison. It should be mentioned that CS_2 interacts with the GC column.

Filtration test

For the filtration test, iodobenzene and phenylboronic acid were reacted under standard conditions (see Suzuki-Miyaura coupling reactions) except a total reaction time of eight hours instead of 14 hours to ensure that no complete conversion is achieved at the final point. As a control experiment, one test was conducted without filtration of the reaction mixture. The catalytic tests were started as usual by UV radiation and the temperature was elevated to 100°C. After 2.5 hours, the sample was filtered over celite in a glass pipette. The yellow-coloured, clear reaction solution was added to 20 mg K_2CO_3 since loss of the base during the filtration is highly likely due to insolubility reasons. It should be noted that the filtration had to be conducted in an Ar-filled glovebox to ensure air- and moisture-free conditions. However, hereby a sudden drop in temperature might have caused partial catalyst loss due to a lower solubility of **24** at room temperature. As a control experiment, new substrates, solvent and base are added to the filter aid, which is allowed to react for the same total reaction time (8 h) and at the same temperature as the filtrate. After continuation of the catalytic test for additional 5.5 hours, the reaction mixtures were filtered and analysed by GC-MS.

9.6   Syntheses

9.6.1   General substances

Tetraphenyl diphosphine oxide (PPO/POP)

The PPO/POP ligand was synthesised according to a modified literature procedure.[24] Diphenylphosphine oxide (1.01 g, 5 mmol) was dissolved in toluene (50 mL) and triethyl amine (Et_3N, 0.8 mL, 0.58 g, 5.7 mmol) was added. At 0–5°C chlorodiphenylphosphine (0.9 mL, 1.12 g, 5 mmol) was added dropwise to the solution. The reaction proceeded for 3 hours and was filtered afterwards to remove residual triethylammonium chloride. The saturated solution was stored at −18°C to grow colourless crystals of PPO. The crystals were washed with *n*-pentane and dried *in vacuo*. Crystalline yield: 1.20 g, 3.10 mmol, 62%.

^{1}H NMR (298 K, CDCl$_3$, 400 MHz), δ [ppm] = 7.83–7.72 (m, 4H, P(IV)–Ph–H-*ortho*), 7.64–7.54 (m, 4H, P(II)–Ph–H-*ortho*), 7.47–7.40 (m, 2H, P(IV)–Ph–H-*para*), 7.41–7.34 (m, 4H, P(IV)–Ph–H-*meta*), 7.34–7.28 (m, 2H, P(II)–Ph–H-*para*), 7.28–7.21 (m, 4H, P(II)–Ph–H-*meta*).

^{31}P{^{1}H} NMR (298 K, CDCl$_3$, 162 MHz), δ [ppm] = 35.8 (d, $^1J_{PP}$ = 227.7 Hz, P(IV)), −22.5 (d, $^1J_{PP}$ = 227.7 Hz, P(II)).

^{13}C NMR (298 K, CDCl$_3$, 101 MHz), δ [ppm] = 135.7–135.3 (m, P(II)–Ph–C-*ortho*), 134.6–133.3 (m, P(IV)–Ph–C-*ipso*), 131.8–131.1 (m, P(IV)–Ph–C-*ortho*, *para*), 130.3–130.0 (m, P(II)–Ph–C-*ipso*), 129.8 (s, P(II)–Ph–C-*para*), 128.8–128.4 (m, P(IV)/P(II)–Ph–C-*meta*).

Elemental analysis, calculated [%] for PPO/POP·2 Toluene: C 79.98, H 6.36; found C 79.90, H 5.20.

ATR-IR [cm^{-1}]: $\tilde{v}$ = 1958 (w), 1888 (w), 1811 (w), 1675 (w), 1583 (w), 1479 (m), 1433 (s), 1329 (w), 1305 (w), 1245 (w), 1175 (vs), 1109 (m), 1091 (m), 1071 (m), 1029 (w), 996 (w), 922 (w), 854 (w), 736 (m), 715 (m), 692 (vs), 557 (s), 513 (m), 496 (s), 460 (m), 432 (m), 375 (m).

Tetraphenyl diphosphine sulphide (PPS/PSP)

For the preparation of the PPS/PSP ligand, diphenylphosphine sulphide (1 g, 4.582 mmol, 1 eq.) was dissolved in toluene (20 mL) and Et$_3$N (0.61 g, 0.83 mL, 1.3 eq.) was added. The reaction mixture was cooled with an ice bath to 0-5°C and chlorodiphenylphosphine (1.03 g, 0.84 mL, 4.582 mmol, 1 eq.) diluted in toluene, was added dropwise. The reaction mixture was stirred overnight. The next day the solution was filtered and the solvent was partially evaporated *in vacuo*. The saturated solution was cooled to −30°C and overnight colourless crystals could be grown. The crystals were washed with *n*-pentane and dried *in vacuo*. Crystalline yield: 0.977 g, 2.428 mmol, 53.0%.

^{1}H NMR (298 K, C$_6$D$_6$, 400 MHz), δ [ppm] = 8.25–8.05 (m, 4H, P(IV)–Ph–H-*ortho*), 7.79–7.63 (m, 4H, P(II)–Ph–H-*ortho*), 7.07–6.86 (m, 12H, P(IV)–Ph–H-*meta/para*, P(II)–Ph–H-*meta/para*).

^{31}P{^{1}H} NMR (298 K, C$_6$D$_6$, 162 MHz), δ [ppm] = 44.3 (d, $^1J_{PP}$ = 247.3 Hz, P(IV)), −13.8 (d, $^1J_{PP}$ = 247.3 Hz, P(II)).

Potassium diphenylphosphine oxide (KPO)

A THF (40 mL) solution of diphenylphosphine oxide (2.02 g, 10 mmol) was added slowly to potassium bis(trimethylsilyl)amide (KBTSA) (1.98 g, 10 mmol) in THF (40 mL) at 0-5°C. The yellow reaction mixture was stirred overnight at room temperature. The next day, the solvent was removed *in vacuo* to obtain the product as a pale-yellow powder which was washed with *n*-pentane. Powder yield: 2.05 g, 8.5 mmol, 85%.

^{1}H NMR (298 K, d$_8$-THF, 400 MHz), δ [ppm] = 7.54–7.40 (m, 4H, Ph-H-*ortho*), 7.14 (t, 4H, $^1J_{HH}$ = 7.3 Hz, Ph-H-*meta*), 7.01 (t, 2H, $^1J_{HH}$ = 7.3 Hz, Ph-H-*para*).

^{31}P{^{1}H} NMR (298 K, d$_8$-THF, 162 MHz), δ [ppm] = 86.1 (s).

Potassium diphenylphosphine sulphide (KPS)

A solution of diphenylphosphine sulphide (200.0 mg, 0.9 mmol) in THF (10 mL) was added slowly to a solution of KBTSA (182.8 mg, 0.9 mmol) in THF (15 mL) at 0-5°C. The yellow reaction mixture was stirred overnight. The next day, the product was obtained by adding *n*-pentane as a colourless powder. The product was washed with *n*-pentane and dried *in vacuo*. Powder yield: 112.9 mg, 0.4 mmol, 48%.

^{1}H NMR (298 K, d$_8$-THF, 400 MHz), *δ* [ppm] = 7.75 (m, 4H, Ph-H-*ortho*), 7.06 (t, 4H, $^1J_{HH}$ = 7.2 Hz, Ph-H-*meta*), 6.97 (m, 2H, $^1J_{HH}$ = 7.2 Hz, Ph-H-*para*).

^{31}P{^{1}H} NMR (298 K, d$_8$-THF, 162 MHz), *δ* [ppm] = 27.1 (s).

9.6.2 Transition metal complexes of the PPO/POP-based ligand

Synthesis of [FeCl$_2$(PPO)$_2$] (1)

FeCl$_2$ (8.3 mg, 0.07 mmol) and PPO/POP (54.9 mg, 0.14 mmol) were dissolved in toluene (10 mL) and stirred for 3 days at room temperature. Afterwards, the yellow solution was filtered and layered with *n*-pentane. Pale-yellow crystals could be obtained after 3 days suitable for single-crystal XRD. The crystals were washed with *n*-pentane and dried *in vacuo*. Crystalline yield: 23.6 mg, 0.03 mmol, 37%. Due to the paramagnetic iron(II) centre NMR data could not be obtained.

Elemental analysis, calculated [%] for [FeCl$_2$(PPO)$_2$]: C 64.10, H 4.48; found C 64.24, H 4.26.

ATR-IR [cm^{-1}]: $\tilde{v}$ = 3051 (m), 2914 (w), 2849 (w), 1958 (w), 1888 (w), 1811 (w), 1675 (w), 1583 (w) 1479 (m), 1433 (vs), 1333 (w), 1305 (w), 1169 (m), 1137 (vs), 1108 (m), 1086 (s), 1068 (m), 1026 (m), 996 (m), 920 (w), 843 (w), 736 (s), 719 (m), 689 (vs), 561 (m), 500 (m), 496 (s), 460 (m), 432 (m), 389 (m).

[YCl$_3$(THF)$_2$(PPO)]·0.5THF (2)

2 was synthesised by stirring YCl$_3$ (30.0 mg, 0.15 mmol) and PPO/POP (59.4 mg, 0.15 mmol) in THF (10 mL) for 3 hours. The colourless reaction mixture was filtered and layered with *n*-pentane. Colourless crystals suitable for single-crystal XRD could be obtained which were washed with *n*-pentane and dried *in vacuo*. Crystalline yield: 20 mg, 0.03 mmol, 16%.

^{1}H NMR (298 K, d$_8$-THF, 400 MHz), *δ* [ppm] = 8.23–8.04 (br, 4H, P(IV)–Ph–H-*ortho*), 7.93–7.74 (br, 4H, P(II)–Ph–H-*ortho*), 7.53–7.44 (br, 2H, P(IV)–Ph–H-*para*), 7.44–7.33 (br, 4H, P(IV)–Ph–H-*meta*), 7.30–7.24 (br, 6H, P(II)–Ph–H-*meta*, *para*).

^{31}P{^{1}H} NMR (298 K, d$_8$-THF, 162 MHz), *δ* [ppm] = 51.8–44.1 (m, P(IV)), −19.9 (d, $^1J_{PP}$ = 271.7 Hz, P(II)).

^{13}C NMR (298 K, CDCl$_3$, 101 MHz), *δ* [ppm] = 136.2–135.9 (m, P(II)–Ph–C-*ortho*), 134.9–134.2 (br, P(IV)–Ph–C-*ipso*), 133.3–133.0 (br, P(IV)–Ph–C-*para*), 132.6–131.9 (br, P(IV)–Ph–C-*ortho*), 131.1–130.7 (m, P(II)–Ph–C-*para*), 130.6–130.1 (br, P(II)–Ph–C-*ipso*), 129.7–129.2 (m, P(II)–Ph–C-*meta*), 129.2–128.8 (m, P(IV)–Ph–C-*meta*).

Notes: A ^{89}Y NMR spectra could not be obtained and the solvent residual peaks of THF overlap with the signals of the coordinated THF molecules.

Elemental analysis, calculated [%] for [YCl$_3$(THF)$_2$(PPO)]·0.5 THF: C 53.60, H 5.29; found C 53.67 H 5.17.

ATR-IR [cm^{-1}]: $\tilde{v}$ = 3051 (w), 2979 (m), 2871 (w), 1621 (vw), 1585 (vw), 1481 (m), 1432 (s), 1307 (vw), 1245 (w), 1134 (vs), 1083 (s), 1010 (s), 918 (w), 860 (s), 740 (s), 690 (vs), 561 (m), 499 (s), 438 (w), 401 (w).

[Cu$_2$(MeCN)$_n$(μ$_2$-POP)$_2$](PF$_6$)$_2$ (3)

[Cu(MeCN)$_4$]PF$_6$ (100.0 mg, 0.27 mmol) and PPO/POP (103.7 mg, 0.27 mmol) were stirred in MeCN (10 mL) for 3 hours. Afterwards, the colourless reaction mixture was filtered and MeCN was removed *in vacuo* and the solid was re-dissolved in DCM. Layering with *n*-heptane provided pale yellow crystals of the product after one day suitable for single-crystal XRD. The crystals were washed with *n*-heptane and dried *in vacuo*. Crystalline yield: 100.0 mg, 0.10 mmol, 38%.

^{1}H NMR (298 K, CD$_2$Cl$_2$, 400 MHz), δ [ppm] = 7.58–7.52 (m, 8H, Ph–H-*para*), 7.43–7.38 (m, 32H, Ph–H-*meta*, *ortho*), 2.00 (s, 12H, MeCN).

^{31}P{^{1}H} NMR (298 K, CD$_2$Cl$_2$, 162 MHz), δ [ppm] = 106.1 (s, POP), −144.5 (sep, $^1J_{PF}$ = 707.8 Hz, PF$_6^-$).

^{13}C NMR (298 K, CD$_2$Cl$_2$, 101 MHz), δ [ppm] = 135.3–134.7 (m, Ph–C-*ortho*, *meta*), 132.9–132.6 (m, Ph–C-*para*), 131.8–131.3 (m, Ph–C-*ortho*, *meta*), 129.8–129.5 (m, Ph–C-*ortho*, *meta*, *para*), 128.7–127.6 (m, Ph–C-*ipso*), 118.7 (s, MeCN), 2.3 (s, MeCN).

^{19}F NMR (298 K, CD$_2$Cl$_2$, 377 MHz), δ [ppm] = −72.9 (d, $^1J_{PF}$ = 707.8 Hz, PF$_6^-$).

Elemental analysis, calculated [%] for [Cu$_2$(MeCN)$_3$(μ$_2$-POP)$_2$](PF$_6$)$_2$: C 49.40 H 3.76 N 3.20; found C 50.36 H 3.40 N 3.41.

ATR-IR [cm^{-1}]: $\tilde{v}$ = 2943 (w), 1958 (vw), 1888 (vw), 1811 (vw), 1675 (vw), 1587 (w), 1585 (w), 1480 (w), 1437 (m), 1400 (w), 1366 (w), 1329 (w), 1311 (w), 1184 (w), 1157 (w), 1103 (m), 1071 (w), 1029 (w), 996 (w), 922 (w), 874 (m), 833 (vs), 745 (m), 718 (m), 692 (s), 557 (s), 520 (m), 477 (m), 420 (w).

[Au$_2$Cl$_2$(μ$_2$-POP)] (4) and [AuCl(PPO)] (4′)

[Au(tht)Cl] (40.0 mg, 0.12 mmol) and PPO/POP (24.1 mg, 0.06 mmol) were reacted in DCM (10 mL) for 3 hours. The colourless reaction mixture was filtered and layered with *n*-pentane and was stored in the freezer at –18°C. Colourless crystals and a white powder could be obtained. The crystals could be analysed with single-crystal XRD. The crystals and the powder were washed with *n*-pentane and dried *in vacuo*. Crystalline yield: 40.0 mg, 0.05 mmol, 50%.

^{1}H NMR (298 K, CDCl$_3$, 400 MHz), δ [ppm] = 7.96–7.87 (m, 8H, POP–Ph–H-*meta*), 7.76–7.65 (br, 8H, PPO–P(IV)/P(II)–Ph–H-*ortho*), 7.63–7.52 (br, 6H, PPO–P(IV)–Ph–H-*meta*, *para*),

7.52–7.48 (br, 6H, PPO–P(II)–Ph–H-*meta, para*), 7.48–7.44 (m, 4H, POP–Ph–H-*para*), 7.44–7.38 (m, 8H, POP–Ph–H-*ortho*).

^{31}P{^{1}H} NMR (298 K, CDCl$_3$, 162 MHz), δ [ppm] = 116.1 (s, POP), 32.2 (d, $^1J_{PP}$ = 33.0 Hz, P(IV)–PPO), 16.7 (d, $^1J_{PP}$ = 33.0 Hz, P(II)–PPO).

^{13}C NMR (298 K, CDCl$_3$, 101 MHz), δ [ppm] = 133.9 (m, Ph–C-*para*), 132.8–132.4 (m, Ph–C-*meta*), 129.8–129.5 (m, Ph–C-*ortho*), 129.5–129.1 (m, Ph–C-*ipso*).

Elemental analysis, calculated [%] for 80% [Au$_2$Cl$_2$(μ_2-POP)] and 20% [AuCl(PPO)]: C 35.82 H 2.51; found C 35.45 H 2.75.

ATR-IR [cm^{-1}]: $\tilde{v}$ = 1568 (w), 1476 (m), 1437 (s), 1404 (w), 1315 (m), 1184 (m), 1155 (m), 1130 (w), 1095 (s), 1069 (m), 1027 (w), 999 (m), 952 (w), 855 (w), 838 (w), 745 (s), 550 (w), 509 (m), 482 (m), 444 (m).

[Au$_2$(μ_2-POP)$_2$](OTf)$_2$ (5)

[Au(tht)OTf] (37.0 mg, 0.07 mmol) and PPO/POP (27.0 mg, 0.07 mmol) were stirred in DCM (10 mL) for 3 hours. The yellow reaction mixture was filtered and layered with *n*-heptane. Colourless crystals suitable for single-crystal XRD analysis could be obtained after two days at –18°C which were washed with *n*-heptane and dried *in vacuo*. Crystalline yield: 25.0 mg, 0.02 mmol, 24%.

^{1}H NMR (298 K, CDCl$_3$, 400 MHz), δ [ppm] = 7.81–7.73 (m, 16H, Ph–H-*meta*), 7.61–7.55 (m, 8H, Ph–H-*para*), 7.56–7.49 (m, 16H, Ph–H-*ortho*).

^{31}P{^{1}H} NMR (298 K, CDCl$_3$, 162 MHz), δ [ppm] = 132.0 (s, POP).

^{13}C NMR (298 K, CDCl$_3$, 101 MHz), δ [ppm] = 134.4–134.3 (m, Ph–C-*para*), 133.3–132.9 (m, Ph–C-*meta*), 130.2–129.9 (m, Ph–C-*ortho*), 129.6–129.4 (m, Ph–C-*ipso*).

^{19}F NMR (298 K, CD$_3$CN, 377 MHz), δ [ppm] = −79.7 (s, OTf$^-$).

Elemental analysis, calculated [%] for [Au$_2$(μ_2-POP)$_2$](OTf)$_2$·*n*-heptane: C 44.66 H 3.48; found C 44.96 H 2.79.

ATR-IR [cm^{-1}]: $\tilde{v}$ = 2957 (w), 1684 (vw), 1653 (vw), 1587 (w), 1485 (w), 1480 (w), 1437 (s), 1393 (w), 1300 (m), 1278 (s), 1247 (s), 1220 (s), 1186 (m), 1148 (s), 1103 (s), 1026 (s), 998 (m), 934 (m), 911 (s), 745 (m), 718 (m), 687 (s), 633 (s), 572 (w), 524 (m), 498 (m), 426 (w).

9.6.3 Trinuclear copper complexes and photo-optical properties

[Cu$_3$(μ_3-cl)$_2$(μ_2-POP)$_3$]PF$_6$ (6)

ClPPh$_2$ (24.1 μL, 29.6 mg, 0.13 mmol) was added to a mixture of [Cu(MeCN)$_4$]PF$_6$ (50.0 mg, 0.13 mmol) and KPO (32.2 mg, 0.13 mmol) in fluorobenzene (8 mL). The colourless reaction mixture was stirred for 3 h and filtered afterwards. Through layering a fluorobenzene solution with *n*-heptane colourless crystals suitable for single-crystal XRD could be obtained. The crystals were washed with *n*-heptane and dried *in vacuo*. Crystalline yield: 45.3 mg, 0.028 mmol, 64%.

^{1}H NMR (298 K, CDCl$_3$, 400 MHz), δ [ppm] = 7.50–7.39 (m, 24H, Ph-H-*ortho*), 7.28–7.23 (m, 12H, Ph-H-*para*), 7.23–7.16 (m, 24H).

^{31}P{^{1}H} NMR (298 K, CDCl$_3$, 162 MHz), δ [ppm] = 101.7 (s, POP), −144.2 (sep, $^1J_{PF}$ = 711.9 Hz, PF$_6^-$).

^{13}C NMR (298 K, CDCl$_3$, 101 MHz), δ [ppm] = 134.4–133.7 (br, Ph-C-*ipso*), 131.9 (s, Ph-C-*ortho*), 131.9–131.6 (br, Ph-C-ortho, *meta*, *para*), 131.5 (s, Ph-C-*meta*), 128.8 (s, Ph-C-*ortho*), 128.7 (s, Ph-C-*meta*).

^{19}F NMR (298 K, CDCl$_3$, 377 MHz), δ [ppm] = −74.3 (d, $^1J_{PF}$ = 711.9 Hz, PF$_6^-$).

Elemental analysis, calculated [%] for C$_{72}$H$_{60}$Cl$_2$Cu$_3$F$_6$O$_3$P$_7$·0.5 CH$_2$Cl$_2$: C 54.15 H 3.82; found C 54.68 H 3.69.

ATR-IR [cm^{-1}]: $\tilde{v}$ = 3059 (w), 1589 (w), 1479 (m), 1433 (s), 1313 (w), 1103 (s), 888 0(s), 831 (vs), 739 (m), 688 (vs), 555 (w), 535 (m), 486 (s).

[Cu$_3$(μ$_3$-Br)$_2$(μ$_2$-POP)$_3$]PF$_6$ (7)

BrPPh$_2$ (28.4 μL, 35.6 m g, 0.13 mmol) was added to a mixture of [Cu(MeCN)$_4$]PF$_6$ (50.0 mg, 0.13 mmol) and KPO (32.2 mg, 0.13 mmol) in DCM (8 mL). After 3 h of reaction time, the solution was filtered and layered with *n*-heptane. Colourless crystals suitable for single-crystal XRD could be obtained. The crystals were washed with *n*-heptane and dried *in vacuo*. Crystalline yield: 33.9 mg, 0.019 mmol, 44%.

^{1}H NMR (298 K, CDCl$_3$, 400 MHz), δ [ppm] = 7.40–7.32 (m, 12H, Ph-H-*para*), 7.25–7.18 (m, 24H, Ph-H-*ortho*), 7.13 (t, 24H, J_{HH} = 7.7 Hz, Ph-H-*meta*).

^{31}P{^{1}H} NMR (298 K, CDCl$_3$, 162 MHz), δ [ppm] = 99.4 (s, POP), −144.2 (sep, $^1J_{PF}$ = 712.3 Hz, PF$_6^-$).

^{13}C NMR (298 K, CDCl$_3$, 101 MHz), δ [ppm] = 134.7–133.7 (br, Ph-C-*ipso*), 132.4–131.6 (m, Ph-C-ortho, *para*), 128.7 (s, Ph-C-*meta*).

^{19}F NMR (298 K, CDCl$_3$, 377 MHz), δ [ppm] = −74.3 (d, $^1J_{PF}$ = 712.5 Hz, PF$_6^-$).

Elemental analysis, calculated [%] for C$_{72}$H$_{60}$Br$_2$Cu$_3$F$_6$O$_3$P$_7$·1.5 CH$_2$Cl$_2$: C 49.54 H 3.56; found C 49.56 H 3.28.

ATR-IR [cm^{-1}]: $\tilde{v}$ = 3739 (w), 3060 (w), 1749 (w), 1477 (w), 1433 (m), 1100 (s), 1611 (vs), 837 (vs), 744 (w), 690 (vs), 523 (m), 482 (w).

[Cu$_3$(μ$_3$-I)$_2$(μ$_2$-POP)$_3$]PF$_6$ (8)

IPPh$_2$ (33.0 μL, 41.9 mg, 0.13 mmol) was added to a mixture of [Cu(MeCN)$_4$]PF$_6$ (50.0 mg, 0.13 mmol) and KPO (32.2 mg, 0.13 mmol) in DCM (8 mL). The reagents were reacted for 3 h and filtered afterwards. By layering the solution with *n*-heptane, colourless crystals were provided. The crystals were washed with *n*-heptane and dried *in vacuo*. Crystalline yield: 28.2 mg, 0.015 mmol, 35%.

^{1}H NMR (298 K, CDCl$_3$, 400 MHz), δ [ppm] = 7.42–7.33 (m, 12H, Ph-H-*para*), 7.23–7.16 (m, 24H, Ph-H-*ortho*), 7.13 (t, 24H, J_{HH} = 7.5 Hz, Ph-H-*meta*).

^{31}P{^{1}H} NMR (298 K, CDCl$_3$, 162 MHz), δ [ppm] = 95.1 (s, POP), −144.2 (sep, $^1J_{PF}$ = 711.9 Hz, PF$_6^-$).

^{13}C NMR (298 K, CDCl$_3$, 101 MHz), δ [ppm] = 134.5–134.1 (br, Ph-C-*ipso*), 132.1–131.6 (m, Ph-C-*ortho*, *para*), 128.8–128.6 (br, Ph-C-*meta*).

^{19}F NMR (298 K, CDCl$_3$, 377 MHz), δ [ppm] = −74.2 (d, $^1J_{PF}$ = 711.9 Hz, PF$_6^-$).

Elemental analysis, calculated [%] for C$_{72}$H$_{60}$I$_2$Cu$_3$F$_6$O$_3$P$_7$·4 CH$_2$Cl$_2$: C 43.71 H 3.28; found C 43.75 H 2.99.

ATR-IR [cm^{-1}]: $\tilde{v}$ = 3751 (w), 3047 (w), 1477 (w), 1433 (s), 1101 (s), 1617 (s), 835 (m), 743 (m), 690 (vs), 524 (m), 486 (m), 469 (m), 426 (w).

[Cu$_4$(μ$_3$-I)$_4$(IPPh$_2$)$_4$] (9)

If the synthesis of **8** was conducted in an excess of IPPh$_2$, crystals of **9** can be obtained by layering the saturated DCM solution with *n*-heptane.

[Cu$_3$(μ$_3$-Cl)$_2$(μ$_2$-PSP)$_3$]PF$_6$ (10)

ClPPh$_2$ (24.1 μL, 29.6 mg, 0.13 mmol) was added to a solution of [Cu(MeCN)$_4$]PF$_6$ (50.0 mg, 0.13 mmol) and KPS (34.4 mg, 0.13 mmol) in DCM (8 mL). Thereby the colour turned from pale yellow to colourless. After 3 h of reaction time, the reaction mixture was filtered and layered with *n*-heptane. Colourless crystals suitable for single-crystal XRD could be obtained. The crystals were washed with *n*-heptane and dried *in vacuo*. Crystalline yield: 18.0 mg, 0.011 mmol, 24%.

^{1}H NMR (298 K, CDCl$_3$, 400 MHz), δ [ppm] = 7.24–7.17 (m, 12H, Ph-H-*para*), 7.17–7.08 (m, 24H, Ph-H-*ortho*), 7.00 (t, 24H, $^1J_{HH}$ = 7.6 Hz, Ph-H-*meta*).

^{31}P{^{1}H} NMR (298 K, CDCl$_3$, 162 MHz), δ [ppm] = 23.9 (s, PSP), −144.2 (sep, $^1J_{PF}$ = 712.5 Hz, PF$_6^-$).

^{13}C NMR (298 K, CDCl$_3$, 101 MHz), δ [ppm] = 133.5–132.4 (m, Ph-C-*ortho*), 132.0–131.2 (br, Ph-C-*ipso*), 131.3–130.7 (m, Ph-C-*para*), 128.7 (s, Ph-C-*meta*).

^{19}F NMR (298 K, CDCl$_3$, 377 MHz), δ [ppm] = −74.1 (d, $^1J_{PF}$ = 712.5 Hz, PF$_6^-$).

Elemental analysis, calculated [%] for C$_{72}$H$_{60}$Cl$_2$Cu$_3$F$_6$S$_3$P$_7$: C 53.59 H 3.75 S 5.96; found C 53.06 H 3.68 S 5.29.

ATR-IR [cm^{-1}]: $\tilde{v}$ = 3747 (w), 3059 (w), 1740 (m), 1655 (w), 1558 (w) 1473 (w), 1436 (m), 1087 (m), 831 (s), 739 (m), 690 (m), 545 (m), 493 (m), 463 (m), 432 (m).

[Cu$_3$(μ$_3$-Br)$_2$(μ$_2$-PSP)$_3$]PF$_6$ (11)

BrPPh$_2$ (28.4 μL, 35.6 mg, 0.13 mmol) was added to a yellow reaction mixture of [Cu(MeCN)$_4$]PF$_6$ (50.0 mg, 0.13 mmol) and KPS (34.4 mg, 0.13 mmol) in 8 mL DCM. The reaction was proceeded for 3 h and afterwards filtration and layering with *n*-heptane were carried out providing pale-yellow crystals. The crystals were washed with *n*-heptane and dried *in vacuo*. Crystalline yield: 21.7 mg, 0.012 mmol, 27%.

^{1}H NMR (298 K, CDCl$_3$, 400 MHz), *δ* [ppm] = 7.22–7.17 (m, 12H, Ph-H-*para*), 7.17–7.12 (m, 24H, Ph-H-*ortho*), 7.00 (t, 24H, $^1J_{HH}$ = 7.6 Hz, Ph-H-*meta*).

^{31}P{^{1}H} NMR (298 K, CDCl$_3$, 162 MHz), *δ* [ppm] = 21.2 (s, PSP), −144.2 (sep, $^1J_{PF}$ = 712.5 Hz, PF$_6^-$).

^{13}C NMR (298 K, CDCl$_3$, 101 MHz), *δ* [ppm] = 133.0–132.6 (m, Ph-C-*ortho*), 131.7–131.3 (br, Ph-C-*ipso*), 131.2–130.7 (m, Ph-C-*para*), 128.7 (s, Ph-C-*meta*).

^{19}F NMR (298 K, CDCl$_3$, 377 MHz), *δ* [ppm] = −74.1 (d, $^1J_{PF}$ = 712.5 Hz, PF$_6^-$).

Elemental analysis, calculated [%] for C$_{72}$H$_{60}$Br$_2$Cu$_3$F$_6$S$_3$P$_7$·1.5 CH$_2$Cl$_2$: C 48.24 H 3.47 S 5.26; found C 48.62 H 3.09 S 4.35.

ATR-IR [cm^{-1}]: $\tilde{v}$ = 3747 (m), 3057 (m), 1740 (m), 1477 (m), 1432 (s), 1367 (w), 1310 (w), 1211 (w), 1095 (s), 1026 (w), 995 (w), 831 (vs), 740 (s), 692 (s), 550 (m), 500 (s), 460 (m), 426 (w).

[Cu$_3$(μ$_3$-I)$_2$(μ$_2$-PSP)$_3$]PF$_6$ (12)

IPPh$_2$ (33.0 μL, 41.9 mg, 0.13 mmol) was added to a mixture of [Cu(MeCN)$_4$]PF$_6$ (50.0 mg, 0.13 mmol) and KPS (34.4 mg, 0.13 mmol) in 8 mL DCM. The yellow mixture was stirred for 3 h and subsequently filtered. Through layering with *n*-heptane pale yellow crystals could be obtained suitable for single-crystal XRD. The crystals were washed with *n*-heptane and dried *in vacuo*. Crystalline yield: 12.7 mg, 0.007 mmol, 16%.

^{1}H NMR (298 K, CDCl$_3$, 400 MHz), *δ* [ppm] = 7.24–7.18 (m, 12H, Ph-H-*para*), 7.17–7.07 (m, 24H, Ph-H-*ortho*), 7.05–6.96 (m, 24H, Ph-H-*meta*).

^{31}P{^{1}H} NMR (298 K, CDCl$_3$, 162 MHz), *δ* [ppm] = 15.2 (s, PSP), −144.2 (sep, $^1J_{PF}$ = 712.5 Hz, PF$_6^-$)

^{13}C NMR (298 K, CDCl$_3$, 101 MHz), *δ* [ppm] = 133.4–132.5 (m, Ph-C-*ortho*), 131.7–131.1i (br, Ph-C-*ipso*), 131.0 (s, Ph-C-*para*), 128.9–128.4 (br, Ph-C-*meta*).

^{19}F NMR (298 K, CDCl$_3$, 377 MHz), *δ* [ppm] = −74.1 (d, $^1J_{PF}$ = 712.5 Hz, PF$_6^-$).

Elemental analysis, calculated [%] for C$_{72}$H$_{60}$I$_2$Cu$_3$F$_6$S$_3$P$_7$: C 48.13 H 3.37 S 5.35; found C 47.46 H 3.32 S 4.79.

ATR-IR [cm^{-1}]: $\tilde{v}$ = 3051 (m), 1650 (w), 1577 (m), 1435 (m), 1380 (w), 1304 (w), 1180 (w), 1160 (w), 1090 (m), 1028 (w), 993 (w), 918 (w), 831 (vs), 737 (m), 685 (m), 613 (w), 546 (m), 494 (m), 461 (m), 430 (w).

[Cu$_3$(μ$_3$-I)$_2$(μ$_2$-I)(μ$_2$-PSP)$_2$] (13)

An excess of IPPh$_2$ (100.0 μL, 127.0 mg, 0.41 mmol) was added to [Cu(MeCN)$_4$]PF$_6$ (50.0 mg, 0.13 mmol) and KPS (34.4 mg, 0.13 mmol) in DCM (8 mL). The yellow mixture was stirred for 3 h and subsequently filtered. Layering with *n*-heptane provided yellow crystals of **13** which were washed with *n*-heptane and dried *in vacuo*. Crystalline yield: 54.8 mg, 0.040 mmol, 89%.

^{1}H NMR (298 K, CDCl$_3$, 400 MHz), *δ* [ppm] = 7.77–7.67 (m, 8H, P1-Ph-H-*meta*), 7.58–7.48 (m, 8H, P2-Ph-H-*ortho*), 7.36–7.30 (m, 4H, P1-Ph-H-*para*), 7.30–7.25 (m, 4H, P2-Ph-H-*para*), 7.25–7.19 (m, 8H, P1-Ph-H-*ortho*), 7.19–7.10 (m, 8H, P2-Ph-H-*meta*).

^{31}P{^{1}H} NMR (298 K, CDCl$_3$, 162 MHz), *δ* [ppm] = 20.2 (br, P1), 5.5 (br, P2).

^{13}C NMR (298 K, CDCl$_3$, 101 MHz), *δ* [ppm] = 134.3 (d, P1-Ph-C-meta), 134.2–134.0 (m, P2-Ph-C-*ipso*), 133.7–133.3 (br, P2-Ph-C-*ortho*), 133.1–132.9 (br, P1-Ph-C-*ipso*), 130.4 (s, P2-Ph-C-*para*), 130.1 (s, P1-Ph-C-*para*), 128.6–127.9 (m, P2-Ph-C-*meta*; P2-Ph-C-*ortho*).

Elemental analysis, calculated [%] for C$_{48}$H$_{40}$I$_3$Cu$_3$S$_2$P$_4$: C 41.89 H 2.93 S 4.66; found C 42.02 H 2.83 S 2.27.

ATR-IR [cm^{-1}]: $\tilde{v}$ = 3747 (w), 3051 (m), 1741 (m), 1580 (w), 1479 (m), 1430 (vs), 1381 (w), 1300 (w), 1209 (w), 1178 (w), 1151 (w), 1089 (s), 843 (w), 741 (vs), 689 (vs), 548 (m), 501 (s), 484 (s), 436 (m), 391 (m).

[Cu$_2$(MeCN)$_4$(Ph$_2$PPPh$_2$)$_2$] (14)

[Cu(MeCN)$_4$]PF$_6$ (100.0 mg, 0.27 mmol) and PPS/PSP (103.7 mg, 0.27 mmol) were reacted in MeCN (10 mL) for 3 hours. The colourless solution was filtered and MeCN was removed *in vacuo*. The solid was re-dissolved in DCM and layered with *n*-heptane to form pale yellow crystals suitable for single-crystal X-ray diffraction analysis.

Synthesis of ligand-decorated nanoparticles

For the synthesis of POP-stabilised nanoparticles (20 mg), compound **6** was dissolved in THF (4 mL) and stirred vigorously. A solution of NaBH$_4$ (7.4 mg in 1.5 mL THF) was injected quickly at 0-5°C. After 30 minutes, the reaction mixture was filtered and *n*-heptane was added to the supernatant. The brownish product was allowed to settle down and was collected the next day by filtration and subsequent drying under vacuum. The nanoparticles were analysed by IR spectroscopy.

9.6.4 Short-bite PSP-type ligands for nickel halide complexes

[NiBr$_2$(PSP)] (15)

NiBr$_2$ (100.0 mg, 0.46 mmol, 1 eq.) and PPS (Ph$_2$P(=S)–PPh$_2$; 184.2 mg, 0.46 mmol, 1 eq.) were heated to reflux in acetonitrile (6 mL) for 5 hours. Afterwards, the red-violet reaction mixture was filtered. The solvent was removed *in vacuo* and the solid was re-dissolved in DCM. The DCM solution was layered with *n*-heptane to provide red-violet crystals of **15**. The crystals were washed with *n*-heptane and dried *in vacuo*. Crystalline yield: 139.8 mg, 0.23 mmol, 50%.

^{1}H NMR (298 K, CD_2Cl_2, 400 MHz), δ [ppm] = 8.11 (m, 8H, Ph-H-*ortho*), 7.66 (t, 4H, $^1J_{HH}$ = 7.6 Hz, Ph-H-*para*); 7.56 (t, 8H, $^1J_{HH}$ = 7.6 Hz, Ph-H-*meta*).

^{31}P{^{1}H} NMR (298 K, CD_2Cl_2, 162 MHz), δ [ppm] = −17.5 (s, PSP).

^{13}C NMR (298 K, CD_2Cl_2, 101 MHz), δ [ppm] = 134.0 (br, Ar-C-*ortho*), 133.1 (s, Ar-C-*para*), 129.5 (br, Ar-C-*meta*).

Elemental analysis, calculated [%] for $C_{24}H_{20}Br_2NiP_2S$·0.5 DCM: C 44.36, H 3.19, S 4.83; found: C 44.36, H 3.26, S 4.88.

ATR-IR [cm^{-1}]: $\tilde{v}$ = 1478 (w), 1431(m), 1382(vw), 1330 (vw), 1305 (vw), 1182 (w), 1161 (vw), 1139 (vw), 1088 (m), 1066 (w), 1022 (vw), 995 (w), 970 (vw), 921 (vw), 838 (vw), 754 (w), 740 (s), 710 (w), 694 (m), 682 (vs), 617 (vw), 561 (vs), 534 (w), 507 (vs), 474 (w), 468 (vs), 459 (s), 434 (m).

UV/Vis in DCM, [nm] ([$mol^{-1}dm^3cm^{-1}$]): λ_{max} (ε) = 510 (2391), 304 (17069), 277 (21175), 255 (24981).

[NiI$_2$(PSP)] (16)

NiI$_2$ (100.0 mg, 0.32 mmol, 1 eq.) and PPS (128.8 mg, 0.32 mmol, 1 eq.) were heated to reflux in acetonitrile (6 mL) for 5 hours. Afterwards, the reaction mixture was filtered and the solvent was removed *in vacuo*. Dark-violet crystals could be obtained from layering the dark-violet DCM solution with *n*-heptane. The crystals were washed with *n*-heptane and dried *in vacuo*. Crystalline yield: 105.7 mg, 0.15 mmol, 46%.

^{1}H NMR (298 K, CD_2Cl_2, 400 MHz), δ [ppm] = 8.10 (m, 8H, Ph-H-*ortho*), 7.64 (t, 4H, $^1J_{HH}$ = 7.5 Hz, Ph-H-*para*); 7.56 (t, 8H, $^1J_{HH}$ = 7.5 Hz, Ph-H-*meta*).

^{31}P{^{1}H} NMR (298 K, CD_2Cl_2, 162 MHz), δ [ppm] = −14.5 (s, PSP).

^{13}C NMR (298 K, CD_2Cl_2, 101 MHz), δ [ppm] = 134.3 (m, Ar-C-*ortho*), 132.9 (s, Ar-C-*para*), 129.3 (m, Ar-C-*meta*).

Elemental analysis, calculated [%] for $C_{24}H_{20}I_2NiP_2S$: C 40.32, H 2.82, S 4.48; found: C 40.22, H 3.03, S 4.00.

ATR-IR [cm^{-1}]: $\tilde{v}$ = 1478 (w), 1431 (m), 1383 (vw), 1330 (vw), 1303 (vw), 1178 (w), 1161 (vw), 1141 (vw), 1088 (m), 1066 (vw), 1022 (vw), 995 (w), 970 (vw), 923 (vw), 835 (vw), 754 (w), 739 (s), 710 (w), 694 (m), 685 (vs), 615 (vw), 557 (vs), 528 (m), 505 (vs), 474 (w), 464 (s), 453 (s), 434 (m).

UV/Vis in DCM, [nm] ([$mol^{-1}dm^3cm^{-1}$]): λ_{max} (ε) = 564 (2297), 387 (3347), 303 (18242), 250 (24786).

[Ni$_2$(Ph$_2$PSS)$_2$(Ph$_2$PS)(Ph$_2$P)] (17)

NiCl$_2$ (70.0 mg, 0.54 mmol, 1 eq.) and PPS (217.3 mg, 0.54 mmol, 1 eq.) were heated under reflux in acetonitrile (6 mL). The reaction was proceeded for 5 h and afterwards the reaction mixture was filtered and the solvent was removed *in vacuo*. Redissolving the solid in DCM

and layering with *n*-pentane provided dark-brown crystals suitable for single-crystal XRD. The crystals were washed with *n*-pentane and dried *in vacuo*. Crystalline yield: 17.0 mg, 0.017 mmol, 6%.

^{1}H NMR (298 K, CD$_2$Cl$_2$, 400 MHz), δ [ppm] = 8.06–7.93 (m, 8H, Ph$_2$PSS$^-$-*ortho*), 7.70–7.64 (m, 2H, Ph$_2$PS$^-$-*para*), 7.64–7.58 (m, 4H, Ph$_2$P$^-$-*ortho*), 7.58–7.54 (m, 2H, Ph$_2$P$^-$-*para*), 7.54–7.48 (m, 4H, Ph$_2$P$^-$-*meta*), 7.48-7.41 (m, 8H, Ph$_2$PS$^-$-*ortho,meta*), 7.41-7.28 (m, 8H, Ph$_2$PSS$^-$-*meta*), 7.27–7.18 (m, 4H, Ph$_2$PSS$^-$-*para*).

^{31}P{^{1}H} NMR (298 K, CD$_2$Cl$_2$, 162 MHz), δ [ppm] = 92.0 (dt, 1 P$_b$, $^2J_{PP}$ = 49.0 Hz, $^3J_{PP}$ = 3.6 Hz, Ph$_2$PS$^-$), 72.7 (s, 1 P$_d$, Ph$_2$PSS$^-$), 72.0 (t, 1 P$_a$, $^3J_{PP}$ = 3.6 Hz, Ph$_2$PSS$^-$), 60.4 (dd, 1 P$_c$, $^2J_{PP}$ = 49.0 Hz, $^3J_{PP}$ = 3.6 Hz, Ph$_2$P$^-$).

^{13}C NMR (298 K, CD$_2$Cl$_2$, 101 MHz), δ [ppm] = 135.8, 134.5 (d), 132.8 (d), 131.9 (dd), 130.1 (br), 129.8 (dd), 128.5 (dd), 128.5 (s), 128.0 (d), 127.4 (d).

Elemental analysis, calculated [%] for C$_{48}$H$_{40}$Ni$_2$P$_4$S$_5$: C 56.61, H 3.96, S 15.74; found: C 56.24, H 4.03, S 15.97.

ATR-IR [cm^{-1}]: $\tilde{v}$ = 3043 (vw), 1961 (vw), 1877 (vw), 1810 (w), 1774 (w), 1697 (w), 1653 (w), 1616 (vw), 1577 (w), 1561 (w), 1540 (w), 1523 (vw), 1508 (vw), 1475 (m), 1432 (m), 1395 (w), 1328 (w), 1305 (m), 1264 (w), 1179 (m), 1158 (w), 1094 (s), 1067 (m), 1026 (m), 994 (m), 972 (w), 920 (w), 847 (w), 741 (s), 706 (s), 687 (vs), 628 (m), 607 (m), 571 (vs), 520 (m), 488 (s), 475 (s).

[Ni$_3$(Ph$_2$PS)$_4$(Ph$_2$P)$_2$] (18)

At room temperature [Ni(COD)$_2$] (50.0 mg, 0.18 mmol, 1 eq.) and PPS (146.3 mg, 0.36 mmol, 2 eq.) were stirred overnight in DCM (6 mL). The next day, the reaction solution was filtered and layered with *n*-pentane. Dark red crystals suitable for single-crystal XRD could be obtained after two days. The crystals were washed with *n*-pentane and dried *in vacuo*. Crystalline yield: 23.2 mg, 0.015 mmol, 27%.

^{1}H NMR (298 K, CDCl$_3$, 400 MHz), δ [ppm] = 8.00–7.73 (m, 4H, Ph$_2$PS$^-$$_{intern}$-*para*), 7.72–7.57 (m, 4H, Ph$_2$P$^-$-*para*), 7.56–7.44 (m, 4H, Ph$_2$PS$^-$$_{terminal}$-*para*), 7.42–7.27 (m, 8H, Ph$_2$PS$^-$$_{intern}$-*ortho*), 7.28–6.78 (m, 40H: 8H Ph$_2$PS$^-$$_{intern}$-*meta*, 8H Ph$_2P^-$-*meta*, H Ph$_2P^-$-*ortho*, 8H Ph$_2PS^-$$_{terminal}$-*meta*, 8H Ph$_2PS^-$$_{terminal}$-*ortho*).

^{31}P{^{1}H} NMR (298 K, CDCl$_3$, 162 MHz), δ [ppm] = 98.1 (br, 2 P$_c$, Ph$_2$PS$^-$$_{intern}$), 41.4 (br, 2 P$_b$, Ph$_2P^-$), 30.0 (br, 1 P$_a$, Ph$_2PS^-$$_{terminal}$), 23.2 (2 m, 1 P$_a$, Ph$_2PS^-$$_{terminal}$).

^{13}C NMR (298 K, CDCl$_3$, 101 MHz), δ [ppm] = 135.0 (br), 133.9 (br), 133.1–132.3 (br), 128.5 (br), 128.4 (br), 127.1 (br).

Elemental analysis, calculated [%] for C$_{72}$H$_{60}$Ni$_3$P$_6$S$_4$: C 61.1, H 4.27, S 9.06; found: C 60.63, H 4.40, S 8.51.

ATR-IR [cm^{-1}]: $\tilde{v}$ = 3068 (w), 3049 (w), 1953 (vw), 1882 (vw), 1805 (w), 1772 (vw), 1699 (w), 1650 (w), 1616 (w), 1580 (w), 1558 (w), 1539 (w), 1520 (vw), 1506 (vw), 1475 (m), 1432 (s),

1395 (w), 1323 (w), 1304 (m), 1267 (m), 1243 (m), 1182 (m), 1155 (m), 1128 (m), 1089 (s), 1066 (m), 1026 (m), 997 (m), 968 (w), 918 (w), 844 (w), 736 (s), 687 (vs), 617 (m), 582 (m), 557 (s), 516 (m), 498 (s), 486 (vs), 473 (s).

[Ni$_2$(Ph$_2$PSS)(Ph$_2$PS)$_2$(Ph$_2$P)] (19)

At room temperature [Ni(COD)$_2$] (50.0 mg, 0.18 mmol, 1 eq.) and KPPh$_2$ (93.2 mg, 0.36 mmol, 2 eq.) were reacted with ClPPh$_2$ (80.2 mg, 67 mL, 0.36 mmol, 2 eq.) in toluene (6 mL). The reaction mixture was stirred overnight, filtered and layered with *n*-pentane to obtain dark brown crystals which were washed with *n*-pentane and dried *in vacuo*. Crystalline yield: 13.3 mg, 0.006 mmol, 15%.

^{1}H NMR (298 K, CD$_2$Cl$_2$, 400 MHz), δ [ppm] = 8.08–7.97 (m, 4H, Ph$_2$PSS$^-$-*ortho*), 7.68–7.57 (m, 4H, Ph$_2$PS$^-_{intern}$-*ortho*), 7.57–7.35 (m, 18H, Ph$_2$PSS$^-$-*meta*, 2H, Ph$_2$PSS$^-$-*para*, 4H, Ph$_2$PS$^-_{intern}$-*meta*, 2H, Ph$_2$PSS$^-$-*para*, 2H, Ph$_2$P$^-$-*para*, 4H, Ph$_2$PS$^-_{terminal}$-*meta*) 7.30–7.18 (m, 4H, Ph$_2$PS$^-_{terminal}$-*ortho*), 7.18–7.09 (m, 4H, Ph$_2$P$^-$-*meta*), 7.03–6.96 (m, 2H, Ph$_2$PS$^-_{terminal}$-*para*), 6.96–6.85 (m, 4H, Ph$_2$P$^-$-*ortho*).

^{31}P{^{1}H} NMR (298 K, CD$_2$Cl$_2$, 162 MHz), δ [ppm] = 90.1 (ddd, 1 P$_b$, $^2J_{PP}$ = 42.9 Hz, $^3J_{PP}$ = 6.7 Hz, $^3J_{PP}$ = 3.3 Hz, Ph$_2$PS$^-_{intern}$), 73.0 (t, 1 P$_a$, $^3J_{PP}$ = 3.3 Hz, Ph$_2$PSS$^-$), 56.3 (ddd, 1 P$_c$, $^2J_{PP}$ = 42.9 Hz, $^2J_{PP}$ = 31.0 Hz, $^3J_{PP}$ = 3.3 Hz, Ph$_2$P$^-$), 31.0 (dd, 1 P$_d$, $^2J_{PP}$ = 31.0 Hz, $^3J_{PP}$ = 6.7 Hz, Ph$_2$PS$^-_{terminal}$).

^{13}C NMR (298 K, CD$_2$Cl$_2$, 101 MHz), δ [ppm] = 134.3 (d), 133.4–133.0 (m), 132.2 (br), 131.2 (br), 130.2 (d), 128.8 (t), 128.7 (br), 128.4 (br), 127.7 (br), 127.6 (br).

Elemental analysis, calculated [%] for C$_{48}$H$_{40}$Ni$_2$P$_4$S$_4$·0.7 toluene: C 60.46, H 4.37, S 12.2; found: C 60.45, H 4.81, S 11.76.

ATR-IR [cm^{-1}]: $\tilde{v}$ = 3068 (vw), 3049 (vw), 1801 (vw), 1770 (vw), 1699 (vw), 1681 (vw), 1648 (vw), 1581 (w), 1558 (vw), 1539 (vw), 1523 (vw), 1506 (vw), 1475 (w), 1433 (m), 1389 (vw), 1327 (vw), 1306 (w), 1273 (vw), 1182 (w), 1157 (w), 1093 (m), 1068 (w), 1026 (w), 997 (w), 970 (vw), 919 (vw), 847 (vw), 741 (s), 689 (vs), 635 (vw), 619 (vw), 577 (m), 559 (s), 517 (m), 488 (vs).

9.6.5 Diphenylphosphine sulphide-stabilised coinage metal clusters

[Au$_6$(μ$_2$-Ph$_2$PS)$_6$] (20)

[Au(tht)Cl] (40 mg, 0.125 mmol) was either reacted with PPS (50 mg, 0.125 mmol, 1 eq.) or with Ph$_2$PSK (32.0 mg, 0.125 mmol, 1 eq.) in DCM (5 mL). The colourless solution was stirred over night and was afterwards layered with *n*-pentane. After two days colourless crystals, suitable for single-crystal XRD were obtained. The crystals were washed with *n*-pentane and dried *in vacuo*. Crystalline yield: 10.1 mg, 0.004 mmol, 19%.

^{1}H NMR (298 K, CDCl$_3$, 400 MHz), δ [ppm] = 7.82–7.70 (m, 24H, Ar-H-*meta*), 7.46–7.30 (m, 36H, Ar-H-*ortho*, Ar-H-*para*).

^{31}P{^{1}H} NMR (298 K, CDCl$_3$, 162 MHz), δ [ppm] = 50.8 (s, PS$^-$).

Elemental analysis, calculated [%] for $C_{72}H_{60}Au_6P_6S_6 \cdot 0.5$ *n*-pentane: C 35.49, H 2.64, S 7.63; found: C 35.53, H 2.52, S 7.99.

ATR-IR [cm^{-1}]: $\tilde{v}$ = 3066 (w), 1478 (m), 1433 (vs), 1303 (w), 1181 (w), 1090 (s), 1067 (w), 1025 (w), 998 (w), 738 (m), 686 (vs), 619 (w), 569 (m), 560 (m), 515 (vs), 473 (m), 443 (w).

[Cu$_{14}$(μ$_6$-S)$_1$(μ$_3$-Ph$_2$PS)$_{12}$] (21)

CuMes (mesityl copper, 100.0 mg, 0.55 mmol) and Ph$_2$PSH (120.0 mg, 0.55 mmol, 1 eq.) were dissolved in THF (8 mL) and stirred at room temperature. Afterwards, the reaction mixture was filtered off and layered with *n*-heptane or *n*-diethylether. After two days, yellow crystals were obtained suitable for single-crystal XRD. The crystals were washed with *n*-heptane or *n*-diethylether and dried *in vacuo*. Crystalline yield: 16.1 mg, 0.004 mmol, 11%.

^{1}H NMR (298 K, C$_6$D$_6$, 400 MHz): δ [ppm] = 8.17-6.32 (br, all H-atoms).

^{31}P{^{1}H} NMR (298 K, C$_6$D$_6$, 162 MHz): δ [ppm] = 30.8 (br), 23.0 (br); *in solution clusters might degrade.*

^{13}C NMR (298 K, C$_6$D$_6$, 101 MHz): δ [ppm] = 132.1 (br, Ar-C-*meta*), 128.4 (br, Ar-C-*para*), 127.9 (br, Ar-C-*ortho*).

Elemental analysis, calculated [%] for $C_{144}H_{120}Cu_{14}P_{12}S_{13} \cdot THF \cdot$*n*-pentane: C 50.03, H 3.84 S 11.35; found: C 50.58, H 3.64, S 11.34.

ATR-IR [cm^{-1}]: $\tilde{v}$ = 3045 (m), 3012 (w), 1697 (w), 1648 (w), 1539 (w), 1473 (m), 1481 (s), 1298 (w), 1176 (w), 1119 (w), 1086 (m), 1026 (w), 997 (w), 841 (vw), 733 (m), 685 (vs), 529 (w), 503 (s), 471 (w).

HR-MS (ESI): *m/z* calculated for [$C_{144}H_{120}Cu_{14}P_{12}S_{13}$+H]$^+$: 3529.28 [*M*]; found: 3529.24.

[Cu$_{24}$(μ$_5$-S)$_6$(μ$_3$-Ph$_2$PS)$_{12}$] (22)

CuMes (mesityl copper, 100.0 mg, 0.55 mmol) and Ph$_2$PSH (120.0 mg, 0.55 mmol, 1 eq.) were dissolved in toluene (6 mL) and heated to 88°C. After 20 minutes of reaction time, the reaction mixture was filtered and layered either with *n*-heptane or with *n*-diethylether. After two days, orange crystals could be isolated suitable for single-crystal XRD. The crystals were washed with *n*-heptane or *n*-diethylether and dried *in vacuo*. Reaction conditions had to be strictly controlled since otherwise a mixture of **21** and **22** is obtained. Crystalline yield: 17.0 mg, 0.005 mmol, 9%.

^{1}H NMR (298 K, C$_6$D$_6$, 298 K): δ [ppm] = 8.26-6.82 (br, all H-atoms).

^{31}P{^{1}H} NMR (298 K, C$_6$D$_6$, 162 MHz): δ [ppm]= 22.1 (br), 8.3 (br); *in solution clusters might degrade since formation of PPS is visible.*

^{13}C NMR (298 K, C$_6$D$_6$, 101 MHz): δ [ppm]= 132.7 (br, Ar-C-*meta*), 128.4 (br, Ar-C-*para*), 128.0 (br, Ar-C-*ortho*).

Elemental analysis, calculated [%] for $C_{144}H_{120}Cu_{24}P_{12}S_{18}$: C 40.00, H 2.80 S 13.34; found: C 40.01, H 2.50, S 13.02.

ATR-IR [cm^{-1}]: $\tilde{v}$ = 3049 (w), 2982 (m), 2898 (m), 1701 (m), 1655 (m), 1560 (m), 1539 (m), 1522 (w), 1477 (m), 1435 (s), 1255 (w), 1086 (m), 1024 (w), 739 (m), 687 (vs), 528 (m), 507 (vs), 472 (w).

HR-MS (ESI): m/z calculated for [$C_{144}H_{120}Cu_{24}P_{12}S_{18}$+H]$^+$: 4323.43 [$M$]; found: 4323.41.

[Cu$_4$(dppe)$_2$(Ph$_2$PS)$_4$] (23)

For the synthesis of **23**, Ph$_2$P(=S)K (40.0 mg, 0.15 mmol) was stirred in THF (5 mL) with [Cu(MeCN)$_4$]PF$_6$ (49.4 mg, 0.13 mmol, 0.85 eq.) and dppe (15.5 mg, 0.04 mmol, 0.25 eq.) over night. The reaction mixture was filtered and evaporated in *vacuo*. The solid was dissolved in DCM, layered with *n*-heptane to give pale yellow crystals suitable for single-crystal XRD after two days. The crystals were washed with *n*-heptane and dried *in vacuo*. Crystalline yield: 16.3 mg, 0.009 mmol, 22%.

^{1}H NMR (298 K, C$_6$D$_6$, 400 MHz): δ [ppm] = 7.86 (br, 16H, Ph$_2$PS-Ar-H-*ortho*), 7.45 (m, 24H, Ph$_2$PS-Ar-H-*meta+para*), 6.99 (m, 16H, dppe-Ar-H-*ortho*), 6.59 (m, 8H, dppe-Ar-H-*para*), 6.36 (m, 16H, dppe-Ar-H-*meta*), 2.73 (m, 8H, dppe-CH$_2$).

^{31}P{^{1}H} NMR (298 K, C$_6$D$_6$, 162 MHz): δ [ppm] = 20.9 (br, Ph$_2$PS$^-$), −11.2 (br, dppe).

^{13}C NMR (298 K, C$_6$D$_6$, 101 MHz): δ [ppm] = 130.3 (m, Ph$_2$PS-Ar-C-*meta*), 129.5 (br, dppe-Ar-C-*meta*), 128.4 (s, Ph$_2$PS-Ar-C-*para*), 126.9 (s, Ph$_2$PS-Ar-C-*ortho*), 126.7 (br, dppe-Ar-C-*para*), 126.6 (br, dppe-Ar-C-*ortho*), 25.6 (br, dppe-Alkyl-C).

Elemental analysis, calculated [%] for C$_{96}$H$_{92}$Cu$_4$P$_8$S$_4$·1 *n*-pentane: C 62.27, H 5.38 S 6.58; found: C 62.77, H 5.054, S 5.598.

9.6.6 A bench-stable fluorophosphine nickel(0) complex

[Ni(MeCN)$_4$](BF$_4$)$_2$

[Ni(MeCN)$_4$](BF$_4$)$_2$ was synthesised according to modified literature procedures.[340] Therefore, a solution of NOBF$_4$ (2g) in MeCN was added to a suspension of Ni (0.5 g) in MeCN. Activation of the reaction could be achieved through heating and the reaction mixture was stirred over night. When no further gas formation can be observed, the mixture is stirred for additional 3 hours and filtered afterwards. Diethylether is added to the blue solution and at 4°C, purple-blue crystals of the title compound can be grown. Attention has to be paid due to the gas formation during the whole course of the reaction. Therefore, a suitable gas relief has to be ensured.

[Ni(PFPh$_2$)$_4$] (24)

PPO (109.0 mg, 0.282 mmol, 2 eq.) and [Ni(MeCN)$_4$](BF$_4$)$_2$ (56.0 mg, 0.141 mmol) were stirred for two hours in DCM (5 mL). A colour change from blue-greenish to brown can be observed during the course of the reaction. Subsequent filtration and layering with MeCN provided yellow needle-like crystals suitable for single-crystal XRD overnight. The crystals were washed with MeCN and dried *in vacuo*. Crystalline yield: 30.6 mg, 0.035 mmol, 25%.

m.p.: At 161°C **24** starts to decompose in the solid state

^{1}H NMR (298 K, C_6D_6, 400 MHz): δ [ppm] = 7.53 (br, 16H, Ar-H-*meta*), 6.92 (br, 16H, Ar-H-*ortho*), 6.91 (br, 8H; Ar-H-*para*).

^{31}P{^{1}H} NMR (298 K, C_6D_6, 162 MHz): δ [ppm] = 173.1 (AA'A''A'''XX'X''X''', $^2J_{PP}$ = 23.26 Hz, $^1J_{PF}$ = 850.25 Hz, $^3J_{PF}$ = 45.50 Hz).

^{13}C NMR (298 K, C_6D_6, 101 MHz): δ [ppm] = 130.3 (br, Ar-C-*meta*), 129.0 (s, Ar-C-*para*), 127.7 (s, Ar-C-*ortho*, signal is superimposed by solvent).

^{13}C NMR (298 K, CD_2Cl_2, 101 MHz): δ [ppm] = 130.0 (br, Ar-C-*meta*), 129.5 (s, Ar-C-*para*), 128.0 (s, Ar-C-*ortho*).

^{19}F{^{1}H} NMR (298 K, C_6D_6, 377 MHz): δ [ppm] = −134.5 (AA'A''A'''XX'X''X''', $^1J_{PF}$ = 850.25 Hz, $^3J_{PF}$ = 45.50 Hz, $^4J_{FF}$ = 1.4 Hz).

^{11}B NMR (298 K, C_6D_6, 96 MHz) δ [ppm] = no signal.

Elemental analysis, calculated [%] for $C_{48}H_{40}F_4NiP_4$: C 65.86, H 4.61; found: C 66.11, H 4.228.

ATR-IR [cm^{-1}]: $\tilde{v}$ = 3542(w), 3051(w), 3015(vw), 2948(vw), 2917(w), 2846(vw), 1548(vw), 1571(w), 1478(w), 1431(m), 1397(vw), 1373(vw), 1310(w), 1276(vw), 1234(w), 1182(vw), 1154(w), 1127(vw), 1098(s), 1068(w), 1023(w), 997(w), 981(w), 927(vw), 912(vw), 858(vw), 754(w), 743(w), 729(vs), 692(vs), 615(w), 523(s), 489(m), 459(m), 435(m).

HR-MS (ESI): *m/z* calculated for $[C_{48}H_{40}F_4NiP_4+H]^+$: 875.14 [*M*]; found: 875.14.

UV/Vis in DCM, [nm] ([mol^{-1}dm^{3}cm^{-1}]): λ_{max} (ε) = 310 (6600), 235 (10200).

[Ph$_2$PO$_2$(BF$_2$)$_2$O$_2$PPh$_2$] (25)

If the reaction mixture (DCM) of **24** is layered with *n*-pentane or *n*-heptane instead of MeCN, colourless crystals of **25** and **26** could be obtained suitable for single-crystal XRD. It should be mentioned that the formation of **25** also occurs if the reaction is conducted in an Argon-filled glovebox under the complete exclusion of air to prove that **25** is not formed due to air-contamination.

^{1}H and ^{13}C NMR spectra are influenced by the paramagnetic character of **25**.

^{31}P{^{1}H} NMR (298 K, CDCl$_3$, 162 MHz): δ [ppm] = 33.6 (m, $^3J_{PF}$ = 10.9 Hz).

^{19}F{^{1}H} NMR (298 K, CDCl$_3$, 377 MHz): δ [ppm] = −139.9 (m, $^3J_{PF}$ = 10.9 Hz).

^{11}B NMR (298 K, CDCl$_3$, 96 MHz): δ [ppm] = −0.5.

It should be noted that in ^{31}P and ^{19}F NMR spectra, the formation of Ph$_2$P(=O)F can be observed, which is due to deoxyfluorination of Ph2POO$^-$.

[Ni(OPOPh$_2$)$_6$(BF)$_2$] (26)

If the reaction mixture (DCM) of **24** is layered with *n*-pentane or *n*-heptane instead of MeCN, colourless crystals of **25** and **26** could be obtained, suitable for single-crystal XRD. Compound **26** is also formed if the reaction is conducted in an Argon-filled glovebox to ensure complete

exclusion of air. This procedure proves that the formation of **26** is a result of the formation mechanism of **24** and that the oxygen stems from the PPO ligand. **26** can also be obtained if the synthesis of **24** is conducted for five hours under a controlled addition of air into the reaction mixture. Filtering and layering the reaction solution with *n*-heptane provides pale yellow crystals of **26**.

No ^{1}H, ^{31}P and ^{13}C signals can be detected due to paramagnetic character.

^{19}F{^{1}H} NMR (298 K, CDCl$_3$, 400 MHz): δ [ppm] = −147.2 (d, $^1J_{BF}$ = 11.0 Hz).

^{11}B NMR (298 K, CDCl$_3$, 96 MHz): δ [ppm] = −0.8.

Isolation of Ph$_2$PPPh$_2$ (27)

Ph$_2$PPPh$_2$ could be isolated as a by-product of the synthesis of **24**. Therefore, the obtained crystal mixture from layering the reaction solution with *n*-pentane was washed with acetonitrile. Whereas **24** remains undissolved, other compounds are dissolved in MeCN. MeCN was evaporated *in vacuo* up to the point where the precipitation of the colourless solid can be observed. The brownish supernatant was filtered off and the colourless powder of **27** was carefully washed with MeCN and dried *in vacuo*.

^{1}H NMR (298 K, CD$_3$CN, 400 MHz): δ [ppm] =7.48–7.41 (m, 8H, Ar-H-*meta*), 7.35–7.21 (m, 12H, Ar-H-*ortho/para*).

^{31}P{^{1}H} NMR (298 K, CD$_3$CN, 162 MHz): δ [ppm] = −18.1 (s).

^{13}C NMR (298 K, CD$_3$CN, 101 MHz): δ [ppm] = 136.7 (br, Ar-C-*meta*), 135.2 (m, Ar-C-*meta*), 130.1 (br, Ar-C-*ortho*/*para*), 129.5 (br, Ar-C-*ortho*/*para*).

^{19}F{^{1}H} NMR (298 K, CD$_3$CN, 377 MHz): δ [ppm] = no signal.

^{11}B NMR (298 K, CD$_3$CN, 96 MHz): δ [ppm] = no signal.

Elemental analysis, calculated [%] for C$_{24}$H$_{20}$P$_2$: C 77.83, H 5.44; found: C 78.39, H 4.918.

10 Literature

1.   P. W. N. M. v. Leeuwen, *Homogeneous Catalysis: Understanding the Art*, Springer Dordrecht, 2004.
2.   A. L. Clevenger, R. M. Stolley, J. Aderibigbe and J. Louie, *Chem. Rev.*, 2020, **120**, 6124-6196.
3.   P. W. N. M. v. Leeuwen, P. C. J. Kamer and J. N. H. Reek, *Pure Appl. Chem.*, 1999, **71**, 1443-1452.
4.   P. Dierkes and P. W. N. M. v. Leeuwen, *J. Chem. Soc., Dalton Trans.*, 1999, 1519-1530.
5.   C. Fliedel, A. Ghisolfi and P. Braunstein, *Chem. Rev.*, 2016, **116**, 9237-9304.
6.   P. W. N. M. v. Leeuwen and P. C. J. Kamer, *Catal. Sci. Technol.*, 2018, **8**, 26-113.
7.   A. Miyashita, H. Takaya, T. Souchi and R. Noyori, *Tetrahedron*, 1984, **40**, 1245-1253.
8.   H. Nöth and L. Meinel, *Z. Anorg. Allg. Chem.*, 1967, **349**, 225-240.
9.   O. Schmitz-DuMont, B. Ross and H. Klieber, *Angew. Chem., Int. Ed.*, 1967, **6**, 875-876.
10.   T. Appelby and J. D. Woollins, *Coord. Chem. Rev.*, 2002, **235**, 121-140.
11.   H. Einspahr and J. Donohue, *Inorg. Chem.*, 1974, **13**, 1839-1843.
12.   E. H. Wong, L. Prasad, E. J. Gabe and F. C. Bradley, *J. Organomet. Chem.*, 1982, **236**, 321-331.
13.   E. H. Wong, R. M. Ravenelle, E. J. Gabe, F. L. Lee and L. Prasad, *J. Organomet. Chem.*, 1982, **233**, 321-331.
14.   I. F. Lutsenko and V. L. Foss, *Pure Appl. Chem.*, 1980, **52**, 917-944.
15.   S. Yogendra, S. S. Chitnis, F. Hennersdorf, M. Bodensteiner, R. Fischer, N. Burford and J. J. Weigand, *Inorg. Chem.*, 2016, **55**, 1854-1860.
16.   F. Flecken and S. Hanf, *Dalton Trans.*, 2024, **53**, 17123-17131.
17.   Y. Sato, S.-i. Kawaguchi, A. Nomoto and A. Ogawa, *Chem. Eur. J.*, 2018, **25**, 2295-2302.
18.   Z. Fei, R. Scopelliti and P. J. Dyson, *EurJIC*, 2004, **2004**, 530-537.
19.   Z. Fei, N. Biricik, D. Zhao, R. Scopelliti and P. J. Dyson, *Inorg. Chem.*, 2004, **43**, 2228-2230.
20.   A. B. Burg and J. Heners, *J. Am. Chem. Soc.*, 1965, **87**, 3092-3097.
21.   R. D. Riley, K. N. Robertson and J. A. C. Clyburne, *Can. J. Chem.*, 2022, **100**, 737-750.
22.   H. Liu, M. J. Calhorda, M. G. B. Drew, V. Félix, J. Novosad, L. F. Veiros, F. F. d. Biani and P. Zanello, *J. Chem. Soc., Dalton Trans.*, 2002, 4365-4374.
23.   D. Hunter, J. K. Michie and W. Stewart, *Phosphorus Sulfur Relat. Elem.*, 1981, **10**, 267-270.
24.   S. Jin, G. C. Haug, V. T. Nguyen, C. Flores-Hansen, H. D. Arman and O. V. Larionov, *ACS Catal.*, 2019, **9**, 9764-9774.
25.   V. L. Foss, V. A. Solodenko and I. F. Lutsenko, *Zh. Obshch. Khim.*, 1979, **49**, 2418-2428.
26.   S. Inokawa, Y. Tanaka, H. Yoshida and T. Ogata, *Chem. Lett.*, 1972, **1**, 469-470.
27.   P. E. Sues, A. J. Lough and R. H. Morris, *Chem. Commun.*, 2014, **50**, 4707-4710.
28.   K. M. Cooke, T. P. Kee, A. L. Langton and M. Thornton-Pett, *J. Organomet. Chem.*, 1991, **419**, 171-180.
29.   C.-Y. Chen and R. J. W. L. Fèvre, *J. Chem. Soc.*, 1965, 3473-3504.
30.   R. F. Hudson, R. J. G. Searle and F. H. Devitt, *J. Chem. Soc. B*, 1966, 789-792.
31.   M. Gruber, P. G. Jones and R. Schmutzler, *Chem. Ber.*, 1990, **123**, 1313-1317.
32.   M. Aydemir, A. Baysal and B. Gümgüm, *J. Organomet. Chem.*, 2008, **693**, 3810-3814.
33.   S. Priya, M. S. Balakrishna and S. M. Mobin, *Polyhedron*, 2005, **24**, 1641-1650.
34.   T. Posset, F. Rominger and J. Blümel, *Chem. Mater.*, 2005, **17**, 586-595.
35.   K. Naktode, R. K. Kottalanka, H. Adimulam and T. K. Panda, *J. Coord. Chem.*, 2014, **67**, 3042-3053.
36.   R. S. Davidson, R. A. Sheldon and S. Trippett, *J. Chem. Soc. C*, 1967, 1547-1552.

37. D. J. Irvine, C. Glidewell, D. J. Cole-Hamilton, J. C. Barnes and A. Howie, *J. Chem. Soc., Dalton Trans.*, 1991, 1756-1772.
38. Y. Sato, S.-i. Kawaguchi, A. Nomoto and A. Ogawa, *Synth.*, 2017, **49**, 3558-3567.
39. J. L. Virlichie and P. Dagnac, *Rev. Chim. Miner.*, 1977, **14**, 355-358.
40. W. Dabkowski, A. Ozarek, S. Olejniczak, M. Cypryk, J. Chojnowski and J. Michalski, *Chem. Eur. J.*, 2009, **15**, 1747-1756.
41. Y. Sato, S.-i. Kawaguchi, A. Nomoto and A. Ogawa, *Angew. Chem., Int. Ed.*, 2016, **55**, 9700-9703.
42. Y. Yamamoto, R. Tanaka, M. Ota, M. Nishimura, C. C. Tran, S.-i. Kawaguchi, S. Kodama, A. Nomoto and A. Ogawa, *J. Org. Chem.*, 2020, **85**, 14708-14719.
43. Y. Yamamoto and A. Ogawa, *Chem. Asian J.*, 2023, **18**, e202201269.
44. H. Takano, H. Katsuyama, H. Hayashi, W. Kanna, Y. Harabuchi, S. Maeda and T. Mita, *Nat. Commun.*, 2022, **13**, 7034.
45. J. Yang, L. Fan, C. Chen, M. Wang, B. Sun, S. Wang, H. Zhong and Y. Zhou, *Org. Biomol. Chem.*, 2023, **21**, 494-498.
46. S.-i. Kawaguchi, M. Kotani, T. Ohe, S. Nagata, A. Nomoto, M. Sonoda and A. Ogawa, *Phosphorus Sulfur Silicon Relat. Elem.*, 2010, **185**, 1090-1097.
47. Y. Yamamoto, K. Fujiwara and A. Ogawa, *Organometallics*, 2023, **42**, 2590-2597.
48. P. W. N. M. v. Leeuwen, I. Cano and Z. Freixa, *ChemCatChem*, 2020, **12**, 3982-3994.
49. P. Braunstein, J. Durand, X. Morise, A. Tiripicchio and F. Ugozzoli, *Organometallics*, 2000, **19**, 444-450.
50. Y. Yang, K. A. Abboud and L. McElwee-White, *Dalton Trans.*, 2003, 4288-4296.
51. S. Becker, *ChemPlusChem*, 2024, **89**, e202300619.
52. M. Dahlen, N. Reinfandt, C. Jin, M. T. Gamer, K. Fink and P. W. Roesky, *Chem. Eur. J.*, 2021, **27**, 15128-15136.
53. P. G. Jones, A. K. Fischer, M. Farkens and R. Schmutzler, *Acta. Cryst. E*, 2002, **58**, m478-m479.
54. T. S. Sukhikh, R. M. Khisamov and S. N. Konchenko, *Molecules*, 2021, **26**, 2030.
55. S. G. Bott, J. C. Wang and M. G. Richmond, *J. Chem. Crystallogr.*, 1999, **29**, 603-608.
56. F.-Y. Chen, M.-Y. Hu, X.-L. Gu, X.-F. Liu and P.-H. Zhao, *Transit. Met. Chem.*, 2021, **46**, 645-653.
57. L.-C. Song, M. Cao, Z.-Q. Du, Z.-H. Feng, Z. Ma and H.-B. Song, *EurJIC*, 2014, **2014**, 1886-1895.
58. Y.-F. Liu, *Inorg. Chim. Acta*, 2011, **378**, 338-341.
59. X.-F. Liu and X.-Y. Yu, *Acta. Cryst. E*, 2011, **67**, m1552.
60. M. R. Kopp and B. Neumüller, *Z. Anorg. Allg. Chem.*, 1999, **625**, 739-745.
61. T. Ogawa, Y. Kajita and H. Masuda, *Acta. Cryst. E*, 2009, **65**, m1129.
62. A. M. Lifschitz, N. A. Hirscher, H. B. Lee, J. A. Buss and T. Agapie, *Organometallics*, 2017, **36**, 1640-1648.
63. V. R. Naina, A. K. Singh, S. Shubham, F. Krätschmer, S. Lebedkin, M. M. Kappes and P. W. Roesky, *Dalton Trans.*, 2023, **52**, 12618-12622.
64. V. W.-W. Yam, W. K.-M. Fung and M.-T. Wong, *Organometallics*, 1997, **16**, 1772-1778.
65. S. Naik, S. Kumar, J. T. Mague and M. S. Balakrishna, *Dalton Trans.*, 2016, **45**, 18434-18437.
66. A. Ghisolfi, F. Condello, C. Fliedel, V. Rosa and P. Braunstein, *Organometallics*, 2014, **34**, 2255-2260.
67. K. Blann, A. Bollmann, J. T. Dixon, F. M. Hess, E. Killian, H. Maumela, D. H. Morgan, A. Neveling, S. Otto and M. J. Overett, *Chem. Commun.*, 2005, 620-621.
68. R. J. Puddephatt, *Chem. Soc. Rev.*, 1983, **12**, 99-127.
69. I. Cano, M. A. Huertos, A. M. Chapman, G. Buntkowsky, T. Gutmann, P. B. Groszewicz and P. W. N. M. v. Leeuwen, *J. Am. Chem. Soc.*, 2015, **137**, 7718-7727.
70. E. H. Wong, F. C. Bradley, L. Prasad and E. J. Gabe, *J. Organomet. Chem.*, 1984, **263**, 167-177.
71. C. Zeiher, J. Mohyla, I. P. Lorenz and W. Hiller, *J. Organomet. Chem.*, 1985, **286**, 159-170.

72. A. D. Burrows, M. F. Mahon, M. T. Palmer and M. Varrone, *Inorg. Chem.*, 2002, **41**, 1695-1697.
73. Y. Zhao, Y. Zhou, T. Chen, S.-F. Yin and L.-B. Han, *Inorg. Chim. Acta*, 2014, **422**, 36-39.
74. Y. Zhou, S. Yin, Y. Gao, Y. Zhao, M. Goto and L.-B. Han, *Angew. Chem., Int. Ed.*, 2010, **49**, 6852-6855.
75. A. Aloisi, J.-C. Berthet, C. Genre, P. Thuéry and T. Cantat, *Dalton Trans.*, 2016, **45**, 14774-14788.
76. M. P. Duffy, Y. Lin, L. Y. Ting and F. Mathey, *New J. Chem.*, 2011, **35**, 2001-2003.
77. S. Hoehne, E. Lindner and J.-P. Gumz, *Chem. Ber.*, 1978, **111**, 3818-3822.
78. F. C. Bradley, E. H. Wong, E. J. Gabe, F. L. Lee and Y. Lepage, *Polyhedron*, 1987, **6**, 1103-1110.
79. J. Bravo, J. Castro, S. García-Fontán, M. C. Rodríguez-Martínez and P. Rodríguez-Seoane, *EurJIC*, 2006, **2006**, 3028-3040.
80. S. Pavlik, K. Mereiter, M. Puchberger and K. Kirchner, *Organometallics*, 2005, **24**, 3561-3575.
81. D. J. Irvine, D. J. Cole-Hamilton, J. Barnes and P. K. G. Hodgson, *Polyhedron*, 1989, **8**, 1575-1577.
82. E. Piras, B. Powietzka, F. Wurst, D. Neumann-Walter, H.-J. Grützmacher, T. Otto, T. Zevaco and O. Walter, *Catal. Letters*, 2013, **143**, 673-680.
83. F. A. Cotton, L. R. Falvello, M. Tomas, G. M. Gray and C. S. Krainhanzel, *Inorg. Chim. Acta*, 1984, **82**, 129-139.
84. Hubert Schmidbaur and Annette Schier, *Chem. Soc. Rev.*, 2012, **41**, 370-412.
85. F. Scherbaum, A. Grohmann, B. Huber, C. Krüger and H. Schmidbaur, *Angew. Chem., Int. Ed.*, 1988, **27**, 1544-1546.
86. J. Campos, *Nat. Rev. Chem.*, 2020, **4**, 696-702.
87. M. H. Pérez-Temprano, J. A. Casares, Á. R. d. Lera, R. Álvarez and P. Espinet, *Angew. Chem., Int. Ed.*, 2012, **51**, 4917-4920.
88. M. Knorr and C. Strohmann, *Organometallics*, 1999, **18**, 248-257.
89. M. Haehnel, S. Hansen, A. Spannenberg, P. Arndt, T. Beweries and U. Rosenthal, *Chem. Eur. J.*, 2012, **18**, 10546-10553.
90. P. Steil, U. Nagel and W. Beck, *J. Organomet. Chem.*, 1989, **366**, 85-93.
91. J. Parr, M. B. Smith and M. R. J. Elsegood, *J. Organomet. Chem.*, 2002, **664**, 85-93.
92. G. R. M. Dowson, M. F. Haddow, J. Lee, R. L. Wingad and D. F. Wass, *Angew. Chem., Int. Ed.*, 2013, **52**, 9005-9008.
93. R. Fischer, J. Langer, A. Malassa, D. Walther, H. Görls and G. Vaughan, *Chem. Commun.*, 2006, 2510-2512.
94. M. M. Olmstead, C. L. Lee and A. L. Balch, *Inorg. Chem.*, 2002, **21**, 2712-2716.
95. F. Faraone, G. Bruno, S. L. Schiavo, G. Tresoldi and G. Bombieri, *J. Chem. Soc., Dalton Trans.*, 1983, 433-438.
96. J. C. Jeffrey and T. B. Rauchfuss, *Inorg. Chem.*, 1979, **18**, 2658-2666.
97. T. S. Sukhikh, R. M. Khisamov, D. A. Bashirov, V. Y. Komarov, M. S. Molokeev, A. A. Ryadun, E. Benassi and S. N. Konchenko, *Cryst. Growth Des.*, 2020, **20**, 5796-5807.
98. H. Yersin, A. F. Rausch, R. Czerwieniec, T. Hofbeck and T. Fischer, *Coord. Chem. Rev.*, 2011, **255**, 2622-2652.
99. A. Barbieri, G. Accorsi and N. Armaroli, *Chem. Commun.*, 2008, 2185-2193.
100. P.-T. Chou, Y. Chi, M.-W. Chung and C.-C. Lin, *Coord. Chem. Rev.*, 2011, **255**, 2653-2665.
101. A. Jabłoński, *Zeitschrift für Physik*, 1935, **94**, 38-46.
102. J. R. Lakowicz, *Principles of Fluorescence Spectroscopy*, Springer New York, New York, 3 edn., 2006.
103. H. Yersin, R. Czerwieniec, U. Monkowius, R. Ramazanov, R. Valiev, M. Z. Shafikov, W.-M. Kwok and C. Ma, *Coord. Chem. Rev.*, 2023, **478**, 214975.
104. J. Föller, M. Kleinschmidt and C. M. Marian, *Inorg. Chem.*, 2016, **55**, 7508-7516.
105. L. Lv, K. Liu, K. Yuan, Y. Zhu and Y. Wang, *RSC Adv.*, 2018, **8**, 28421-28432.

106. Y. Zhang, M. Schulz, M. Wächtler, M. Karnahl and B. Dietzek, *Coord. Chem. Rev.*, 2018, **356**, 127-146.
107. S. C. Vincenzo Balzani, *Photochemistry and Photophysics of Coordination Compounds I*, Springer, Heidelberg, 2007.
108. R. H. Adnan, J. M. L. Madridejos, A. S. Alotabi, G. F. Metha and G. G. Andersson, *Adv. Sci.*, 2022, **9**, 2105692.
109. Y. Yamazaki, T. Tsukuda, S. Furukawa, A. Dairiki, S. Sawamura and T. Tsubomura, *Inorg. Chem.*, 2020, **59**, 12375-12384.
110. S.-M. Kuang, D. G. Cuttell, D. R. McMillin, P. E. Fanwick and R. A. Walton, *Inorg. Chem.*, 2002, **41**, 1772-1778.
111. R. Donamaría, V. Lippolis, J. M. López-de-Luzuriaga, M. Monge, M. Nieddu and M. E. Olmos, *Inorg. Chem.*, 2018, **57**, 11099-11112.
112. A. Ghisolfi, C. Fliedel, P. d. Frémont and P. Braunstein, *Dalton Trans.*, 2017, **46**, 5571.
113. M. Nazari and H. R. Shahsavari, *Appl. Organomet. Chem.*, 2019, **33**, e5020.
114. T.-C. Cheung, K.-K. Cheung, S.-M. Peng and C.-M. Che, *J. Chem. Soc., Dalton Trans.*, 1996, 1645-1651.
115. D. Li, C.-M. Che, W.-T. Wong, S.-J. Shieh and S.-M. Peng, *J. Chem. Soc., Dalton Trans.*, 1993, 653-654.
116. E. Leoni, J. Mohanraj, M. Holler, M. Mohankumar, I. Nierengarten, F. Monti, A. Sournia-Saquet, B. Delavaux-Nicot, J.-F. i. Nierengarten and N. Armaroli, *Inorg. Chem.*, 2018, **57**, 15537-15549.
117. Chi-Ming Che, Hoi-Lun Kwong, V. Wing-Wah Yam and Kar-Cheong Cho, *J. Chem. Soc., Chem. Commun.*, 1989, 885-886.
118. J. S. Field, J. Grieve, R. J. Haines, N. May and M. M. Zulu, *Polyhedron*, 1998, **17**, 3021-3029.
119. R. Provencher and P. D. Harvey, *Inorg. Chem.*, 1996, **35**, 2235-2241.
120. J. K. Bera, M. Nethaji and A. G. Samuelson, *Inorg. Chem.*, 1999, **38**, 218-228.
121. R. Franke, D. Selent and A. Börner, *Chem. Rev.*, 2012, **112**, 5675-5732.
122. Z. Freixa and P. W. N. M. v. Leeuwen, *Dalton Trans.*, 2003, 1890-1901.
123. C. A. Tolman, *J. Am. Chem. Soc.*, 1970, **92**, 2956-2965.
124. S. M. Mansell, *Dalton Trans.*, 2017, **46**, 15157-15174.
125. P. W. N. M. v. Leeuwen, Paul C. J. Kamer, J. N. H. Reek and P. Dierkes, *Chem. Rev.*, 2000, **100**, 2741-2770.
126. C. A. Tolman, *Chem. Rev.*, 1977, **77**, 313-348.
127. J. N. L. Dennett, A. L. Gillon, K. Heslop, D. J. Hyett, J. S. Fleming, C. E. Lloyd-Jones, A. G. Orpen, P. G. Pringle, D. F. Wass, J. N. Scutt and R. H. Weatherhead, *Organometallics*, 2004, **23**, 6077-6079.
128. N. A. Cooley, S. M. Green, D. F. Wass, K. Heslop, A. G. Orpen and P. G. Pringle, *Organometallics*, 2001, **20**, 4769-4771.
129. S. J. Dossett, A. Gillon, A. G. Orpen, J. S. Fleming, P. G. Pringle, D. F. Wass and M. D. Jones, *Chem. Commun.*, 2001, 699-700.
130. C. S. Browning and D. H. Farrar, *J. Chem. Soc., Dalton Trans.*, 1995, 521-530.
131. A. M. King, H. A. Sparkes, R. L. Wingad and D. F. Wass, *Organometallics*, 2020, **39**, 3873-3878.
132. S. M. Reid, J. T. Mague and M. J. Fink, *J. Am. Chem. Soc.*, 2001, **123**, 4081-4082.
133. T. Kohara, T. Yamamoto and A. Yamamoto, *J. Organomet. Chem.*, 1980, **192**, 265-274.
134. H.-L. Shek, C.-F. Yeung, L.-H. Chung and C.-Y. Wong, *Polyhedron*, 2021, **197**, 115023.
135. B. Hao, F. Alam, Y. Jiang, L. Wang, H. Fan, J. Ma, Y. Chen, Y. Wang and T. Jiang, *Inorg. Chem. Front.*, 2023, **10**, 2860-2902.
136. T. Imamoto, *Chem. Rev.*, 2024, **124**, 8657-8739.
137. J. C. Córdoba, A. Vidal-Ferran, M. Font-Bardia and A. Grabulosa, *Organometallics*, 2020, **39**, 2511-2525.
138. A. Togni, C. Breutel, A. Schnyder, F. Spindler, H. Landert and A. Tijani, *J. Am. Chem. Soc.*, 1994, **116**, 4062-4066.

139.   T. P. Dang and H. B. Kagan, *J. Chem. Soc. D*, 1971, 481.
140.   T. P. Yoon and E. N. Jacobsen, *Science*, 2003, **299**, 1691-1693.
141.   Y. Yamanoi and T. Imamoto, *J. Org. Chem.*, 1999, **64**, 2988-2989.
142.   G. Hoge, H.-P. Wu, W. S. Kissel, D. A. Pflum, D. J. Greene and J. Bao, *J. Am. Chem. Soc.*, 2004, **126**, 5966-5967.
143.   M. Revés, C. Ferrer, T. León, S. Doran, P. Etayo, A. Vidal-Ferran, A. Riera and X. Verdaguer, *Angew. Chem., Int. Ed.*, 2010, **49**, 9452-9455.
144.   E. Cristóbal-Lecina, P. Etayo, S. Doran, M. Revés, P. Martín-Gago, A. Grabulosa, A. R. Costantino, A. Vidal-Ferran, A. Riera and X. Verdaguer, *Adv. Synth. Catal.*, 2014, **356**, 795-804.
145.   T. León, A. Riera and X. Verdaguer, *J. Am. Chem. Soc.*, 2011, **133**, 5740-5743.
146.   L. Ackermann, *Synth.*, 2006, **2006**, 1557-1571.
147.   G. Y. Li and W. J. Marshall, *Organometallics*, 2002, **21**, 590-591.
148.   D. Zell, S. Warratz, D. Gelman, S. J. Garden and L. Ackermann, *Chem. Eur. J.*, 2015, **22**, 1248-1252.
149.   P. W. N. M. v. Leeuwen, C. F. Roobeek, J. H. G. Frijns and A. G. Orpen, *Organometallics*, 1990, **9**, 1211-1222.
150.   I. Cano, L. M. Martínez-Prieto, L. Vendier and P. W. N. M. v. Leeuwen, *Catal. Sci. Technol.*, 2018, **8**, 221-228.
151.   T. M. Shaikh, C.-M. Weng and F.-E. Hong, *Coord. Chem. Rev.*, 2012, **256**, 771-803.
152.   J. R. Khusnutdinova and D. Milstein, *Angew. Chem., Int. Ed.*, 2015, **54**, 12236-12273.
153.   T. Ghaffar and A. W. Parkins, *Tetrahedron Lett.*, 1995, **36**, 8657-8860.
154.   F. Flecken, T. Grell and S. Hanf, *Dalton Trans.*, 2022, **51**, 8975–8985.
155.   S. D. Orth, M. R. Terry, K. A. Abboud, B. Dodson and L. McElwee-White, *Inorg. Chem.*, 1996, **35**, 916-922.
156.   Y. Peng, H. Kaemmerer and A. K. Powell, *Chem. Eur. J.*, 2021, **27**, 15044-15066.
157.   M. Wallesch, M. Nieger, D. Volz and S. Bräse, *Inorg. Chem. Commun.*, 2017, **86**, 232-240.
158.   T.-H. Huang, M.-H. Zhang, M.-L. Tao and X.-J. Wang, *Synth. React. Inorg. M.*, 2014, **44**, 986-990.
159.   M. I. Bruce, B. K. Nicholson, B. W. Skelton, A. H. White and N. N. Zaitseva, *Inorg. Chim. Acta*, 2016, **453**, 647-653.
160.   J. A. Dean, *Lange's Handbook Of Chemistry*, McGraw-Hill Professional Publishing, University of Virginia, 15 edn., 1998.
161.   P. Lange, A. Schier and H. Schmidbaur, *Z. Naturforsch. B*, 1997, **52**, 769.
162.   P. C. Healy, *Acta. Cryst. E,* 2003, **59**, m1112-m1114.
163.   Q.-Y. Cao, B. Yin and J.-H. Liu, *Acta. Cryst. E*, 2006, **62**, m2730-m2731.
164.   D. Li, X. Sun, N. Shao, G. Zhang, S. Li, H. Zhou, J. Wu and Y. Tian, *Polyhedron*, 2015, **93**, 17-22.
165.   S. Pal, N. Kathewad, R. Pant and S. Khan, *Inorg. Chem.*, 2015, **54**, 10172-10183.
166.   I. J. B. Lin, J. M. Hwang, D.-F. Feng, M. C. Cheng and Y. Wang, *Inorg. Chem.*, 1994, **33**, 3467-3472.
167.   A. Bauer and H. Schmidbaur, *J. Chem. Soc., Dalton Trans.*, 1997, 1115-1116.
168.   R. C. Dobbie, M. J. Hopkinson and B. P. Straughan, *J. Mol. Struct.*, 1974, **23**, 141-143.
169.   N. Kathewad, N. Kumar, R. Dasgupta, M. Ghosh, S. Pal and S. Khan, *Dalton Trans.*, 2019, **48**, 7274-7280.
170.   M. E. S. Moussa, S. Evariste, H.-L. Wong, L. L. Bras, C. Roiland, L. L. Polles, B. L. Guennic, K. Costuas, V. W.-W. Yam and C. Lescop, *Chem. Commun.*, 2016, **52**, 11370-11373.
171.   W.-F. Fu, X. Gan, C.-M. Che, Q.-Y. Cao, Z.-Y. Zhou and N. N.-Y. Zhu, *Chem. Eur. J.*, 2004, **10**, 2228-2236.
172.   D. Volz, M. Nieger, J. Friedrichs, T. Baumann and S. Bräse, *Langmuir*, 2013, **29**, 3034-3044.
173.   D. M. Zink, M. Bächle, T. Baumann, M. Nieger, M. Kühn, C. Wang, W. Klopper, U. Monkowius, T. Hofbeck, H. Yersin and S. Bräse, *Inorg. Chem.*, 2012, **52**, 2292-2305.

174. A. V. Shamsieva, E. I. Musina, T. P. Gerasimova, I. D. Strelnik, A. G. Strelnik, I. E. Kolesnikov, A. A. Kalinichev, D. R. Islamov, A. I. Samigullina, P. Lönnecke, S. A. Katsyuba, E. Hey-Hawkins, A. A. Karasik and O. G. Sinyashin, *Dalton Trans.*, 2020, **49**, 11997-12008.
175. F. Monnier and M. Taillefer, *Angew. Chem., Int. Ed.*, 2009, **48**, 6954-6971.
176. X. Ribas and I. Güell, *Pure Appl. Chem.*, 2014, **86**, 345-360.
177. G.-G. Luo, R.-B. Huang, L.-R. Lin and L.-S. Zheng, *Inorg. Chem. Commun.*, 2008, **11**, 818-821.
178. J. L. Shott, M. B. Freeman, N.-A. Saleh, D. S. Jones, D. W. Paley and C. Bejger, *Inorg. Chem.*, 2017, **56**, 10984-10990.
179. W.-B. Zhou, Z.-C. Dong, J.-L. Song, H.-Y. Zeng, R. Cao, G.-C. Guo, J.-S. Huang and J. Li, *J. Clust. Sci.*, 2002, **13**, 119-136.
180. J. Ruiz, M. P. Gonzalo, M. Vivanco, R. Quesada and M. E. G. Mosquera, *Dalton Trans.*, 2009, 9280-9290.
181. A. Zavras, G. N. Khairallah, T. U. Connell, J. M. White, A. J. Edwards, P. S. Donnelly and R. A. J. O. Hair, *Angew. Chem., Int. Ed.*, 2013, **52**, 8392-8394.
182. J. Ellermann, M. Schütz, F. W. Heinemann, M. Moll and W. Bauer, *Z. Naturforsch. B*, 1997, **52**, 795-800.
183. R. Ahuja, M. Nethaji and A. G. Samuelson, *Inorg. Chim. Acta*, 2011, **372**, 220-226.
184. D. A. Morgenstern, R. E. Wittrig, P. E. Fanwick and C. P. Kubiak, *J. Am. Chem. Soc.*, 1993, **115**, 6470-6471.
185. D. A. Morgenstern, Gregory M. Ferrence, John Washington, Jason I. Henderson, L. Rosenheim, J. D. Heise, P. E. Fanwick and C. P. Kubiak, *J. Am. Chem. Soc.*, 1996, **118**, 2198-2207.
186. V. R. Naina, A. K. Singh, P. Rauthe, S. Lebedkin, M. T. Gamer, M. M. Kappes, A.-N. Unterreiner and P. W. Roesky, *Chem. Eur. J.*, 2023, **29**, e202300497.
187. P. Kögerler, B. Tsukerblat and A. Müller, *Dalton Trans.*, 2009, **39**, 21-36.
188. E. T. Spielberg, A. Gilb, D. Plaul, D. Geibig, D. Hornig, D. Schuch, A. Buchholz, A. Ardavan and W. Plass, *Inorg. Chem.*, 2015, **54**, 3432-3438.
189. P. C. Ford, E. Cariati and J. Bourassa, *Chem. Rev.*, 1999, **99**, 3625-3648.
190. M. F. Galimova, E. M. Zueva, A. B. Dobrynin, I. E. Kolesnikov, R. R. Musin, E. I. Musina and A. A. Karasik, *Dalton Trans.*, 2021, **50**, 13421-13429.
191. A. Antiñolo, S. García-Yuste, A. Otero, J. C. Pérez-Flores, R. Reguillo-Carmona, A. M. Rodríguez and E. Villaseñor, *Organometallics*, 2006, **25**, 1310-1316.
192. A. Franken, T. D. McGrath and F. G. A. Stone, *Organometallics*, 2010, **29**, 2234-2247.
193. D. M. Stefanescu, H. F. Yuen, D. S. Glueck, J. A. Golen, L. N. Zakharov, Christopher D. Incarvito and A. L. Rheingold, *Inorg. Chem.*, 2003, **42**, 8891-8901.
194. U. Flörke and H.-J. Haupt, *Acta. Cryst. B*, 1991, **47**, 1535-1537.
195. F. Flecken, A. Knapp, T. Grell, C. Dreßler and S. Hanf, *Inorg. Chem.*, 2023, **62**, 13038-13049.
196. Z. Yu, Q.-F. Zhang, Y. Song, W.-Y. Wong, A. Rothenberger and W.-H. Leung, *EurJIC*, 2007, **2007**, 2189-2197.
197. C. D. Nicola, Effendy, F. Fazaroh, C. Pettinari, B. W. Skelton, N. Somers and A. H. White, *Inorg. Chim. Acta*, 2005, **358**, 720-734.
198. S. Jamali, M. Rashidi, M. C. Jennings and R. J. Puddephatt, *Dalton Trans.*, 2003, 2313-2317.
199. E. Baggaley, S. W. Botchway, J. W. Haycock, H. Morris, I. V. Sazanovich, J. A. G. Williams and J. A. Weinstein, *Chem. Sci.*, 2014, **5**, 879-886.
200. H. Shi, L. Song, H. Ma, C. Sun, K. Huang, A. Lv, W. Ye, H. Wang, S. Cai, W. Yao, Y. Zhang, R. Zheng, Z. An and W. Huang, *J. Phys. Chem. Lett.*, 2019, **10**, 595-600.
201. C. Lee, W. Yang and R. G. Parr, *Phys. Rev. B*, 1988, **37**, 785.
202. A. D. Becke, *J. Phys. Chem.*, 1993, **98**, 5648-5652.
203. P. J. Stephens, F. J. Devlin, C. F. Chabalowski and M. J. Frisch, *J. Chem. Phys.*, 1994, **98**, 11623-11627.
204. F. Weigend, *Phys. Chem. Chem. Phys.*, 2006, **8**, 1057-1065.
205. F. Weigend and R. Ahlrichs, *Phys. Chem. Chem. Phys.*, 2005, **7**, 3297-3305.

206. R. Schira and C. Latouche, *Dalton Trans.*, 2021, **50**, 746-753.
207. M. A. Ortuño, Núria López, M. A. Ortuño and Núria López, *Catal. Sci. Technol.*, 2019, **9**, 5173-5185.
208. A. Heuer-Jungemann, N. Feliu, I. Bakaimi, M. Hamaly, A. Alkilany, I. Chakraborty, A. Masood, M. F. Casula, A. Kostopoulou, E. Oh, K. Susumu, M. H. Stewart, I. L. Medintz, E. Stratakis, W. J. Parak and A. G. Kanaras, *Chem. Rev.*, 2019, **119**, 4819-4880.
209. K. Tamao, K. Sumitani and M. Kumada, *J. Am. Chem. Soc.*, 1972, **94**, 4374-4376.
210. M. Kumada, *Pure Appl. Chem.*, 1980, **52**, 669-679.
211. D. Lomjanský, C. Rajnák, J. Titiš, J. Moncoľ, L. Smolko and R. Boča, *Inorg. Chim. Acta*, 2018, **483**, 352-358.
212. J. A. Rahn, A. Delian and J. H. Nelson, *Inorg. Chem.*, 1989, **28**, 215-217.
213. F. Flecken, T. Grell and S. Hanf, PSP-coordinated nickel(II) complexes as Kumada coupling catalysts, ChemRxiv, 2024, 10.26434/chemrxiv-2024-fdgcn,
214. A. Okuniewski, D. Rosiak, J. Chojnacki and B. Becker, *Polyhedron*, 2015, **90**, 47-57.
215. J. E. Fergusson and P. F. Heveldt, *Inorg. Chim. Acta*, 1978, **31**, 145-154.
216. H.-K. Fun, S. Chantrapromma, I. A. Razak, Q.-F. Zhang and X.-Q. Xin, *Acta. Cryst. E*, 2001, **57**, m190-m191.
217. W. Kläui, W. Eberspach and R. Schwarz, *J. Organomet. Chem.*, 1983, **252**, 347-357.
218. P. Porta, A. Sgamellotti and N. Vinciguerra, *Inorg. Chem.*, 1971, **10**, 541-547.
219. J. M. Coleman and L. F. Dahl, *J. Am. Chem. Soc.*, 1967, **89**, 542-552.
220. S. Ataie and R. T. Baker, *Inorg. Chem.*, 2022, **61**, 19998-20007.
221. A. Neyyathala, E. Fako, S. De, D. Gashnikova, F. Maurer, J.-D. Grunwaldt, S. A. Schunk and S. Hanf, *Small Structures*, 2025, **6**, 2400260.
222. N. Palaychuk, T. J. DeLano, M. J. Boyd, J. Green and U. K. Bandarage, *Org. Lett.*, 2016, **18**, 6180-6183.
223. A. W. Dombrowski, N. J. Gesmundo, A. L. Aguirre, K. A. Sarris, J. M. Young, A. R. Bogdan, M. C. Martin, S. Gedeon and Y. Wang, *ACS Med. Chem. Lett.*, 2020, **11**, 597-604.
224. R. Jana, T. P. Pathak and M. S. Sigman, *Chem. Rev.*, 2011, **111**, 1417-1492.
225. A. Piontek, W. Ochędzan-Siodłak, E. Bisz and M. Szostak, *Adv. Synth. Catal.*, 2019, **361**, 2329-2336.
226. Y. An, Y. Ren, M. Bick, A. Dudek, E. H.-W. Waworuntu, J. Tang, J. Chen and B. Chang, *Biosens. Bioelectron.*, 2020, **154**, 112078.
227. O. Fuhr, S. Dehnen and D. Fenske, *Chem. Soc. Rev.*, 2013, **42**, 1871-1906.
228. V. W.-W. Yam and K. M.-C. Wong, in *Nanoscale Phenomena*, eds. Z. Tang and P. Sheng, Springer, New York, 2008, vol. 2.
229. S. Dehnen, D. Fenske and A. C. Deveson, *J. Clust. Sci.*, 1996, **7**, 351-369.
230. X. Yang, I. Isaac, C. Persau, R. Ahlrichs, O. Fuhr and D. Fenske, *Inorg. Chim. Acta*, 2014, **421**, 233-245.
231. A. Jana, S. Duary, A. Das, A. R. Kini, S. Acharya, J. Machacek, B. Pathak, T. Base and T. Pradeep, *Chem. Sci.*, 2024, **15**, 13741-13752.
232. P. Alayoglu, S. C. Rathnayaka, T. Chang, S. G. Wang, Y.-S. Chen and N. P. Mankad, *Chem. Sci.*, 2024, **15**, 13668-13675.
233. Q.-J. Wu, D.-H. Si, P.-P. Sun, Y.-L. Dong, S. Zheng, Q. Chen, S.-H. Ye, D. Sun, R. Cao and Y.-B. Huang, *Angew. Chem., Int. Ed.*, 2023, **62**, e202306822.
234. F. Li and Q. Tang, *Journal of Catalysis*, 2020, **387**, 95-101.
235. Q. Tang, Y. Lee, D.-Y. Li, W. Choi, C. W. Liu, D. Lee and D. Jiang, *J. Am. Chem. Soc.*, 2017, **139**, 9728-9736.
236. P.-P. Sun, B.-L. Han, H.-G. Li, C.-K. Zhang, X. Xin, J.-M. Dou, Z.-Y. Gao and D. Sun, *Angew. Chem., Int. Ed.*, 2022, **61**, e202200180.
237. H. Li, H. Zhai, C. Zhou, Y. Song, F. Ke, W. W. Xu and M. Zhu, *J. Phys. Chem. Lett.*, 2020, **11**, 4891-4896.
238. Y.-J. Cheng, R.-R. Wu, J.-Q. Zhao, E.-X. Chen, X. Zhou, Y. Dai, H.-L. Zheng and Q. Lin, *Cryst. Growth Des.*, 2023, **23**, 5421-5427.
239. G.-N. Liu, R.-D. Xu, J.-S. Guo, J.-L. Miao, M.-J. Zhang and C. Li, *J. Mater. Chem. C*, 2021, **9**, 8589-8595.

240. S. W. Jaros, J. Sokolnicki, A. Wołoszyn, M. Haukka, A. M. Kirillov and P. Smoleński, *J. Mater. Chem. C*, 2018, **6**, 1670-1678.
241. F. Sabin, C. K. Ryu, P. C. Ford and A. Vogler, *Inorg. Chem.*, 1992, **31**, 1941-1945.
242. A. Avdeef and J. J. P. Fackler, *Inorg. Chem.*, 1978, **17**, 2182-2187.
243. M. Stollenz and F. Meyer, *Organometallics*, 2012, **31**, 7708-7727.
244. H. T. Evans, *Z. Kristallogr. – Cryst. Mater.*, 1979, **150**, 299-320.
245. S. Bestgen, O. Fuhr, P. W. Roesky and D. Fenske, *Dalton Trans.*, 2016, **45**, 14907-14910.
246. C.-R. Wang, K. K.-W. Lo and V. W.-W. Yam, *Chem. Phys. Lett.*, 1996, **262**, 91-96.
247. C.-R. Wang, K. K.-W. Lo and V. W.-W. Yam, *J. Chem. Soc., Dalton Trans.*, 1997, 227-230.
248. C. G. Barlow, J. F. Nixon and M. Webster, *J. Chem. Soc. A.*, 1968, **0**, 2216-2223.
249. N. Fey, M. Garland, J. P. Hopewell, C. L. McMullin, S. Mastroianni, A. G. Orpen and P. G. Pringle, *Angew. Chem., Int. Ed.*, 2012, **51**, 118-122.
250. N. Fey, A. G. Orpen and J. N. Harvey, *Coord. Chem. Rev.*, 2009, **253**, 704-722.
251. F. D. Calvo, V. Mirabello, M. Caporali, W. Oberhauser, K. Raltchev, K. Karaghiosoff and M. Peruzzini, *Dalton Trans.*, 2016, **45**, 2284-2293.
252. P. M. Miura-Akagi, T. W. Chapp, W. Y. Yoshida, G. P. A. Yap, A. L. Rheingold, R. P. Hughes and M. F. Cain, *Organometallics*, 2023, **42**, 672-688.
253. M. Pabel, A. C. Willis and S. B. Wild, *Angew. Chem., Int. Ed.*, 1994, **33**, 1835-1837.
254. M. Fild and R. Schmutzler, *J. Chem. Soc. A.*, 1970, 2359-2364.
255. L. Riesel, D. Sturm, A. Nagel, S. Taudien, A. Beuster and A. Karwatzki, *Z. Anorg. Allg. Chem.*, 1986, **542**, 157-166.
256. D. Gudat, A. Haghverdi, H. Hupfer and M. Nieger, *Chem. Eur. J.*, 2000, **6**, 3414-3425.
257. L. Riesel, J. Haenel and G. Ohms, *J. Fluor. Chem.*, 1988, **38**, 335-340.
258. O. Stelzer and R. Schmutzler, *J. Chem. Soc. A.*, 1971, **0**, 2867-2873.
259. A. B. Burg, *Inorg. Nucl. Chem. Letters*, 1977, **13**, 199-203.
260. L. Heuer, P. G. Jones and R. Schmutzler, *J. Fluor. Chem.*, 1990, **46**, 243-254.
261. F. C. Bradley and E. H. Wong, *Inorg. Chim. Acta*, 1986, **120**, L21-L22.
262. R. H. Morris, J. F. Sawyer, C. T. Schweitzer and A. Sella, *Organometallics*, 1989, **8**, 2099-2106.
263. S. A. Macgregor, D. C. Roe, W. J. Marshall, K. M. Bloch, V. I. Bakhmutov and V. V. Grushin, *J. Am. Chem. Soc.*, 2005, **127**, 15304-15321.
264. V. V. Grushin and W. J. Marshall, *J. Am. Chem. Soc.*, 2004, **126**, 3068-3069.
265. A. W. Kyri, G. Schnakenburg and R. Streubel, *Organometallics*, 2017, **36**, 3605-3612.
266. J. B. Diccianni and T. Diao, *Trends. Chem.*, 2019, **1**, 830-844.
267. Z. Li and L. Liu, *Chinese J. Catal.*, 2015, **36**, 3-14.
268. S. Z. Tasker, E. A. Standley and T. F. Jamison, *Nature*, 2014, **509**, 299-309.
269. V. P. Ananikov, *ACS Catal.*, 2015, **5**, 1964-1971.
270. S.-S. Wang and G.-Y. Yang, *Catal. Sci. Technol.*, 2016, **6**, 2862-2876.
271. V. M. Chernyshev and V. P. Ananikov, *ACS Catal.*, 2022, **12**, 1180-1200.
272. A. K. Cooper, M. E. Greaves, W. Donohoe, P. M. Burton, T. O. Ronson, A. R. Kennedy and D. J. Nelson, *Chem. Sci.*, 2021, **12**, 14074-14082.
273. A. K. Cooper, D. K. Leonard, S. Bajo, P. M. Burton and D. J. Nelson, *Chem. Sci.*, 2020, **11**, 1905-1911.
274. O. Kühl, P. C. Junk and E. Hey-Hawkins, *Z. Anorg. Allg. Chem.*, 2000, **626**, 1591-1594.
275. J. Mautz, K. Heinze, H. Wadepohl and G. Huttner, *EurJIC*, 2008, **2008**, 1413-1422.
276. T. Tanase, H. Takahata and Y. Yamamoto, *Inorg. Chim. Acta*, 1997, **264**, 5-9.
277. E. A. Standley, S. J. Smith, P. Müller and T. F. Jamison, *Organometallics*, 2014, **33**, 2012-2018.
278. E. Richmond and J. Moran, *Synth.*, 2018, **50**, 499-513.
279. V. T. Tran, N. Kim, C. Z. Rubel, X. Wu, T. Kang, T. C. Jankins, Z.-Q. Li, M. V. Joannou, S. Ayers, M. Gembicky, J. Bailey, E. J. Sturgell, B. B. Sanchez, J. S. Chen, S. Lin, M. D. Eastgate, S. R. Wisniewski and K. M. Engle, *Angew. Chem., Int. Ed.*, 2023, **62**, e202211794.

280. V. T. Tran, Z.-Q. Li, O. Apolinar, J. Derosa, M. V. Joannou, S. R. Wisniewski, M. D. Eastgate and K. M. Engle, *Angew. Chem., Int. Ed.*, 2020, **59**, 7409-7413.
281. L. Nattmann and J. Cornella, *Organometallics*, 2020, **39**, 3295-3300.
282. L. Nattmann, R. Saeb, N. Nöthling and J. Cornella, *Nat. Catal.*, 2020, **3**, 6-13.
283. E. A. Standley and T. F. Jamison, *J. Am. Chem. Soc.*, 2013, **135**, 1585-1592.
284. J. B. Sweeney, A. K. Ball, P. A. Lawrence, M. C. Sinclair and L. J. Smith, *Angew. Chem., Int. Ed.*, 2018, **57**, 10202-10206.
285. S. Hanf, T. Grell, J. E. Waters, R. García-Rodríguez, E. Hey-Hawkins and D. S. Wright, *Chem. Commun.*, 2020, **56**, 7893-7896.
286. J. Reedijk, *Comments Inorganic Chem.*, 1981, **1**, 379-389.
287. R. F. Jordan, W. E. Dasher and S. F. Echols, *J. Am. Chem. Soc.*, 1986, **108**, 1718-1719.
288. M. R. Mason and J. G. Verkade, *Organometallics*, 1990, **9**, 864-865.
289. P. A. McLaughlin and J. G. Verkade, *Organometallics*, 1998, **17**, 5937-5940.
290. M. R. Mason and J. G. Verkade, *Organometallics*, 1992, **11**, 2212-2220.
291. W. S. Sheldrick and O. Stelzer, *J. Chem. Soc., Dalton Trans.*, 1973, 926-929.
292. F. Flecken, A. Neyyathala, T. Grell and S. Hanf, A bench-stable fluorophosphine nickel(0) complex and its catalytic application, ChemRxiv, 2024, 10.26434/chemrxiv-2024-vtmqd,
293. A. F. Gushwa, Y. Belabassi, J.-L. Montchamp and A. F. Richards, *J. Chem. Crystallogr.*, 2008, **39**, 337-347.
294. L. P. Miller, J. A. Vogel, S. Harel, J. M. Krussman and P. R. Melvin, *Org. Lett.*, 2023, **25**, 1834-1838.
295. B. Bogdanović, M. Kröner and G. Wilke, *Justus Liebigs Annalen der Chemie*, 1966, **699**, 1-23.
296. C. A. Tolman, W. C. Seidel and L. W. Gosser, *J. Am. Chem. Soc.*, 1974, **96**, 53-60.
297. J. F. Nixon and R. Schmutzler, *Spectrochim. Acta A*, 1964, **20**, 1835-1842.
298. A. K. Cooper, P. M. Burton and D. J. Nelson, *Synth.*, 2020, **52**, 565-573.
299. V. V. Grushin and H. Alper, *Chem. Rev.*, 1994, **94**, 1047-1062.
300. F.-S. Han, *Chem. Soc. Rev.*, 2013, **42**, 5270-5298.
301. A. J. Nett, W. Zhao, P. M. Zimmerman and J. Montgomery, *J. Am. Chem. Soc.*, 2015, **137**, 7636-7639.
302. D. D. Dawson, V. F. Oswald, A. S. Borovik and E. R. Jarvo, *Chem. Eur. J.*, 2020, **26**, 3044-3048.
303. D. Gärtner, S. Sandl and A. J. v. Wangelin, *Catal. Sci. Technol.*, 2020, **10**, 3502-3514.
304. D. R. Anton and R. H. Crabtree, *Organometallics*, 1983, **2**, 855-859.
305. T. M. Maier, S. Sandl, P. Melzl, J. Zweck, A. J. v. Wangelin and R. Wolf, *Chem. Eur. J.*, 2020, **26**, 6113-6117.
306. S. Baweja, T. Gabler, P. Lönnecke and E. Hey-Hawkins, *Dalton Trans.*, 2023, **52**, 6494-6500.
307. J. Hamlin, K. Hirai, A. Millan and P. M. Maitlis, *J. Mol. Catal. A Chem.*, 1980, **7**, 543-544.
308. J. M. Thomas, R. Raja and D. W. Lewis, *Angew. Chem., Int. Ed.*, 2005, **44**, 6456-6482.
309. MestReNova, Mestrelab Research S.L., Santiago de Compostela, Spain, 2020
310. OriginPro, OriginLab Corporation, Northampton, MA, USA, 2022
311. C. F. Macrae, I. Sovago, S. J. Cottrell, P. T. A. Galek, P. McCabe, E. Pidcock, M. Platings, G. P. Shields, J. S. Stevens, M. Towler and P. A. Wood, *J. Appl. Crystallogr.*, 2020, **53**, 226-235.
312. Stoe&Cie, X-RED, Program for data reduction and absorption correction, Stoe & Cie GmbH, Darmstadt, Germany, 2005
313. G. M. Sheldrick, *Acta. Cryst. A*, 2015, **71**, 3-8.
314. G. M. Sheldrick, *Acta. Cryst. B*, 2015, **71**, 3-8.
315. L. J. Farrugia, *J. Appl. Crystallogr.*, 2012, **45**, 849-854.
316. K. Brandenburg and M. Berndt, Diamond - Crystal and Molecular Structure Visualization, Crystal Impact, Bonn, Germany, 1999
317. J. C. d. Mello, H. F. Wittmann and R. H. Friend, *Adv. Mater.*, 1997, **9**, 230-232.

318. M. Dahlen, E. H. Hollesen, M. Kehry, M. T. Gamer, S. Lebedkin, D. Schooss, M. M. Kappes, W. Klopper and P. W. Roesky, *Angew. Chem., Int. Ed.*, 2021, **60**, 23365-23372.
319. F. Neese, *WIREs Comput. Mol. Sci.*, 2017, **8**, e1327.
320. F. Neese, *WIREs Comput. Mol. Sci.*, 2011, **2**, 73-78.
321. S. Grimme, J. Antony, S. Ehrlich and H. Krieg, *J. Phys. Chem.*, 2010, **132**, 154104.
322. S. Grimme, S. Ehrlich and L. Goerigk, *J. Comp. Chem.*, 2011, **32**, 1456-1465.
323. F. Neese, F. Wennmohs, A. Hansen and U. Becker, *Chem. Phys.*, 2009, **356**, 98-109.
324. A. D. Becke, *Phys. Rev. A*, 1988, **38**, 3098.
325. E. Caldeweyher, C. Bannwarth and S. Grimme, *J. Phys. Chem.*, 2017, **147**, 034112.
326. T. Yanai, D. P. Tew and N. C. Handy, *Chem. Phys. Lett.*, 2004, **393**, 51-57.
327. C. Adamo and V. Barone, *J. Phys. Chem.*, 1999, **110**, 6158-6170.
328. Y. Zhao and D. G. Truhlar, *J. Phys. Chem.*, 2006, **125**, 194101.
329. J. Sun, A. Ruzsinszky and J. P. Perdew, *Phys. Rev. Lett.*, 2015, **115**, 036402.
330. A. Najibi and L. Goerigk, *J. Chem. Theory Comput.*, 2018, **14**, 5725-5738.
331. B. d. Souza, G. Farias, F. Neese and R. Izsák, *J. Chem. Theory Comput.*, 2019, **15**, 1896-1904.
332. R. Ahlrichs and K. May, *Phys. Chem. Chem. Phys.*, 2000, **2**, 943-945.
333. J. Tao, J. P. Perdew, V. N. Staroverov and G. E. Scuseria, *Phys. Rev. Lett.*, 2003, **91**, 146401-146404.
334. V. N. Staroverov, G. E. Scuseria, J. Tao and J. P. Perdew, *J. Phys. Chem.*, 2004, **121**, 11507.
335. C. M. Breneman and K. B. Wiberg, *J. Comp. Chem.*, 1990, **11**, 361-373.
336. A. E. Reed, L. A. Curtiss and F. Weinhold, *Chem. Rev.*, 1988, **88**, 899-926.
337. A. E. Reed, R. B. Weinstock and F. Weinhold, *J. Phys. Chem.*, 1985, **83**, 735-746.
338. E. D. Glendening, K. B. J, A. E. Reed, J. E. Carpenter, J. A. Bohmann, C. M. Morales, P. Karafiloglou, C. R. Landis and F. Weinhold, NBO 7.0, Theoretical Chemistry Institute, University of Wisconsin, Madison, 2018
339. C. Adamo and D. Jacquemin, *Chem. Soc. Rev.*, 2013, **42**, 845-856.
340. A. Sen, T.-W. Lai and R. R. Thomas, *J. Organomet. Chem.*, 1988, **358**, 567-588.
341. H. Schmidbaur, A. Wohlleben, F. Wagner, O. Orama and G. Huttner, *Chem. Ber.*, 1977, **110**, 1748-1754.
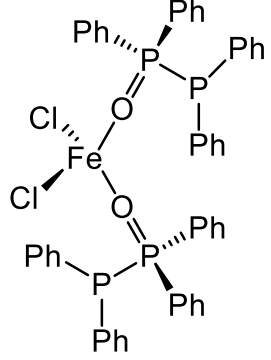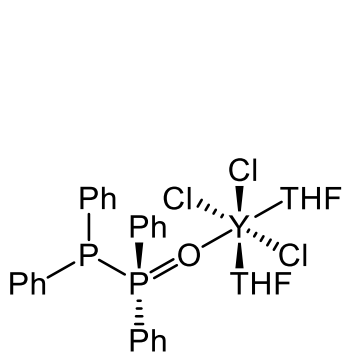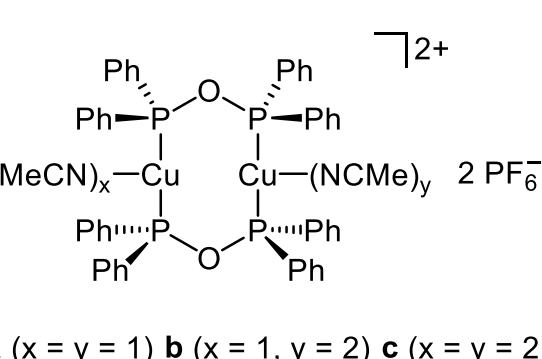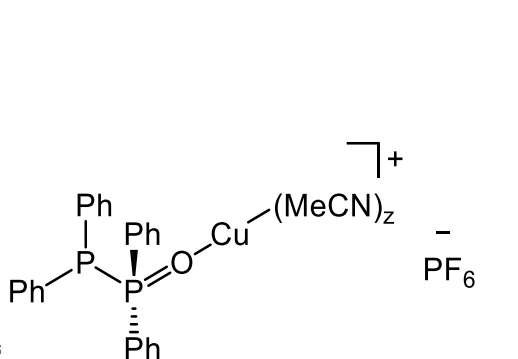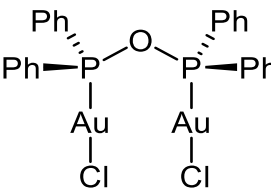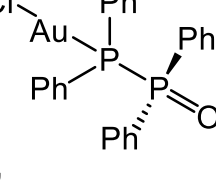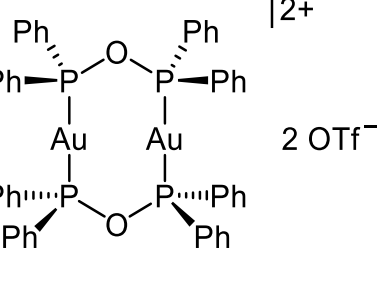
11 Appendix

11.1 Colour code for solid state structures
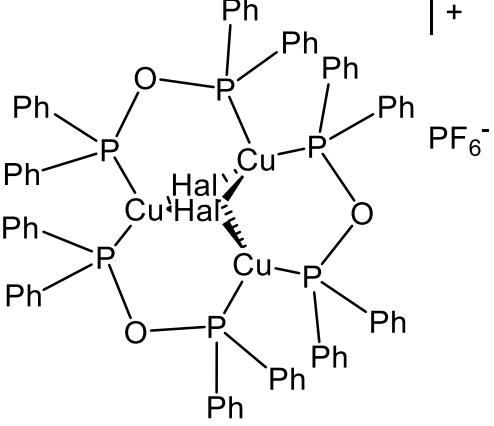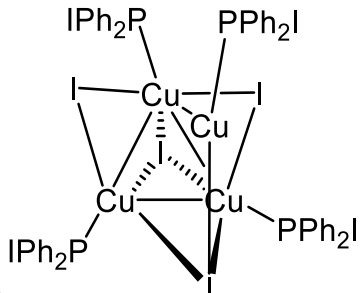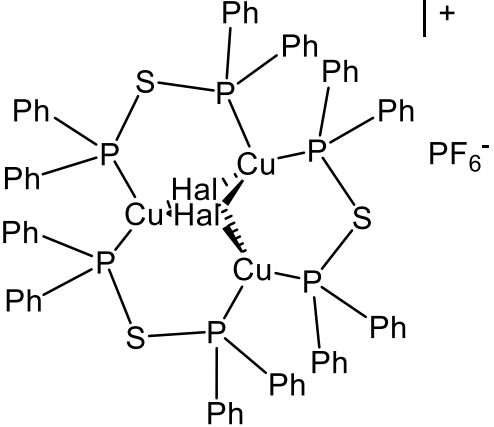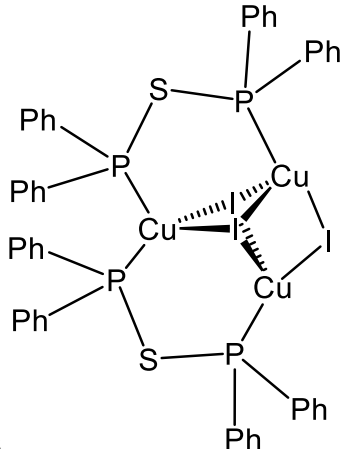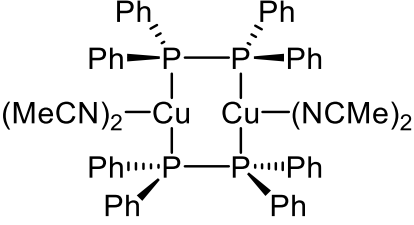
P	
O	
C	
S	
N	
Fe	
Ni	
Cu	
½ Cu	
Y	
Au	
F	
Cl	
Br	
I	
B	

11.2 Overview of numbered compounds
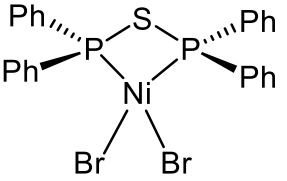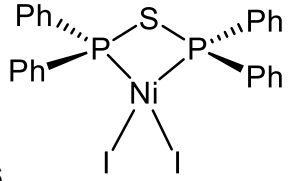
Transition metal complexes of the PPO/POP-based ligand
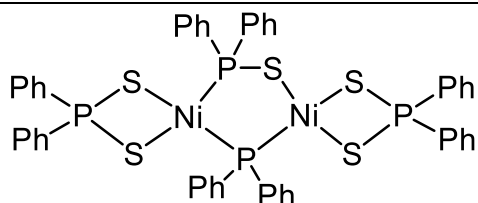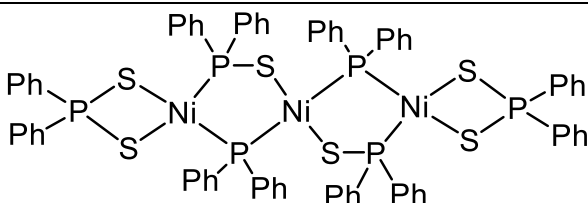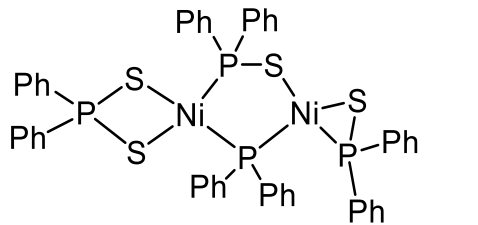
1	**2**
3 **a** (x = y = 1) **b** (x = 1, y = 2) **c** (x = y = 2)	**3'**
4	**4'**
5	

Trinuclear copper complexes and photo-optical properties

6 Hal = Cl
7 Hal = Br
8 Hal = I

9

10 Hal = Cl
11 Hal = Br
12 Hal = I

13

14

Short-bite PSP-type ligands for nickel halide complexes
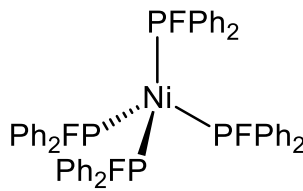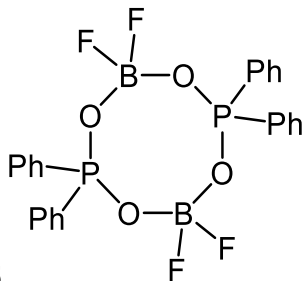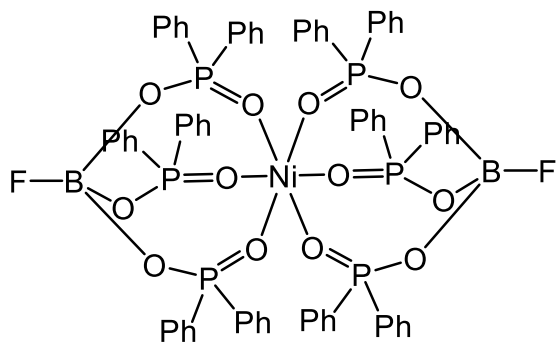
15

16

 17	 **18**
 19	

Diphenylphosphine sulphide-stabilised coinage metal clusters

20 $[Au_6(Ph_2PS)_6]$	**21** $[Cu_{14}S(Ph_2PS)_{12}]$
22 $[Cu_{24}S_6(Ph_2PS)_{12}]$	**23** $[Cu_4(Ph_2PS)_4(dppe)_2]$

A bench-stable fluorophosphine nickel(0) complex and its catalytic application

 24	 **25**
 26	

11.3 Abbreviations

BINAP	2,2′-bis(diphenylphosphino)-1,1′-binaphthyl
^{3}CC	Triplet cluster centred
COD	1,5-cyclooctadiene
δ	Chemical shift
DCM	Dichloromethane
DFT	Density functional theory
DIOP	2,3-*O*-isopropylidene-2,3-dihydroxy-1,4-bis(diphenylphosphino)butane
DPEphos	Bis[(2-diphenylphosphino)phenyl] ether
Dppa	1,1-Bis(diphenylphosphino)amine
Dppb	1,4-Bis(diphenylphosphino)butane
Dppe	1,2-Bis(diphenylphosphino)ethane
Dppm	1,1-Bis(diphenylphosphino)methane
Dppp	1,3-Bis(diphenylphosphino)propane
EPR	Electron paramagnetic resonance
ESI-MS	Electrospray Ionization Mass Spectrometry
EWG	Electron withdrawing group
GGA	Generalized Gradient Approximation
h	Hour
HE	High energy
HOMO	Highest occupied molecular orbital
HSAB	Hard and soft Lewis acids and bases
IC	Internal conversion
IR spectroscopy	Infrared spectroscopy
ISC	Intersystem crossing
Josiphos	*R*)-1-[(*S*$_P$)-2-(diphenylphosphino)-ferrocenyl]-ethyldicyclohexylphosphine
K	Kelvin
kJ	Kilojoule
KPO	Potassium diphenylphosphine oxide
KPS	Potassium diphenylphosphine sulphide
LE	Low energy
LMCT	Ligand to metal charge transfer
LUMO	Lowest unoccupied molecular orbital
MC	Metal centred
Me	Methyl
MeCN	Acetonitrile
Mes	Mesityl
MLCT	Metal to ligand charge transfer
M–M	Metal–metal (distance)
m.p.	Melting point
MS	Mass spectrometry
NBO	Natural bond orbital

NIR	Near-infrared
NMR	Nuclear magnetic resonance spectroscopy
NPA	Natural population analysis
PCP	Class of ligands based on a P–$(CH_2)_n$–P bridge; n = 1, 2, 3, etc.
Ph	Phenyl
PL	Photo-luminescence emission
PLE	Photo-luminescence excitation
PNP	Class of ligands based on a P–N(R)–P bridge; N = alkyl, aryl
POP	Class of ligands based on a P–O–P bridge: R_2P–O–PR_2; in this work POP is specifically used for R = Ph
ppm	Parts per million
PPN	Iminobiphosphines, R_2P–PR_2=N–R'
PPO	Tautomer R_2P(=O)–PR_2 of POP
PPS	Tautomer R_2P(=S)–PR_2 of POP
PPX/PXP	X = O, S
PS	Ph_2PS^-
PSP	Class of ligands based on a P–S–P bridge: R_2P–S–PR_2; in this work POP is specifically used for R = Ph
PXRD	Powder XRD
Ref	Reference catalysts ($[NiBr_2dppe]$)
RISC	Reverse intersystem crossing
r.t.	Room temperature
S_0/S_1	Singlet ground (S_0) and excited (S_1) state
SOC	Spin-orbit coupling
SMCT	Sulphur to metal charge transfer
SPO	Secondary phosphine oxide
T_1	Triplet excited state
TADF	Thermally-activated delayed fluorescence
^{t}-Bu	Tert Buthyl
TD	Time dependent density-functional theory
Tamm−Dancoff approximation	Tamm−Dancoff approximation
TEP	Tolman electronic parameter
THF	Tetrahydrofuran
TM	Transition metal
Tol	Toluene
$\tau_{eff.}$	Effective lifetime
τ'_4	Structural index parameter
UV/Vis	Ultraviolet/Visible
Xantphos	4,5-bis(diphenylphosphino)-9,9-dimethylxanthene
XLCT	Halogen-to-ligand charge transfer
XRD	X-ray diffraction

11.4 Analytical and reference data

Table 15. Comparison of P–X–P angles [°] of **3-5** with literature known dppa and dppm analogues and variation Δ of this angle in the different compounds for the POP-, PNP- and PCP-compounds. Y = PF_6^-, BF_4^-, SbF_6^-, ClO_4^-.

PXP	[Cu$_2$(PXP)$_2$]Y$_2$	[Au$_2$Cl$_2$(PXP)]	[Au$_2$(PXP)$_2$]Y$_2$	Δ of P–X–P angles
POP	119.85(12)	125.3(2)	131.2(2)–131.7(2)	11.9
dppa	123.1(4)[22]	122.4(4)[a][161]	117(1)[118]	6.1
dppm	113.63(6)[159]	115.62[341]	112.6(3)[163]	3.0

[a] N(R): ethyl
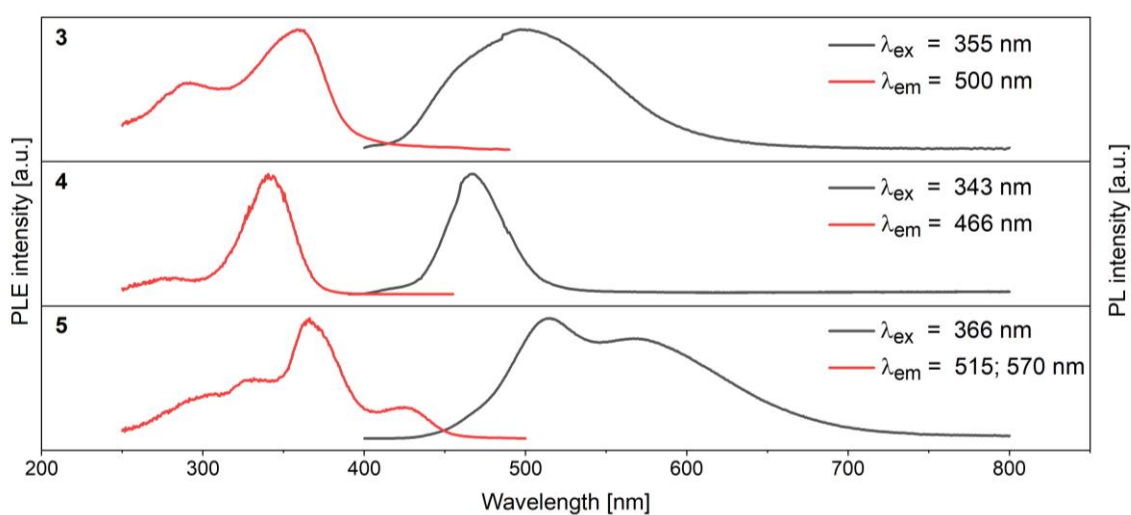
Figure 53. Photo-luminescence excitation (PLE, red) and emission (PL, black) spectra of **3-5** at 77 K in DCM solution.
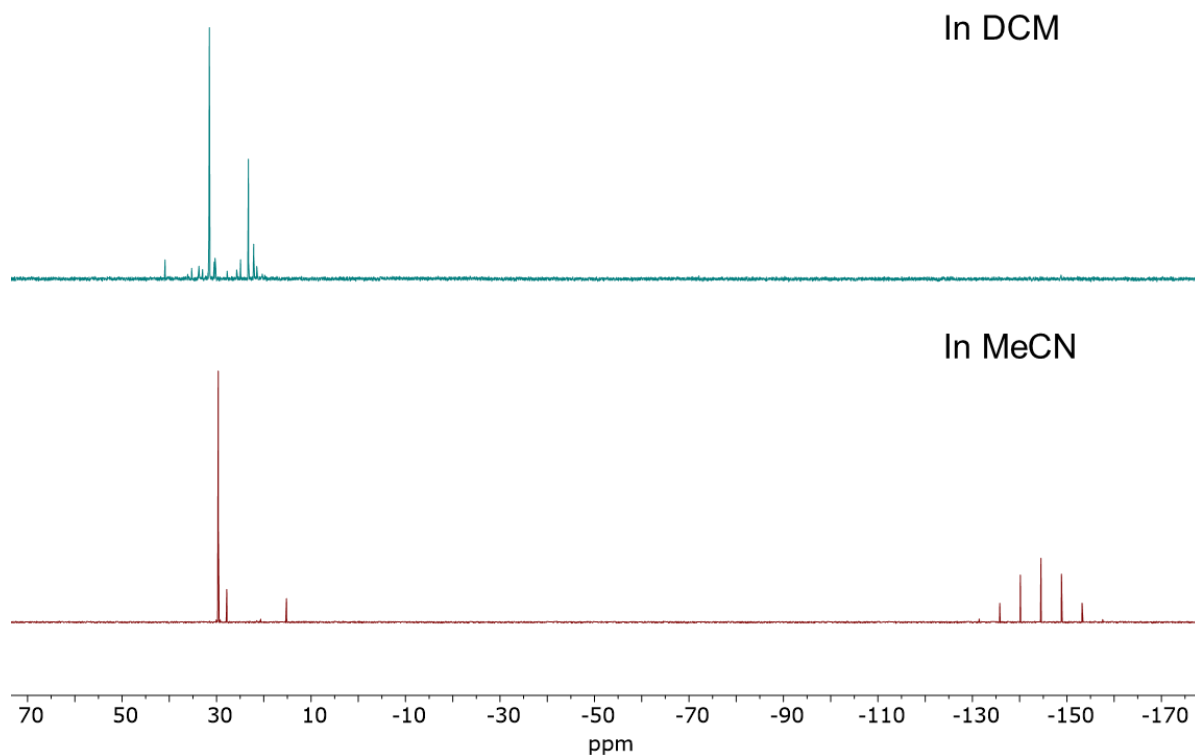
Figure 54. $^{31}P\{^1H\}$ NMR spectra of reaction mixtures of Ullmann-type couplings using **3** in DCM and **3'** in MeCN as (pre-)catalysts.
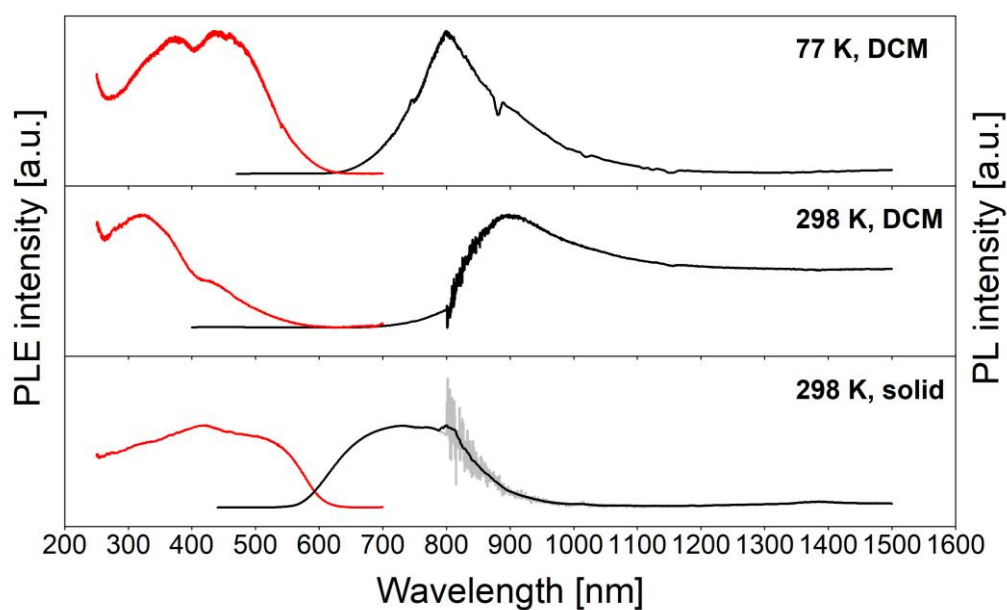
Figure 55. Photo-luminescence excitation (PLE, red) and emission (PL, black) spectra of **22** at 77 K in DCM solution ($3 \cdot 10^{-5}$ M), at 298 K in DCM solution ($3 \cdot 10^{-5}$ M) and at 298 K in the solid state. Starting from a wavelength of 800-1500 nm, a different detector has to be used, which is less sensitive. Therefore, correction of the graphs had to be conducted for the two r.t. samples. In the 298 K solid sample the graph was smoothened, whereby the original graph is indicated in grey.
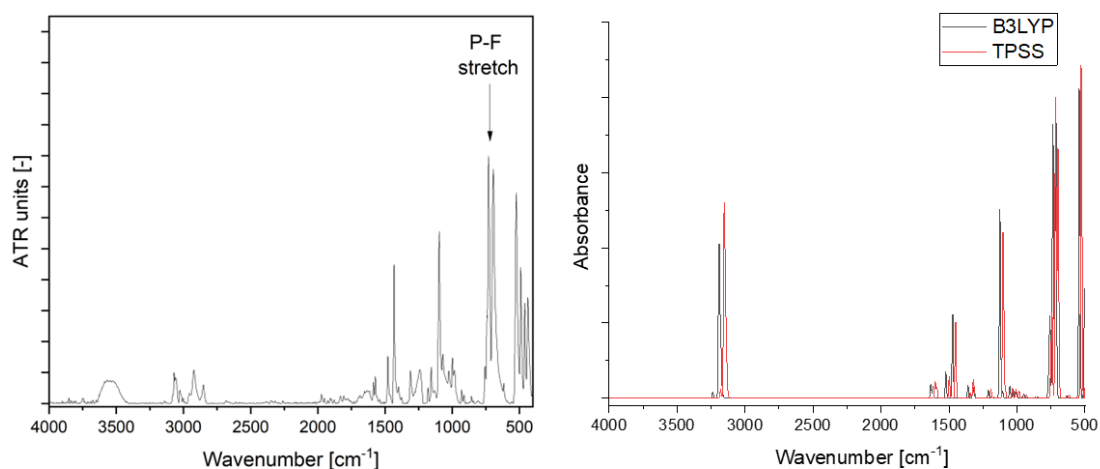
Figure 56. Recorded IR spectra of **24 (**298 K, left) and calculated IR spectra of **24** (right). This figure has been adapted from [292] (license BY NC ND 4.0).
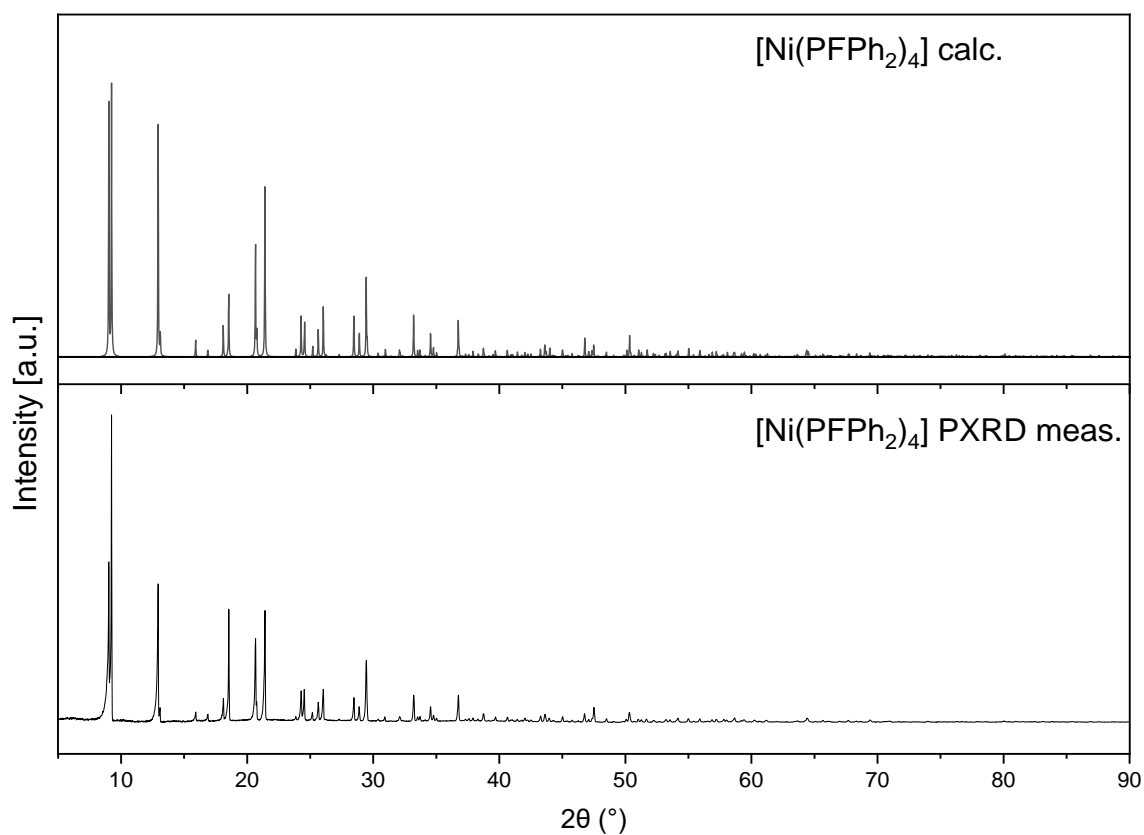
Figure 57. Calculated (top) and recorded (bottom) powder PXRD diffractograms of **24**. This figure has been adapted from [292] (license BY NC ND 4.0).

Figure 58. Space filling diagram of **24,** confirming the steric bulk around the Ni(0) centre. This figure has been adapted from [292] (license BY NC ND 4.0).
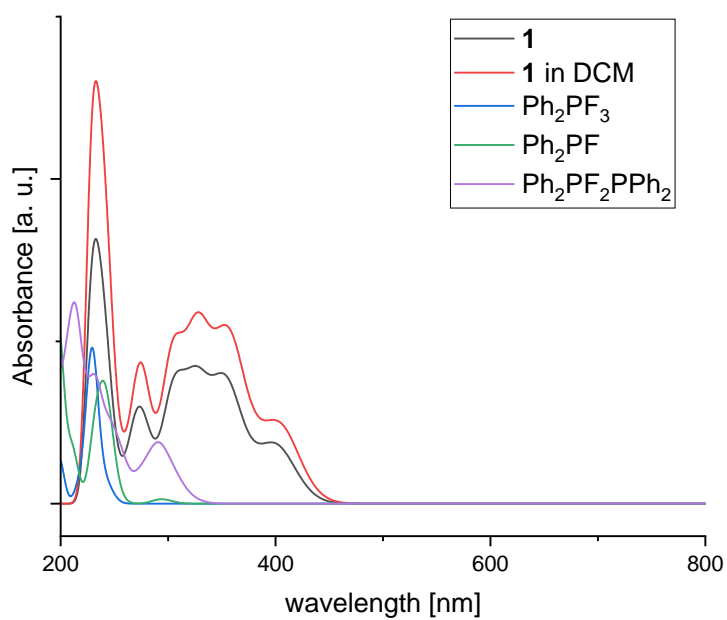
Figure 59. TD-DFT calculated UV/Vis spectra of **24** and of potential decomposition products. Level of theory: B3LYP, def2-TZV. This figure has been adapted from [292] (license BY NC ND 4.0).

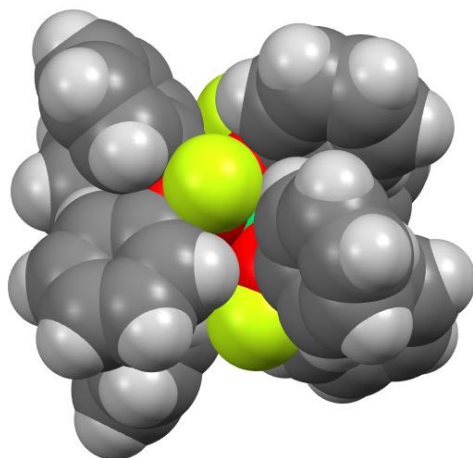| Compound	**1**	**2**·0.5THF	**3**	**4**	**5**·2.3DCM
CCDC No.	2163970	2163971	2163973	2163972	2163974
Formula	$C_{48}H_{40}Cl_2FeO_2P_4$	$C_{34}H_{40}Cl_3O_{3.50}P_2Y$	$C_{54}H_{49}Cu_2F_{12}N_3O_2P_6$	$C_{24}H_{20}Au_2Cl_2OP_2$	$C_{52.28}H_{44.56}Au_2Cl_{4.56}F_6O_8P_4 S_2$
Formula weight	899.43	761.86	1312.86	851.17	1658.48
Crystal system	Orthorhombic	Triclinic	Triclinic	Monoclinic	Monoclinic
Space group	$Pna2_1$	P	P	$P2_1/c$	$C2/c$
a [Å]	18.2692(8)	10.0759(11)	10.708(6)	8.9878(11)	20.9822(6)
b [Å]	10.0180(4)	10.3953(13)	12.106(8)	16.301(2)	15.6904(3)
c [Å]	23.2815(8)	16.487(2)	12.285(4)	16.7718(18)	35.7489(10)
α [°]	90	87.021(11)	112.48(4)	90	90
β [°]	90	86.896(10)	96.83(4)	102.113(9)	102.180(2)
γ [°]	90	81.16(4)	104.09(4)	90	90
V [Å³]	4261.0(3)	1702.2(4)	1386.8(13)	2402.6(5)	11504.3(5)
Z	4	2	1	4	8
Radiation type	Mo-Kα	Mo-Kα	Mo-Kα	Mo-Kα	Mo-Kα
Temp. [K]	100	100	100	100	150
μ [mm⁻¹]	0.669	2.078	1.025	12.569	5.563
Reflections collected/ unique[a]	46568 / 11147	20687 / 9113	17633 / 7480	14860 / 6619	66001 / 10752
R_{int}	0.0491	0.0647	0.0808	0.0264	0.0312
Final R indices (I > 2σ(I))[b]	$R_1 = 0.0380$, $wR_2 = 0.0784$	$R_1 = 0.0751$, $wR_2 = 0.1715$	$R_1 = 0.0553$, $wR_2 = 0.1440$	$R_1 = 0.0297$, $wR_2 = 0.0698$	$R_1 = 0.0360$, $wR_2 = 0.0901$
R indices (all data)	$R_1 = 0.0544$, $wR_2 = 0.0850$	$R_1 = 0.1143$, $wR_2 = 0.2175$	$R_1 = 0.0857$, $wR_2 = 0.1596$	$R_1 = 0.0379$, $wR_2 = 0.0731$	$R_1 = 0.0469$, $wR_2 = 0.095$
Goodness of fit[c] on F^2	1.016	1.035	1.054	1.025	1.058

Compound	$6 \cdot F\text{-}C_6H_5$	$7 \cdot DCM$	$8 \cdot DCM$	$9 \cdot 2DCM$	**10**
CCDC No.	2176829	2176828	2176834	2176831	2176830
Formula	$C_{78}H_{65}Cl_2Cu_3F_7O_3P_7$	$C_{73}H_{62}Br_2Cl_2Cu_3F_6O_3P_7$	$C_{73}H_{62}Cl_2Cu_3F_6I_2O_3P_7$	$C_{50}H_{44}Cl_4Cu_4I_8P_4$	$C_{72}H_{60}Cl_2Cu_3F_6P_7S_3$
Formula weight	1661.61	1739.35	1833.33	2179.89	1613.69
Crystal system	Monoclinic	Monoclinic	Monoclinic	Tetragonal	Monoclinic
Space group	$C2/c$	$C2/c$	$P2/c$	$P4_2/n$	$P2_1/n$
a [Å]	20.560(4)	20.473(2)	20.8074(8)	16.3887(4)	10.2889(4)
b [Å]	18.891(4)	18.4149(18)	18.2639(7)	16.3887(4)	30.3138(9)
c [Å]	20.052(4)	19.8987(17)	21.4232(8)	11.3801(3)	22.3753(11)
α [°]	90	90	90	90	90
β [°]	108.68(3)	109.647(8)	116.268(3)	90	91.545(4)
γ [°]	90	90	90	90	90
V [Å³]	7378(3)	7065.1(12)	7300.6(5)	3056.57(17)	6976.2(5)
Z	4	4	4	2	4
Radiation type	Mo-Kα	Mo-Kα	Mo-Kα	Ga-Kα	Mo-Kα
Temp. [K]	150(2)	100(2)	150(2)	150(2)	150(2)
μ [mm^{-1}]	1.147	2.324	2.000	30.572	1.292
Reflections collected/ unique[a]	58642 / 18504	30735 / 9597	56007 / 17954	30847 / 3187	58061 / 13166
R_{int}	0.0565	0.0958	0.1423	0.0301	0.0607
Final R indices (I > 2σ(I))[b]	$R_1 = 0.0404$, $wR_2 = 0.0839$	$R_1 = 0.0948$, $wR_2 = 0.1919$	$R_1 = 0.0611$, $wR_2 = 0.1652$	$R_1 = 0.0225$, $wR_2 = 0.0591$	$R_1 = 0.1009$, $wR_2 = 0.2727$
R indices (all data)	$R_1 = 0.0842$, $wR_2 = 0.0915$	$R_1 = 0.1696$, $wR_2 = 0.2141$	$R_1 = 0.0915$, $wR_2 = 0.1750$	$R_1 = 0.0322$, $wR_2 = 0.0612$	$R_1 = 0.1130$, $wR_2 = 0.2951$
Goodness of fit[c] on F^2	0.873	1.093	1.084	1.072	1.044

Compound	**11**	**12**	**13**·1.47DCM	**14**	**15**
CCDC No.	2176833	2256153	2176832	2176827	2375582
Formula	$C_{72}H_{60}Br_2Cu_3F_6P_7S_3$	$C_{72}H_{60}Cu_3F_6I_2P_7S_3$	$C_{49.47}H_{42.94}Cl_{2.94}Cu_3I_3P_4S_2$	$C_{59}H_{58}Cl_6Cu_2F_{12}N_4P_6$	$C_{24}H_{20}SP_2NiBr_2$
Formula weight	1702.61	1796.59	1501.11	1576.69	620.93
Crystal system	Orthorhombic	Monoclinic	Monoclinic	Monoclinic	Monoclinic
Space group	*Pnma*	*P2$_1$/n*	*P2$_1$/c*	*C2/c*	*P2$_1$/n*
a [Å]	30.3409(6)	10.4102(3)	13.0874(7)	22.0313(8)	8.6617(4)
b [Å]	22.3462(8)	30.2329(10)	11.8431(3)	12.4552(3)	14.1619(5)
c [Å]	10.3393(3)	22.3208(8)	35.2939(17)	27.0957(13)	19.4168(11)
α [°]	90	90	90	90	90
β [°]	90	91.003(3)	98.082(4)	111.593(3)	92.730(4)
γ [°]	90	90	90	90	90
V [Å^3]	7010.1(4)	7024.0(4)	5416.1(4)	6913.4(5)	2379.08(19)
Z	4	4	4	4	4
Radiation type	Ga-Kα	Mo-Kα	Ga-Kα	Ga-Kα	Ga-Kα
Temp. [K]	150(2)	150(2)	150(2)	150(2)	180
μ [mm^{-1}]	7.642	2.087	17.573	6.008	8.692
Reflections collected/ unique[a]	73679 / 8690	39677 / 15827	37141 / 12847	22201 / 8144	15738 / 5261
R$_{int}$	0.0199	0.0496	0.0252	0.0171	0.0219
Final R indices (I > 2σ(I))[b]	R$_1$ = 0.0370, wR$_2$ = 0.0993	R$_1$ = 0.0580, wR$_2$ = 0.1445	R$_1$ = 0.0566, wR$_2$ = 0.1506	R$_1$ = 0.0446, wR$_2$ = 0.1104	R$_1$ = 0.0276, wR$_2$ = 0.0714
R indices (all data)	R$_1$ = 0.0411, wR$_2$ = 0.1025	R$_1$ = 0.0935, wR$_2$ = 0.1606	R$_1$ = 0.0674, wR$_2$ = 0.1589	R$_1$ = 0.0522, wR$_2$ = 0.1151	R$_1$ = 0.0318, wR$_2$ = 0.0732
Goodness of fit[c] on F^2	1.026	1.030	1.026	1.021	1.044

Compound	**16**	**17**	**18**·DCM	**19**·toluene·*n*-pentane	**20**·DCM
CCDC No.	2375583	2375585	2375584	2375581	
Formula	$C_{24}H_{20}SP_2NiI_2$	$C_{48}H_{40}S_5P_4Ni_2$	$C_{74}H_{46}S_4P_6Ni_3Cl_4$	$C_{108}H_{100}S_8P_8Ni_4$	$C_{73}H_{62}P_6S_6Au_6Cl_2$
Formula weight	714.91	1018.40	1585.24	2136.96	2570.10
Crystal system	Monoclinic	Triclinic	Monoclinic	Triclinic	Triclinic
Space group	*I2*	*P*	*P2$_1$/n*	*P*	*P*
a [Å]	11.983(10)	13.7840(4)	12.1053(5)	13.2596(3)	11.5989(3)
b [Å]	7.826(4)	16.4338(5)	13.2856(4)	20.2572(6)	13.2948(4)
c [Å]	14.014(12)	21.9103(7)	22.4508(9)	20.9388(6)	13.8411(4)
α [°]	90	93.043(2)	90	115.888(2)	108.677(2)
β [°]	108.88(4)	96.228(2)	96.619(3)	99.709(2)	96.213(2)
γ [°]	90	110.795(2)	90	90.394(2)	110.081(2)
V [Å^3]	1243.5(16)	4590.0(2)	3586.6(2)	4966.7(2)	1841.07(10)
Z	2	4	2	2	1
Radiation type	Ga-Kα	Ga-Kα	Ga-Kα	Mo-Kα	Ga-Kα
Temp. [K]	150	180	180	100	150(2)
μ [mm^{-1}]	19.034	7.003	6.946	1.092	17.590
Reflections collected/ unique[a]	6318 / 1900	59741 / 18781	40865 / 8653	73285 / 24081	23483 / 8666
R$_{int}$	0.0540	0.0397	0.0266	0.0932	0.0168
Final R indices (I > 2σ(I))[b]	R$_1$ = 0.0387, wR$_2$ = 0.1099	R$_1$ = 0.0374, wR$_2$ = 0.0728	R$_1$ = 0.0319, wR$_2$ = 0.0720	R$_1$ = 0.0455, wR$_2$ = 0.1178	R$_1$ = 0.0248, wR$_2$ = 0.0618
R indices (all data)	R$_1$ = 0.0387, wR$_2$ = 0.1099	R$_1$ = 0.0797, wR$_2$ = 0.0815	R$_1$ = 0.0439, wR$_2$ = 0.0768	R$_1$ = 0.0659, wR$_2$ = 0.1294	R$_1$ = 0.0276, wR$_2$ = 0.062
Goodness of fit[c] on F^2	1.066	0.890	1.026	1.023	1.034

Compound	**21**·2THF·*n*-pentane	**22**·DCM	**23**·THF	**24**	**25**	**26**
CCDC No.				2379067	2379068	2379069
Formula	$C_{165}Cu_{14}P_{12}S_{13}O_4H_{164}$	$C_{145}H_{122}Cl_2Cu_{24}P_{12}S_{18}$	$C_{116}H_{120}Cu_4O_4P_8S_4$	$C_{48}H_{40}P_4NiF_4$	$C_{24}H_{20}B_2F_4O_4P_2$	$C_{72}H_{60}B_2F_2NiO_{12}P_6$
Formula weight	3888.93	4409.00	2208.27	875.39	531.96	1421.35
Crystal system	Monoclinic	Monoclinic	Orthorombic	Tetragonal	Monoclinic	Trigonal
Space group	C2/c	P2₁/n	Fddd	*I*4₁/*a*	*Rc*	*C*2/*c*
a [Å]	29.9614(9)	17.1253(4)	29.908(6)	19.0448(7)	18.0250(7)	13.0353(8)
b [Å]	22.6898(5)	18.0030(3)	46.663(9)	19.0448(7)	8.8487(4)	13.0353(8)
c [Å]	26.6469(10)	25.5114(6)	14.788(3)	11.2888(4)	16.7535(8)	68.555(7)
α [°]	90	90	90	90	90	90
β [°]	103.406(3)	97.831(2)	90	90	116.271(3)	90
γ [°]	90	90	90	90	90	120
V [Å³]	17621.4(10)	7792.0(3)	20638(7)	4094.5(3)	2396.14(19)	10088.1(16)
Z	4	2	8	4	4	6
Radiation type	GaKα	GaKα	Mo-Kα	Ga-Kα	Ga-Kα	Mo-Kα
Temp. [K]	150(2)	150(2)	293(2)	150(2)	180(2)	100(2)
μ [mm⁻¹]	10.820	20.023	1.072	3.841	1.436	0.500
Reflections collected/ unique[a]	52313 / 20343	46843 / 16238	24942 / 5571	5965 / 2428	13369 / 2828	13371 / 2716
R_{int}	0.0504	0.0448	0.0348	0.0143	0.0178	0.1426
Final R indices (I > 2σ(I))[b]	R_1 = 0.0593, wR_2 = 0.1223	R_1 = 0.0532, wR_2 = 0.0977	R_1 = 0.0565, wR_2 = 0.1485	R_1 = 0.0371, wR_2 = 0.0889	R_1 = 0.0295, wR_2 = 0.0847	R_1 = 0.0451, wR_2 = 0.1147
R indices (all data)	R_1 = 0.1141, wR_2 = 0.1459	R_1 = 0.1011, wR_2 = 0.1142	R_1 = 0.0716, wR_2 = 0.1560	R_1 = 0.0382, wR_2 = 0.0895	R_1 = 0.0310, wR_2 = 0.0857	R_1 = 0.0597, wR_2 = 0.1176
Goodness of fit[c] on F²	1.015	1.031	1.058	1.042	1.089	0.992

[a] $R_{int} = \Sigma|F_o^2 - F_o^2(mean)|/\Sigma F_o^2$, [b] $R_1 = \Sigma||F_o| - |F_c||/\Sigma|F_o|$, $wR_2 = \{\Sigma[w(F_o^2 - F_c^2)^2]/\Sigma[w(F_o^2)^2]\}^{1/2}$, [c] $GooF = \{S/(n-p)\}^{1/2} = \{\Sigma[w(F_o^2 - F_c^2)^2]/(n-p)\}^{1/2}$.

12 Personal data

12.1 Curriculum vitae

Name	Franziska Flecken
Date of birth	03.09.1996
Place of birth	Neuss, Germany
Marital status	Single
Gender	Female
Nationality	German

Education

11/2020 – Present	Ph.D. studies in Chemistry
	Karlsruhe Institute of Technology (KIT)
	Institute for Inorganic Chemistry
	in the group of T.T.-Prof. Dr. S. Hanf
08/2023 – 10/2023	Research stay, University of Calgary, Canada
10/2017 – 09/2020	Masters's degree in Chemistry, RWTH Aachen
	Master thesis: "Plasma Induced C–H Activation of Small Organic Molecules"
09/2017 – 02/2018	ERASMUS semester, Università di Bologna, Italy
10/2014 – 09/2017	Bachelor's degree in Chemistry, RWTH Aachen
09/2006 – 06/2014	Gymnasium Marienberg, Neuss (High school)
09/2002 – 06/2006	Münsterschule, Neuss (Elementary school)

Scholarships

05/2021 – 10/2024	PhD Scholarship of the Stiftung der Deutschen Wirtschaft
08/2023 – 10/2023	Research Travel Grant of the Karlsruhe House of Young Scientists, Karlsruhe Institute for Technology
10/2018 – 09/2019	Educational fond of the RWTH Aachen, by Fuchs Petrolub SE

12.2 Attended conferences

European Workshop on Phosphorus Chemistry (EWPC-18): 14.-16.09.2022 in Rostock, Germany (Talk: Coordination chemistry and photo-luminescence properties of PPO/POP-based transition metal complexes; F. Flecken, S. Hanf)

21st Conference on Inorganic Chemistry: 26.-28.09.2022 in Marburg, Germany (Poster presentation: Coordination chemistry of PPX/PXP-type ligands (X = O, S) and their photo-optical properties; F. Flecken, T. Grell, S. Hanf)

GeCatS Infoday "Electrification of catalytic processes": 04.12.2023 in Frankfurt, Germany (Poster presentation: Plasma-induced C–H activation of small organic molecules; F. Flecken, S. Hanf, I. Jevtovikj, S. A. Schunk)

European Workshop on Phosphorus Chemistry (EWPC-20): 04.-06.03.2024 in Würzburg, Germany (Poster presentation: Transition metal complexes of tautomeric PPX/PXP (X = O, S) ligands; F. Flecken, T. Grell, S. Hanf)

12.3 Publications

Peer-reviewed articles
Transition metal complexes of the PPO/POP ligand: variable coordination chemistry and photo-luminescence properties, F. Flecken, T. Grell and S. Hanf, *Dalt. Trans.*, **2022**, 51, 8975-8985.

A supported Palladium Phosphide Catalyst for the Wacker-Tsuji-Oxidation of Styrene, F. Flecken,[+] A. Neyyathala,[+] S. Hanf, *ChemplusChem*, **2023**, 88, e202200431

Acute Bite Angle POP- and PSP-Type Ligands and Their Trinuclear Copper(I) Complexes: Synthesis and Photo-Luminescence Properties, F. Flecken, A. Knapp, T. Grell, C. Dreßler, S. Hanf, Inorg. Chem., **2023**, 62, 13038-13049

Support Engineering for the Stabilisation of Heterogeneous Pd_3P-Based Catalysts for Heck Coupling Reactions, F. Flecken,[+] A. Neyyathala,[+] F. Rang, C. Papke, S. Hanf, *Chem. Eur. J.*, **2024,** 30, e202402825

PPX/PXP-type ligands (X = O and S) and their transition metal complexes: synthesis, properties and applications, F. Flecken and S. Hanf, *Dalton Trans.*, **2024**, 53, 17123-17131.

Binuclear gold phosphine complexes as single-source precursors for CO oxidation catalysts: insights into the formation of surface-stabilized Au particles, F. Rang, T. Delrieux, F. Maurer, F. Flecken, J.-D. Grunwaldt, S. Hanf, *Small Sci.*, **2024**, 4, 2400345

Other publications
Blickpunkt Anorganik: Was ein Einzelnes vermag – Single Atom Catalysts, F. Flecken and S. Hanf, *Nachrichten aus der Chemie*, **2021**, 69, 58-61.

PSP-coordinated nickel(II) complexes as Kumada coupling catalysts, F. Flecken, T. Grell, S. Hanf, **2024**, DOI: 10.26434/chemrxiv-2024-fdgcn[§]

A bench-stable fluorophosphine nickel(0) complex and its catalytic application, F. Flecken, A. Neyyathala, T. Grell, S. Hanf, **2024**, DOI: 10.26434/chemrxiv-2024-vtmqd[§]

[+] These authors have contributed equally to this work

[§] The manuscript was uploaded on ChemRxiv® and/or submitted to a peer-reviewed journal at the time of the submission of the thesis